Comptes Rendus
de l'Académie des sciences

Physique

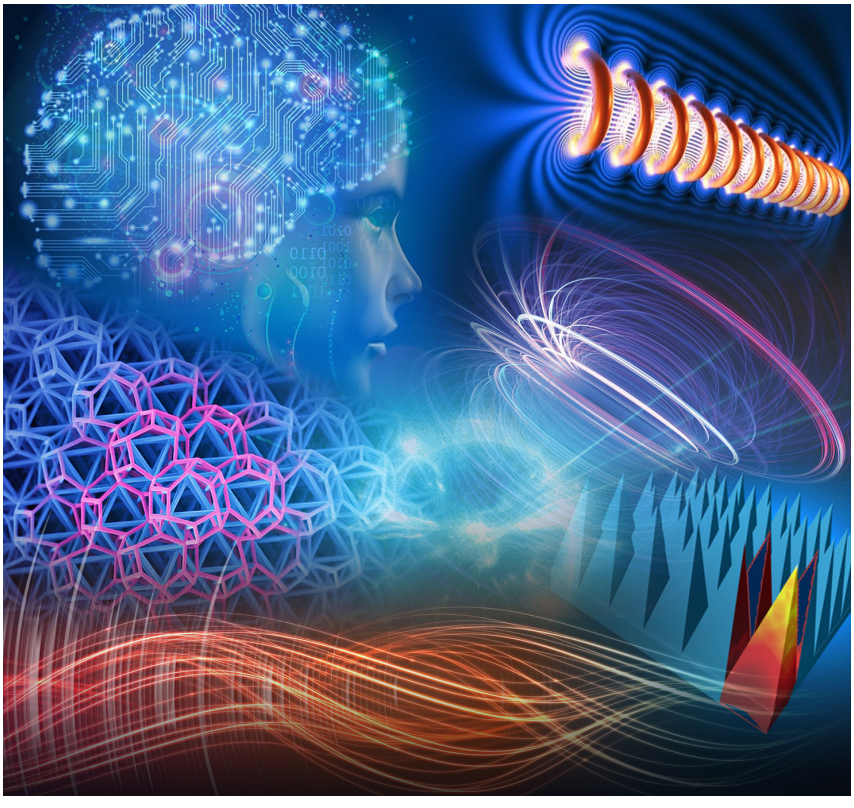

Volume 25, Special Issue S1, 2024

Special issue / *Numéro spécial*

Energy in the heart of EM waves: modelling, measurements and management / *L'énergie au cœur des ondes électromagnétiques : modélisation, mesures et gestion*

Guest editors / *Rédacteurs en chef invités*

Emmanuelle Conil, François Costa, Lionel Pichon

ACADÉMIE DES SCIENCES
INSTITUT DE FRANCE

Académie des sciences — Paris

ISSN: 1878-1535 (electronic)

CENTRE MERSENNE

Comptes Rendus

Physique

Objective of the journal

Comptes Rendus Physique is an international peer-reviewed electronic journal, covering all areas of physics and astrophysics.

It publishes thematic issues, original research articles, review articles, historical perspectives, pedagogical texts or conference proceedings, without length limit, in English or in French and in a format as flexible as necessary (figures, associated data, etc.).

Comptes Rendus Physique is published since 2020 with the centre Mersenne pour l'édition scientifique ouverte (Mersenne Center for open scientific publishing), according to a virtuous Diamond Open Access policy, free for authors (no author processing charges nor publishing fees) as well as for readers (immediate and permanent open access).

About the journal

Comptes Rendus Physique is published exclusively in electronic format.

All information on the journal, as well as the full text of all articles, is available on its website at: https://comptes-rendus.academie-sciences.fr/physique/.

Author enquiries

For any inquiries about submitting a manuscript, please refer to the journal's website: https://comptes-rendus.academie-sciences.fr/physique/.

Contact

Académie des sciences
23 quai de Conti
75006 Paris (France)
cr-physique@academie-sciences.fr

Comptes Rendus
Physique
2024, 25, nº S1

Contents / *Sommaire*

ACADÉMIE DES SCIENCES
INSTITUT DE FRANCE

Comptes Rendus. Physique
2024, Vol. 25, Special issue S1, p. 1-3
https://doi.org/10.5802/crphys.209

Energy in the heart of EM waves: modelling, measurements and management / *L'énergie au cœur des ondes électromagnétiques : modélisation, mesures et gestion*

Energy in the heart of EM waves: modelling, measurements and management—Foreword

L'énergie au cœur des ondes électromagnétiques : modélisation, mesures et gestion — Avant-propos

Emmanuelle Conil [a], François Costa [b] and Lionel Pichon [*, c]

[a] Agence nationale des fréquences, ANFR, Maisons-Alfort, France

[b] ENS Paris-Saclay, Université Paris-Saclay, Université Paris-Est Créteil, France

[c] CNRS, CentraleSupélec, Université Paris-Saclay, Sorbonne Université, France

E-mail: Lionel.Pichon@centralesupelec.fr (L. Pichon)

Energy is more relevant than ever: modes of transmission, harvesting, conversion, storage as well as associated materials and systems are interdisciplinary issues in many sectors of activity (mobility, communication, etc.). Electromagnetic waves play an increasing role in the transmission, control and management of energy, both through fundamental aspects, technological developments and analysis tools.

Electromagnetics engineering related to waves involves appropriate numerical modeling and simulation tools for analysis and design. Experimental protocols are simultaneously required to measure electromagnetic fields according to energy levels, frequencies, etc., particularly in case of human exposure considerations and biomedical engineering. Also, management strategies including virtual prototyping and electromagnetic compatibility analysis (EMC) are currently widely adopted in the design of electrical and electronic systems over a wide range of frequencies from DC to hundreds of GHz.

The URSI-France 2023 workshop, organized under the auspices of the French Academy of Sciences, focused on "Energy in the heart of waves". It was jointly organized by SATIE (Information and Energy Technology, Systems and Applications) and GeePs (Group of electrical engineering—Paris). The workshop was held on the campus of CentraleSupélec, in Gif-sur-Yvette (France), from March 21 to March 22, 2023.

The following special issue is organized in 9 papers covering different aspects and challenges related to electromagnetic waves including: modelling, measurement and management.

* Corresponding author

This special issue is introduced by an invited "review paper" from Prof. Stavros Koulouridis (University of Patras) dealing with wireless power transfer in biomedical engineering. It presents an analysis of implantable antenna systems using the scattering matrices formalism.

Electromagnetic fields interact with living matter driving an exhaustive research related to human exposure. **A first group of four papers** is related to public exposure to electromagnetic waves including in-situ measurement techniques and dedicated simulation tools. These contributions cover both public area in case of radio-communications systems (5G for example) and industrial workplaces in case of electromagnetic fields radiated by power systems (in the kHz range).

The first paper entitled "*A Simulation Method Suited for the Whole French Territory Electromagnetic Waves* Exposure" and authored by Nicolas Noé, Lydia Sefsouf, Jean-Benoit Dufour, Samuel Carré, Emmanuelle Conil, Nabila Bounoua and Jean-Benoit Agnani presents a dedicated simulation method for the numerical modeling of the whole French territory's exposure to Electromagnetic fields. The method accounts for EMF exposure everywhere (outdoors and inside buildings), while performing fast enough to fulfill operational constraints.

The second paper entitled "*Monitoring of the exposure to electromagnetic fields with autonomous probes installed outdoors in France*" is authored by Ourouk Jawad, Emmanuelle Conil, Jean-Benoît Agnani, Shanshan Wang and Joe Wiart. It draws statistical conclusions on the exposure of the population based on temporal analysis of exposure monitored by autonomous broadband probes. It shows that monitoring probes are able to detect the seasonality of the exposure and provide analysis of correlation between monitoring probes and radio environment.

The third paper entitled "*Extensive 5G measurement campaign to monitor EMF exposure in France*" is authored by Lydia Sefsouf, Emmanuelle Conil and Jean-Benoît Agnani. It focuses on the exposure evolution related to the deployment of 5G on the French national territory during the year 2021. More than 5000 measurements were part of a large exposure monitoring program at nearly 2000 sites.

The fourth paper entitled "*Electromagnetic compatibility of active cardiovascular implants to occupational magnetic field environments: impact of the field direction*" is authored by Lucien Hammen, Lionel Pichon, Yann Le Bihan, Mohamed Bensetti and Gérard Fleury. It presents a new testing method to assess the electromagnetic compatibility method of active implantable medical devices against occupational magnetic field sources. It is based on an experimental approach using a specific test bench able to generate a controlled magnetic field in all space directions up to the high occupational exposure limits between 50 Hz and 3 kHz.

Appropriate 3D modeling approaches and computational methods are required to understand the interaction between electromagnetic fields and the environment and also to design and optimize complex structures. **A second group of four papers** shows dedicated numerical methods and simulation tools for investigations in realistic environments.

The fifth paper entitled "*3D Computation of Lightning Leader Stepped Propagation Inside a Realistic Cloud*" is authored by Philippe Dessante. It studies the propagation of leaders in clouds or toward the ground and structures. It describes a modeling approach involving a macro model and a heuristic based on the electric potential's maximization to find a leader's direction in case of a real cloud space charge repartition.

The sixth paper entitled "*Multi-label classification with deep learning techniques applied to the B-Scan images of GPR*" is authored by Soukayna El Karakhi, Alain Reineix and Christophe Guiffaut. It is related to object detection with ground penetrating radar. It presents a multi-label classification model based on transfer learning and data augmentation dedicated to B-scan images.

The seventh paper entitled "Design and optimization of inductive power transfer systems by metamodeling techniques" is authored by Yao Pei, Lionel Pichon, Mohamed Bensetti and Yann Le Bihan. It addresses wireless power transfer for charging batteries of electric vehicles. It presents

a fast design and optimization methodology of a power transfer systems based of metamodeling techniques.

The eighth paper entitled "*Matching of an observed event and its virtual model in relation to smart theories, coupled models and supervision of complex procedures—A review*" is authored by Adel Razek. It aims to illustrate the nature of the observation–modeling (or real–virtual) link, the importance of the exact model in the matching involved in this link and the use of this link in the supervision of complex procedures via the digital twin concept.

We believe that this Special Issue will provide readers with a valuable opportunity to have an overview of the challenges and progress in the field of electromagnetics and waves. We hope that all contents of this Special Issue demonstrate useful and insightful knowledge to the community.

First, we thank the authors who decided to submit their work and contribute to this Special Issue. Second, we are indebted with anonymous expert reviewers, who devoted considerable time and efforts in the review of the submitted manuscripts, providing always valuable feedback to the authors. Finally, we would like to thank the scientific committee of the URSI-France 2023 workshop for its contribution to the development of the program and the *Comptes Rendus Physique* editorial committee for agreeing to publish this special issue.

ACADÉMIE DES SCIENCES
INSTITUT DE FRANCE

Comptes Rendus. Physique
2024, Vol. 25, Special issue S1, p. 5-22
https://doi.org/10.5802/crphys.208

Review article / *Article de synthèse*

Energy in the heart of EM waves: modelling, measurements and management / *L'énergie au cœur des ondes électromagnétiques : modélisation, mesures et gestion*

Implantable T_X–R_X wireless systems. An overview of their efficiency analysis through scattering matrix formalism

Systèmes implantables sans contact. Analyse de l'efficacité du transfert par le formalisme de la matrice de diffusion

Stavros Koulouridis [a]

[a] University of Patras, 26504, Rio-Patra, Greece
E-mail: stavros.koulouridis@upatras.gr

Abstract. Looking at wireless implantable systems as a pair of or more T_X–R_X components, we discuss how their efficiency can be calculated in order to achieve an optimum result that can be evaluated over measurements and literature. To that end, scattering parameters' notation is introduced instead of considerations of the gain, the propagation losses and the radiation patterns. Looking at the system as a black box, remarks on optimum link calculation in relation to frequency, antenna size, phantom use, matching circuit integration and efficiency intensifiers are being carried out. International standards for allowed power and safety levels are added to the discussion. Different scenarios including telemetry, wireless harvesting and sensor transmission information are included as examples.

Résumé. En considérant un système implantable sans contact comme une paire de composants T_X–R_X (émetteur-récepteur), l'article montre que l'efficacité de transfert peut être calculée en vue d'obtenir un résultat optimal pouvant être évalué au moyen de mesures ou de résultats issus de la littérature. À cette fin, le formalisme des paramètres S (matrice de diffusion) est introduit à la place des quantités généralement utilisées (gain, pertes, diagramme de rayonnement). En considérant le système comme une boîte noire, des remarques sur le calcul de la liaison optimale sont formulées selon la fréquence, la taille de l'antenne, l'utilisation d'un fantôme, l'intégration de circuits d'adaptation et d'amplificateurs d'efficacité. Les normes internationales relatives à la puissance autorisée et aux niveaux de sécurité à respecter sont inclues dans la discussion. Différents scénarios incluant la télémétrie, la récupération d'énergie sans fil et la transmission d'informations par des capteurs sont présentés à titre d'exemples.

Keywords. Scattering parameters, Friis equation, Link budget, SAR, Wireless harvesting systems.

Mots-clés. Paramètres S, Equation de Friis, Bilan de liaison, DAS (débit d'absorption spécifique), Récupération d'énergie sans fil.

Note. This article follows the URSI-France workshop held on 21 and 22 March 2023 at Paris-Saclay.

Manuscript received 22 May 2024, revised 12 August 2024, accepted 13 September 2024.

1. Introduction

Significant research has been focused on studying, realizing, and implementing wireless body area networks. Applications include among others implantable devices for vital data recording, cameras that wirelessly transmit low-bit images, or wireless energy harvesting systems for unobtrusive and sustainable implantable sensors. For example, continuous non-invasive glucose measurements can help diabetes patients [1]. Under a usual scenario, an implantable device will obtain measurements, it will transmit them to an external relay through an antenna, and the relay will transmit the information to a party of "interest", like a patient, hospital or a doctor.

Electromagnetic propagation inside the lossy inhomogeneous body which is composed of various organs of different electric properties causes increased absorption in the body. In addition, the complex environment introduces multiple reflections that can derange expected antenna performance. In addition, the inhomogeneous body structure has an effect on antenna behavior since it creates impedance mismatches. In effect the antenna radiation properties are affected by the body and the optimum performance of an implantable antenna design is not a straightforward process.

Research has considered several frequency bands for implantable sensors' design. Higher frequencies permit the use of larger electrical designs (while being physically small). However, when the depth increases, the higher frequencies lead to increased losses, even higher than the theoretically predicted ones [2]. In some cases, the large distances between an external relay and the implantable antenna makes obligatory the use of smaller frequencies. Of course, the frequency selection is also related to the specific scenario examined. Dual (or triple) frequency implantable systems can be also proposed, sending a wake signal at higher frequency and relaying medical information at lower frequency [3], or using a higher frequency where nominally higher power is permitted for wireless energy transfer [4, 5]. Interestingly, when ideal scenarios are considered, an optimum frequency for the implantable antenna can be determined [6]. However, when some of the parameters are altered, optimum design frequency can actually change.

Wireless Power Transfer systems introduce additional complexity in the implantable sensor design. First, their use can allow, in some cases, for battery-less designs or, in general, avoiding use of wires. Still, a rectenna is to be used, meaning that the receiving antenna needs to be connected to a rectifying circuit and sometimes voltage boosters or other electronic components [5]. In such cases, the antenna is coupled with the circuit and its design is seen as a single component, i.e., the "rectenna", which introduces additional design parameters but also adds degrees of freedom in the final device.

In other cases, extra components are introduced in addition to the implantable antenna. For example, external "facilitators" that are applied to the body and can increase implantable antenna reception or the link with an external antenna are proposed. Or, more than one implantable antenna may be considered that needs to communicate or relay information to other components, etc.

Obtaining the optimum design is hence a complex process that can be affected by different factors. In order to simplify the study and also offer a measure of achievement, the use of scattering matrix can be introduced. In that case, we study a system that has two ports and includes the implanted and the external antenna, the multiple implanted antennas or all the components that constitute the design. In the end the system has two ports, one input and one output, that can be used to evaluate the system efficiency and determine its performance. The simulations can be directly compared with measurements and with several designs in the litterature.

In this paper, after a short introduction into scattering parameters use for the system under consideration, we determine how the system efficiency can be calculated for two cases. When simply two antennas (Section 2.1) are used and when additional circuits connected to the antennas are considered in the case of harvesting systems for example (Section 2.1.1). Link budget considerations follow for telemetry systems. International restrictions for wireless systems used in implantable designs are then presented, accompanied by power limitations as reported in international standards. Some examples are discussed in Section 3. First, we briefly discuss about ideal frequency for optimum efficiency when two implantable antennas are communicating with each other. Then, we examine how antenna size and radiation pattern can affect efficiency by analyzing four implantable microstrip antennas operating at MedRadio Band (400 MHz region). This region is selected, since it seems to be ideal for deeply implantable systems. When maximum allowed power for antennas is also considered, discussion for optimum frequency is then carried out, in order to close a link between an external antenna and an implantable antenna as is required for telemetry systems. Next, a couple of rectennas is considered in order to present an example of the necessity to include circuits in the scattering matrix consideration. Section 3 ends with a short comment on how added surfaces, on the skin, can increase the system efficiency. Some very simple solutions are presented in comparison with much more sophisticated ones based on metasurfaces for example. Finally, some conclusions are drawn in Section 4.

2. System overview

While the implantable antenna design demands considerable efforts, in order to evaluate the proposed setup performance, the problem needs to be examined as a system composed of two, three or multiple components. In a system design point of view, the implantable and the external antennas or multiple implantable antennas will be part of a two-port system represented by the well-known scattering S-parameters [7] as shown in Figure 1. In that system, the communication between two antennas can be one scattering matrix with individual scattering parameters, and the intercommunication between antenna pairs can be represented by a total scattering matrix which has been produced by a chain of separate scattering matrices. Selection of the system under examination relates to the problem under investigation. In any case, we can choose port 1 to be T_x antenna's feeding point and port 2 to be R_x antenna's (R_x) reception point. In a multi antenna system, one antenna would be the T_x antenna and one other would be the R_x antenna, while the others could be intermediate parts of the system. The scattering 2×2 S-matrix which is generated represents the path link between the two antennas independently of what lies between them. Their input impedance is also included as part of the scattering matrix. Notably, in such a setting the two antennas system is the same for examining the reception/transmission of data or a wireless harvesting setup. Furthermore, the in-between distance (near, intermediate or far-field conditions) does not affect the system overview. Hence, the coupling between the antennas is also included in the matrix. While the S-matrix should be symmetric for a passive and/or linear element system, let us assume that, in general, we can have an asymmetric system, where non-linear components can be integrated into the system, and therefore:

$$S = \begin{bmatrix} S_{11} & S_{12} \\ S_{21} & S_{22} \end{bmatrix} \tag{1}$$

where $S_{12} \neq S_{21}$ and of course $S_{11} \neq S_{22}$ since the two antennas can be different. S-parameter matrix can be obtained from an electromagnetic solver and/or measurements for the fabricated system. Notably, comparison between measurements and simulations can be straightforward, adding another advantage on using S-parameters. The final 2×2 scattering matrix, representing either each itemized link or the total link, will be connected to a load (either the R_x antenna

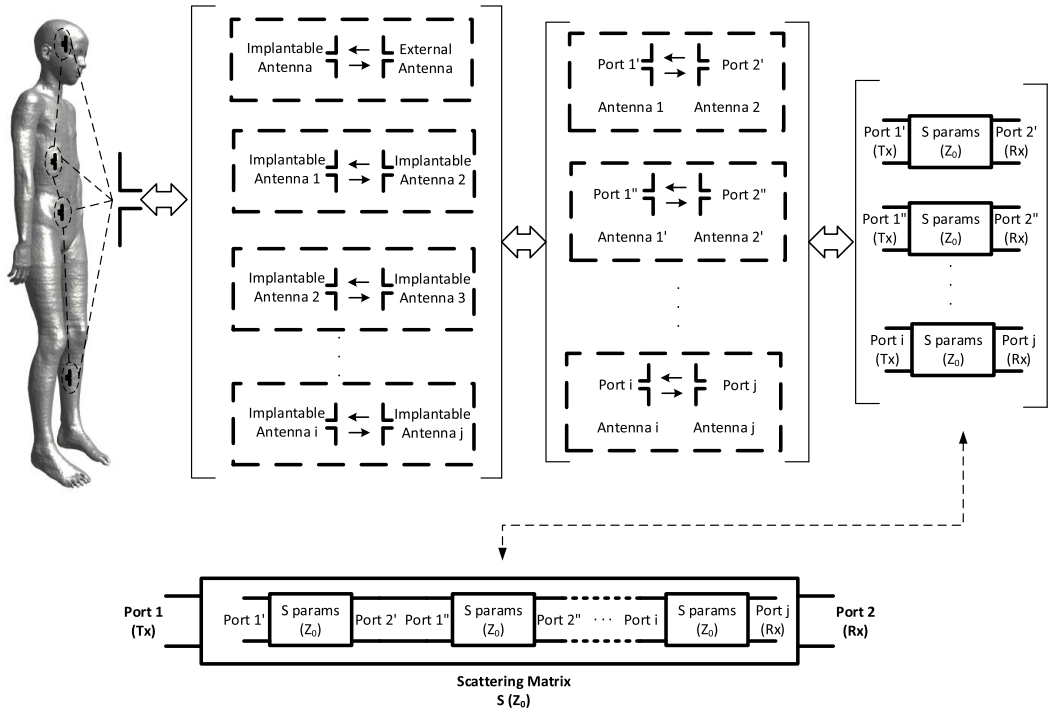

Figure 1. Communication link between implantable antennas or implantable antennas and external antenna replaced by one or more scattering matrices. Each scattering matric can represent an antenna pair. The interconnection between the antenna pairs can be replaced by a chain of scattering matrices, or at the end by a total scattering matrix.

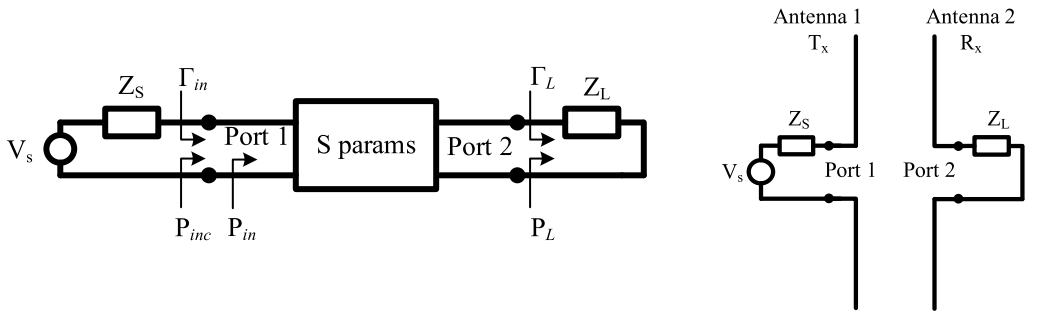

Figure 2. *S*-parameter circuit of an antenna pair with voltage source and termination load.

termination or another circuit) and will be fed by a voltage source with its internal impedance. This is shown in Figure 2.

2.1. *Evaluation of system efficiency*

In order to calculate the power received from the external or the implantable antenna, the well-known Friis formula can be utilized. This predicts the power received from an antenna in relation

to the power radiated from a transmitting antenna, their gain, path loss, antennae's matching and polarization. It is given by the following equation.

$$P_{\mathrm{r}} = \frac{\lambda^2}{(4\pi r)^2} \cdot G_{\mathrm{r}} \cdot G_{\mathrm{t}} \cdot (1 - |S_{11}|^2) \cdot (1 - |S_{22}|^2) \cdot \mathrm{PLF} \cdot P_{\mathrm{t}} \tag{2}$$

where P_{r} and P_{t} are the power received and transmitted respectively, G_{r} and G_{t} are the antennas' received and transmitted realized gain respectively, λ is the wavelength of the intermediate medium, r is the in-between distance and PLF is the polarization factor (equal to 1 when the antennas are for example aligned and linearly polarized). It should be noted that the first product term and especially the wavelength/distance term (i.e., $\lambda^2/(4\pi r)^2$) expresses the free space (inside air or in a homogeneous infinite material) path loss, representing a spherical plane wave. Hence, far-field conditions and unobtrusive, free of hurdles, propagation should be observed. When an implantable antenna is for example receiving signal from an external transmitter the electromagnetic wave propagates into air and the body while multiple reflections are occurring as the signal passes through the complex body environment. To take into account non-ideal propagation (but without being able to avoid the far-field restriction) the above equation can be transformed into

$$P_{\mathrm{r}} = \frac{\lambda^2}{(4\pi)^2} \left(\frac{1}{r}\right)^{\gamma} \cdot G_{\mathrm{r}} \cdot G_{\mathrm{t}} \cdot (1 - |S_{11}|^2) \cdot (1 - |S_{22}|^2) \cdot \mathrm{PLF} \cdot P_{\mathrm{t}}. \tag{3}$$

Index γ can have theoretically any value from 1 to infinity. For implantable antenna systems values are definitely higher than 2. Index γ, in implantable antenna problems is obtained via simulation or measurements since no theoretical model exists. The process involves the curve fitting of measurements obtained at variable distances [8]. The outcome is unique to the system under investigation. Defining the path loss exponent can be of course useful but, in reality, it cannot offer a better overview of how well the pair implantable antenna/external antenna operates.

Equation (2) permits us to focus on the parameters that affect the reception of an antenna. These are the transmitting antenna gain, the receiving antenna gain, the matching of each antenna, the path losses that occur between the transmitting and receiving antenna and of course their polarization mismatch. While using Equation (2), would make the case ideal, in reality it is easily understood from the above discussion that in the case of implantable antenna and external transmitter, the predicted received power is simply the highest achievable [9], and there can be many factors that can affect this link. Since we are interested in estimating how well the system implantable antenna/external antenna behaves, we should actually use the scattering parameters of S-matrix. From the scattering parameter theory [7], it is very easily understood that:

$$|S_{21}|^2 = \frac{P_{\mathrm{r}}}{P_{\mathrm{t}}}. \tag{4}$$

In that case from Equation (2)

$$|S_{21}|^2 = \frac{\lambda^2}{(4\pi r)^2} \cdot G_{\mathrm{r}} \cdot G_{\mathrm{t}} \cdot (1 - |S_{11}|^2) \cdot (1 - |S_{22}|^2) \cdot \mathrm{PLF}. \tag{5}$$

It is easily understood that efficiency n of the system is expressed by the ratio of received power P_{r} over the transmitted power P_{t}. Then:

$$n = |S_{21}|^2 \tag{6}$$

where $|S_{21}|^2$ can be calculated by Equation (5). However, it might be more useful, sometimes, to calculate a slightly altered efficiency where the mismatch has been removed from the

calculations. This would be useful in the case we would like to study how the intermediate path can affect the system. Indeed, if we transform Equation (5) into:

$$\frac{|S_{21}|^2}{(1-|S_{11}|^2)\cdot(1-|S_{22}|^2)} = \frac{\lambda^2}{(4\pi r)^2}\cdot G_\mathrm{r}\cdot G_\mathrm{t}\cdot \mathrm{PLF} \tag{7}$$

the right part refers to the system path loss, antenna gain and polarization factor and therefore it can actually reveal how the antenna gain (which can be affected by the surrounding complex environment) and the losses in between can affect the system "efficiency" n'. In that case we can write

$$n' = \frac{|S_{21}|^2}{(1-|S_{11}|^2)\cdot(1-|S_{22}|^2)}. \tag{8}$$

Notably, in order to have equivalency with the circuit of Figure 2 we should note that received power $P_\mathrm{r} = P_\mathrm{L}$ when $Z_\mathrm{L} = Z_0$ while transmitted power P_t is equal to the power provided by a source at the $\mathrm{T_x}$ antenna input, that is $P_\mathrm{t} = P_\mathrm{in}$.

2.1.1. *Evaluation of system efficiency at load. Use of matching circuits*

The system efficiency calculations at the antenna point do not consider the power offered to the system, or the power that would be delivered to a load attached at the $\mathrm{R_x}$ system component. In addition, it does not take into account the use of antenna input impedance in order, for example, to match the antenna to a harvesting circuit or other kind of circuits implemented in the design. With reference to Figure 2, the efficiency can be calculated from [3, 10, 11]:

$$n = \frac{P_\mathrm{L}}{P_\mathrm{in}} = \frac{P_\mathrm{L}}{(1-|\Gamma_\mathrm{in}|^2)P_\mathrm{inc}} = \frac{|S_{21}|^2(1-|\Gamma_\mathrm{L}|^2)}{(1-|\Gamma_\mathrm{in}|^2)(1-|S_{22}\Gamma_\mathrm{L}|^2)} \tag{9}$$

where P_L is the power delivered to the load of the receiving antenna and P_in is the power offered to antenna. Γ_in is the reflection coefficient at port 1 and is equal [7] to

$$\Gamma_\mathrm{in} = S_{11} + \frac{S_{12}S_{21}\Gamma_\mathrm{L}}{1-S_{22}\Gamma_\mathrm{L}} \tag{10}$$

and Γ_L is the reflection coefficient at the load calculated by

$$\Gamma_\mathrm{L} = \frac{Z_\mathrm{L}-Z_0}{Z_\mathrm{L}+Z_0}. \tag{11}$$

The S-matrix can include, for example, the $\mathrm{T_x}$ antenna with a matching circuit and the $\mathrm{R_x}$ antenna which is connected to a harvesting circuit that will feed the load Z_L. It is noted that the S-matrix can be obtained for characteristic impedance $Z_0 = 50\ \Omega$. Still, the antenna input impedance can differ from the ideal Z_0. The ultimate criterion for such a design is always the maximization of the system efficiency. In addition, by relaxing the antenna input impedance requirements, we can seek much more efficient harvesting circuits.

2.2. *Link budget for wireless communications*

For some scenarios thar require telemetry or generally consider the transmission of information, the link budget needs to be considered. Link budget should consider the antenna losses, path losses, required bit rate, antenna gain, etc. Power input is controlled by electromagnetic compatibility safety standards for maximum power absorption from the tissues and electromagnetic interference avoidance and it variates with frequency and antenna size. In order to secure a communication link, one needs to achieve a positive carrier-to-noise density ratio C/N_0 budget. C/N_0 describes the strength of the power wave related to the noise. In Table 1, an example link budget is shown, including parameters to examine and indicative specifications of a satisfactory communication link [12, 13].

Table 1. Link budget parameters

Component	Description	Notation	Formula/data
Transmitter T_x	T_x Power (dBW)	P_{Tx}	
	Cable/feeding losses (dB)	L_{Tx}	
	T_x Antenna gain (dBi)	G_{Tx}	
Propagation	Frequency	f	
	Space path loss (dB)	P_{Loss}	$10\log_{10}\left(\frac{(4\pi)^2}{\lambda^2} r^{\gamma}\right)$
Receiver R_x	R_x Power (dBW)	P_{Rx}	
	Cable/feeding losses (dB)	L_{Rx}	
	R_x Antenna gain (dBi)	G_{Rx}	
	Ambient temperature (K)	T_0	293
	Boltzman constant	k	1.38×10^{-23}
	Noise figure (dB)	NF	2.5
	Noise power density (dB/Hz)	N_0	-201.7
Signal quality	Bit Rate (b/s)	B_r	10^6
	Bit error rate	BER	1×10^{-5}
	E_b/N_0 (ideal PSK) (dB)	E_b/N_0	9.6
	Coding gain (dB)	G_c	0
	Fixing deterioration (dB)	G_d	2.5

Cable/feeding losses in Table 1 include mismatch losses as a positive number. In the same manner, space path losses have been reversed since they should be retracted from final link budget. Equations to calculate the required link budget follow:

$$N_0 = 10\log_{10}(k) + \log_{10}(T_i) \text{ (dB/Hz)} \tag{12}$$

$$T_i = T_0(NF - 1) \text{ (K)} \tag{13}$$

$$\text{Achievable link } C/N_0 = P_{Tx} - L_{Tx} + G_{Tx} - P_{Loss} + P_{Rx} - L_{Rx} + G_{Rx} - N_0 \text{ (dB/Hz)} \tag{14}$$

$$\text{Required link } C/N_0 = \frac{E_b}{N_0} + 10\log_{10}(B_r) - G_c + G_d \text{ (dB/Hz)}. \tag{15}$$

For a successful link we should have a positive margin (dB) where this is given by Equation (16)

$$\text{Margin} = \text{Achievable link } C/N_0 - \text{Required link } C/N_0 \text{ (dB)}. \tag{16}$$

When the S scattering matrix is used, the link budget can be also calculated. In that case, S_{21} parameter will include all losses and gain occurred as can be easily seen by Equations (2)–(4). In that case, S_{21} in dB will be given by

$$S_{21} = G_{Tx} - L_{Tx} - P_{Loss} - L_{Rx} + G_{Rx} \text{ (dB)}. \tag{17}$$

And the Achievable and Required Link Budgets, considering Equation (4), will be finally:

$$\text{Achievable link } C/N_0 = P_{Tx} + S_{21} + 201.7 \text{ (dB/Hz)} \tag{18}$$

$$\text{Required link } C/N_0 = 72.1 \text{ (dB/Hz)}. \tag{19}$$

2.3. *Frequency, safety and radiated power*

Implantable devices and systems are mainly developed in sub-GHz or a few GHz region. While mm waves have been employed for wearable devices, this is not preferred for the embedded

Table 2. Typical medical frequencies for implantable devices

NameTag	Frequency (MHz)	ERP (dBm)	Reference
MedRadio	401–406	−16	[14–16]
	413–419	−16[a]	[14]
	426–432	−16[a]	[14]
	438–444	−16[a]	[14]
	451–457	−16[a]	[14]
	2360–2400	−16[a]	[14]
Wireless medical telemetry service (WMTS)	608–614	31.8	[17]
	1395–1400	31.8	[17]
	1427–1432	31.8	[17]
Industrial, scientific and medical services band/ISM	433.05–434.79	10	[18]
	863–870	14	[18]
	902–928	30 (36 EIRP)	[19]
	2400–2484	30 (36 EIRP)[b]	[19]
	5725–5875	30 (36 EIRP)[b]	[19]

[a] It is assumed that it is incorporated from the main restriction for 401–406 MHz region.

[b] In general, EIRP can be larger for specific cases [19].

into tissue systems because of high absorption losses. The device development is regulated by several organizations around the world. Low MHz and kHz region has been used for inductive wireless charging and animal tags. However, wireless device development for communication is not practical and it is not considered in such low frequencies.

The main restriction for wireless implantable communication systems, apart from the operating frequency, is the maximum emitted power. It should be noted that this restriction is not necessarily related to the safety of the user but mostly to avoiding electromagnetic interference issues. Two quantities are usually used. ERP or Effective Radiated Power which represents the power fed to a matched antenna, and Equivalent Isotropically Radiated Power or EIRP which represents the maximum power radiated from an antenna, that is the power fed to matched antenna (in Watts) times the antenna gain over isotropic radiator. In an overview of the frequencies (Table 2), it is seen that specific frequencies have very low power limit. In that case the main goal is to perform close distance communication. In other cases, high emitted power is allowed, especially when telemetry is sought.

For the frequencies shown in Table 2, electromagnetic safety for avoiding effects from electromagnetic waves to humans is represented by Specific Absorption Rate, or SAR (W/kg). SAR is calculated inside biological tissues and is given by:

$$\mathrm{SAR} = \frac{\sigma E^2}{2\rho} \ (\mathrm{W/kg}) \tag{20}$$

where σ and ρ are tissue conductivity (S/m) and density (kg/m^3) respectively while E represents electric field magnitude. Standards for safety levels, with respect to human exposure to radiofrequency electromagnetic fields are provided in Table 3 [20, 21]. General public safety is usually considered.

Table 3. SAR safety levels (100 kHz–6 GHz)

Exposure conditions	General public SAR (W/kg)[a]	Persons in restricted environment SAR (W/kg)[a]
Whole body	0.08	0.4
(Local) head and torso [b]	2	10
(Local) limbs and pinae[b]	4	20

[a] Averaged over 30 min for whole body exposure and 6 min for local exposure.

[b] Averaged over any 10 g of tissue formed in cubical volume.

3. Investigation of S_{21} link

3.1. *System efficiency under homogeneous environments*

There is certainly an optimum efficiency that can be achieved by an antenna. There are several discussions around its definition. In order to achieve it, ideal environment can be considered. For example, in [6] a capsule antenna embedded in the middle of a three layer spherical phantom is examined. The three layers represent from center to surface, muscle, fat and skin tissues. It is verified that an optimum efficiency exists for such a small antenna (detained in a specific sphere of small radius) while maximum optimum efficiency decreases with sphere radius increase. Naturally, such an ideal environment can be hardly met. Still, the contribution of the work is significant since it shows that for deep implantation the optimum frequency becomes lower. It should not be forgotten however that the antenna electrical size is competing against physical size and therefore for lower frequencies (Medradio band of 400 MHz for example), the antenna electrical size needs to be very small leading to inefficient antennas but with less propagation losses because of the higher wavelength. On the other hand, the higher frequencies (of 2.4 GHz ISM band for example) allow for electrically larger and of higher efficiency antennas with the cost of higher body losses because of the smaller wavelength. This fact leads us to the observation that while general conclusions can be made for optimum frequency and antenna size, the T_x–R_x pair should be always seen as a system where the system efficiency is obtained per case.

In [22] two identical directive wire dipole antennas are designed and used to investigate the link between them when they are both implanted inside a muscle tissue phantom (see Figure 3). Examined frequency region varies from 0.8 GHz to 2.8 GHz. Detailed comparison for a loss-less or lossy environment is carried out accompanied by measurements when the two antennas are embedded inside minced pork meat. As shown the achieved measured link (measured $|S_{21}|^2$) is around -35 and -40 dB for 6 cm and 8 cm distance respectively and for the 1 GHz to 1.2 GHz frequency window where the antenna is also matched. Interestingly, as discussed in [22], a similar problem for a loop antenna and for a realistic phantom when the antenna is placed in several positions, reveals the in-body $|S_{21}|^2$ to be around -50 dB for the same frequency region [23], while in [24] and a 2.4 GHz bow-tie antenna link for a spherical three-layer phantom gives a -70 dB result. As can be seen by the above results, the simulation scenario examined can reveal different results and, in that sense, each problem is unique. While general conclusions can be drawn, results can differentiate when parameters of the problem do change. Frequency can obviously differentiate the results. What is sometimes forgotten, however, is that antenna behavior and radiation mechanism can also affect the results. Antenna size can be a crucial parameter.

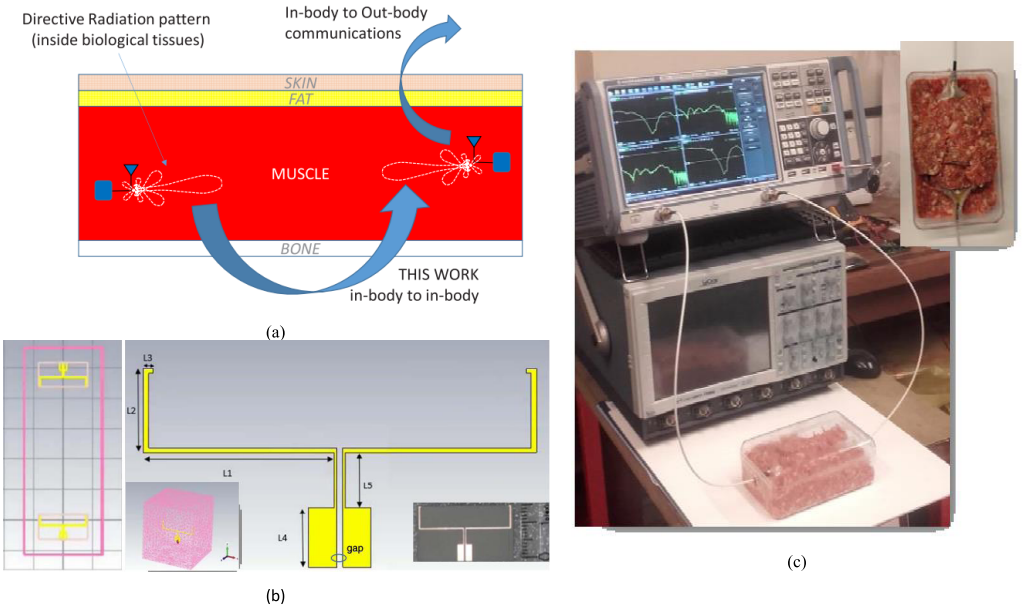

Figure 3. From [22]. Link simulation and measurements for two identical antennas inside tissue environment. (a) Problem under investigation; (b) directive antennas used in the simulation environment (dielectric muscle tissue box shown with pink color); (c) experimental measurement for minced pork meat.

Table 4. Implantable antennas tested for link estimation in scenarios of Figure 4

Antenna	Design/characteristics	Frequency of operation (MHz)	SAR_{1g} (W/kg)	Volume (mm^3)
"A" from [25]	Spiral, one layer	402–405	100	3457
"B" from [3]	Serpentine, one layer	402–405, 2.4–2.48	360 (402 MHz)	608
"C" from [26]	Stacked PIFA, double layer	402–405	300	336
"D" from [27]	Stacked, serpentine, double layer	402–405	660	33

3.2. *System efficiency for complex environments*

A computational experiment is carried out for four implantable microstrip antennas taken from [3, 25–27] whose details are shown in Table 4. Several other antennas could be considered. Microstrip antennas are usually chosen since they carry a ground plane and they can support the electronic circuitry on their back. The antennas of [3, 25–27] operate in the MedRadio band [14], at 402–405 MHz but they have different size and overall volume. In Figure 5d, the S_{21} link is investigated for a $100 \times 100 \times 100$ mm^3 skin box between two identical versions of the antennas facing each-other at variable distances. As seen, the maximum S_{21} link variates from -25 dB for the larger antenna to -50 dB for the smaller antenna for a 20 mm in-between distance. The lowest link variates from -40 dB to -85 dB for 80 mm in-between distance.

While this distance falls in the near to medium field region, certain conclusions can be drawn. In comparison to [22] and for distance of 6 cm, maximum S_{21} value is at an almost equal value of -35 dB. Notably, this happens for different frequencies with a ratio of 3:1. Of course, the antenna in [22] is intentionally designed to realize an implantable-to-implantable link and is relatively

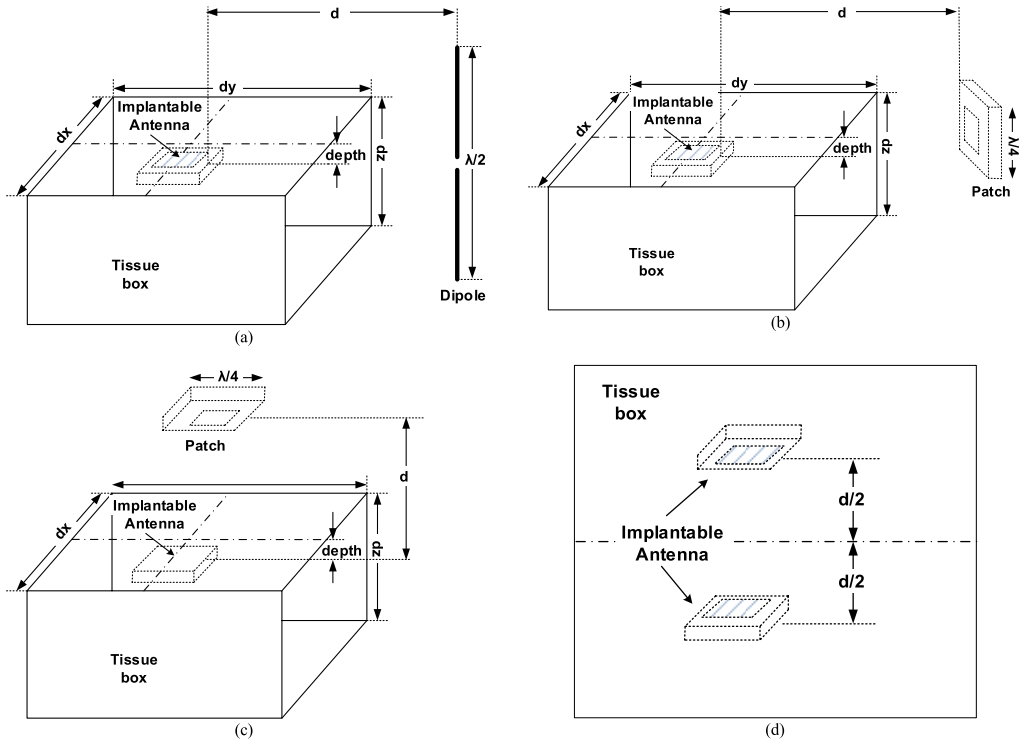

Figure 4. Implantable microstrip antenna (see Table 4) in a tissue skin box 100 × 100 × 100 mm^3 and an external dipole or patch antenna at broadside or at the side of the implantable antenna. Tests (see Figure 5) were run for 402 MHz for the antennas from [3, 25–27] and included either the link calculation between the external and the implantable antennas (a, b, c) or between the implantable antennas (d).

electrically large. Electrical size can indeed affect efficiency. As shown in Figure 5d, the smallest antenna achieves multiple dB lower link as compared to its larger counterparts. In addition, the four tested antennas do not follow the same linear variation with distance in the calculated S_{21}. The antenna radiation mechanism and the boundary of the skin box can obviously affect the maximum achievable link. In addition, there might be an optimum frequency in relation to the antenna size and tissue properties for minimizing the internal losses [6].

In a homogeneous environment the frequency region of 900 MHz to 1.5 GHz could be the optimum one [6,7]. Still, as has been noted, the implantable antenna design can affect the results while the non-homogeneous environment has not been extensively studied.

It should be noted that the calculated SAR_{1g} in Table 4 is for input power of 1 W (30 dbm) and is naturally high. It has been provided for comparison between the different antennas. Still, as has been discussed in Section 2.3 maximum allowable power for implantable antennas varies. For example, at 400 MHz band (Medradio) maximum allowable power is −16 dbm (25 μW). In that case the results in Table 4 should be divided by 40,000 (=1 W/25 μW).

When the discussion moves to the link between an implantable antenna and an external antenna, different remarks could be drawn. Firstly, the implantable antenna far-field radiation properties need to be taken into account. Secondly, the external antenna type can also affect the outcome. Concerning the numerical experiment shown in Figure 4, a $\lambda/2$ dipole or a $\lambda/4$ rectangular patch are used as external antennas when the previously discussed microstrip

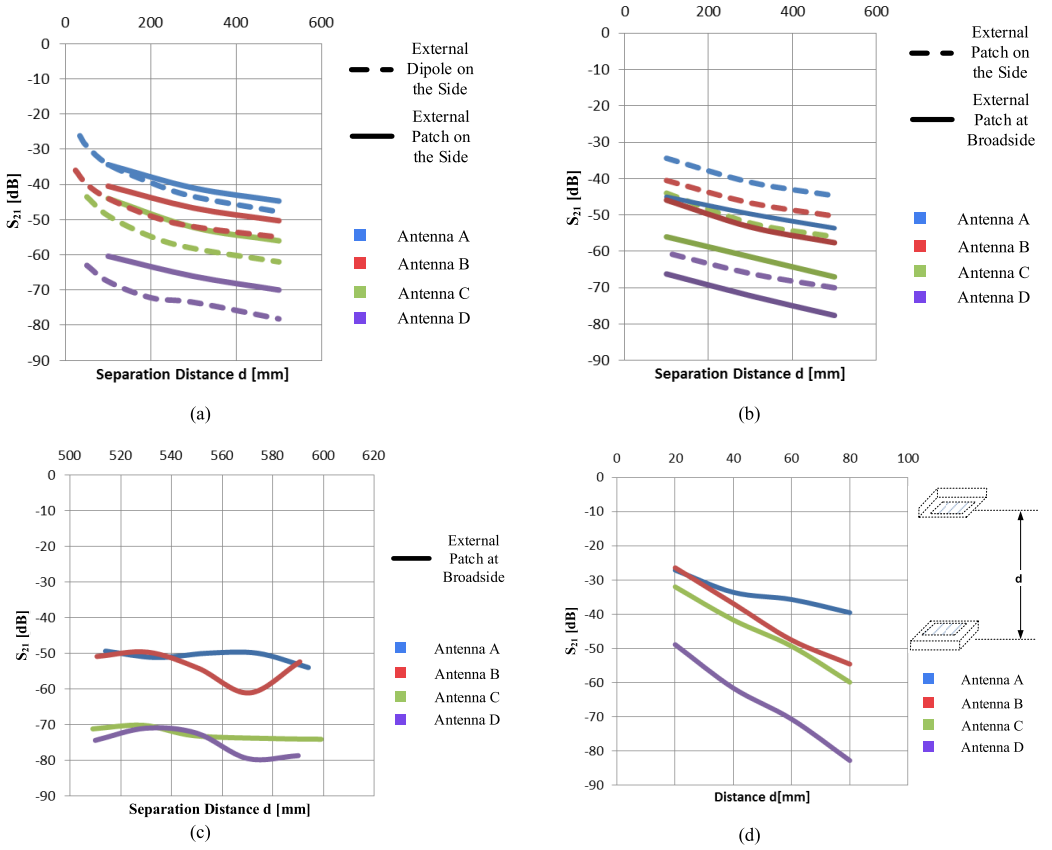

Figure 5. $|S_{21}|^2$ (dB) for either an external dipole and/or a microstrip patch or two identical implantable antennas at $f = 402$ MHz. Implantable antennas "A", "B", "C", "D" are described in Table 4. Cases examined: (a) External dipole (Figure 4a) or microstrip patch (Figure 4b) on the side when the external antenna distance d variates and the implantable antenna is kept at depth = 5 mm; (b) External microstrip patch on the side (Figure 4b) or facing the implantable antenna (Figure 4c) when the external distance d variates and the implantable antenna is kept at depth = 5 mm; (c) External microstrip patch (Figure 4c) with implantable antenna when the external distance from the box surface is kept constant at 500 mm and the implantable antenna depth variates; (d) Identical antennas (A, B, C, D) immersed in the skin box, are facing each-other and their distance variates. Symmetry over box center is kept.

implanted antennas from [3, 25–27] (see Table 4) are immersed inside a $100 \times 100 \times 100$ mm^3 skin box. Experiments include the placement of the external antenna on the side of the implanted antennas (Figures 4a,b) or at broadside facing each other (Figure 4c) and calculation of S_{21} link when the distance of the external antenna to the skin box surface varies (Figure 5a for external antennas on side and Figure 5b for comparison between patch on the side and at broadside) or when the external rectangular patch antenna is kept at fixed distance at broadside and the implantable antenna depth varies (Figure 5c).

External antennas were placed on the side because multiple miniaturized microstrip antennas operate at dipole mode. In that case, the optimum reception occurs when the external antenna

is on the side. For the numerical example investigated, even if we have not followed an optimum placement between the implantable and the external antenna on side, the link is higher. Indeed, for the frequency under investigation (402 MHz), when S_{21} from the external patch antenna on the side is compared against S_{21} from the patch antenna at broadside the link for the patch antenna on the side is 5 to 10 dB higher (see Figure 5b). The smallest difference occurs for the smallest implantable antenna. This result holds for distances from 100 mm to 500 mm. S_{21} varies almost linearly with the external antenna distance to the skin box surface.

For the same experiment, when we use the dipole and the patch antennas on the side, the S_{21} link is higher for the patch antenna (see Figure 5a). This is normally expected since the patch antenna has higher gain. Interestingly, the highest S_{21} difference is more profound for the smallest implantable antenna. Radiation pattern shape of the internal antenna may be the cause. In addition, the boundary effects of the skin box on the smallest antenna could create specific peculiarities. In any case this is another indication of the uniqueness of each case under investigation. Finally, when the external patch antenna is kept at fixed distance (at broadside for example—see Figure 5c), implantable antennas depth does not seem to affect the S_{21} link. This is obviously the outcome of the relative low frequency (i.e., 402 MHz) where the wavelength is relatively large. Since the external distance is kept constant, the internal "sub-wavelength" in-between variable distance does not influence the results. In that case, the implantable antenna volume (see Table 4) is a more crucial factor. Depending on the antenna design, skin box edge boundary also has an effect on the calculated results. In any case, it seems that, for larger distances of the external antenna or deeply implanted antennas, the lower frequency can offer a better link level.

Indeed, when the link between an implantable dipole and an external dipole antenna is examined and for several sub-GHz frequencies the same conclusion can be reached. Consider the problem shown in Figure 6. A simple tissue box is considered 100 mm in width, 100 mm in height, 50 mm in depth, filled with an equivalent tissue with relative dielectric permittivity equal to 2/3 of muscle. It should be noted that in several problems when homogeneous cubical phantoms are considered for representing the body, similar dielectric tissue is considered (for example see [3]). Two half-wavelength dipoles one implanted and the other in free space are considered and efficiency n' (see Equation (8)) denoted by Ga is calculated for a distance of up to 2 m. In Table 5, the frequencies tested are shown, in relation with dielectric properties used and the allowable power per frequency (see Table 2). First, as seen, the dielectric properties variate very little as is actually expected. Secondly, the permissible power increases with frequency. From Figure 6b we can see that obviously n' deteriorate much slower in the 400 MHz group of frequencies as compared to 868 MHz or 915 MHz. This is expected. When permissible power is taken into account and the achievable link is calculated from Equation (18) (here we consider that dipoles are well matched and therefore the denominator of n (Equation (8)) does not affect the final result, that is n and n' (Equation (6)) are practically the same), it is obvious that for every frequency a link can close (communication is successful) since every link is greater than the Required link of Equation (19). However, do not forget that we have considered maximum power emitted from the antenna. In that sense this link would be achieved if the T_x antenna was the external to the body. If we wanted to calculate what is the achievable link for an implantable antenna transmitting to an external to the body antenna, then SAR should have been calculated as has been also discussed above. In other words, while 915 MHz frequency can allow for sending information to an implantable antenna, the implantable antenna would be able to close a link at 400 MHz area where the fed power to the implantable antenna would not create excessive SAR. Furthermore if larger distances are to be considered, there is a point where the lower frequency can offer a better link, even for an external T_x antenna.

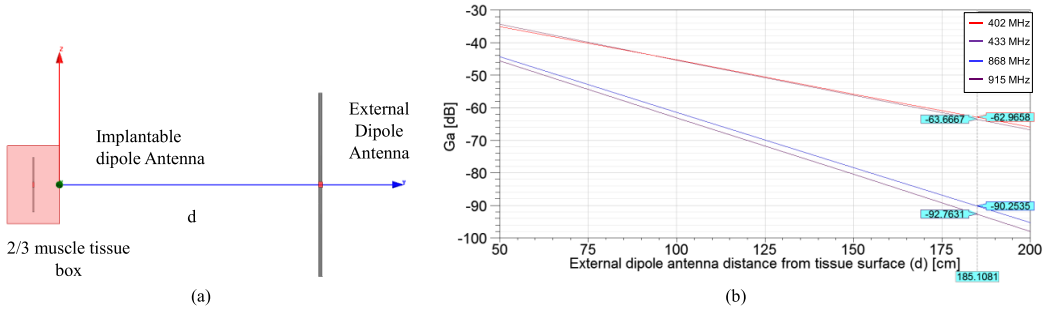

Figure 6. Simplified numerical test for n' efficiency (see Equation (8)) in (dB) (noted with Ga) between an implanted half wavelength dipole inside a 2/3 muscle tissue type box and a free space half wavelength dipole at various distance and frequencies. Tissue box has 100 mm width, 100 mm height and 50 mm depth. The implanted dipole is placed at the box center (25 mm distance from surface).

Table 5. Frequencies tested, dielectric permittivity, allowed effective power and achievable link at 200 cm for the problem of Figure 6

	Electrical properties of tissue-simulating model		ERP = Effective radiated power	Achievable link at 200 cm	Frequency band
f (MHz)	ε_r	σ (Si/m)	ERP_{max} (dBm)	C/N_0 (Equation (18)) (dB/Hz)	Availability
402	38.07	0.53	−16	119.7	MEDS radio (worldwide)
433	37.91	0.54	10	124.7	ISM (Europe, Short range devices)
868	36.74	0.62	14	119.7	ISM (Europe, Short range devices)
915	36.66	0.63	30	133.7	ISM (USA and other parts of the world)

3.3. *Antennas coupled with matching circuits: rectennas*

For wireless harvesting systems, the antenna is coupled with a rectifier which is usually based on a combination of diodes and LC circuits. Other active elements might be also utilized. In that case the active circuit can be a part of scattering matrix. The circuit will have an output impedance equal to 50 Ω. However the antenna is not required to be designed at 50 Ω anymore. Hence, the receiver is a rectenna which is part of the scattering S matrix. In that case the system can be studied following the discussion in Section 2.1.1.

In [4], an implantable rectenna is obtained by combining an antenna (seen in Figure 8a) and a harvesting circuit at $f = 915$ MHz. Defining the system efficiency as the ultimate criterion for the final rectenna system, after selecting the appropriate rectifier circuit the antenna implemented and the rectifier are combined, the circuit is optimized, and the rectenna is obtained. Antenna and the rectifier are studied as one system, and the antenna input impedance is not required to be matched at 50 Ω. A satisfactory efficiency is obtained while satisfying realistic conditions verifiable by measurements. It should be noted that at some proposed solutions in the literature, the obtained circuits are tested under high power which maximizes the efficiency. This is actually unrealistic due to the several design restriction of implantable systems.

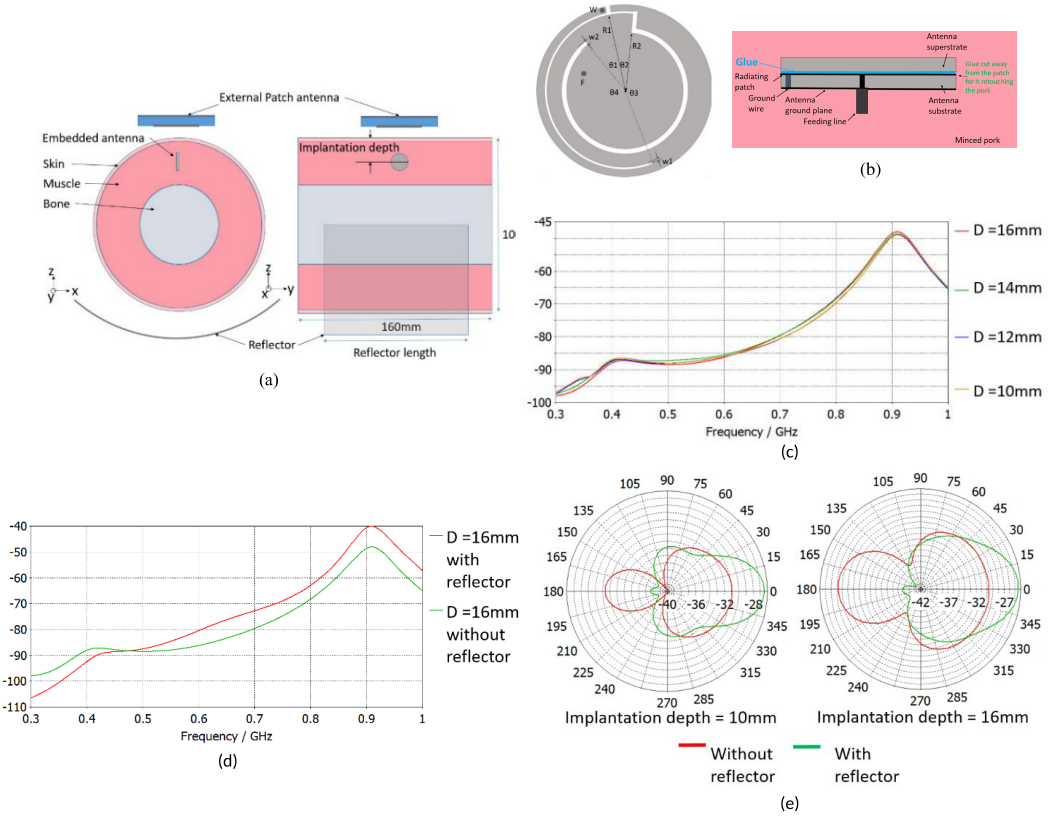

Figure 7. $|S_{21}|^2$ (dB) between a minimized circular slot antenna implanted in a cylindrical arm phantom and an external patch antenna. Implantation depth varies from $D = 10$ mm to $D = 16$ mm. The external patch antenna distance from phantom surface is set at 200 mm. Implantable antenna volume is 120 mm^3. A cylindrical reflector can be also used for electromagnetic focusing as seen in (a). Results in (c) are without use of reflector while (d) (S_{21} link) and (e) (realized implantable rectenna gain) present the effect of reflector use. From [5].

In [5], an implantable rectenna system is obtained also at $f = 915$ MHz. The antenna part of the system (see Figure 7) is extremely minimized. It is found that, taking into account the tissue environment, the antenna optimum performance is achieved at feeding port impedance $Z = 110\ \Omega$. Therefore, the rectenna is built with this parameter in mind. System efficiency is again very good while a very small implantable rectenna is obtained. Results are verified against measurements.

3.4. *System efficiency enhanced by external helpers*

In implantable R_x–T_x systems and in order to enhance the S_{21} link between the external and the internal antennas several external enhancements have been proposed. The most sophisticated, utilize the so-called metasurfaces which are usually applied on the skin covering an area relatively larger than the implantable antenna. Several examples can be found in literature. For example, in [28], a metasurface patch is proposed. Results show an enhancement of S_{21} link (implantable antenna reception) around 6 dB. The metasurface patch seems to operate as a focus lens.

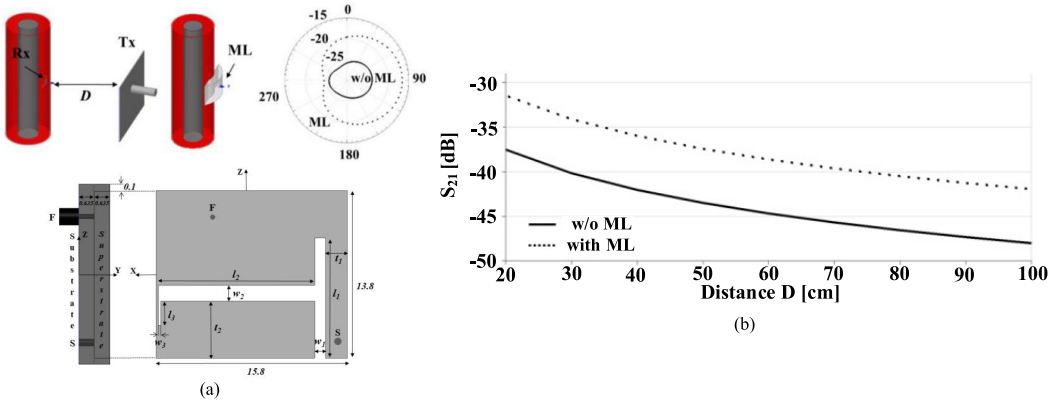

Figure 8. $|S_{21}|^2$ (dB) between an implantable slot antenna at $f = 915$ MHz and a rectangular $\lambda/4$ patch antenna. Implantable antenna is embedded in a cylindrical arm phantom at 10 mm depth. It has a volume of 285 mm^3. A matching gel type ($\varepsilon_r = 20$, $\tan\delta = 3 \times 10^{-3}$) denoted by ML is also used and it increases effectively the link. Results are extracted from [4].

Probably implantable antenna position can greatly affect the results and hence the system could be sensitive to misplacements. Similarly, in [29], an on-body metasurface is investigated. Up to 10 dB enhancements is reported. Still the size of the proposed metasurface could have large physical size. Its application on the skin could be sensitive to surface modification due to the body shape, etc.

Yet, enhancement can be achieved by implementing much simpler solutions which can have a similar effect. In [4], for an implantable rectenna coupled with an external antenna, a simple lubricating gel (appropriate for skin contact) with relative dielectric permittivity of $\varepsilon_r = 20$ and loss tangent equal to $\tan\delta = 3\times10^{-3}$ is being used (system is shown in Figure 8). The gel can cover a small area, somewhat larger that the antenna aperture which is equal to 14×15 mm and can effectively increase the achieved link by 6–7 dB as seen in Figure 8b. It is noted that the simulated results are verified by measurements [4]. As can be understood the gel application is not sensitive to misplacement or deformation because of the body shape and can offer a very simple but also effective solution for S_{21} link increase.

In [5], an alternative path is being proposed. The proposed implantable rectenna can be implanted in an arm (see Figure 7) while a curved metallic reflector is introduced in order to increase the link with an external antenna. The reflector is placed on the opposite side of the arm in relation with the external antenna. The reflector has a length of 16 cm, is placed at a 5 mm distance from the skin (to consider clothing) and covers the arm. As seen in Figure 7d, the reflector increases the S_{21} link by 7 to 8 dB. Simulated effect of reflector use, shown in Figure 7, has been also verified by measurements. While the reflector has a relatively large size, its application on the arm is very practical and can offer a robust solution for practical applications, insensitive as well to misplacement or arm shape.

4. Conclusions

The design of an implantable antenna system that includes T_x and R_x components is governed by several parameters. While the operational frequency ranges from 400 MHz to usually 2.4 GHz or sometimes 5 GHz, depending on the application considered (e.g., communication between

or more implantable components, wireless transmission of medical data from an implantable sensor to an external hub, wireless control of an implantable system, wireless energy transfer) different factors can affect the final design. Since the outmost measure for an effective design is system efficiency, the external and implantable antennas can be considered as a system characterized by a scattering matrix. Calculation of S_{21} parameter is relatively simple and provides direct comparison with measurements. When a matching circuit is also considered either for antenna feeding or for using arbitrary load, this can be also considered as part of the system. Effectively, S_{21} can be used to cover several scenarios to obtain the optimum results. To that end, this paper, after determining S_{21} calculation for covering the above considerations, summarizes how the link budget can be obtained, what are the safety limits for implantable systems at frequencies of interest, and which are the allowable power for external or implantable antennas.

These factors are used to study a number of various scenarios, including S_{21} link calculation between either implantable antennas and/or implantable and external to the body antennas. Among others, this paper also show that while an optimum frequency, for example, can be determined for achieving an optimum link between two implantable antennas under ideal environments, different observations can be drawn when the antenna type, its design and the human phantom are considered. In addition, antenna size or how the antenna radiates can also define the link used. Telemetry cases where the external antenna can operate at its maximum power without violating safety limits are also considered. Interestingly, it is shown that while 915 MHz frequency allow for example much higher power use for an external antenna, when the distance of the external antenna from the body exceeds a limit then the use of a lower frequency with 20 dB less or lower power emission can actually secure a successful link. Finally, it is shown that while meticulously designed metasurfaces applied on the body have been proposed in order to enhance the link budget, much simpler and more robust solutions can be utilized.

In conclusion, the design of an implantable antenna is not exhausted by defining a minimum size or maximum gain. Many times, the T_x and R_x components need to be considered as a system and be investigated using scattering matrixes. This permits to investigate the effect of different parameters and concurrently offer a direct connection between simulations and measurements. Considering the design as a system can allow for generating, at the end, interesting results that will lead to an optimum, robust and well thought outcome.

Declaration of interests

The authors do not work for, advise, own shares in, or receive funds from any organization that could benefit from this article, and have declared no affiliations other than their research organizations.

References

[1] M. Matthaiou, S. Koulouridis, S. Kotsopoulos, “A novel dual-band implantable antenna for pancreas telemetry sensor applications”, *Telecom* **3** (2022), no. 1, p. 1-16.

[2] W. G. Scanlon, B. Burns, N. E. Evans, “Radiowave propagation from a tissue-implanted source at 418 MHz and 916.5 MHz”, *IEEE Trans. Biomed. Eng.* **47** (2000), no. 4, p. 527-534.

[3] T. Karacolak, A. Hood, E. Topsakal, “Design of a dual-band implantable antenna and development of skin mimicking gels for continuous glucose monitoring”, *IEEE Trans. Microw. Theory Tech.* **56** (2008), p. 1001-1008.

[4] S. Bakogianni, S. Koulouridis, “A dual-band implantable rectenna for wireless data and power support at sub-GHz region”, *IEEE Trans. Antennas Propag.* **67** (2019), no. 11, p. 6800-6810.

[5] S. Ding, S. Koulouridis, L. Pichon, “Implantable wireless transmission rectenna system for biomedical wireless applications”, *IEEE Access* **8** (2020), p. 195551-195558.

[6] D. Nikolayev, W. Joseph, M. Zhadobov, R. Sauleau, L. Martens, "Optimal radiation of body-implanted capsules", *Phys. Rev. Lett.* **122** (2019), no. 10, article no. 108101.
[7] D. M. Pozar, *Microwave Engineering*, Wiley, Hoboken, NJ, 2011.
[8] C. Garcia-Pardo, A. Fornes-Leal, N. Cardona *et al.*, "Experimental ultra wideband path loss models for implant communications", in *2016 IEEE 27th Annual International Symposium on Personal, Indoor, and Mobile Radio Communications (PIMRC), Valencia, Spain*, 2016, p. 1-6.
[9] R. Warty, M. R. Tofighi, U. Kawoos, A. Rosen, "Characterization of implantable antennas for intracranial pressure monitoring: reflection by and transmission through a scalp phantom", *IEEE Trans. Microw. Theory Tech.* **56** (2008), no. 10, p. 2366-2376.
[10] Q. Chen, K. Ozawa, Q. Yuan, K. Sawaya, "Antenna characterization for wireless power-transmission system using near-field coupling", *IEEE Antennas Propag. Mag.* **54** (2012), no. 4, p. 108-116.
[11] Y. Li, H. Sato, Q. Chen, "Capsule antenna design based on transmission factor through the human body", *IEICE Trans. Commun.* **101** (2018), no. 2, p. 357-363.
[12] W. Xia, K. Saito, M. Takahashi, K. Ito, "Performances of an implanted cavity slot antenna embedded in the human arm", *IEEE Trans. Antennas Propag.* **57** (2009), no. 4, p. 894-899.
[13] J. Zhang, R. Das, D. Hoare *et al.*, "A compact dual-band implantable antenna for wireless biotelemetry in arteriovenous grafts", *IEEE Trans. Antennas Propag.* **71** (2023), no. 6, p. 4759-4771.
[14] "Medical Device Radiocommunications Service (MedRadio)", Federal Communications Commission. [Available in: https://www.fcc.gov/medical-device-radiocommunications-service-medradio].
[15] ETSI EN 302 537 V2.1.1, "Ultra Low Power Medical Data Service (MEDS) Systems operating in the frequency range 401 MHz to 402 MHz and 405 MHz to 406 MHz; Harmonised Standard covering the essential requirements of article 3.2 of the Directive 2014/53/EU", 2016, European Telecommunications Standards Institute.
[16] ETSI EN 301 839 V2.1.1, "Ultra Low Power Active Medical Implants (ULP-AMI) and associated Peripherals (ULP-AMI-P) operating in the frequency range 402 MHz to 405 MHz; Harmonised Standard covering the essential requirements of article 3.2 of the Directive 2014/53/EU", 2016, European Telecommunications Standards Institute.
[17] "Wireless Medical Telemetry Service, 47 CFR Parts 1, 2, 15, 90 and 95", *Federal Communications Commission, Federal Register (The Daily Journal of United States Government)* **65** (2000), no. 137, p. 43995-44010.
[18] ETSI EN 300 220-2 V3.2.2 (2024-03), "Short Range Devices (SRD) operating in the frequency range 25 MHz to 1,000 MHz with power levels ranging up to 500 mW e.r.p", [Available in https://www.etsi.org/committee/1398-erm].
[19] 47 CFR Part 15, "Part 15. RadioFrequency Devices", [Available in https://www.ecfr.gov/current/title-47/chapter-I/subchapter-A/part-15].
[20] ICNIRP, "Guidelines for limiting exposure to, electromagnetic fields (100 KHz to 300 GHz)", 2020, ICNIRP Guidelines.
[21] IEEE C95.1-2019/Cor 2-2020, "IEEE standard for safety levels with respect to human exposure to electric, magnetic, and electromagnetic fields, 0 Hz to 300 GHz - Corrigenda 2", 2019–2020.
[22] F. Mghar, A. Diet, C. Gannouni, L. Pichon, O. Meyer, S. Koulouridis, "Characterization of an intra-body wireless link in the UHF band", *Prog. Electromagn. Res. M* **111** (2022), p. 247-259.
[23] A. Ibraheem, M. Manteghi, "Intra-body propagation channel investigation using electrically coupled loop antenna", *Prog. Electromagn. Res. M* **40** (2014), p. 57-67.
[24] Y. El-Saboni, G. A. Conway, W. G. Scanlon, "Effect of tissue boundaries on the intra-body communication channel at 2.38 GHz", in *2017 International Workshop on Antenna Technology: Small Antennas, Innovative Structures, and Applications (iWAT)*, 2017, p. 285-288.
[25] P. Soontornpipit, C. M. Furse, Y. C. Chung, "Design of implantable microstrip antennas for communication with medical implants", *IEEE Trans. Microw. Theory Tech.* **52** (2004), no. 8, p. 1944-1951.
[26] C. M. Lee, T. C. Yo, C.-H. Luo, C. H. Tu, T. Z. Juang, "Compact broadband stacked implantable antenna for biotelemetry with medical devices", *Electron Lett.* **43** (2007), p. 660-662.
[27] A. Kiourti, M. Christopoulou, K. S. Nikita, "Performance of a novel miniature antenna implanted in the human head for wireless biotelemetry", in *IEEE AP-S International Symposium on Antennas and Propagation and USNC/URSI, Spokane, Washington, USA*, 2011.
[28] S. Jo, W. Lee, H. Lee, "Metasurface patch for wireless power transfer in implantable devices", *Adv. Funct. Mater.* **33** (2023), no. 38, article no. 2300027.
[29] N. Ghavami, E. Razzicchia, O. Karadima *et al.*, "The use of metasurfaces to enhance microwave imaging: experimental validation for tomographic and radar-based algorithms", *IEEE Open J. Antennas Propag.* **3** (2022), p. 89-100.

ACADÉMIE DES SCIENCES
INSTITUT DE FRANCE

Comptes Rendus. Physique
2024, Vol. 25, Special issue S1, p. 23-39
https://doi.org/10.5802/crphys.170

Research article / *Article de recherche*

Energy in the heart of EM waves: modelling, measurements and management / *L'énergie au cœur des ondes électromagnétiques : modélisation, mesures et gestion*

A Simulation Method Suited for the Whole French Territory Electromagnetic Waves Exposure

Une méthode de simulation adaptée à l'exposition aux ondes électromagnétiques de l'ensemble du territoire français

Nicolas Noé [*,a], Lydia Sefsouf [b], Jean-Benoit Dufour [c], Samuel Carré [a], Emmanuelle Conil [b], Nabila Bounoua [c] and Jean-Benoit Agnani [b]

[a] Centre Scientifique et Technique du Bâtiment, Nantes

[b] Agence nationale des fréquences, Maisons-Alfort

[c] Geomod, Saint-Didier-au-Mont-d'Or

E-mails: nicolas.noe@cstb.fr (N. Noé), lydia.sefsouf@anfr.fr (L. Sefsouf), jean-benoit.dufour@geomod.fr (J.-B. Dufour)

Abstract. As part of the process for monitoring public exposure to electromagnetic waves, the national frequency Agency is carrying out, in collaboration with the Ministry of Ecological Transition and Territorial Cohesion, the Scientific and Technical Center for Building (CSTB) and Geomod, a numerical modeling of the electromagnetic wave exposure levels emitted by mobile telephony base stations on a national scale. This paper presents a dedicated simulation method for the numerical modeling of the whole French territory's exposure to EMF. This method accounts for EMF exposure everywhere (outdoors and inside buildings), while performing fast enough to fulfill operational constraints. The simulation method relies on a ray-based 2.5D and 3D mixed approach that takes into account computation areas depending on the radiated power pattern of the antennas. The method is yet deployed on pilot areas before a full deployment.

Résumé. Dans le cadre de son plan de surveillance de l'exposition du public aux ondes, l'Agence nationale des fréquences réalise, en collaboration avec le ministère de la Transition écologique et de la Cohésion des territoires, le Centre scientifique et technique du bâtiment et Geomod, une modélisation numérique des niveaux d'exposition aux ondes électromagnétiques émises par les antennes relais de téléphonie mobile à l'échelle du territoire national. Cette modélisation nécessite la mise en œuvre d'une méthode de calcul spécifique. La méthode présentée ici permet de restituer un niveau d'exposition en tout lieu (à l'extérieur et à l'intérieur des bâtiments) tout en conservant des temps de calcul compatibles avec les contraintes opérationnelles. La méthode est basée sur une approche à rayons combinée 2,5D et 3D et sur la prise

* Corresponding author

en compte de zones de calcul dépendant des caractéristiques d'émission des antennes. La méthode est aujourd'hui mise en œuvre sur des zones d'expérimentation avant son déploiement complet.

Keywords. EMF exposure, mobile telephony, numerical simulation.

Mots-clés. Exposition aux champs électromagnétiques, Téléphonie mobile, Simulation numérique.

Note. This article follows the URSI-France workshop held on 21 and 22 March 2023 at Paris-Saclay.

Manuscript received 17 July 2023, revised 20 October 2023, accepted 15 November 2023.

1. Context and main goal

Engagement 8 of the fourth health and environment national plan [1, *plan national santé environnement, PNSE4*] aims at containing exposure to electromagnetic waves. It focuses mainly on the knowledge of the electric field generated by mobile telephony base station antennas. Within this plan, the French Frequency Agency (*Agence nationale des fréquences, ANFR*) has been tasked with the Ministry of Ecological Transition (*Ministère de la Transition Écologique et de la Cohésion des territoires*), the Scientific and Technical Center for Building (*Centre Scientifique et Technique du Bâtiment, CSTB*) and the company Geomod, with creating a numerical modelling of electromagnetic wave exposure levels induced by mobile telephony base station antennas at a national scale.

Figure 1 was generated using a beta release of the web service that exposes those simulation results. The left part of the figure is a color map of the exposure level 1.5m above the ground. On the right part of the figure, each building outline (in the horizontal plane) is colored using the maximum indoor exposure level on the frontage, along a vertical line.

One of the specificities of this numerical modelling is the extensive computation area to consider. As a matter of fact, up to this day, most exposure simulations were only performed in the vicinity of the antennas. These simulations are usually dedicated to assessing compliance with exposure standards or to enforcing local regulations. For instance in France, mandatory records based on simulation have to be submitted when a new antenna is deployed [2, *dossiers d'information mairie*]. Similarly, environmental permits in the Bruxelles Capitale region in Belgium [3] also require simulation results. These regulations either (France) conform with the European Commission recommendation on the limitation of exposure of the general public to electromagnetic fields (0 Hz to 300 GHz), based on the guidelines published by the International Commission on Non Ionising Radiation Protection [4, ICNIRP] or can be more restrictive (Bruxelles Capitale region). Nevertheless they are always limited to the vicinity of the antennas. As far as coverage maps are concerned, they span very large areas, but with a low spatial resolution. The aim pursued here is to estimate exposure levels anywhere in space, even far from antennas, along with a precise knowledge of the exposure levels close to the antennas.

Such exposure maps could then be used for statistical analysis (to compare exposure levels between different areas for instance) and to monitor temporal evolution of exposure level (due to the ever changing radioelectric sources) or even to test future scenarios before they are implemented.

2. Implementation

Achieving the aforementioned goal implies being able to produce this whole France map in a reasonable time and to be able to update it on a regular basis. Figure 2 gives an overview of the full simulation process, starting from databases (stage 0) to the final exposure maps (stages 6 and 7).

An adapted computation method is needed, that handles each base station (a batch of antennas) independently, as illustrated on Figure 3, with stages 1 to 5. Results on batches of antennas are merged at local scale, using regular tiles (stage 6) to deliver a cumulated exposure level everywhere in France (stage 7). This cumulated level might be identical to zero, meaning it should be below a measurement threshold (typically 0.05 V/m).

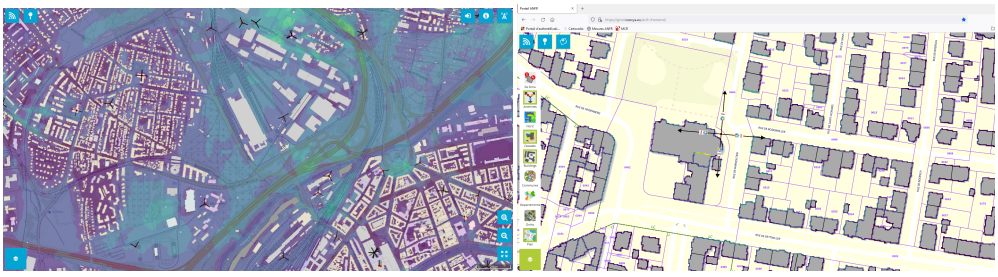

Figure 1. Example of exposure maps : electric field 1.5m above the ground (left) and on the contours of buildings (right).

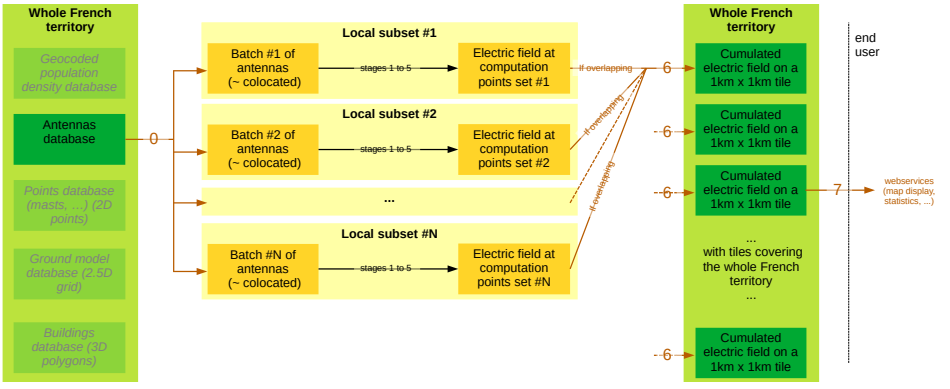

Figure 2. Overview of the full process : from databases to web services for end users.

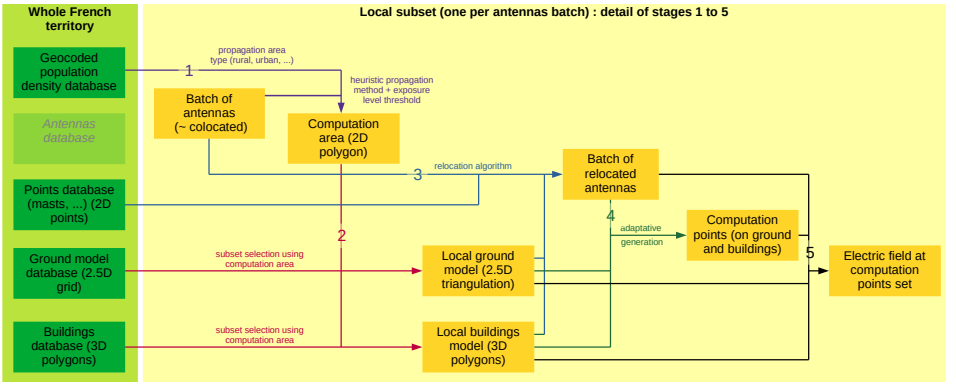

Figure 3. Overview of the simulation process for a single antenna batch.

2.1. *Input data*

2.1.1. *Antennas*

Antennas descriptions come from ANFR database STATIONS (an internal database filled with information by telephone operators). From the computation side, an antenna is associated to a 3D position and an orientation (aiming given as two angles : azimuth in the horizontal plane and mechanical tilt in the vertical plane). An antenna corresponds to a physical "box", and each antenna is made of one or more transmitters (one transmitter per technology - 2G, 3G, 4G, 5G and frequency band). Each transmitter is associated with an EIRP (Effective Isotropic Radiated Power) and a far field radiation pattern (including electrical tilt). This radiation pattern (from manufacturer databases) is usually described by two cut-planes of the gain (one in the horizontal plane and one in the vertical plane). A full 3D radiation pattern is recomposed from these two 2D patterns (see Figure 4) in order to be able to estimate gain in any 3D direction. [5] details a recomposition method and references others but for base station antennas, it appears that the method used by radio planning software [6] is the most suited.

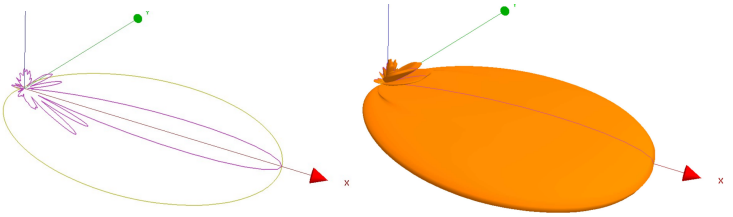

Figure 4. Radiation pattern of an antenna (linear) : on the left, the horizontal and the vertical cut-planes (input data), on the right the recomposed 3D pattern used for simulation.

The STATIONS database does not give a precise location of antennas. There is only a single approximate location of each base station (even if the base station is made of antennas with different azimuths at different corners of a building). This single location (that could be interpreted as the barycenter of all antennas) has also uncertainty due to numerical rounding of latitude and longitude in degree / minute / second natural integers), leading to a potential 20 meters error. Hence, the antennas have to be relocated using a dedicated algorithm. Nevertheless, the type of antenna support (mast or building) is known. For the latter support, the algorithm relocates antennas to the center of the building, while not moving them more than 30 meters from their original position.

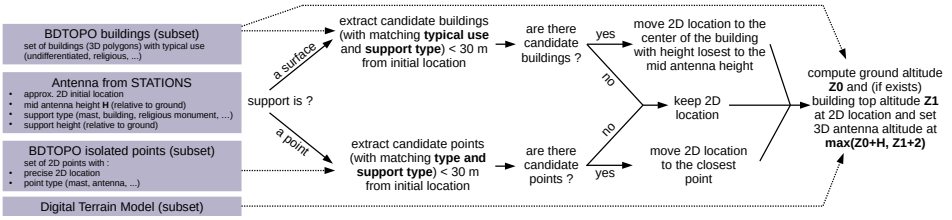

Figure 5. Relocation algorithm.

The relocation algorithm (stage 3 on Figure 3) is illustrated on Figure 5. While more realistic algorithms (dispatching different azimuths to different corners of buildings [7]) could be used,

this choice is a mutual agreement of operators and regulator. The choice of the algorithm is unrelated to the simulation method and precise positions of antennas could be available in a near future or in local databases. Albeit, it must be noted that this introduces extra uncertainty in the simulation results to be discussed later.

2.1.2. *Geometrical model*

The geometrical model (see Figure 6) mostly comes from the BDTOPO geometrical database from the French mapmaking agency (*Institut Géographique National*, IGN). In this case, it is made of 2.5D buildings, i.e. 3D polygons representing the outline of the roof of the building, and the building height. As a consequence, no precise shape of the roof is known. Nevertheless, models with more precise modelling (of the roof) can also be used as no hypothesis is made on the shape of the buildings (that can be true 3D buildings). The digital terrain model also comes from IGN databases (BDALTI).

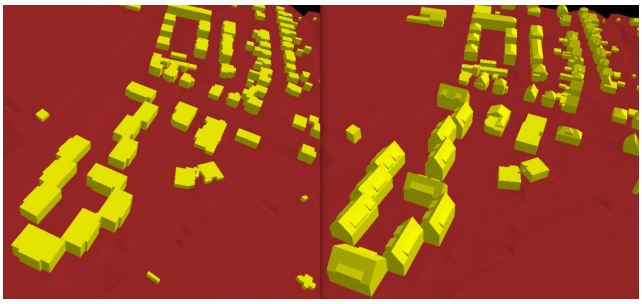

Figure 6. Sample of the geometrical model used for simulation : BDTOPO IGN (on the left), 3D model provided by *Eurométropole de Strasbourg* with more detailed roofs (on the right).

The shape of the roofs and the precise height of buildings is an important parameter in the forecoming simulations, as propagation paths will be computed in a 3D environment, and changing from LOS to NLOS (or reciprocally) due to some different masking effect can lead to important changes in exposure levels.

2.2. *Preprocessing*

2.2.1. *Computation areas*

All horizontally colocated antennas (within a five meter circle) are gathered in so-called batches (stage 0 on Figure 2). For each batch, a computation area surrounding the batch center in the horizontal plane is then precomputed (stage 1 on Figure 3). A minimal electric field threshold is chosen (the minimal level of exposure to be simulated later), and for each azimuth the maximum distance above which the electric field falls below the chosen threshold is computed using a heuristic method (extended Hata model [8]). The heuristic method is instantaneous and only uses the geographical area type (urban, rural, ...), the power and the horizontal pattern of each transmitter in the batch. This approach avoids relying on a general maximum propagation distance and ensures an homogeneous behaviour of the simulation for antennas with heterogeneous powers and is illustrated in Figure 7.

The overall process for a full French department (Bas-Rhin) is illustrated on Figure 8, for a threshold of -40 dBV/m (i.e 0.01 V/m). The geographical area type is translated from the population density P (as inhabitants per square meter) in the city or city district at the antennas location using the formula in Table 1.

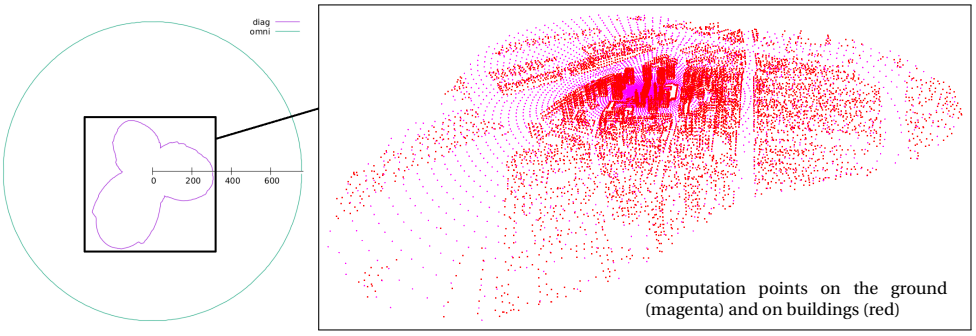

Figure 7. Precomputation of the computation area around an antenna base station made of three antennas with three azimuths (on the left) and computation points (on the right).

Table 1. From population density to environment type for extended Hata precomputation

population density P	$P \leq 25$	$25 < P \leq 300$	$300 < P \leq 1500$	$1500 < P \leq 5000$	$P > 5000$
environment type	rural	suburban	urban (small)	urban (median)	urban (large)

There are 5705 antennas with 21681 transmitters, that are divided into 334 computation batches. On one hand, it can be seen that the areas are larger in rural areas and that they are even parts of the territory where nothing will be computed (no exposure). On the other hand, in dense urban areas, most areas are overlapping, while they are smaller. This precomputation is mandatory for fast, exposure-level oriented simulations.

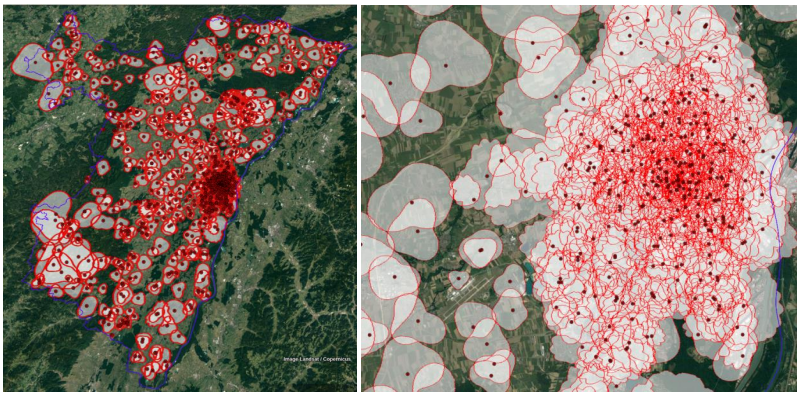

Figure 8. Computation areas for the French Bas-Rhin department. On the left, the full department (within the magenta outline) and on the right Strasbourg city area only.

2.2.2. *Computation model*

After sizing the computation area, the ground and buildings are extracted from geographical databases. The ground is transformed into a TIN (triangular irregular network), with an interpolated normal to ensure continuous reflection. The buildings are made of 3D polygons. The computation area is then populated with computation points (receivers), on the ground and on the building frontages. Calculation point density varies with distance to the center of the area (see Figure 7). The horizontal step ranges from 2 meters to 50 meters at 1 km. Receivers on the front

of buildings are created as vertical columns of multiple points, at different heights (with a vertical step three times smaller than the horizontal one). Far from the antennas, only one receiver per building frontage is created and for far and low individual houses, a single receiver is created atop the roof.

This varying receiver density aims at speeding up computations, but the method used is generic and does not rely on this adaptive receiver mesh.

2.3. *Geometrical computations*

A ray-tracing model is used for simulation, in order to find propagation paths connecting antennas and computation points. These propagation paths take into account reflection and diffraction by ground and buildings. Asymptotic methods (geometrical optics and uniform theory of diffraction) are well suited to the mobile telephony frequency range (700 MHz - 3.5 GHz, i.e. wavelengths ranging from 43 cm to 8 cm) and to the level of detail and precision of the geometrical models (approximately 1 m). Each computation is a two stages process, with a full 3D computation and a 2.5D computation.

2.3.1. *Geometrical computation : 3D stage*

A full 3D computation in done within a horizontal circular area centered on the antennas, with a typical 200 meter radius (see Figure 9, a subset of the model of Figure 7). This 3D computation takes into account reflection and diffraction by buildings (frontages and roofs) and ground, and is based on an adaptive 3D beam tracing algorithm [9]. No assumption is made on the orientation of the reflecting surfaces and diffracting edges, that can be slanted or not. Computations are limited to two reflections (typically one on the buildings, one on the ground) and one diffraction (by building edges).

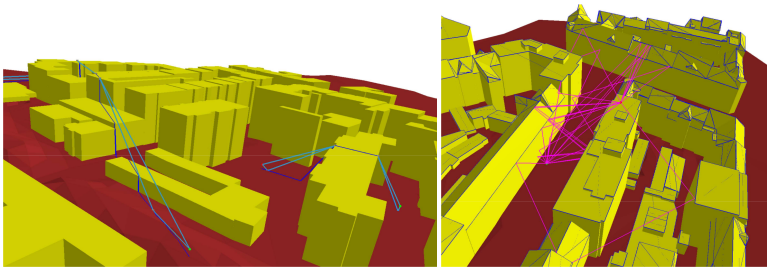

Figure 9. On the left: examples of 2.5D computed paths (ground profile as a navy blue line, and 3D paths including ground reflection as light blue lines). On the right: examples of 3D computed paths.

The purpose of this 3D computation stage is to get more accurate results in the vicinity of the antennas without having to simplify the buildings' shape. Masking effect by different roof shapes (two-pitches, flat, ...) and reflection not only on vertical planes are then enabled.

2.3.2. *Geometrical computation: 2.5D stage*

In addition to the 3D computation, a 2.5D computation is done on the whole area. A double loop spans all pairs of horizontal points (antennas and receivers at the same horizontal location). For each of these pairs, an algorithm (based on a 2D ray-tracer with all non-vertical building and ground edges) extracts the ground profile as seen from atop. Then, using antenna and receiver heights above the ground, an always existing 3D path is computed, using the convex envelop

method [10]. This 3D path can either be direct or made of isolated and / or successive diffractions on the buildings and on the ground. Finally, ground reflections (in a plane perpendicular to the profile plane) are added, with a single reflection between each pair of transmitter / isolated diffraction point / receiver as illustrated in Figure 9.

The purpose of this 2.5D computation stage is to have a result at every computation point as such a path always exists. This stage is also very fast as it's a 2D + 1D algorithm and thus can be done on larger areas. Furthermore, no building reflection is computed and ground reflections and diffractions are approximated compared to a dedicated 3D computation.

2.3.3. *Aggregation of 3D and 2.5D geometrical results*

A final geometrical stage aggregates 3D and 2.5D geometrical results. This is mandatory in order not to compute a similar 3D path in both stages, as this could happen (for direct paths, ground reflected path and others). This aggregation stage uses the path "history" (number and type of interaction - reflection, diffraction ..., and on which objects). In the case of two overlapping paths, the priority is given to the one computed with the 3D algorithm, and the one computed with the 2.5D algorithm is discarded.

Finally, for each antenna - receiver pair, the path difference between the two main paths (with shortest lengths) is also stored. This information will be used later to interpolate the electric field at any location.

2.4. *Physical computation stage*

2.4.1. *Electric field computation*

The physical stage computes for each 3D path (whether it originates from the 2.5D or the 3D computation stage), the associated electric field, generated at the receiver location, for each transmitter associated with the path. The electric field is a complex 3D vector and is computed using the radiation pattern of the transmitter, its polarization, and the reflection and diffraction coefficients along the path. The underlying physical model can handle successive diffractions, whether they are isolated diffractions on edges or creeping waves (by crawling over the top of a building or over a hill), without limitation of the number of diffractions.

While from a theoretical point of view the electromagnetic properties could be different for each building, no such information exists. As a consequence, a global approach is used with unique building and ground materials. The materials are defined by relative permittivity ϵ_r (-) and conductivity σ (S/m). The buildings' material is a concrete like one ($\epsilon_r = 6$ and $\sigma = 0.03$, leading to an average reflection loss of ≈ 6.7 dB in the considered frequency range). The ground material is a very dry ground, taken from an ITU recommendation [11], leading to an average reflection loss of ≈ 9.2 dB.

As far as reflection coefficients are concerned, most construction materials (concrete, brick, wood, ...) have not-so-different reflection loss (≈ 6 dB), so the influence of the materials (aside from metallic ones) is limited.

On the contrary there is as large diversity of the soil type in different areas or even in the same area. Nevertheless it is very likely that no ground reflected path exists without an equivalent path minus this ground reflection, with a higher level, and the diffraction model used does not take into account ground material. Computations without any ground reflections also exhibited that having no ground material downgrades results (compared to measurements).

The electric field is computed 1.5 meters above the ground but also inside buildings, just after the first wall. This is done by using a heuristic transmission model (from [12, COST 231]) that handles incident angle of incoming waves on the outer wall. Once again, a unique transmission loss factor is used, a 3,8 dB normal (typical of a double glazing).

The band associated with each transmitter is sampled in 16 frequencies, each of them carrying a fraction of the power. The electric field is computed at each of these frequencies before a final quadratic summation to get a scalar electric field generated by the transmitter at the receiver location. This scalar value, along with the path difference, is stored in the output files.

2.4.2. *Assessment of first Fresnel ellipsoid clearance*

In the case of a direct path, the first Fresnel ellipsoid is built around it and its clearance $p \in [0;1]$ is computed using ray-tracing, with discretized curved rays as illustrated in Figure 10. For a knife-edge like obstacle [13] this clearance can be related to the υ parameter with $\upsilon = 2\sqrt{|\delta|/\lambda} = (2p-1)/\sqrt{2}$, where δ is the marching difference. An extra path loss $L = 12p$ dB ($p = 0$ for a total clearance, $p \to 1$ for a full obstruction) is then applied to the electric field of this direct path as an approximation of the extra path loss.

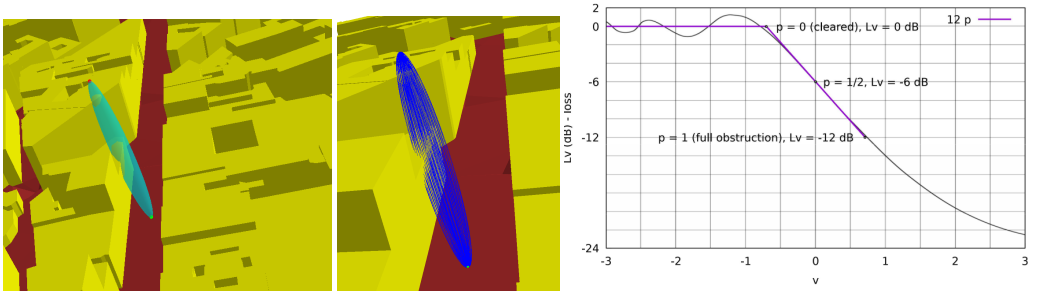

Figure 10. First Fresnel ellipsoid for a direct path, with partial obstruction by two buildings (on the left), sampled curved rays used for the clearance computation (on the middle) and extra path loss approximation (on the right).

One can also notice the successive improvements of the simulation method in Figure 11, from the pure 2.5D method, the 2.5D + 3D method (with 3D reflections on buildings) and the 2.5D + 3D method with first Fresnel ellipsoid clearance, gives the better results up to day.

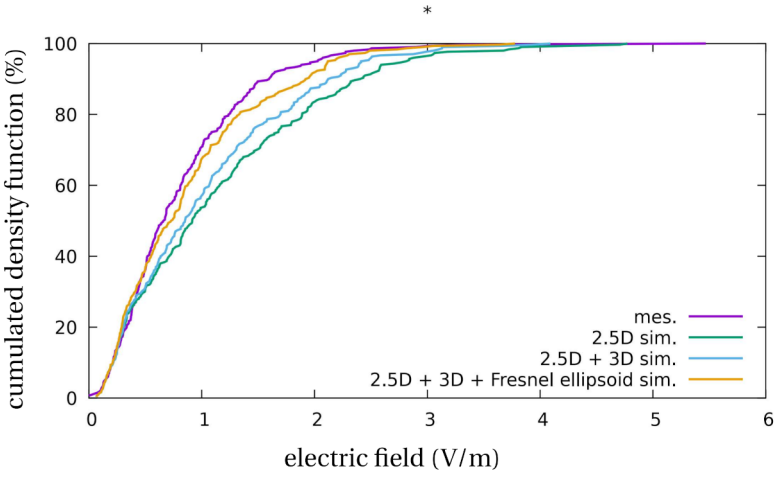

Figure 11. Cumulated density function of total electric field in Paris: evolution of the simulation method.

2.5. *Post-processing*

Some post-processing is done to reduce results variability and to generate global exposure maps.

2.5.1. *Hotspots refinement and vertical smoothing*

The main goal of the simulation is to evaluate the electric field everywhere (exposure maps). But it should also be possible to estimate the higher levels ("hotspots"), close to the antennas. One must notice that there is a strong vertical spatial variability of the electric field in front of the antennas. This is due to the narrow vertical beamwidth of the radiation pattern (usually 6 to 9 degrees, while the horizontal beamwidth is $\approx 60°$). As a consequence, the choice of the (discrete) computation points can lead to high variation of the maximum electric field on a vertical line, as illustrated in Figure 12, and also miss the higher exposure point. To fix this problem, in the case of a line-of-sight from the antenna to the receiver, a new computation point is added.

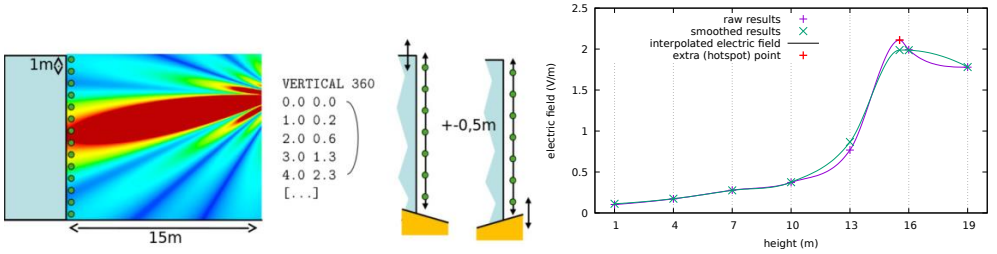

Figure 12. Effect of the vertical sampling on the maximum exposure point computation in front of antennas and simulated electric field on a column of receivers with regular vertical sampling (without and with smoothing), with added hotspot.

These extra computation points are dynamically added during computation by the software. For each column of receivers (receivers at the same horizontal location, with different heights), receivers in LOS of an antenna are tagged. The precise height of the maximum exposure point is determined using the radiation pattern and the possible height ranges (between two or more adjacent LOS points) with a free-field formulation.

The thin violet crosses in Figure 12 are the input computation points on a vertical in front of an antenna. An extra hotspot point (fat red cross) is dynamically added during computation at roughly 15.5 m high. This hotspot captures the maximum exposure level that would otherwise have been underestimated. The interpolation between the points is done using a cubic positive interpolation that allows to estimate the electric field at any height (violet curve).

While this hotspot extension ensures a very stable maximum electric field, it is also quite unrealistic because it is a purely theoretical value located at a very precise point. Hence, a vertical smoothing is applied afterward. Using the previous interpolation, a sliding average with a 1.5 meter window is applied. This smoothing mimics the French measurement protocol where measurement points are averaged over three different heights. Simulation on Paris showed that the average electric field does not change that much (2% to 3% lower with smoothing), while the peak values have more sensitive changes (up to 15% lower).

2.5.2. *Interpolation of results*

As the electric field is computed on a per-base station basis, the computation points are different from one computation batch to another, and there is some overlapping between the computation areas too. Consequently, the electric field from a computation batch has to be

interpolated everywhere in space in order to be able to cumulate electric field from different batches at the same location. This interpolation is done using both the scalar electric field and the path difference to reproduce fading and interferences on exposure maps.

The final rendering is done on a 2 m × 2 m rasterized image and with square tiles covering the whole French territory.

3. Results

3.1. *Computation time*

The validation tests are done with a 14 cores Intel Xeon Gold 6132 CPU machine. The computation on a whole French department (Bas-Rhin) is equivalent to 76 hours on a monothreaded machine but there is a strong dispersion between sites (see Table 2).

Table 2. Computation time per site for full Bas-Rhin department

average	rms	min	max	P50	P90	P95	P99
03mn 04s	03mn 17s	00mn 04s	45mn 44s	02mn 24s	05mn 20s	06mn 58s	13mn 02s

4. Comparison with measurements

4.1. *Methodology*

The electric field has been measured in different (outdoor) locations following ANFR protocol [14]. The measurements evaluate the electric field per band and operator averaged over 6 minutes. The simulations are done with EIRP of transmitters (declared authorized power) and reduction factors are applied to the results to account for the real load. This reduction factor is 4 dB for each technology apart from beamsteering antennas.

The measurement points cover a lot of different situations (LOS, NLOS, rural, urban, ...). There is still uncertainty in the location of the points and the comparisons are carried "as is". Three indicators are used to compare measurements : Pearson correlation p_{lin} (on measured and simulated electric field in V/m), signed mean error $\epsilon_{1,\text{lin}}$ (of difference between measured and simulated electric field in V/m) and quadratic mean error $\epsilon_{2,\log}$ (of difference between measured and simulated electric field in dB).

If $E_{\text{mes},i}$ (respectively $E_{\text{sim},i}$) is the measured (resp. simulated) full band electric field for point $i, i \in \{1,2,\dots n\}$, we have:

$$p_{\text{lin}} = \frac{\sum_{i=1}^{n}(E_{\text{sim},i} - \bar{E}_{\text{sim}})(E_{\text{mes},i} - \bar{E}_{\text{mes}})}{\sqrt{\sum_{i=1}^{n}(E_{\text{sim},i} - \bar{E}_{\text{sim}})^2 \sum_{i=1}^{n}(E_{\text{mes},i} - \bar{E}_{\text{mes}})^2}} \begin{cases} \bar{E}_{\text{sim}} = \frac{1}{n}\sum_{i=1}^{n} E_{\text{sim},i} \\ \bar{E}_{\text{mes}} = \frac{1}{n}\sum_{i=1}^{n} E_{\text{mes},i} \end{cases} \tag{1}$$

$$\epsilon_{1,\text{lin}} = \frac{1}{n}\sum_{i=1}^{n}\left(E_{\text{sim},i} - E_{\text{mes},i}\right)(\text{V/m}) \quad \epsilon_{2,\log} = \sqrt{\frac{1}{n}\sum_{i=1}^{n}\left(L_{\text{sim},i} - L_{\text{mes},i}\right)^2}(\text{dB}) \tag{2}$$

4.2. *Comparison on a city*

The first comparisons were made in the city of Strasbourg (Bas-Rhin, France), located within a 4 km × 4 km square. There are 575 antennas and 2910 transmitters. 48 measurement points are scattered within the city. Two datasets were considered: one based on generic data (called B, representative of future simulations) and one based on more precise data (called A):

- The B dataset uses IGN BDTOPO buildings and ANFR STATIONS database with automatic relocation.
- The A dataset uses 3D buildings with roofs and improved antennas locations (1/3 of manually positioned antennas using Google Street View, 1/3 of antennas using positions from the city database and the last 1/3 with automatic relocation, see Figure 13).
- The BA dataset is a mixed dataset, using A antennas locations and B dataset buildings.

It was not possible to achieve a real "reference" dataset as far as antennas positions are concerned, mainly due to different time stamps for measurements and existing antenna databases.

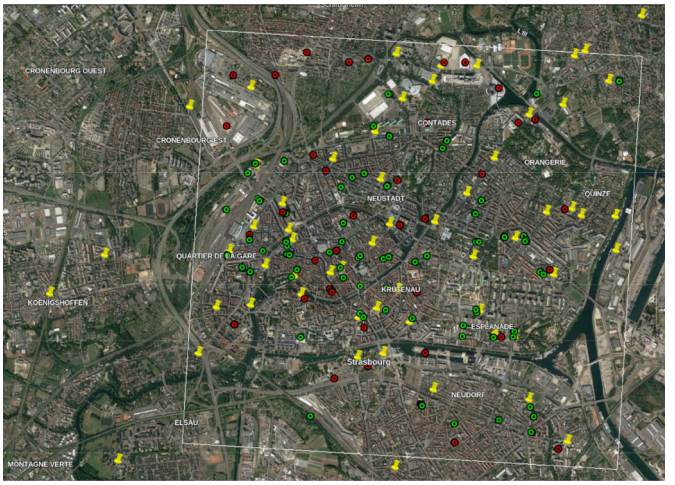

Figure 13. City of Strasbourg antennas (green circles for precise checked locations and red circles for automatically relocated ones) and measurement points (yellow pins).

The simulated indicators are shown in Table 3 and the corresponding scatter plot is in Figure 14. Because of the uncertainties in the input data (antenna locations and radiation patterns, constant reduction factor for load, receivers locations and geometry [7]), the results are on par with previous work [15] and also literature [16], acknowledging that those works relied on a controlled emitter (constant power and well-known radiation pattern). It must also be noted that since the comparisons were carried on isolated points, no spatial averaging could be done on measurements, whereas final exposure maps will have a spatial averaging. The scatter plots show a better agreement with the A dataset than with the B one. Scatter plots for free-field computation (overestimating) and the Hata model (underestimating) prove that simulation can handle heterogeneous exposure cases (LOS, NLOS, both occurring from different antennas in a lot of exposure cases).

Table 3. Comparison between measurements and simulation in Strasbourg city (48 points) for A, B and BA datasets.

dataset / indicator	p_{lin} (-)	$\epsilon_{1,\text{lin}}$ (V/m)	$\epsilon_{2,\log}$ (dB)
A	0.800	0.094	7.6
B	0.537	-0.046	6.3
BA	0.776	0.081	7.2

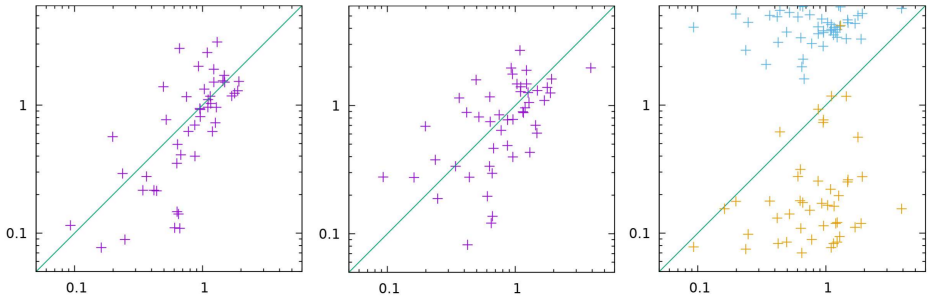

Figure 14. Scatter plot of measurements (horizontal axis, log scale in V/m) and simulations (vertical axis, log scale in V/m) : A dataset on the left, B dataset at the center, free-field (blue) and Hata (orange) on the right.

4.3. *Comparison on a full French department*

4.3.1. *Overview*

There are 200 measurement points in the French Bas-Rhin department (67) including 48 measurement points in Strasbourg, and 300 measurement points in the Paris department (75). See Figure 15. The first result is that for Paris, all measured points are in computation areas of several antennas (because of the dense urban area), i.e. no measured point has a null simulated electric field. To the contrary, in Bas-Rhin there are 17 out of computation areas. For 15 of them, they were labeled as below the sensitivity of measurement (0.05 V/m). The other points are close to the French - German border, and foreign transmitters are not taken into account. These results validate the precomputation stage.

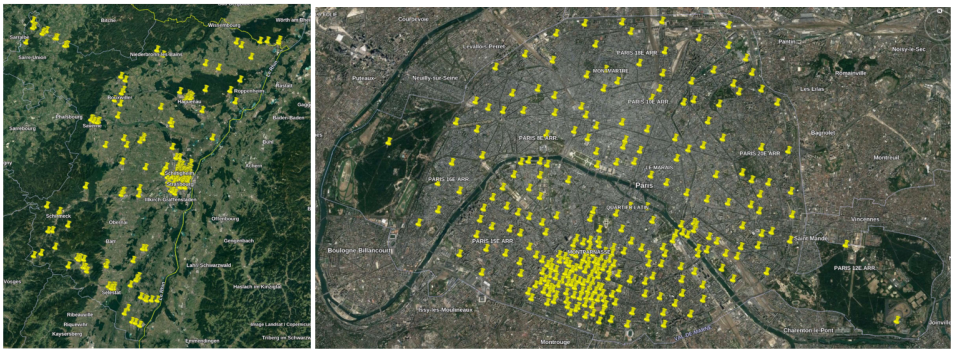

Figure 15. Measured points in Bas-Rhin (left, 200 points) and Paris (right, 300 points).

Table 4. Palette index of electric field value for colormap rendering.

E (V/)	[0;0.4[	[0.4;1[	[1;2[	[2;3[	[3;4[	[4;5[	[5;6[	[6;9[	[9;12[	[12;∞[
index	0	1	2	3	4	5	6	7	8	9
color										

There are 4959 antennas, with 21681 transmitters dispatched in 334 computation batches for Bas-Rhin in a ≈ 4800 km^2 territory. There are 8547 antennas, with 41940 transmitters dispatched in 1458 computation batches for Paris in a ≈ 105 km^2 territory.

The final exposure maps (see Figure 1 for instance) are rendered using a *viridis* palette, with ten indexes given in Table 4. These indexes are a good trade-off between a linear and a logarithmic scale for comparing results, as it does not emphasize errors on high (respectively low) electric field values like a linear (resp. logarithmic or dB) scale does.

4.3.2. *Distribution of errors*

The distribution of errors between simulation and measurements is illustrated in Figure 16. The average error is close to being null, while the distribution shape is close to a normal one. There are a few points where error is quite high. It has been investigated and this could be explained by missing geometry in the case of overestimation (missing large and high cemetery walls, with measurements behind the walls) and by the use of a unique load factor for all antennas. The remaining errors might also be due to incorrect input data (only the overall tilt is known, for instance, and the choice of electrical or mechanical tilt can influence the shape of sidelobes).

In addition to the distribution of relative error in V/m, there is a palette index error. A palette error of zero means that the measured and simulated values are equal. A palette error of one means, for instance, that one of the values is at the lower bound of a class and that the other is at the upper bound, but it could also cover two classes (if both values are in the middle of the class for instance). For Bas-Rhin, more than 80% of points have an index error between 0 and 1 (75% for Paris).

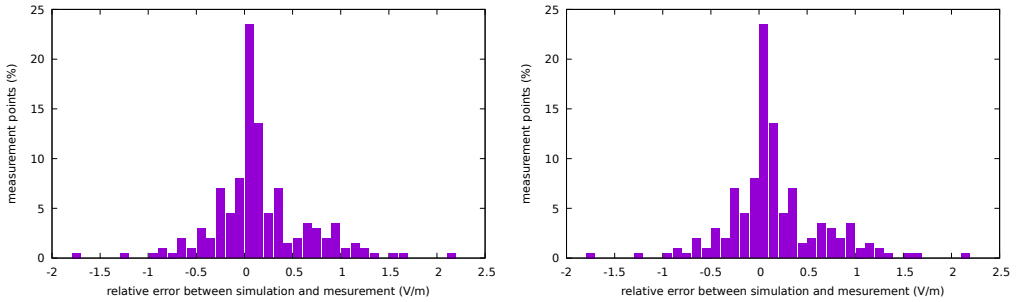

Figure 16. Error distribution in Bas-Rhin (electric field on the left, palette index on the right).

4.3.3. *Cumulated density functions of electric field*

It is also interesting to observe the cumulated density functions (cdf) of the electric field. The cdf for measurements and simulation in Paris is illustrated in Figure 17 for the global electric field (including all bands) and on Figure 18 for specific bands. The 3.5 GHz band (5G only) is not available yet as measurements are too sparse and the simulation method for beamforming antennas is not finalized yet.

The shapes of the distribution are very similar, aside from the maximum value itself.

5. Conclusion and future works

The method presented in this paper allows to tackle the computation of mobile telephony exposure maps at a full country scale. The method is fast and partial recomputations can be done on a regular basis. The first comparisons with measurements give acceptable accuracy given the uncertainties of input data, the most prominent being the precise antenna locations (as

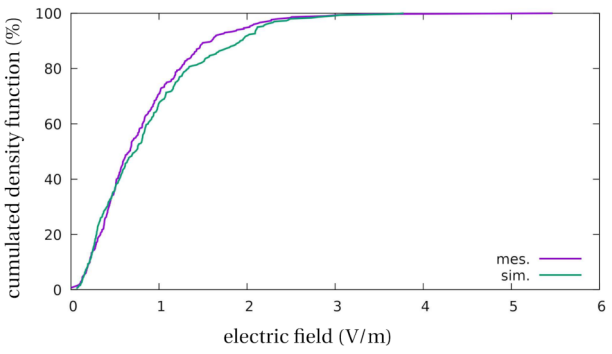

Figure 17. Cumulated density function of total electric field in Paris (including 5G).

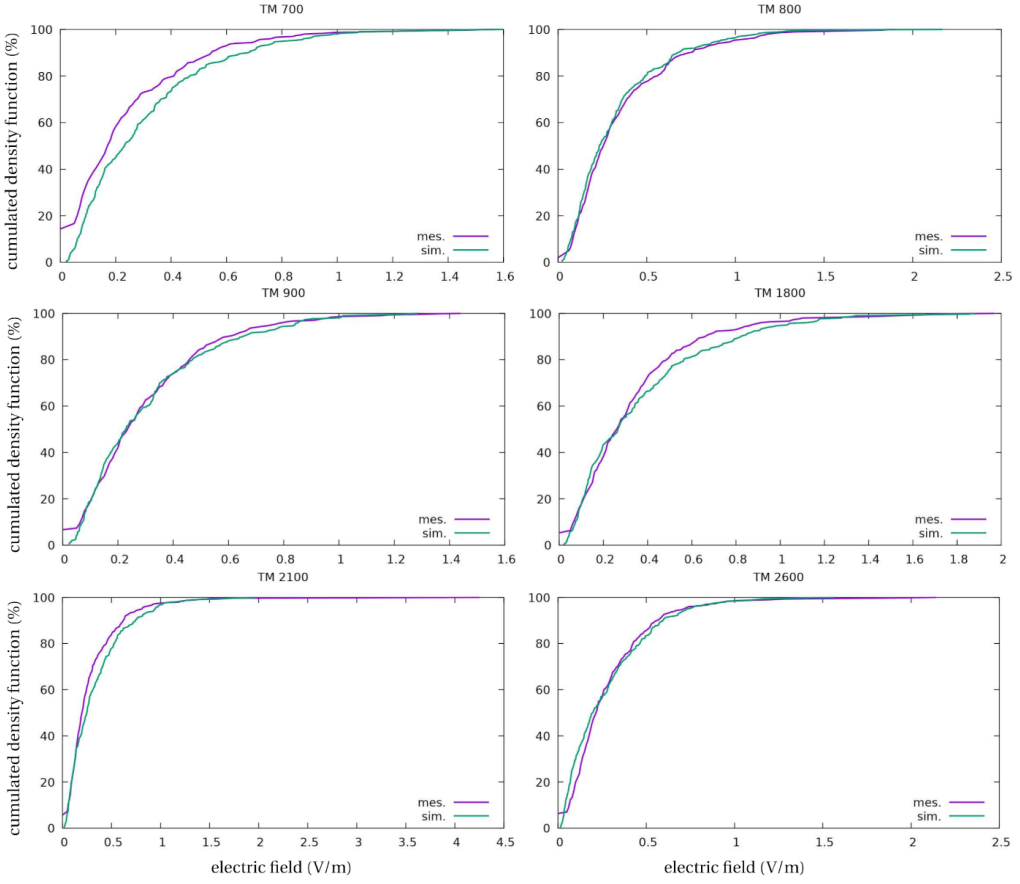

Figure 18. Cumulated density function for the 700 MHz / 800 MHz / 900 MHz / 1800 MHz / 2100 MHz / 2600 MHz bands.

shown by the very similar results between A and B datasets). The results are expected to improve in the future as the quality of input data will increase (precise antenna location from operators database, more detailed buildings database - including roofs, and case dependant load factors).

A large part of the work needed to provide a full France exposure map service has not been addressed in this paper as we only focused on the simulation method. Indeed, the full computation process is automatized and it is an application platform that handles databases, computations and web services for result queries (whether they are electric field at a given location, exposure maps or statistics in cities or countries).

Additional work could be done to improve simulation results. For instance, the Fresnel ellipsoid approach could be extended to one-reflection paths (on the ground or on buildings) and the relocation algorithm will be improved with feedback from initial computations. New validations are carried out on foot tests and drive tests, allowing spatial / time averaging on measurements that could be replicated in simulations.

Finally, for 5G beamforming transmitters, the current simulations are not yet conclusive. The approach used (an envelop of all beams with a load factor, as recommended in [17]) seems not to reflect the current behaviour of antennas. One solution to explore could be taking into account local visibility of 5G antennas to determine which beams are likely to be enabled because users (outside on the street or inside buildings) could stand in these beams, and which beams are likely to be disabled, in a simplified approach like the one in [18].

Declaration of interests

The authors do not work for, advise, own shares in, or receive funds from any organization that could benefit from this article, and have declared no affiliations other than their research organizations.

References

[1] Ministère de la Transition écologique et de la Cohésion des territoires, "'Un environnement, une santé' : le quatrième plan national santé environnement", Tech. report, 2022, https://sante.gouv.fr/IMG/pdf/pnse4.pdf.

[2] ANFR, "Maîtriser l'exposition du public aux ondes / Information du public / Rôle des maires", https://www.anfr.fr/maitriser/information-du-public/role-des-maires.

[3] Bruxelles Environnement / Leefmilieu Brussel, "Comment les normes d'exposition aux ondes sont-elles contrôlées ?", Tech. report, 2023, https://environnement.brussels/citoyen/nos-actions/prevention-et-inspection/comment-les-normes-dexposition-aux-ondes-sont-elles-controlees.

[4] ICNIRP, "Guidelines for Limiting Exposure to Electromagnetic Fields (100 kHz to 300 GHz)", *Health Phys.* **128** (2020), no. 5, p. 483-524.

[5] T. G. Vasiliadis, A. G. Dimitriou, G. D. Sergiadis, "A novel technique for the approximation of 3-D antenna radiation patterns", *IEEE Trans. Antennas Propag.* **53** (2005), no. 7, p. 2212-2219.

[6] "Atoll 3.4.0 Technical Reference Guide for Radio Networks", Tech. report, 2010.

[7] J. Beekhuizen, G. B. M. Heuvelink, A. Huss, A. Bürgi, H. Kromhout, R. Vermeulen, "Impact of input data uncertainty on environmental exposure assessment models: A case study for electromagnetic field modelling from mobile phone base stations", *Environ. Res.* **135** (2014), p. 148-155.

[8] International Telecommunication Union, "Report SM.2028-2: Monte Carlo simulation methodology for the use in sharing and compatibility studies between different radio services or systems", Tech. report, ITU, 2017, https://www.itu.int/dms_pub/itu-r/opb/rep/r-rep-sm.2028-2-2017-pdf-e.pdf.

[9] N. Noé, F. Gaudaire, P. Jean, M. Vermet, "A General Ray-Tracing Solution to Reflection on Curved Surfaces and Diffraction by their Bounding Edges", in 9^{th} *International Conference on Theoretical and Computational Acoustics*, 2009.

[10] T. Alwajeeh, P. Combeau, R. Vauzelle, A. Bounceur, "A high-speed 2.5D ray-tracing propagation model for microcellular systems, application: Smart cities", in *2017 11*th *European Conference on Antennas and Propagation (EUCAP)*, IEEE, 2017, p. 3515-3519.

[11] ITU-R, "Rec. ITU-R P.2040-3: Effects of building materials and structures on radiowave propagation above about 100 MHz", Tech. report, International Telecommunication Union, 2019, https://www.itu.int/dms_pubrec/itu-r/rec/p/R-REC-P.2040-3-202308-I!!PDF-E.pdf.

[12] Directorate-General for the Information Society and Media, "COST Action 231 : Digital mobile radio towards future generation systems - Final Report", Tech. report, European Commission, 1999, https://op.europa.eu/en/publication-detail/-/publication/f2f42003-4028-4496-af95-beaa38fd475f.

[13] ITU-R, "Recommendation ITU-R P.526-15: Propagation by diffraction", Tech. report, International Telecommunication Union, 2019, https://www.itu.int/dms_pubrec/itu-r/rec/p/r-rec-p.526-15-201910-i!!pdf-e.pdf.

[14] ANFR, "Protocole de mesure visant à vérifier sur site, pour les équipements fixes utilisés dans les réseaux de télécommunication ou pour les installations radioélectriques, le respect des niveaux de référence de l'exposition du public aux champs radioélectriques prévus par le décret n°2002-775 du 3 mai 2002", Tech. report, 2019, https://www.anfr.fr/fileadmin/mediatheque/documents/expace/Protocole-mesure-15-4.1.pdf.

[15] N. Noé, F. Gaudaire, M. Diarra Bousso Lo, "Estimating and Reducing Uncertainties in Ray-Tracing Techniques for Electromagnetic Field Exposure in Urban Areas", in *2013 IEEE-APS Topical Conference on Antennas and Propagation in Wireless Communications (APWC)*, IEEE, 2013.

[16] Z. Lai, N. Bessis, G. de laRoche, H. Song, J. Zhang, G. Clapworthy, "An Intelligent Ray Launching for urban prediction", in *2009 3rd European Conference on Antennas and Propagation*, IEEE, 2009, p. 2867-2871.

[17] ANFR, "Lignes directrices nationales sur la présentation des résultats de simulation de l'exposition aux ondes émises par les installations radioélectriques", Tech. report, 2019, https://www.anfr.fr/fileadmin/mediatheque/documents/5G/consultation/consultation-5G-Lignes-directrices-nationales.pdf.

[18] N. Noé, F. Gaudaire, "Numerical modeling of downlink electromagnetic wave exposure generated by 5G beamforming antennas", *Comptes Rendus. Physique* **22** (2021), p. 15-24.

ACADÉMIE DES SCIENCES
INSTITUT DE FRANCE

Comptes Rendus. Physique
2024, Vol. 25, Special issue S1, p. 41-61
https://doi.org/10.5802/crphys.182

Research article / *Article de recherche*

Energy in the heart of EM waves: modelling, measurements and management / *L'énergie au cœur des ondes électromagnétiques : modélisation, mesures et gestion*

Monitoring of the exposure to electromagnetic fields with autonomous probes installed outdoors in France

Surveillance de l'exposition aux ondes électromagnétiques à l'aide de sondes autonomes installées en extérieur en France

Ourouk Jawad [*,a], Emmanuelle Conil [a], Jean-Benoît Agnani [a], Shanshan Wang [b] and Joe Wiart [c]

[a] ANFR, 78 avenue du général de Gaulle, 94700 Maisons-Alfort, France

[b] ETIS, UMR 8051, CY Cergy Paris Université, ENSEA, CNRS, F-95000, France

[c] Chaire C2M, LTCI, Télécom Paris, Institut Polytechnique de Paris, 91120 Palaiseau, France

E-mails: ourouk.jawad@anfr.fr (O. Jawad), emmanuelle.conil@anfr.fr (E. Conil), jean-benoit.agnani@anfr.fr (J.-B. Agnani), shanshan.wang@ensea.fr (S. Wang), joe.wiart@telecom-paris.fr (J. Wiart)

Abstract. The study is based on a new temporal analysis of exposure based on the deployment of autonomous broadband E-field monitoring probes in many French cities. The combination of the probe's data with frequency-selective in situ measurements performed by ANFR and the knowledge of the nearby base station antennas, allows to draw statistical conclusions on the exposure of the population. Indeed, the data collected by the probes reveal that different periodicities exist (seasonality, day/night). This paper shows that the monitoring probes are able to detect the seasonality of the exposure and provide analysis of correlation between monitoring probes and radio environment.

Résumé. L'étude repose sur une nouvelle analyse temporelle de l'exposition se basant sur le déploiement de sondes autonomes large bande pour la surveillance du champ électrique dans plusieurs villes françaises. La combinaison des données issues des sondes avec les mesures in situ sélectives en fréquences effectuées par l'ANFR et la connaissance des stations de base avoisinantes permet de tirer des conclusions sur l'exposition de la population. En effet, les données collectées des sondes révèlent que différentes périodicités existent (saisonnalité, jour/nuit). Cet article montre que les sondes sont capables de détecter la saisonnalité de l'exposition et de fournir une analyse de la corrélation entre les sondes et l'environnement radio.

* Corresponding author

Keywords. Monitoring, Exposure, EMF, In situ measurement, Principal component analysis.

Mots-clés. Surveillance, Exposition, Champs EM, Mesure in situ, Analyse en composante principale.

Note. This article follows the URSI-France workshop held on 21 and 22 March 2023 at Paris-Saclay.

Funding. European Union's Horizon Europe Framework Programme under Grant Agreement number 101057622 (SEAWave Project).

Manuscript received 27 July 2023, revised 11 December 2023 and 5 March 2024, accepted 14 March 2024.

1. Introduction

The topic of assessing human exposure to electromagnetic waves is a continuous subject of discussion leading to important debates in society. Many studies have been conducted worldwide to assess the downlink human exposure due to mobile phone base stations or the uplink exposure due to personal equipment such as mobile phones [1, 2]. In France, the Agence nationale des fréquences (ANFR) is responsible for the surveillance of the exposure of the public to EMF. Thousands of in situ measurements are carried out every year [3], and ANFR has fine-tuned the level of exposure due to the deployment of 5G NR technology through measurements and simulations [4]. Furthermore, the compact electronic integration enables the development of new techniques for EMF monitoring. In fact, city councils and ANFR have installed tens of autonomous monitoring probes that perform broadband measurements of the electric field (E-field) several times a day [5]. This new measurement technique offers the possibility to analyze spatiotemporal variations of the exposure level in different radio environments.

The domain of the continuous monitoring of E-field has achieved several significant milestones. In [6–12], different networks of probes monitoring the E-field are presented. They are located in different countries: Belgium, Greece, Italy, Serbia and Spain. In most of the studies, probes are positioned at a fix position but in [6] they are not fixed. Many of the papers focus on the architecture of the probe networks such as [6, 9, 11] and do not go deeper in the statistical temporal analysis. In [7, 8, 10, 12], temporal analysis of the exposure reveals some interesting phenomena such as traffic fluctuation, variation between day and night or variation between urban and rural area. In [13], a systematic literature review was conducted on EMF exposure monitoring in various countries, the conclusion suggests that there is a need for a common method of temporal analysis. In [12], an important milestone is presented regarding the comparison of temporal analysis of the exposure to EMF in different European countries (Greece, Spain, Romania and Serbia). The study compares statistical parameters of the E-field on a yearly basis in different countries, but it does not include France.

For the first time, this paper presents an analysis of the time variation of the E-field in France by combining measurements by autonomous probe with other sources of information, including the database of in situ measurements and the database of base station antennas. For this purpose, the available data are presented: the database of in situ measurements, carried out near autonomous probes, the database of base station antennas and the database of monitoring probes. Afterwards, the methodologies are presented: a classical statistical analysis and principal component analysis (PCA) principles.

Then, the data analysis is carried out, beginning with a general statistical analysis that reveals daily fluctuations. A general analysis based on PCA is performed to know if there is any correlation between the evolution of the exposure level and the radio environment thanks to in situ measurements and the nearby base stations. The PCA is also used to detect the temporal patterns over 2022 and the spatial dependence on the radio environment. The results indicate that the techniques of statistical analysis are promising methods to reveal global and local patterns of the exposure related to the cellular network environment.

This article presents significant findings on the monitoring of the E-field. The day-and-night fluctuation of the level of exposure is analyzed, and an empirical day/night hour interval is found. Based on the monitoring probes data, for the first time, the daily variation is characterized and confirms the communicated uncertainty contributor. PCA method is used on two different datasets. First, PCA helps to identify the probes which are ideally positioned for monitoring of the exposure due to radio environment, and second, PCA demonstrates the presence of seasonality throughout the year.

2. Available data

2.1. *ANFR's base station antennas database*

ANFR provides open source data regarding exposure of the French population. There are two types of data available in raw data format or plotted on a map [3]. ANFR gives its legal agreement for the installation of base stations and keeps the French national antenna database up-to-date (for antennas with EIRP > 5 W). On the Cartoradio website, it is possible to check the installed base station antennas everywhere in France, including details such as technology (2G–5G), frequency band, mobile operator, azimuthal direction, height of the antenna [3]. Information is provided for different types of networks: TV broadcasting, radio broadcasting, point-to-point fixed radio relay and cellular network. In this article, only base station antennas are used. The Cartoradio website provides the locations of the base stations and shows locations where accredited in situ measurements have been carried out. Details of measurements and base stations are available by clicking on the indicators.

2.2. *Monitoring probe database*

City councils, ANFR, and the C2M team of Telecom Paris have installed autonomous monitoring probes. The monitoring probes were designed by the EXEM company and measure the three components of the E-field between 80 MHz and 6 GHz [14]. The autonomous probe measures the E-field level (equals to the square root of the sum of the squared components of the E-field) integrated over the whole frequency band [15]. Since 2019, 152 autonomous probes have been installed in different cities in France. In general, the probes are attached to outdoor electric poles or other street furniture at a certain height to avoid access by pedestrians (Figure 1). The probes measure at several times of the day and night: every two hours between 1:00 AM and 11:00 PM and each measurement is averaged over 6 min. A website provided by EXEM gives access to the measurement results of the probes [5]. Some of the autonomous probe monitoring data are made publicly available by city councils.

Table 1 below shows the number of autonomous probes per city, the name of the city or conurbation authority where probes are installed, and the department code. Cities and conurbation authorities identify interesting probe locations by targeting locations with a high density of base stations or near children's schools or major public places located in city centers.

2.3. *Broadband and frequency-selective in situ measurement database*

ANFR and its partners conduct thousands of in situ measurements annually. Any French resident can request an in situ measurement at home or in any public space. The accessible results include the broadband E-field measurement and the frequency-selective E-field measurement. In situ measurements follow the ANFR protocol [16], which is in line with standard EN IEC 62232:2022 [17]. The ANFR protocol provides a methodology to assess the level of exposure

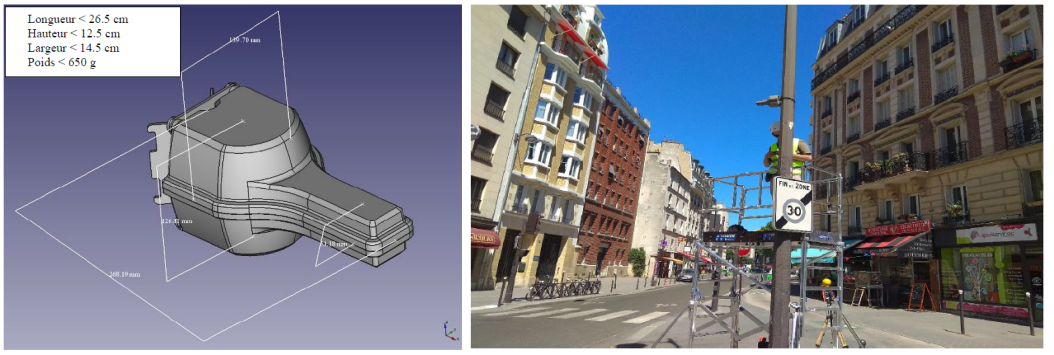

Figure 1. 3D shape of an autonomous probe and a picture taken during the installation of a probe on a street pole in Paris, extracted from EXEM datasheet [14].

Table 1. Number of probes per city or conurbation authority

Number of probes	Name of city or conurbation authority	Department name (number)
5	Lille Métropole	Nord (59)
9	Paris	Paris (75)
19	Massy	Essonne (91)
4	Grand Paris Sud	Essonne (91) and Seine-et-Marne (77)
7	Orléans Métropole	Loiret (45)
8	Eurométropole de Strasbourg	Bas-Rhin (67)
3	Mulhouse	Haut-Rhin (68)
10	Rennes	Ille-et-Vilaine (35)
50	Nantes Métropole	Loire-Atlantique (44)
33	Bordeaux Métropole	Gironde (31)
3	Marseille	Bouches-du-Rhône (13)

in France, while standard EN IEC 62232:2022 is the most detailed standard for determining RF field strength in the vicinity of the radiocommunication base stations. The ANFR measurement protocol is divided into two parts. The first part, called "case A", consists of a broadband E-field measurement at three different heights (1.10 m, 1.50 m, 1.70 m); the level of exposure, expressed in V/m, is the root mean square (RMS) of the E-field measured at the three heights for six minutes. Usually, the position of the probe position is typically based on a hot-spot search, and the technician makes a few measurements to determine where the exposure is maximum. For the measurement at the ground level beneath the monitoring probe, the hot spot search is skipped. The second part of the measurement called "case B" consists of a frequency-selective E-field measurement at the same position as in case A. The results of the measurement provide an overview of the contributions of the different technologies using any bands between 100 kHz and 6 GHz.

ANFR regularly analyzes, the exposure to EMF due to base station antennas with:

- the yearly report which investigates the evolution of the exposure based on the outdoor and indoor in situ measurements (the yearly report is based on the measurement requested by French citizens) [18];
- the report investigating the evolution of exposure specifically due to the 5G deployment [19];

Table 2. Description of the ANFR databases

	Type of data	Description	Applicant
Base station antennas	Information	Base station antennas installed everywhere in France with description of technology (2G–5G), frequency band, mobile operator, azimuthal direction, height of the antenna	Mainly network operators request installation of base station antennas
Monitoring probes	Measurement	Monitoring probes measuring the three components of the E-field between 80 MHz and 6 GHz at multiple times of the day and night: every two hours between 1:00 AM and 11:00 PM and each measurement is averaged over 6 min	City councils, C2M team and ANFR are the main applicants for probe installation
In situ measurements	Measurement	Measurements in two parts: • Case A: broadband measurement at three heights for 6 min • Case B: frequency-selective measurement at the same position as case A from 100 kHz to 6 GHz	Usually, the applicants are citizens who ask for in situ measurements. In this study, ANFR asked for in situ measurements at the ground level under each probe

- the "city hall square" campaign, which is carried out every three years in more than 1000 cities (80% urban areas and sub-urban areas 20%) [20];
- and other specific campaigns (smart meters, subway etc.).

These reports show that in a very high majority of cases, the largest contribution to the overall exposure level is due to cellphone networks (59% in 2021). In more than 20% of the in situ measurements in 2021, there are no major contributions because the measured level is low and close to the sensitivity threshold of measurement instruments. For the rest of the in situ measurements, the major contributions can come from WLAN, HF bands, or private mobile radio.

2.4. *ANFR database in a glance*

In a nutshell, three databases from ANFR are used in this article. For the sake of clarity, these databases are presented at a glance in Table 2.

3. Methodology

3.1. *Classical statistical analysis*

The large amount of data enables to make classical statistical observations on the different magnitudes of the E-field measured by the probes. Since the measurements are made several times per day and per night, starting from the installation of the probe, it is possible to see if there is any common temporal behavior. Comparisons can be made between day and night exposure

levels, or between working hours and off-duty hours. Since the E-field is measured by the probe in volts per meter, the root mean square is used to evaluate the mean of the E-field. For a more general analysis of the variation during 2022, a more sophisticated statistical method must to be used, in particular to correlate the level of exposure with the radio environment. Indeed, the first section highlighted that the seasonality of France has never been shown, and that the correlation with radio environment data has never been done either.

3.2. *Principal component analysis (PCA)*

PCA is a popular method for analyzing high-dimensional data [21]. It is an unsupervised statistical method that allows large datasets of correlated variables to be reduced to a smaller number of uncorrelated principal components that explain most of the variability in the original dataset. Suppose that the dataset X is an N-by-P matrix, where N observations are the rows of the X matrix and P variables are the columns of the X matrix. There are mainly four steps involved in PCA:

(1) Centralization of the dataset X to characterize deviations between the observations. It consists in subtracting the mean value of each variable (i.e. column of X).
(2) Computation of the covariance matrix.
(3) Computation of eigenvalues and eigenvectors of the covariance matrix to identify the principal components. Our principal components that maximize the variance of all projected points onto a 2D space is the eigenvector of the covariance matrix associated with the largest eigenvalue. There are several techniques to compute eigenvalues and eigenvectors, one of the most used within PCA and in this study is the Singular Value Decomposition.
(4) Extraction of scores and loadings: the PCA is then based on the decomposition of the data matrix into two matrices V and U. The matrix V is a k-by-P (where k is the number of principal components) matrix and is usually called the loading matrix. The loadings can be understood as the weights for each original variable in the principal components space. The matrix U is called the score matrix. It contains the original observations in a rotated coordinate system.

PCA is a well-known method to reduce the dimensions of a data set. In our case, it may be helpful to find the main components that characterize the time variability between the autonomous probe measurements. PCA would help to determine whether the recorded shapes of the monitoring probe level have similarities or differences.

4. Data analysis

4.1. *Autonomous probe variability analysis*

In this section, data from monitoring probes described in Section 2.2 are used. Figure 2 displays the Cumulative Distribution Function (CDF) of 110 monitoring probes. The CDF plotted on Figure 2 gather measurements during the year 2022. The average value of the numbers of measurements used to build CDF is 4325 measurements per probe. This figure shows the extend of measured values by monitoring probes. It shows that for a large number of monitoring probes, the measured values are below 1 V/m. These plots also show that the number of measurements is very high and that advanced techniques must be used in order to handle the variability between probes.

Raw data of the E-field measured by probes are too difficult to analyze (raw data of all monitoring probes are presented in Figure 3 without filtering for the year 2022), then a selection

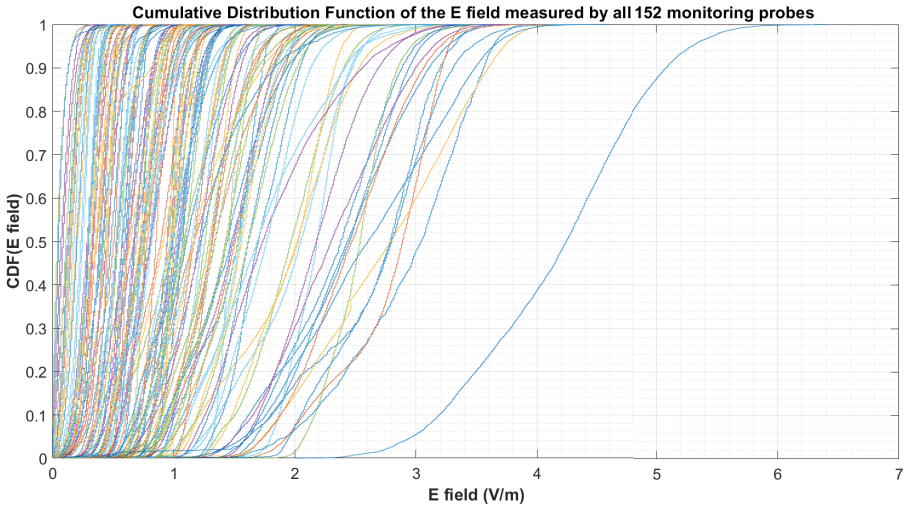

Figure 2. Cumulative Distribution Functions of E-field measured by probes which were operating during 2022.

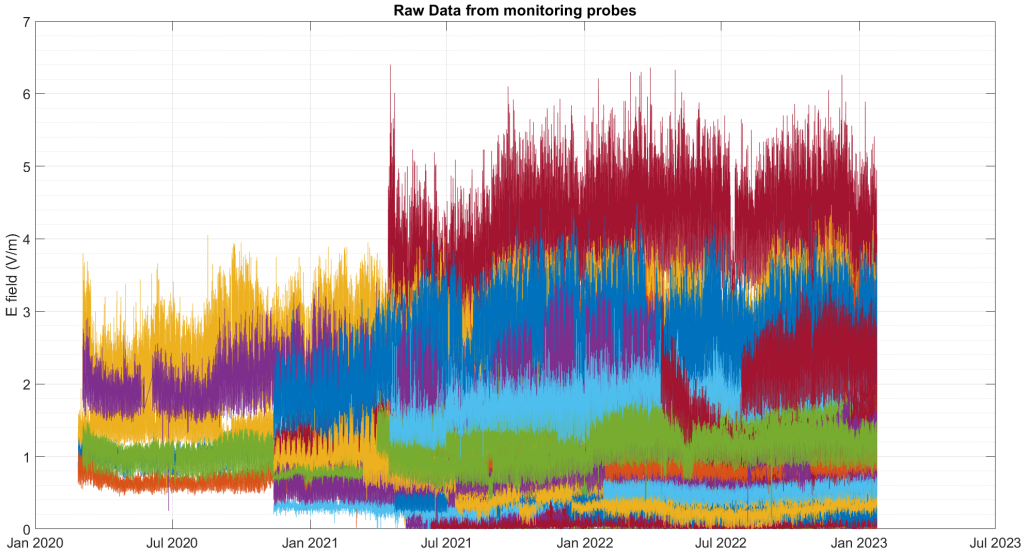

Figure 3. Raw data of E-field measured by all the probes since installation, showing fast variation on a daily basis and very low variation over long periods of time.

of a few probes is necessary. As a starting point, the RMS of the E-field of each probe was calculated, and we selected three probes with the highest RMS value. The RMS value was calculated over the data measured during the year 2022.

A deeper analysis can be made, based on a different time scale analysis. Indeed, since measurements are made day and night, a remaining question is how the level of exposure is evolving between day and night. Figure 4 shows CDF of the 3 selected probes (highest RMS) with an empirical time separation: day is between 8 AM and 11 PM and night is between 11 PM and 8 AM. This plot shows that for the three highest probes the differences are remarkable. In fact, the

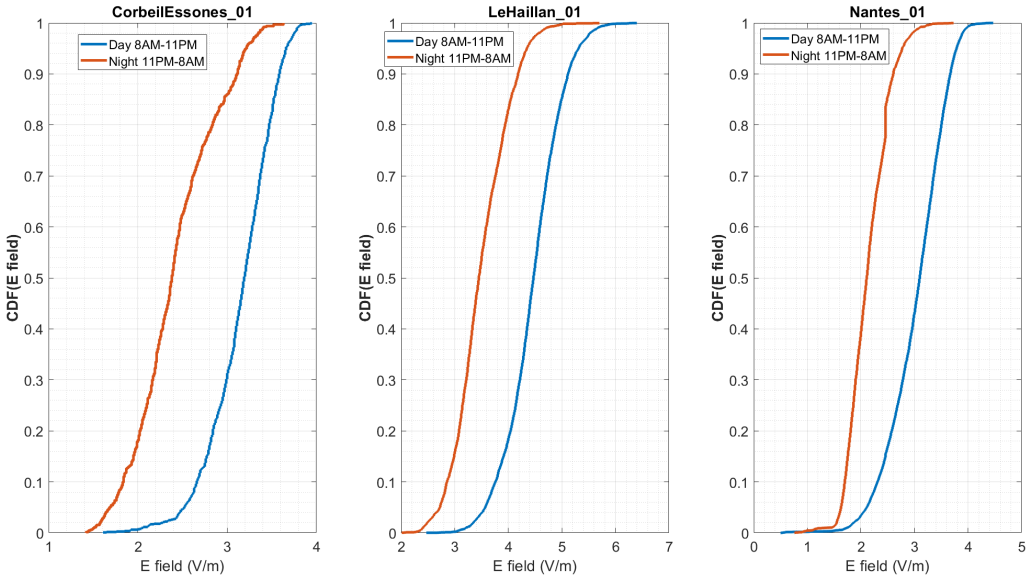

Figure 4. Day and Night CDF of selected probes (Day 8 AM–11 PM and Night 11 PM–8 AM).

ratio of the average day-value over the average night value is 1.30 for CorbeilEssones_01, 1.28 for Le Haillan_01, 1.42 for Nantes_01. For the probes with the lowest RMS level (not presented in this article), the level of exposure is not different during the night compared to the day. This is due to the fact that the lowest RMS probes are installed far from base station antennas and therefore measure very low levels.

The number of measurements and the coverage of many different cities (urban and suburban) allow for another type of analysis. Figure 5 displays the coefficient of variation (also called relative standard deviation) calculated on the basis of the measurements made during working days and hours (Monday to Friday from 8 AM to 5 PM). Figure 5 shows that the coefficient of variation is less than 30% for 86% of the probes. For the 21 probes with variation coefficients higher than 30%, most of the probes measure very low levels of exposure or have large variations due to repairs. This information is valuable for ANFR because the uncertainty budget of the accredited in situ measurements includes a specific contributor for the daily time variation which is equal to 30%. It confirms that the uncertainty contributor due to daily variation is up to 30% and it is consistent with the information provided by ANFR.

4.2. *Data preparation prior to PCA*

4.2.1. *Dataset No. 1*

The purpose of this study is to correlate E-field measurements from monitoring probes with the radio environment. The radio environment is described by two sources of data. The first source of data consists of the “case B” measurement, also known as the frequency-selective E-field measurement per band. The bands covered are 700 MHz, 800 MHz, 900 MHz, 1800 MHz, 2100 MHz, 2600 MHz and 3600 MHz and they encompass every technology (GSM/GPRS, UMTS, LTE and 5G EN-DC) available in France. The second source of data is the number of base station antennas near the probe’s location. The idea is to tally the number of base station antennas per band that fall within a circle surrounding each probe. Figure 6 is a schema illustrating how

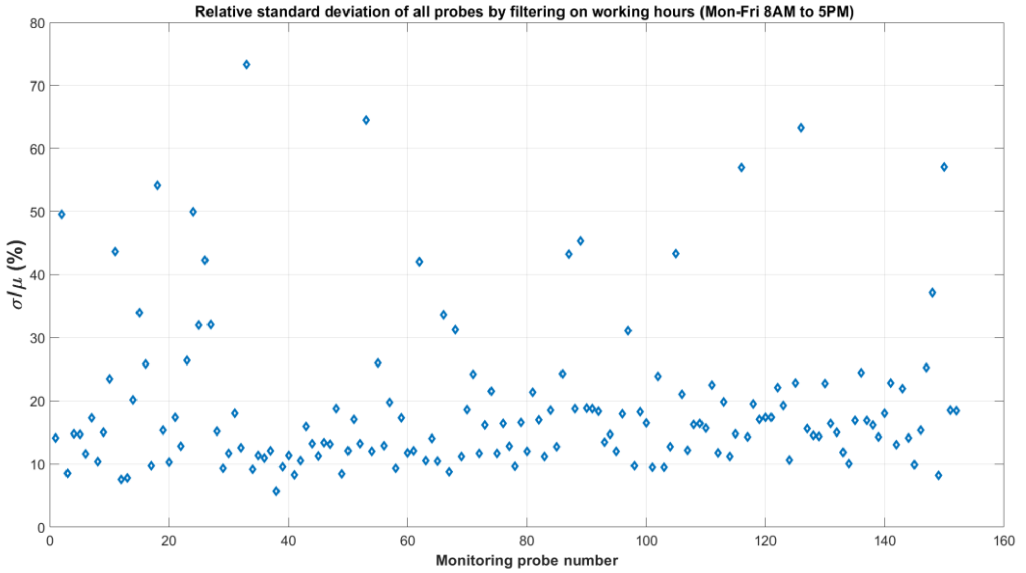

Figure 5. Relative standard deviation of all probes by filtering on working hours (Monday to Friday from 8 AM to 5 PM).

base station antennas are included in the final count. The antennas are oriented to radiate towards a specific direction (called azimuthal direction of radiation, called α and α' in Figure 6) to cover a specific cell. Within the circle surrounding the probe, certain base station antennas are mechanically oriented towards the probe, while others are not. A base station antenna is considered if the bearing angle β (respectively β') of the vector going from the antenna to the probe is in the interval $[\alpha - \Delta\phi/2,\ \alpha + \Delta\phi/2]$ (respectively $[\alpha' - \Delta\phi/2,\ \alpha' + \Delta\phi/2]$). A standard 120° angular spread ($=\Delta\phi$) is used. This rule applied to the base station antennas in Figure 6 means that only one base station is considered in the final count. Regarding the radius of the circle, the assumption has been made that antennas oriented towards the probe and located at a distance of less than 400 m should be counted for each cellular band. The rationale behind this assumption is that for a typical antenna EIRP (average EIRP is 32.6 dBm based on the ANFR base station antenna database) and a distance of 400 m, the E-field in free space can be estimated to be less than 0.02 V/m, which appears to be sufficient to include any contributor per band.

For the sake of clarity, Figure 7 represents the matrix X for dataset No. 1, composed of variables coming from the three databases:

- squared of the E-field monthly averaged from monitoring probe database;
- squared of the E-field per band from case B in situ measurement database;
- and, the number of base stations per band surrounding monitoring probes from the base station antenna database.

In order to make sure that the measurements of monitoring probes are comparable to in situ measurements, a comparison has been made. The Figure 8 presents the comparison of RMS of E-field measured by probes with in situ case A measurements. It appears that the plot is almost linear, which means that both techniques of measurement provide close results. In situ measurement (carried out by ISO17025 accredited laboratories) uncertainty budget ($k = 1.96$) for case A is 2.3 dB and the monitoring probe estimated uncertainty of measurement is 3.8 dB in case the entire bandwidth is considered [3]. The combined uncertainty is equal to 4.1 dB, based on metrology rules, 95% of relative deviation between in situ measurements and E-field measured

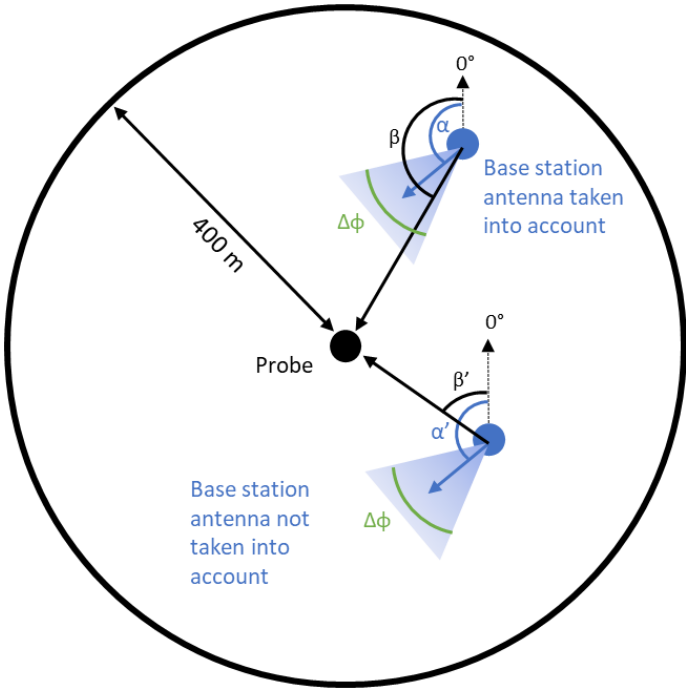

Figure 6. Schema explaining how base station antennas are considered in the final count.

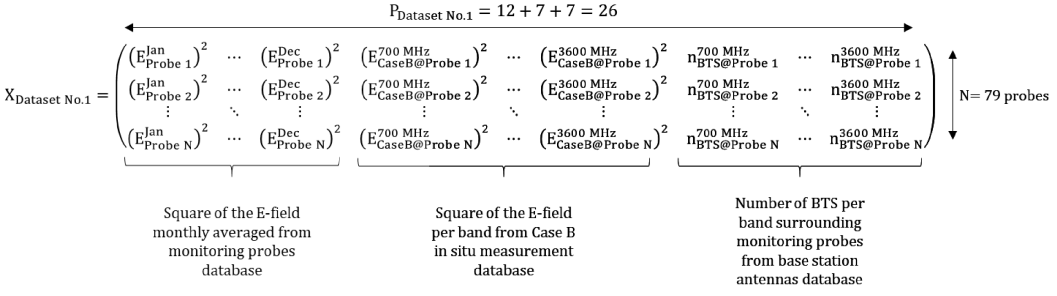

Figure 7. Input matrix for PCA on Dataset No. 1 with indication of the original database.

by the monitoring probes should be within the combined uncertainty. The relative deviations between both techniques of measurement reveal that 95.3% of relative deviations are within the combined uncertainty. This result means that monitoring probes and in situ measurement results are close, even if the measurement positions are separated by a few meters.

As explained in Section 3.1, the dataset needs to be standardized, so in our case it is preferable to use the square of the E-field. The dataset No. 1 is then composed of the following variables: the square of the E-field averaged for each month from January to December 2022, the square of the case B in situ E-field measured under the probes for each band, and the number of base station antennas within the 400 m radius for each band. To facilitate the interpretation of the PCA, the monitoring probes that measure relatively low levels of exposure have been filtered out. The threshold was chosen based on the average outdoor level of exposure measured by ANFR, based on thousands of measurements carried out over many years, and the probes with a 99th

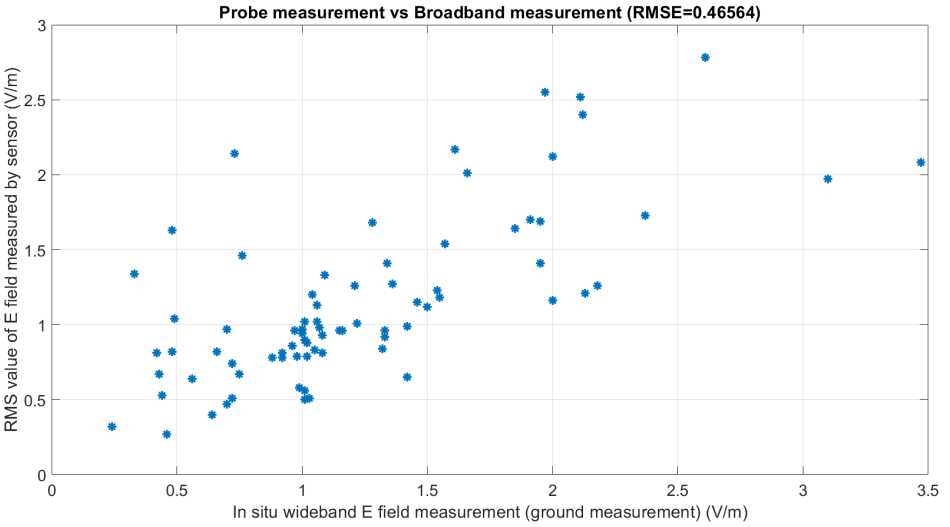

Figure 8. RMS value of E-field measured by monitoring probe (on the same day) in function of in situ broadband E-field measurement ("case A") at the ground under the probe.

$$X_{\text{Dataset No.2}} = \begin{pmatrix} \left(E^{\text{Jan}}_{\text{Probe 1}}\right)^2 & \cdots & \left(E^{\text{Dec}}_{\text{Probe 1}}\right)^2 \\ \left(E^{\text{Jan}}_{\text{Probe 2}}\right)^2 & \cdots & \left(E^{\text{Dec}}_{\text{Probe 2}}\right)^2 \\ \vdots & \ddots & \vdots \\ \left(E^{\text{Jan}}_{\text{Probe N}}\right)^2 & \cdots & \left(E^{\text{Dec}}_{\text{Probe N}}\right)^2 \end{pmatrix} \quad \begin{matrix} \overleftarrow{P_{\text{Dataset No.2}} = 12} \\ \\ \\ \\ \updownarrow \\ \\ \\ \\ \end{matrix} \quad \text{N= 79 probes}$$

Figure 9. Input matrix for PCA on Dataset No. 2.

percentile below 1 V/m were filtered out. The input matrix is composed of $P = 26$ variables and $N = 79$ observation probes.

4.2.2. *Dataset No. 2*

Dataset No. 2 focuses solely on the time domain, i.e. the square of the E-field measured by the monitoring probes from January to December 2022. The objective is to detect any time patterns along the monitoring probes, using the same exposure level filter as in dataset No. 1. The input matrix consists of $P = 12$ variables and $N = 79$ observation probes. For the sake of clarity, Figure 9 represents the matrix X for dataset No. 2, composed of variables coming from the monitoring probes database.

4.3. *PCA's results*

4.3.1. *Dataset No. 1*

Figure 10 shows the dataset No. 1 represented in the two main principal component coordinates. The probes are represented with different markers for each French department. Table 3

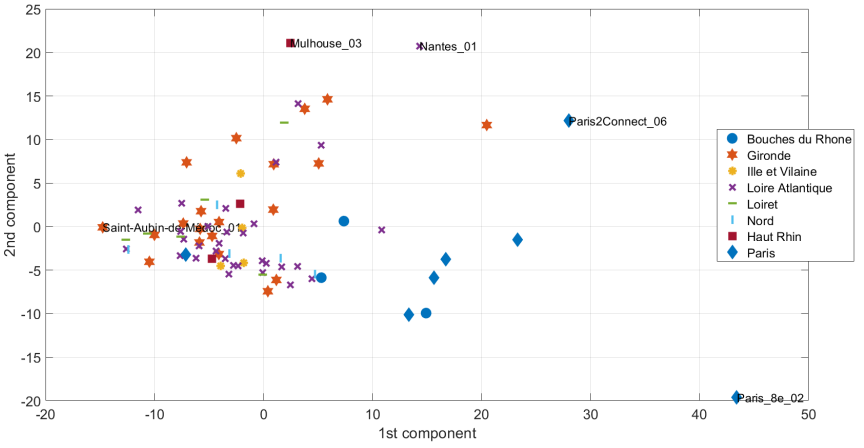

Figure 10. Dataset No. 1 represented on the domain composed by two main principal components.

Table 3. Eigen values for each component and proportion of explained variance for dataset No. 1

# Components	Eigenvalue	Proportion of total explained variance (%)
1	92.3991	62.3
2	46.8840	31.6
3	3.1131	2.1
4	1.5063	1.0
5	1.0244	0.7
6	0.8020	0.5

presents the eigenvalues and the percentage of total explained variance providing insight into the importance of the components in terms of variability. The choice has been made to display only six first parameters in the table. The proportion of total explained variance shows that the first two components represent 94% of the variability.

The point cloud represented in Figure 10 characterizes most of the variability of the original dataset. It means that distant points along the first or second components are very different from each other with respect to their original data. In Figure 10, some distant points/probes in the two principal component coordinate systems are selected. The name of distant probes selected are displayed on the plot. The selection of these probes (Saint-Aubin-de-Médoc_01, Mulhouse_03, Nantes_01, Paris2Connect_06, Paris_8e_02) for deeper analysis has the advantage of surrounding the point cloud and of giving a good interpretation on characterized variability.

Figure 11 shows the correlation circle for the original variables of dataset No. 1 represented in the domain of two components found by PCA. The “Months variable group” is the average monthly squared E-field by the probes, the “in situ frequency selective squared of the E-field variable group” comes from the result of case B measurement per band at the ground level and the “#Antennas variable group” are the number of base station antennas surrounding the probes. It shows that the number of base station antennas per band surrounding the probes is highly correlated with the first component, and that the level of exposure measured by probes and averaged monthly is highly correlated with the second component. The level of exposure

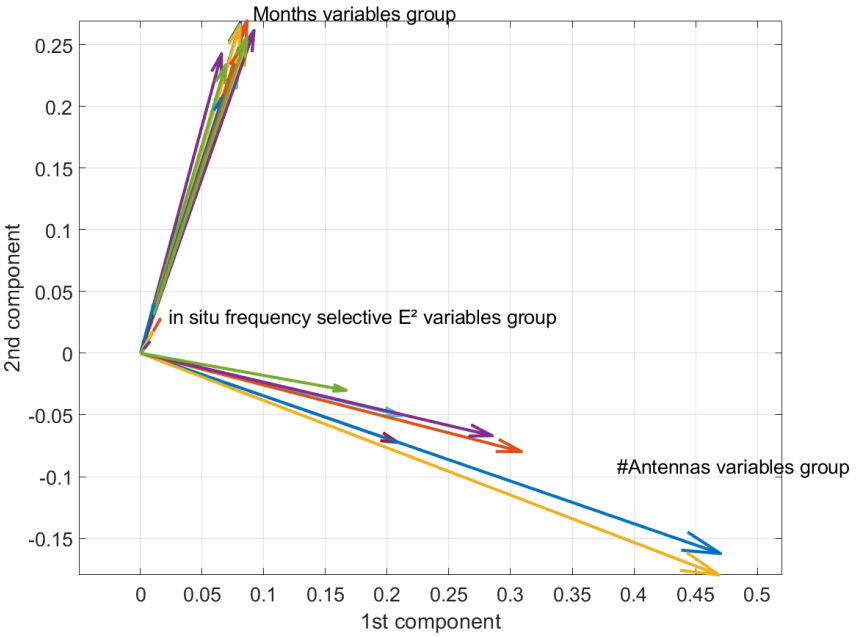

Figure 11. Correlation circle for dataset No. 1 representing variables projected on the two main components.

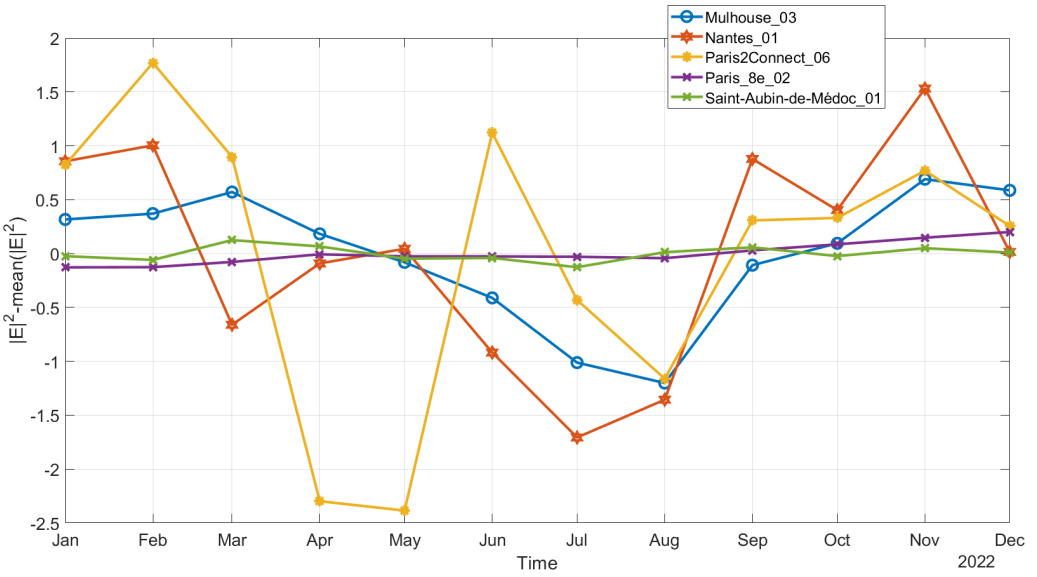

Figure 12. Square of the E-field during 2022 for the probes surrounding the principal components.

measured through case B measurements on the ground is more correlated with the second component than with the first.

To analyze the principal components characterization, the original data has been plotted for the five probes surrounding the point cloud. Figure 12 represents the square of the E-field per month minus its yearly average for the five probes surrounding the two components space.

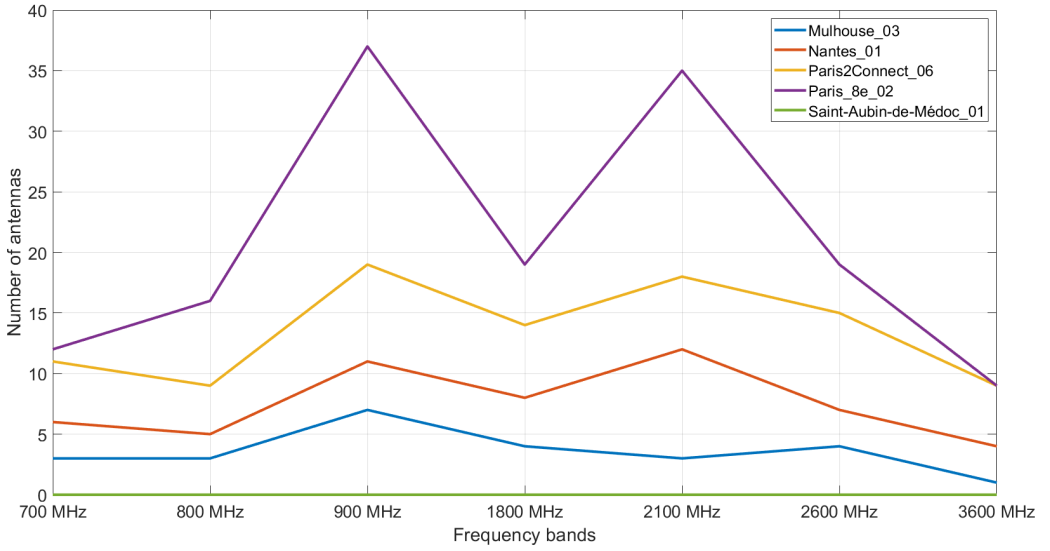

Figure 13. Number of base station antennas close to the probes surrounding the principal components.

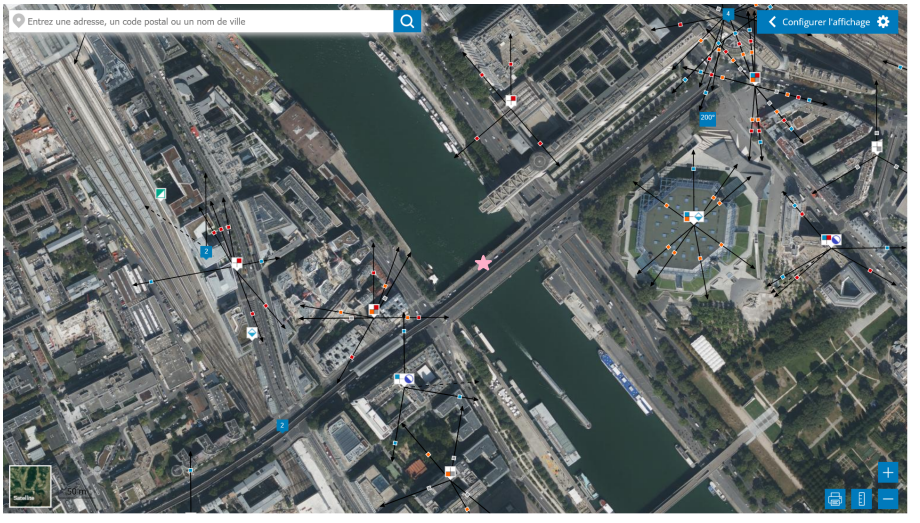

Figure 14. Picture of the position of the Paris2Connect_06 probe with surrounding base station antennas.

Figure 13 represents the number of base station antennas per band for the probes surrounding the two component space. The PCA reveals that the first component distinguishes between the probes located near a high number of base station antennas (on the right side) and those located near very few antennas (on the left side). The second component separates the probes with a high variability (top side) from those with very low variability (bottom side). These interpretations can be confirmed by comparing the locations of the different probes. Mulhouse_03, Nantes_01 and Paris2Connect_06 are installed in open areas (in front of a market, university hospital, or in the middle of a bridge) but with a high density of base station antennas. The Paris8e_02 probe

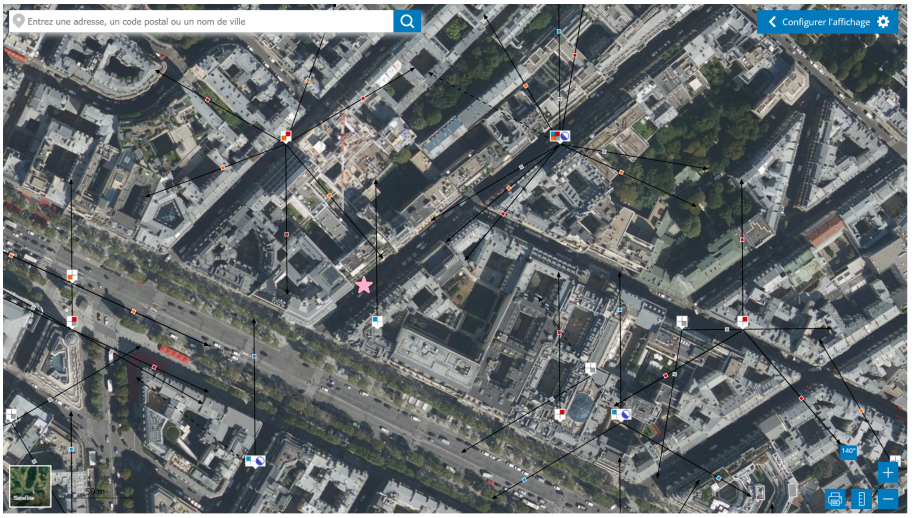

Figure 15. Picture of the location of the Paris8e_02 probe with surrounding base station antennas.

is located in a highly concentrated area of base station antennas near the Avenue des Champs Elysées, despite being situated on a narrow street without line-of-sight exposure. Figure 14 displays the location of the Paris2Connect_06 probe (pink star) with surrounding base station antennas, the arrows indicating the azimuthal directions of the base station antennas. Figure 15 displays the location of probe Paris8e_02 with surrounding base station antennas. Since the PCA shows that there is a correlation (Figure 11) between the continuous broadband monitoring of the E-field and the frequency-selective case B measurements, it is worth investigating the impact of base station antennas on exposure levels. Figure 16 presents the frequency-selective[1] measurements of the E-field for the surrounding probes of the PCA on dataset No. 1 (Mulhouse 03, Nantes_01, Paris2connect_06, Paris_8e_02 and SaintAubindeMedoc_01). It shows that the main contribution to the exposure level comes from cellular networks. Moreover, it shows that Mulhouse_03, Nantes_01 and Paris2Connect_06 have higher contributions in cellular bands than Paris_8e_02 and SaintAubindeMedoc_01. The cellular contributions of Paris_8e_02 and SaintAubindeMedoc_01 are close to the noise level of the measurement system. It confirms that the PCA on dataset No. 1 reveals:

- probes located in a dense area of base station antennas and measuring a high variability of exposure levels (high level on 1st component and high level on 2nd component, for instance Paris2Connect_06);
- probes located in a dense area of base station antennas and measuring a low variability of exposure levels (high level on 1st component and low level on 2nd component, for instance Paris_8e_02);

[1] Detailed frequency bands: HF = [100 kHz; 30 MHz], Private Mobile Radio (PMR) = [30 MHz; 47 MHz] ∪ [68 MHz; 87.5 MHz], FM Broadcasting = [87.5 MHz; 108 MHz] ∪ [174 MHz; 223 MHz], PMR/Radio Beacon = [108 MHz; 880 MHz] ∪ [921 MHz; 925 MHz], TV = [47 MHz; 68 MHz] ∪ [470 MHz; 694 MHz], 700 MHz band = [758 MHz; 788 MHz], 800 MHz band = [791 MHz; 821 MHz], 900 MHz band = [925 MHz; 960 MHz], Radars/Radio beacon = [960 MHz; 1710 MHz], 1800 MHz band = [1805 MHz; 1880 MHz], DECT = [1880 MHz; 1900 MHz], 2100 MHz band = [2100 MHz; 2170 MHz], 2600 MHz band = [2620 MHz; 2690 MHz], 3600 MHz band = [3490 MHz; 3800 MHz], Radars/Wireless local loop (WLL) = [2200 MHz; 6000 MHz], WLAN [2400 MHz; 2483.5 MHz] ∪ [5150 MHz; 5350 MHz] ∪ [5470 MHz; 5725 MHz].

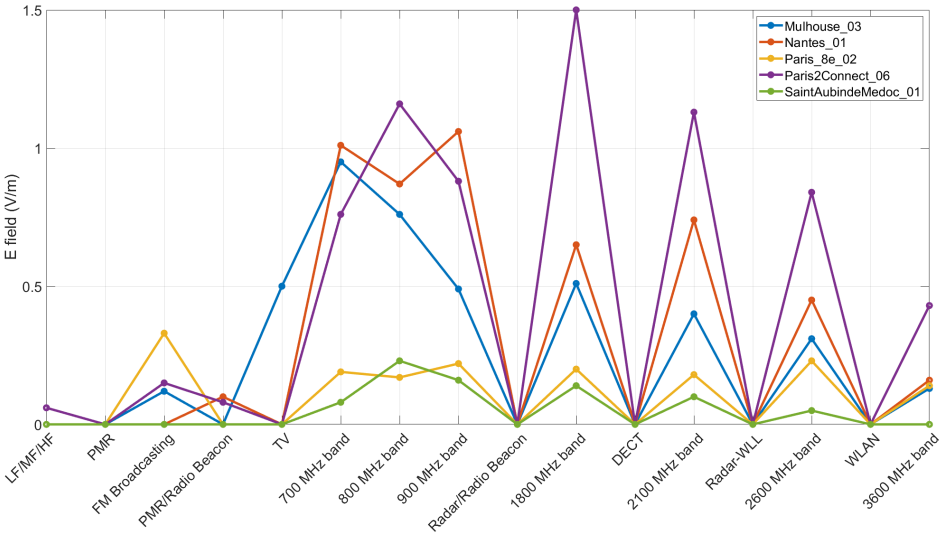

Figure 16. Frequency-selective E-field measurements (case B) for surrounding probes of PCA.

- probes located in a relatively dense area of base stations antennas and measuring a high variability of exposure levels (average level on 1st component and high level on 2nd component, for instance Mulhouse_03 and Nantes_01);
- probes located in the vicinity of few base station antennas and measuring a very low variability of exposure levels (low level on both components, for instance SaintAubindeMedoc_01).

4.3.2. *Dataset No. 2*

In Figure 17, Dataset No. 2 is represented in the two main principal component coordinates. Similar to dataset No. 1, the most distant probes surrounding the point cloud in the principal component graph are selected to highlight most of the variability. Table 4 presents the eigenvalues and the percentage of total explained variance, which gives an idea of how important the components are in terms of variability. The proportion of total explained variance shows that the first two components represent 98.5% of the variability. Figure 18 displays the correlation circle for the original variables of dataset No. 2 represented in the domain of two components found by PCA. It indicates that all months are equally correlated to the first component but the second component distinguishes summer months (top side) from winter months (bottom side). Figure 19 illustrates the original dataset No. 2 for the five probes surrounding the point cloud.

The PCA on dataset No. 2 shows that the first component distinguishes probes with high variability from those with low variability. The second principal component distinguishes probes installed in cities where the population density is higher in summer compared to winter, especially cities located in the south of France. Indeed, Orléans_01 is located near a skating rink and a school while Bègles_01 is located near a big hub of railway lines connecting to the Bordeaux-Saint-Jean train station. Marseille_03 is situated near the beach in downtown Marseille. It can be assumed that the probes surrounding the second component of the PCA in Figure 17 (Marseille_03, Bègles_01) experience a higher level of exposure during the summer months due to

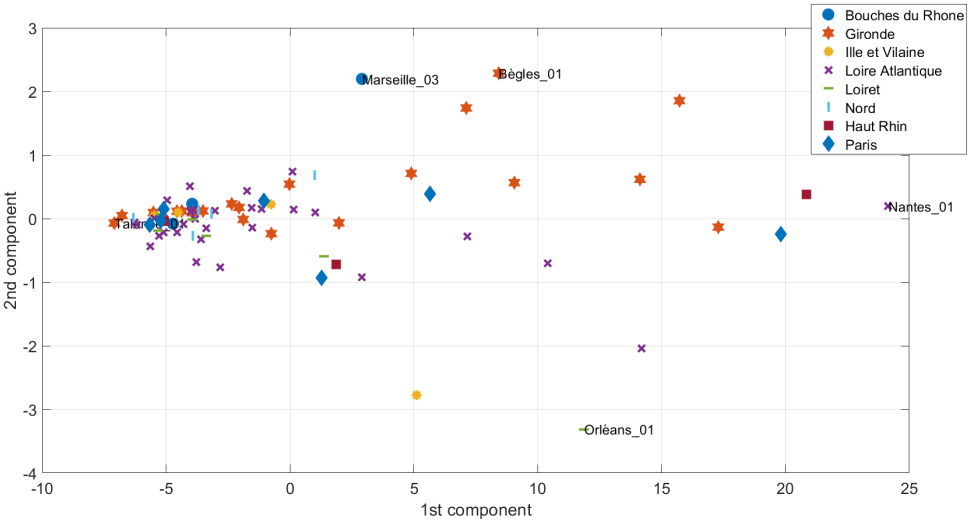

Figure 17. Dataset No. 2 represented on the domain composed by two main principal components.

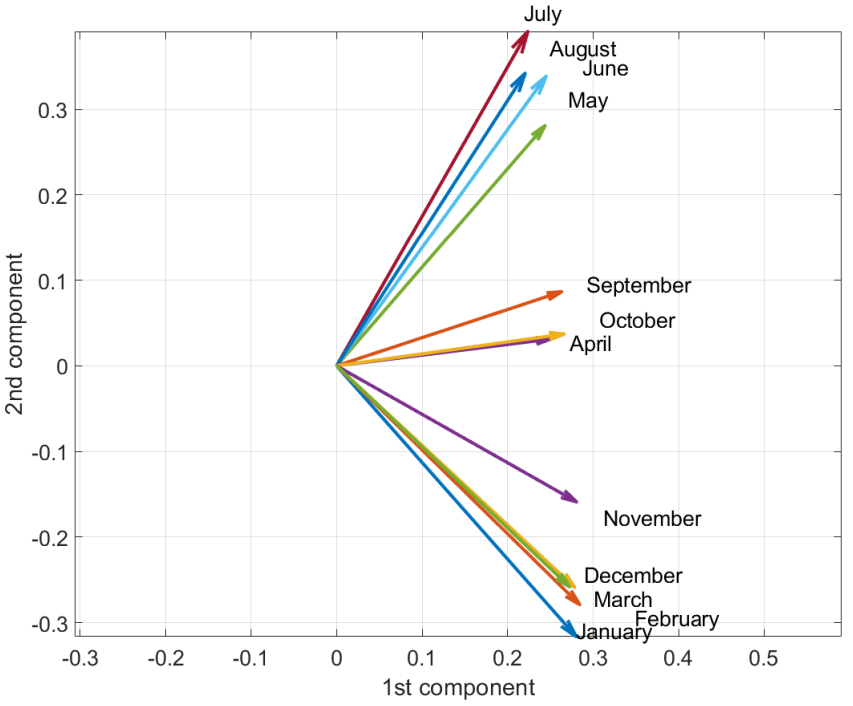

Figure 18. Correlation circle for dataset No. 2 representing variables projected on the two main components.

their proximity to frequently used areas (beach and railway lines) during summer time. The Orléans_01 probe measures low level of exposure during summer time because the skating rink and schools are closed during the summer months.

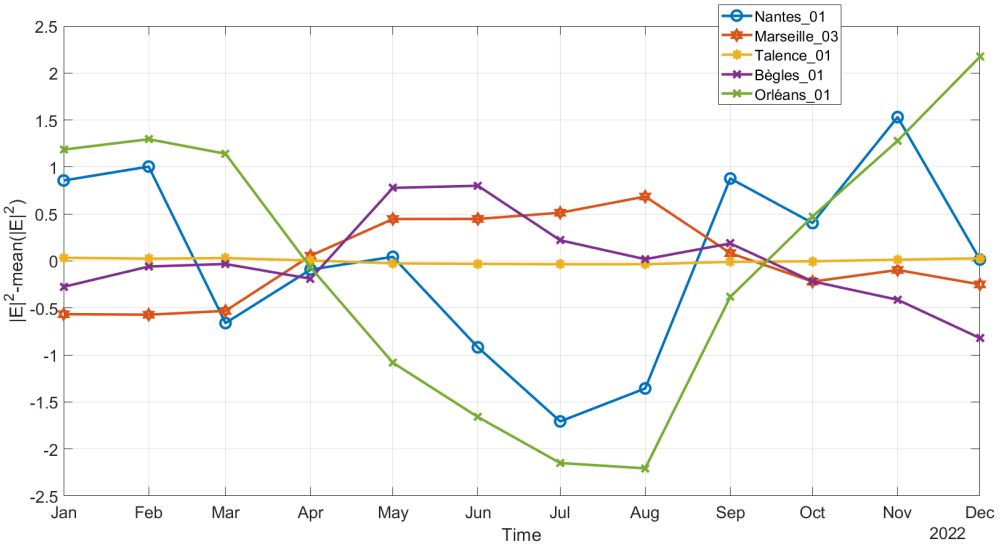

Figure 19. Square of the E-field during 2022 for the probes surrounding the principal components.

Table 4. Eigen values for each component and proportion of explained variance for dataset No. 2

# Components	Eigenvalue	Proportion of total explained variance (%)
1	50.6853	97.4
2	0.6201	1.1
3	0.2890	0.6
4	0.1992	0.4
5	0.0867	0.2
6	0.0605	0.1163

4.4. *Discussion of PCA results*

4.4.1. *Dataset No. 1*

Dataset No. 1 includes monthly averaged E-field measurements from monitoring probes, frequency-selective E-field measurements (case B) from in situ measurements and the number of base station antennas per cellular band surrounding each probe. The purpose of this dataset is to examine the correlation between the level measured by autonomous probes and the radio environment described by case B in situ measurements and number of base station antennas surrounding the probe. Principal component analysis has revealed probes that are located in dense areas of base station antennas or probes positioned in areas with very few base station antennas. PCA reveals probes that measure a high level of variability and are strongly dependent on the radio environment (high level on 1st component, high level on 2nd component). PCA reveals probes which measure a low level of variability and are not impacted by the radio environment (high level on 1st component, low level on 2nd component). Finally, the PCA of Dataset No. 1 reveals probes that are positioned correctly to monitor the E-field produced by the radio environment. Probes measuring a very low level of exposure can then be identified easily

and repositioned to positions that lead to a higher fluctuation of the exposure levels. However, some probes are positioned close to specific buildings (such as schools) and their role is to monitor low levels of exposure.

4.4.2. *Dataset No. 2*

Dataset No. 2 contains monthly averaged squared E-field measurements from monitoring probes. The purpose is to analyze whether there is a seasonal pattern within the monitoring probes. The principal component analysis on dataset No. 2 highlights probes that measure temporal E-fields that present a seasonal pattern. Indeed, probes with 1st component value higher than zero show a seasonal pattern, probes with high value on the 2nd component show a higher average level of exposure during summer time compared to winter time. Probes with negative level on the 2nd component present a higher averaged level of exposure during winter compared to summer. Finally, PCA helps us to identify the probes measuring seasonal patterns (1st component > 0), but also identifies how the summer season is compared to the winter. It shows that the type of neighborhood where the probe is installed plays a significant role.

5. Conclusion and perspectives

This study introduces a novel method for monitoring exposure to electromagnetic fields emitted by radio base stations. It shows that monitoring probes installed by ANFR, the C2M team of Télécom Paris, city councils or metropolitan authorities enable the analysis of the time domain aspect of exposure and the extraction of several noteworthy observations.

The analysis indicates that the monitoring probes have varying exposure levels. Probes measuring significant levels show a difference in exposure between day and night, a phenomenon observed for the first time in France. An empirical time interval from 8 AM to 11 PM enables to calculate the ratio of averaged E-field levels between day and night. This ratio is between 1.28 and 1.42 for the three probes with the highest RMS level. Several papers, such as [8–10], have characterized the day and night fluctuation, but this has never been demonstrated using French data.

For the first time, the variability of daily working hours has been quantified for all the probes installed in France. The data shows that most of the probes exhibit a 30% variation percentage based on the data gathered from 8 AM to 5 PM. Based on our knowledge, this is the first time that the assessment of the daily variation contributor based on more than 150 probes installed in different environments is achieved. It confirms the level of daily variation contributor to the in situ measurement uncertainty budget, as communicated in the accredited in situ measurement reports [3, 16, 17].

In this study, one of the goals was to correlate different sources of measurement: monitoring probe measurements and in situ measurements. In [12], an attempt was made to compare different types of monitoring probes installed in various countries. However, in this study, we compare in situ measurements to monitoring probes. It has been shown that measurements by monitoring probes installed on street furniture and in situ measurements on the ground level beneath the probes are nearly linear and that the relative deviations are bounded by the combined uncertainty. This is a satisfactory result, particularly given that the in situ measurement is taken only a few meters below the monitoring probe.

The published literature has shown several examples of monitoring probes [6–13], but for the first time a methodology based on PCA on dataset No. 1 has enabled the detection of probes that are in the best position to monitor radio environment radiation. Although the effect of antenna density on the measured field has been addressed in many studies mentionned in the introduction, for the first time, a methodology is proposed to detect which probes present a

strong correlation with antenna density. This methodology can also be useful to displace some of the probes which are installed in high density of base station area but not in a good configuration of exposure.

For the first time, the seasonality of the level of exposure has been analyzed at the French national level. The PCA on dataset No. 2 emphasizes the observation that the positioning of the probe is crucial to observe a remarkable variation of the exposure level. The probe must not only be installed in an area with many base stations, but also in close proximity to them and in a line-of-sight position for the exposure. A large number of probes measuring low exposure levels can be explained by the fact that the probes are not in a line-of-sight situation. In some cities, probes were installed in low-density areas rather than in front of base stations due to public concern over electromagnetic waves. Upon analysis, we find that some probes measure a lower level of exposure in summer time. This interpretation was confirmed with the Principal Component Analysis, which showed that the second component of the PCA characterizes the difference between probes with higher exposure in summer or winter. This phenomenon can be explained by the fact that some of the cities are very touristic during the summer, leading to increased use of the telecommunication infrastructure. In general, the exposure levels measured by the autonomous probe are very low compared to the limits. The increase of the exposure level is relatively slow, as it has been shown in several ANFR studies [4, 18–20].

In future work, statistical clustering methods can be used to group probes in PCA coordinates and enhance the methodology for detecting probes with the same E-field pattern.

Declaration of interests

The authors do not work for, advise, own shares in, or receive funds from any organization that could benefit from this article, and have declared no affiliations other than their research organizations.

Funding

Funding for this research was provided by the European Union's Horizon Europe Framework Programme under Grant Agreement number 101057622 (SEAWave Project) [22].

Acknowledgments

We thank C2M Telecom Paris for their very valuable input. We greatly acknowledge EXEM company (ANFR's subcontractor) for conducting in situ measurements, installing monitoring probes, and sharing all the probe results with ANFR.

References

[1] WHO, The International EMF project, https://www.who.int/initiatives/the-international-emf-project/.

[2] ICNIRP, "Guidelines for limiting exposure to electromagnetic fields (100 kHz to 300 GHz)", *Health Phys.* **118** (2020), no. 5, p. 483-524.

[3] Cartoradio by ANFR, "La carte des sites et des mesures radioélectriques", https://www.cartoradio.fr/.

[4] ANFR, "Multiple reports on exposure to 5G technology", https://www.anfr.fr/maitriser/les-installations-radioelectriques/etudes-sur-les-installations-radioelectriques/5g.

[5] Observatoire des ondes, https://www.observatoiredesondes.com/fr/.

[6] J. Wout, V. Leen, T. Emmeric, M. Luc, "In-situ measurement procedures for temporal RF electromagnetic field exposure of the general public", *Health Phys.* **96** (2009), no. 5, p. 529-542.

[7] D. Gallo, C. Landi, N. Pasquino, "Multisensor network for urban electromagnetic field monitoring", *IEEE Trans. Instrum. Meas.* **58** (2009), no. 9, p. 3315-3322.
[8] M. Athanasios, B. Achilles, S. Theodoros, J. N. Sahalos, "Continuous electromagnetic radiation monitoring in the environment: analysis of the results in Greece", *Radiat. Prot. Dosim.* **151** (2012), no. 3, p. 437-442.
[9] D. Nikola, K. Dragan, K.-L. Karolina, B. Vera, "The SEMONT continuous monitoring of daily EMF exposure in an open area environment", *Environ. Monitor. Assessment* **187** (2015), article no. 191.
[10] D. Luis, R. Agüero, L. Muñoz, "Electromagnetic field assessment as a smart city service: the smartsantander use-case", *Sensors* **17** (2017), no. 6, article no. 1250.
[11] N. Djuric, N. Kavecan, M. Mitic, N. Radosavljevic, A. Boric, "The concept review of the EMF RATEL monitoring system", in *2018 22nd International Microwave and Radar Conference (MIKON), Poznan, Poland*, 2018, p. 258-260.
[12] I. Serafeim, C. Apostolidis, A. Manassas, T. Samaras, "Electromagnetic fields exposure assessment in Europe utilizing publicly available data", *Sensors* **22** (2022), no. 21, article no. 8481.
[13] S. Sanjay, D. Stefan, S. Anna *et al.*, "Radiofrequency electromagnetic field exposure in everyday microenvironments in Europe: a systematic literature review", *J. Exp. Sci. Environ. Epidemiol.* **28** (2018), p. 147-160.
[14] Exem company, https://www.exem.fr/.
[15] P. Pinel, P. Tajan, Y. Poiré, L. Ourak, "EMF observatory, an answer to the societal debate", in *Proceeding of Journées scientifiques de l'URSI France*, 2020, p. 27-33.
[16] ANFR, "Protocole de mesure V4.1", https://www.anfr.fr/fileadmin/mediatheque/documents/expace/2017-08-28_Protocole_de_mesure_V4.pdf.
[17] EN IEC 62232, "Determination of RF field strength, power density and SAR in the vicinity of radiocommunication base stations for the purpose of evaluating human exposure", 2022, https://webstore.iec.ch/publication/64934.
[18] Annual report on In situ measurement web page on ANFR's website, https://www.anfr.fr/maitriser/les-installations-radioelectriques/etudes-sur-les-installations-radioelectriques/rapports-annuels-des-mesures.
[19] ANFR, "Study of the 5G contribution to exposure of the general public to electromagnetic waves", 2021, https://www.anfr.fr/fileadmin/mediatheque/documents/5G/20211214-exposition-5G-EN.pdf.
[20] "City hall square" report web page on ANFR's website, https://www.anfr.fr/maitriser/les-installations-radioelectriques/etudes-sur-les-installations-radioelectriques/mairies.
[21] I. T. Jolliffe, *Principal Component Analysis*, Springer, New York, NY, 2002.
[22] SEAWave Project, "5G and beyond", https://seawave-project.eu/.

ACADÉMIE DES SCIENCES
INSTITUT DE FRANCE

Comptes Rendus. Physique
2024, Vol. 25, Special issue S1, p. 63-73
https://doi.org/10.5802/crphys.183

Research article / *Article de recherche*

Energy in the heart of EM waves: modelling, measurements and management / *L'énergie au cœur des ondes électromagnétiques : modélisation, mesures et gestion*

Extensive 5G measurement campaign to monitor EMF exposure in France

Vaste campagne de mesures 5G pour surveiller l'exposition aux ondes éléctromagnétiques en France

Lydia Sefsouf [*,a], **Emmanuelle Conil** [a] **and Jean-Benoît Agnani** [a]

[a] Agence Nationale des fréquences (ANFR), Maisons-Alfort, France

E-mails: lydia.sefsouf@anfr.fr (L. Sefsouf), emmanuelle.conil@anfr.fr (E. Conil), jean-benoit.agnani@anfr.fr (J.-B. Agnani)

Abstract. As part of its mission to monitor public exposure, the French National Frequency Agency (ANFR) has launched an extensive measurement program at nearly 2000 sites to assess exposure following the deployment of the new 5G mobile technology starting at the end of 2020. For each site identified in the program, an initial measurement was conducted prior to the deployment of 5G, followed by two additional measurements after the sites had been in operation for approximately 4 months and 8 months, in order to monitor the evolution of exposure as a function of traffic growth and operational deployment. The measurements were performed in accordance with the ANFR protocol referenced in the French Official Journal, which is the reference text for accredited laboratories carrying out field measurements (E in situ). In addition to the global and detailed frequency exposure measurements, specific measurements were made by downloading a 1 GB file on the 3500 MHz band. This approach allows to artificially generate additional traffic according to the exposure indicator proposed by ANFR for steerable beam antennas and to estimate the local exposure level that would statistically be reached by 5G in the long term.

Résumé. Dans le cadre de ses missions de surveillance de l'exposition du public aux ondes électromagnétiques, l'Agence nationale des fréquences (ANFR) a lancé un vaste programme de mesures sur près de 2000 sites pour évaluer l'exposition à la suite du déploiement de la nouvelle technologie mobile 5G dès fin 2020. Pour chaque site identifié dans le programme, une mesure initiale est réalisée avant le rajout de la 5G sur ces sites, une deuxième et troisième mesure sont réalisées à environ 4 mois et 8 mois de mise en service dans le but de suivre l'évolution de l'exposition en fonction du déploiement opérationnel et de l'accroissement du trafic. Les mesures sont réalisées selon le protocole de l'ANFR référencé au Journal Officiel, constituant le texte de référence des laboratoires accrédités qui réalisent des mesures sur le terrain (E in situ). En complément des mesures d'exposition globale et détaillées en fréquences, des mesures spécifiques ont été effectuées en téléchargeant un fichier de 1 Go sur la bande 3500 MHz. Ce mode opératoire permet de générer artificiellement un trafic supplémentaire correspondant à l'indicateur d'exposition proposé par l'ANFR pour les antennes à faisceaux orientables et permet d'estimer le niveau d'exposition local qui serait statistiquement atteint à terme en 5G.

* Corresponding author

Keywords. Exposure to EMF, 5G, Exposure monitoring.

Mots-clés. Exposition aux ondes électromagnétiques, 5G, Surveillance de l'exposition.

Note. This article follows the URSI-France workshop held on 21 and 22 March 2023 at Paris-Saclay.

Manuscript received 31 July 2023, revised 6 March 2024, accepted 15 March 2024.

1. Introduction

5G is now being deployed in mainland France on several frequency bands: the so-called low-frequency bands 700 MHz and 2100 MHz, which have been used for many years by previous generation mobile phone networks (3G and 4G), and the new 3500 MHz band, which offers a wider bandwidth for higher data rates.

The French Frequency Agency (Agence nationale des fréquences ANFR) ensures compliance with the limits for public exposure to electromagnetic waves set by decree [1]. To this end, it develops and updates the exposure measurement protocol. As part of its mission to monitor public exposure, the ANFR has launched a major program of in situ electric field measurements to characterize the impact of 5G on exposure levels [2]. This huge operation covered almost 2000 radio stations throughout mainland France. From the end of 2020 to the end of 2021, three phases were carried out at sites identified to host 5G: an initial measurement before the arrival of 5G at these sites (phase 1), a second measurement carried out about 4 months after the start of service (phase 2) and finally a third measurement at an interval of about 8 months (phase 3). This campaign continued in 2022 and 2023 with 4 additional phases.

This paper focuses on the results up to the end of 2021 and includes a global exposure assessment based on broadband measurements, a detailed frequency assessment to obtain the contribution of each frequency band, and specific measurements with forced traffic in the 3500 band.

2. Measurement protocol and locations

2.1. *Measurement protocol*

Since 2001, the ANFR has been responsible for defining and updating the in situ measurement protocol to verify that the radiofrequency (RF) exposure levels of the general public are in compliance with the French exposure limits. The ANFR protocol is referenced in the French Official Journal [3] and is used by ISO IEC 17025 [4] accredited laboratories. It complies with the international standard EN IEC 62232 [5] section 6.3 "Evaluation processes for in situ RF exposure assessment".

The current ANFR measurement protocol version 4 was used [6]. A global measurement covering all significant radio sources between 100 kHz and 6 GHz is made at the selected measurement point. It is based on the use of a broadband probe with a sensitivity of 0.38 V/m. This assessment shall be made using a spatial averaging over a minimum of three heights (1.1 m, 1.5 m and 1.7 m) and a time averaging over 6 min (a shorter duration may be sufficient as long as the root mean square (RMS) average remains stable).

A detailed measurement (case B) can then be made at the same position as in case A to determine the exposure for each frequency band and for each operator (detailed measurement of each exposure contribution in the same frequency range). Case B involves the use of a spectrum analyzer with a minimum sensitivity of 0.05 V/m per frequency band. The results include the integration per service (e.g., mobile phone band or TV band) and the sources of concern per service that are defined as a significant emission with a minimum level of 0.3 V/m (more than

Figure 1. Typical configurations of measurement.

40 dB below the lowest regulatory limit). Spatial averaging over at least three heights (1.1 m, 1.5 m and 1.7 m) and temporal averaging over 6 min is also required for Case B (the root mean square (RMS) of the E-field measured at the three heights over 6 min).

In the framework of this campaign, case B was not systematically performed at every measurement point. During the second phase of measurements in 2021, it was mostly carried out only at points where the global level was greater than or equal to 2 V/m.

All measurements were performed outdoors and during daytime, in direct view of the main lobe of the antennas (line-of-sight) and at a distance of about 100 m. Figure 1 shows a typical configuration of this campaign.

For the current uses of the previous technologies (2G/3G/4G), the level measured with a broadband probe (case A) is a good indicator of exposure regardless of the time of day, and is generally close to the level observed with continuous measurements averaged over a period of 6 min: the amplitude of the variations observed in the studies during the day is generally small, less than 30%. However, with the 5G steerable beam antennas, greater spatial and temporal variability is expected. As a result, the level measured with a broadband probe at any one time may no longer be a good indicator of exposure. The level of exposure will strongly depend on the usage, and in particular on the data request made by the terminal. For this reason, ANFR proposed in [7], a new indicator, based on a foreseeable use of 5G. This consists of sending 1 GB of data every 6 min in a given direction. Assuming an average data rate of 500 Mbps, the antenna will only transmit in the given direction for about 15 s out of the 6 min (about 4% of the time).

At the beginning of the roll-out of a new technology, the load is low, mainly because only a few users have the appropriate terminals and subscriptions. Thus, when 5G was launched in the 3.4–3.8 GHz band, which is used exclusively for 5G, the levels measured were very low, as expected, because the 5G network would be very lightly loaded. In order to measure an exposure level that might be more representative of what 5G will eventually generate in the long term, the ANFR opted to voluntarily solicit the 5G antennas by downloading a 1 GB file in order to consider a realistic antenna load according to the assumptions made to define the exposure indicator described above.

The measurement consists of two assessments in the 3500 MHz band: when the network is not voluntarily solicited and when it is solicited by a mobile phone by downloading a 1 GB file

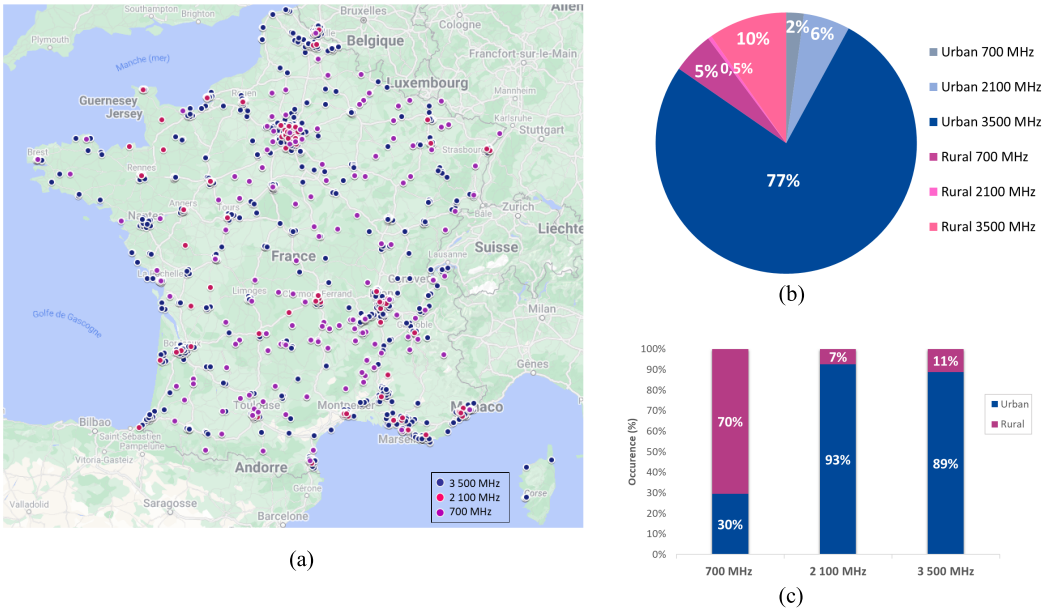

Figure 2. (a) Geographical distribution. (b) Environment type distribution. (c) Frequency bands distribution.

from a server, ensuring that the server's performance allows the expected 5G speeds (500 Mbps on average) at the measurement point. It is also necessary to ensure that the download occurs in the 3500 MHz band. This approach for in situ measurements using emulated base station load profiles is described in Annex B of the IEC 62232 standard [5].

It is worth noting that the RMS electric field level averaged over 6 min without network solicitation can be evaluated over a period of less than 6 min, as long as the averaged RMS value is stable. The RMS electric field level averaged over 6 min can then be evaluated from the measurement averaged over the duration of the download according to the following equation:

$$E_{\text{estim\_6 min}} = \sqrt{\left(\frac{T_t}{360}\right) \times E_{\text{at}}^2 + \left(1 - \frac{T_t}{360}\right) \times E_{\text{st}}^2} \tag{1}$$

where:

$E_{\text{estim\_6 min}}$: field strength in V/m averaged over 6 min
T_t: duration of the 1 GB file download in seconds
E_{at}: average field strength in V/m measured during the download time
E_{st}: average field strength in V/m measured without artificial network load.

2.2. *Measurement locations*

The distribution of 5G sites in mainland France is shown in Figure 2(a)[1], with 85% of sites located in urban areas and 15% in rural areas (Figure 2(b)). This distribution is close to the share of urban population in the total population of France (80% in urban areas) [8].

In the remainder of this paper, a measurement taken before 5G was activated will be noted as a "before" measurement, representing Phase 1, the one performed after approximately 4 months of 5G activation will be noted as an "after 1" measurement, representing Phase 2, and

[1] From 2022, the ANFR has extended its program to include the DROM-COM.

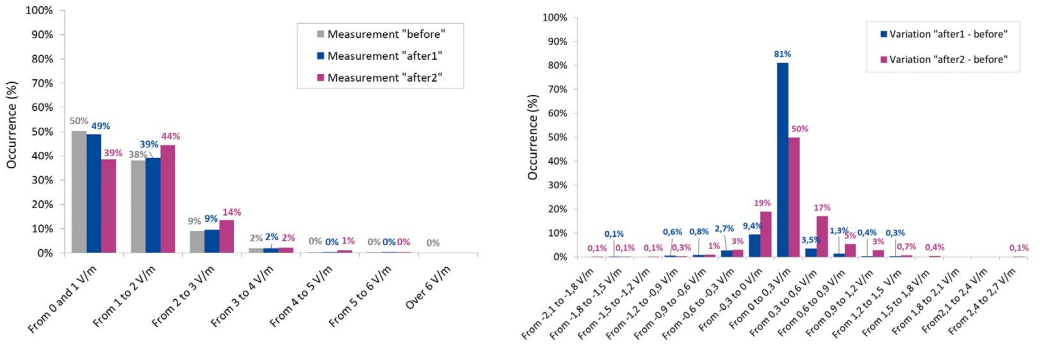

(a) (b)

Figure 3. (a) Distribution of overall exposure levels before and after 5G roll out on 3500 MHz band; (b) distribution of differences between overall exposure levels before and after 5G roll out on 3500 MHz band.

the one performed after approximately 8 months of operational deployment will be referred to as an "after 2" measurement, representing Phase 3. Depending on the phase of the campaign considered, a pair of measurements taken before and after 5G is activated will be recorded as "before–after1" or "before–after2". A trio of measurements representing the three phases of the campaign will be noted "before–after1–after2".

3. Results

3.1. *Analysis of the overall exposure levels on sites hosting 5G in the 3500 MHz band*

In this section, the analysis of the overall exposure levels (case A) is studied at about 1360 sites hosting 5G in the 3500 MHz band. Figure 3(a) shows the distribution of measurements by 1 V/m increments on the overall exposure levels observed before and after the activation of 5G during phases 2 and 3 of the campaign.

These histograms show that exposure remains steady between phases 1 and 2. This trend has changed in phase 3, where an increase is observed. In fact, 11% of the points that were in the "from 0 to 1 V/m" range in phase 1 leave this range and move to the higher ranges because they become more exposed, as can be seen from the histograms plotted in Figure 3(a). However, this increase is moderate, as can be seen, 83% of the "after2" measurements remain below 2 V/m, compared to 88% of the "before" and "after1" measurements.

This first conclusion is confirmed by a comparison of the statistical parameters shown in Table 1. The average exposure levels are 1.16 V/m for the "before" measurement, 1.17 V/m for the "after1" measurement and 1.34 V/m for the "after2" measurement, i.e., an average variation that increases from 0.01 V/m (close to zero) for phase 2 to 0.18 V/m for phase 3.

In order to better characterize the variation between the "before" and "after1–after2" measurements, the local variation is studied to observe how the electric field levels are distributed locally (i.e. site by site). For this purpose, the statistical distribution of the differences between the trio of "before–after1–after2" measurements is characterized by histograms of 0.3 V/m steps in Figure 3(b) and modeled by the normal distribution probability density and its cumulative distribution function (CDF) in Figure 4.

The histograms show a greater variation in phase 3 than in phase 2, where in more than 90% of the cases, the variation was between −0.3 V/m and 0.3 V/m (non-significant), compared to 69%

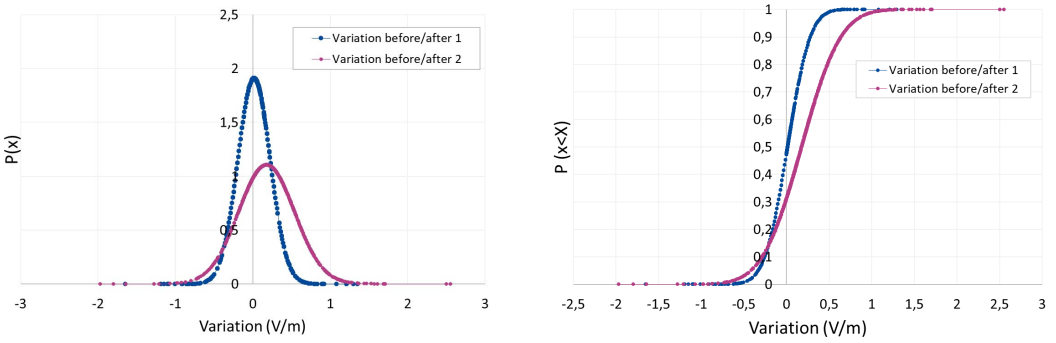

Figure 4. Probability density function (a) and cumulative distribution function (b) of differences between overall exposure levels before and after 5G roll out on 3500 band. See Figure 3(b) for real data.

Table 1. Comparison of overall exposure filed level statistics before and after 5G roll out

	Nb measurements	Mean (V/m)	Median (V/m)	Std Deviation (V/m)	Max (V/m)
Overall exposure "before"	1358	1.16	0.99	0.75	6.19
Overall exposure "after1"	1358	1.17	1.01	0.74	5.41
Overall exposure "after2"	1358	1.34	1.19	0.79	5.83
	Nb measurements	Mean variation	Median variation	Std deviation variation	Max variation
"after1–before" Variation	1358	0.01	0.02	−0.01	−0.78
"after2–before" Variation	1358	0.18	0.2	0.04	−0.36

in phase 3. From the probability density and CDF, it can be clearly seen that the distribution of the "before–after2" variation is no longer centered on zero as it was for the "before–after1" variation. It also shows that the 90% and 99% values are larger for the "before–after2" variation.

The results conclude that 4 months after 5G became operational, there was no significant change in overall exposure compared to before 5G started. However, after 8 months, an increase in overall levels was observed: the average overall exposure level increased from 1.16 V/m to 1.34 V/m.

It should be further noted that as only the global exposure was investigated, it is not possible at this stage of the study to identify which frequency bands are contributing to this increase. The detailed frequency measurements (case B), discussed in the next section, provide a comprehensive exposure assessment with a frequency-selective analyzer that can identify the sources contributing to the exposure, as described above in the measurement protocol.

3.2. *Analysis of the contribution of the 3500 MHz band*

For a more detailed analysis of the increase highlighted in the case A study, the detailed frequency measurements (case B) will be discussed by isolating the contribution of the telephony service in the 3500 MHz band, but also in the other frequency bands. Among the 1358 sites previously analyzed, 141 of the most exposed sites (where at least one measurement has an overall value of 2 V/m) were covered by detailed measurements during phases 2 and 3 of the campaign.

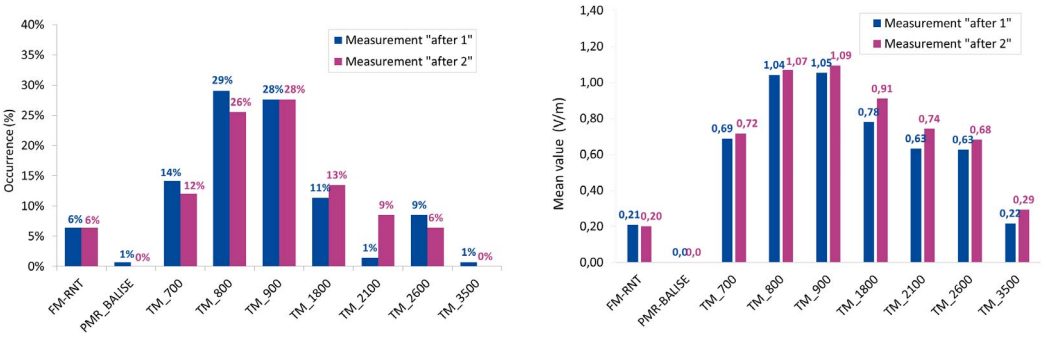

(a) (b)

Figure 5. Distribution of main contributions to overall exposure (a) by service/frequency band and evolution of their mean value (b). (FM-RNT: Radio broadcasting, PMR-Balise: Private Mobile Radio, TM: Mobile Telephony (cellular network).)

Firstly, the Figure 5(a) shows the service contributing most to the overall exposure, where it can be seen that the 800 MHz and 900 MHz bands are the main contributors in about 55% of the cases in both phase 2 and phase 3. The 2100 MHz band appears to be the main contributor in 9% of cases in phase 3, compared to 1% in phase 2. The 3500 MHz band could not a priori be the cause of the increase in total exposure in phase 3 as it is not the main contributor.

Secondly, to better illustrate the exposure by service, the histograms in Figure 5(b) show the increase in average exposure, particularly for mobile services, between phases 2 and 3. The increase in average exposure per frequency band is relatively significant for frequencies where LTE (4G) is present (TM_1800 and TM_2100). For the 3500 MHz band, it is not possible to conclude that there is an increase as the levels are not significant. It is important to point out that the levels measured remain very low compared to the regulatory limit values (36 V/m for the lowest mobile telephony band and 61 V/m for the highest band).

At least, these selective E-field measurements show that the observed increase in total exposure is not due to an increase in field strength in the 3500 MHz band, but to an increase in exposure in the other mobile phone bands, especially those allocated to 4G.

3.3. *5G specific measurements with data download*

At the launch of the campaign, few users are soliciting 5G antennas, so it seemed interesting to artificially generate traffic to study the impact of 5G on overall exposure by simulating higher usage in this band. As described in the protocol section, the traffic is generated by downloading 1 GB of data, which is equivalent to the exposure indicator proposed by the ANFR. Measurements from 464 sites are studies in this section.

Figure 6 shows in grey the average field strength during the download of the 1 GB file in the 3500 MHz band, and in pink and blue the levels over 6 min with and without artificial download. The levels with download averaged over 6 min are calculated from Equation (1) using the download time and the mean level measured during the download.

For each site, the levels shown here are the maximum levels observed between phases “after1” and “after2”.

The mean increase calculated between the measurement on the 3500 MHz band with artificial download averaged over 6 min (shown in blue) and the average level without download (shown in pink) on the same band is 0.54 V/m. The average level calculated from the single download

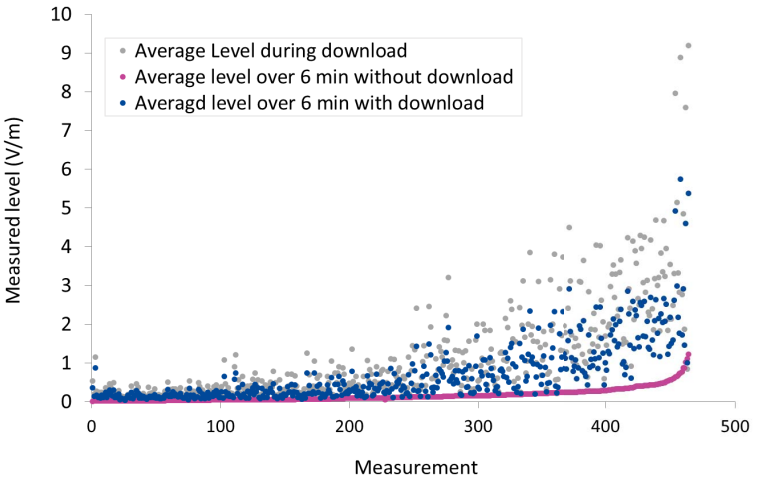

Figure 6. Average field strength while downloading a 1 GB file compared with the average level without downloading on the 3500 MHz band.

Table 2. Statistics on the 3500 MHz band with and without downloading

	Nb measurements	Mean (V/m)	Median (V/m)	Standard deviation	Max (V/m)
Exposure on the band 5G 3500 MHz without download	464	0.16	0.10	0.16	1.22
Exposure on the band 5G 3500 MHz with download	464	0.70	0.38	0.79	5.75
	Nb measurements	Mean variation	Median variation	Std deviation variation	Max variation
Variation with and without download (V/m)		0.54	0.28	0.63	4.53

of the 1 GB data file is 0.68 V/m, close to 0.70 V/m, almost the same as the average level from the download measurements including existing traffic, suggesting no significant traffic yet in this band.

The Table 2 shows the statistics calculated for the 3500 MHz band with and without artificial downloading.

To evaluate the impact on the global exposure level, the average level over 6 min related to the download of the isolated 1 GB file, resulting from the specific measurement with 5G artificial solicitation, is integrated by calculation to the global exposure case A and the cumulative overall exposure case B without specific solicitation of the network (only with existing traffic). The Figure 7(a) shows the distribution of the overall exposure levels "case A" with and without artificial downloading. The Figure 7(b) shows the distribution of the overall cumulative exposure "case B" with and without artificial downloading.

The comparison between the statistical parameters of case A and case B with and without downloading in the 3500 MHz band is shown in Table 3.

The average increase observed between the global exposure without downloading a file (only with existing traffic) and the global exposure relative to the single download of the 1 GB file is

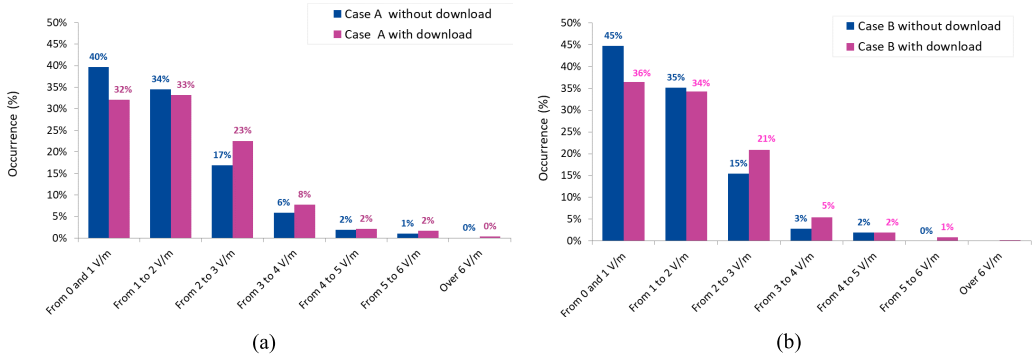

Figure 7. Distribution of the overall exposure (case a) (a) and overall cumulative exposure (case B) (b) with 5G solicitation computationally integrated and compared to the measurement without specific solicitation (with existing traffic only).

Table 3. Comparison of field strength statistics of overall exposure with and without downloading at 464 sites operating on 3500 MHz band

	Number of measures	Average (V/m)	Median (V/m)	Standard deviation
Overall exposure case A without download	464	1.51	1.24	1.00
Overall exposure case A with download	464	1.74	1.53	1.12
Variation (V/m)		0.23	0.29	0.12
Overall cumulative exposure case B without download	464	1.33	1.13	0.89
Overall cumulative case B with download	464	1.58	1.38	1.03
Variation (V/m)		0.25	0.25	0.15

21% (0.23 V/m) for case A and 31% (0.25 V/m) for the cumulative level for case B, in line with the exposure indicator introduced by the ANFR [9].

In fact, in order to assess the use of the 3500 MHz band with respect to the indicator proposed by ANFR, based on the expected use of 5G (1 GB of data sent in a given direction every 6 min), the relative usage rate is calculated from the level measured in the 3500 MHz band without download (corresponding to the existing traffic) and the level measured in the 3500 MHz band with download (corresponding to the estimated future traffic). This rate reached an average of 12% (median 6%), which means that the exposure indicator proposed by ANFR remains relevant and has not yet been reached (it would be reached when the rate reaches 100%). This means that 5G usage in the 3500 MHz band was still low at the end of 2021.

3.4. *Results on sites hosting 5G on low bands (700 MHz and 2100 MHz)*

It should be noted that these frequency bands are not reserved exclusively for 5G, the resources are shared with 4G technology and the measurement equipment does not allow to distinguish the 5G contribution from the 4G contribution in the level measured in the band.

To study the exposure created by the 5G roll out in these bands, 101 sites deploying 5G in the 2100 band and 142 sites in the 700 band were measured three times: an initial measurement before 5G deployment corresponding to phase 1 (“before”), and two measurements after 4 and 8 months of operation, corresponding to phase 2 (“after 1”) and phase 3 (“after 2”) respectively.

Regarding the 700 MHz sites, the overall level results show an average increase in overall exposure of 0.1 V/m between September and December 2021 (during phase 3) compared to an increase of 0.06 V/m at the same sites between May and September 2021 (during phase 2).

The statistics for the overall exposure levels measured at the 2100 MHz 5G sites exposure remained stable between phases 1 and 2 (average variation of −0.02 V/m). An upward trend was observed in phase 3 (average variation of 0.11 V/m).

In sum, as for measurements on 3500 MHz sites, the results of the low band measurements show an increasing trend in the overall exposure level during the period of the end of 2021.

The analysis of the detailed frequency measurements reveals that the 800 MHz, 900 MHz and 1800 MHz bands are the main bands contributing to the overall exposure.

4. Conclusion

This paper focused on analyzing the exposure evolution related to the deployment of 5G on the French national territory. More than 5000 measurements were part of a large exposure monitoring program on sites deploying 5G in the 700 MHz and 2100 MHz low frequency bands already used for 3G and 4G networks, as well as in the new 3500 MHz band exclusively dedicated to 5G. This paper was dedicated to the results of measurements performed on sites deploying 5G during the year 2021.

First, the analysis of the overall measurements allowed to observe a slight increase on 1358 sites, measured at 4 months and then 8 months intervals after their 5G deployment. Then, a sample was taken of the most exposed sites, where the analysis of detailed measurements showed an increase in the average exposure on all the mobile telephony bands. It also showed that the 800 MHz and 900 MHz bands are the main contributors to exposure, followed by the 700 MHz, 1800 MHz, 2600 MHz, 2100 MHz and 3500 MHz bands respectively for phase 2 and the 1800 MHz, 700 MHz and 2100 MHz bands respectively for phase 3 (the 3500 MHz band was not identified as the main contributor in phase 3).

As 5G traffic is still low at this stage of deployment, additional 5G specific measurements were performed in the 3500 MHz band in the presence of artificially generated traffic to solicit the 5G antenna by downloading a 1 GB file using a 5G phone. The first results suggest an increase of about 30% of the overall exposure.

It can be conclude that the increase in the overall levels at 5G 3500 MHz sites is not a priori related to an increase in the field strength in this band, but to an increase in levels in all other frequency bands of mobile telephony, reflecting an increase in traffic. It is important to remember that phase 3 of the campaign took place at the end of 2021 where an increase in traffic could be observed.

The results of the low band measurements also show an increasing trend in overall exposure levels by the end of 2021. The average increase is 0.11 V/m for 5G sites operating in the 2100 MHz band, and 0.09 V/m for sites deploying 5G in the 700 MHz band. The frequency analysis showed that this increase is not correlated with the deployment of 5G in these bands.

The measurement campaign has continued in 2022 and 2023 and will assess exposure after 1 to 2 years of 5G deployment.

Declaration of interests

The authors do not work for, advise, own shares in, or receive funds from any organization that could benefit from this article, and have declared no affiliations other than their research organizations.

Acknowledgements

The authors would like to greatly acknowledge EXEM company (ANFR'S subcontractor) for the successful running of this measurement campaign and for all the help given to launch this vast program.

References

[1] Decree no. 2002-775 of 3 May 2002 issued in application of 12° of article L. 32 of the French Post and Telecommunications Code and relating to limit values for public exposure to electromagnetic fields emitted by equipment used in telecommunications networks or by radio installations. https://www.legifrance.gouv.fr/loda/id/JORFTEXT000000226401/.

[2] ANFR, "Study of the 5G contribution to exposure of the general public to electromagnetic waves", https://www.anfr.fr/maitriser/les-installations-radioelectriques/etudes-sur-les-installations-radioelectriques/5g.

[3] Ministerial Order of 23 October 2015 amending the order of 3 November 2003 on the in situ measurement protocol aimed at verifying, for fixed transmitting stations, compliance with the limitations, in terms of reference levels, of public exposure to electromagnetic fields provided for by decree no. 2002-775 of 3 May 2002. https://www.legifrance.gouv.fr/jorf/id/JORFTEXT000031418195.

[4] ISO/IEC 17025, *General Requirements for the Competence of Testing and Calibration Laboratories*, 2017.

[5] EN IEC 62232, *Determination of RF Field Strength, Power Density and SAR in the Vicinity of Radiocommunication Base Stations for the Purpose of Evaluating Human Exposure*, 2022.

[6] ANFR, Measurement Protocole V4.0 aimed at verifying on site, for fixed equipment used in telecommunications networks or for radio installations, compliance with the reference levels for public exposure to radio frequency fields provided for in decree no. 2002-775 of 3 May 2002. https://www.anfr.fr/fileadmin/mediatheque/documents/expace/2017-08-28__Protocole_de_mesure_V4.pdf.

[7] ANFR, "National guidelines on the presentation of simulation results on exposure to radio waves from radio installations", V 2.0, october, 2019. https://www.anfr.fr/fileadmin/medias/exposition-ondes/20191001-Lignes-directrices-nationales.pdf.

[8] Distribution of the French population in 2017 by size of urban unit; National Institute of Statistics and Economic Studies; https://www.insee.fr/fr/statistiques/4806684.

[9] ANFR, "Evaluation of public exposure to 5G electromagnetic waves: First results from measurements on 5G pilots", https://www.anfr.fr/fileadmin/mediatheque/documents/expace/CND/Rapport-ANFR-resultats-mesures-pilotes-5G.pdf.

ACADÉMIE DES SCIENCES
INSTITUT DE FRANCE

Comptes Rendus. Physique
2024, Vol. 25, Special issue S1, p. 75-86
https://doi.org/10.5802/crphys.187

Research article / *Article de recherche*

Energy in the heart of EM waves: modelling, measurements and management / *L'énergie au cœur des ondes électromagnétiques : modélisation, mesures et gestion*

Electromagnetic compatibility of active cardiovascular implants to occupational magnetic field environments: impact of the field direction

Etude de la compatibilité électromagnétique des dispositifs cardiaques actifs aux champs magnétiques industriels basses fréquences : impact de l'orientation du champ

Lucien Hammen [*, a, b, c], **Lionel Pichon** [b, c], **Yann Le Bihan** [b, c], **Mohamed Bensetti** [b, c] **and Gérard Fleury** [a]

[a] Laboratoire d'Electromagnétisme, Vibrations et Optique Institut national de recherche et de sécurité (INRS) Vandœuvre-lès-Nancy, France

[b] Laboratoire de Génie Electrique et Electronique de Paris Université Paris-Saclay, CentraleSupelec, CNRS Gif-sur-Yvette, France

[c] Laboratoire de Génie Electrique et Electronique de Paris Sorbonne Université, CNRS Paris, France

E-mail: lucien.hammen@inrs.fr (L. Hammen)

Abstract. Active Implantable Medical Devices (AIMD) are nowadays a part of everyday life, with for example more than one million pacemakers (PMs) implanted each year worldwide. Like every electronic devices they are sensitive to electromagnetic interferences but the consequences are potentially severe. A large number of publications deals with electromagnetic compatibility (EMC) with common equipment but only a few concern industrial sources. Furthermore, the field encountered at workplace is potentially higher. Taking these into account, a new test method to assess the EMC of AIMDs against occupational magnetic field sources was developed. It is based on an experimental approach using a specific test bench able to generate a controlled magnetic field in all space directions up to the high occupational exposure limits between 50 Hz and 3 kHz. To do this, three Helmholtz coil systems are combined on three orthogonal space directions. This specificity makes it possible to take into account the high variability of the operator's position compared to the industrial source.

* Corresponding author

In this paper, the study focused on the impact of the magnetic field direction on the PM's functioning with bipolar leads, as is the case for the vast majority of devices implanted nowadays. It appears that the magnetic field direction has an impact on the PM's functioning and is consequently a relevant parameter for evaluating their EMC. These observations led us to the hypothesis that the lead in bipolar mode is more sensitive to electric field than magnetic field. This assumption remains to be confirmed by further studies.

Résumé. Les dispositifs médicaux implantables actifs (DMIA) font aujourd'hui partie de la vie courante, en effet plus d'un million de pacemakers sont implantés chaque année dans le monde. Comme tous les appareils électroniques, ceux-ci sont susceptibles d'être perturbés par les champs électromagnétiques environnants. De telles interférences peuvent avoir des conséquences dramatiques sur la santé du porteur. Un grand nombre de publications traitent de la compatibilité électromagnétique (CEM) des DMIA avec des équipements de la vie courante. Cependant, peu d'études concernent les sources de champ industrielles. De plus, les limites d'exposition professionnelle étant supérieures à celles pour la population générale, l'exposition est potentiellement plus intense au poste de travail. Compte tenu de ces éléments, une nouvelle méthode d'essai pour évaluer la CEM des DMIA en milieu industriel a été mise au point. Elle repose sur l'utilisation d'un banc d'essai spécifique capable de générer un champ magnétique entre 50 Hz et 3 kHz dans toutes les directions de l'espace et jusqu'aux limites hautes concernant l'exposition professionnelle. Pour ce faire, trois systèmes de Helmholtz ont été combinés selon trois directions de l'espace orthogonales. Cette spécificité permet de considérer la grande variabilité du positionnement de l'opérateur vis-à-vis d'une source industrielle.

L'étude présentée dans cet article s'est portée sur l'impact de l'orientation du champ magnétique sur le fonctionnement des pacemakers munis de sondes bipolaires, comme c'est le cas de la quasi-totalité des dispositifs implantés de nos jours. Il apparaît que la direction du champ magnétique a un impact sur le fonctionnement des pacemakers et constitue ainsi un paramètre pertinent pour l'évaluation de la CEM. Ces observations nous ont conduit à formuler l'hypothèse selon laquelle la sonde en mode bipolaire serait plus sensible aux champs électriques qu'aux champs magnétiques. Cette hypothèse demande à être confirmée par d'autres études.

Keywords. AIMD, Pacemaker, EMC, Occupational exposure, Magnetic fields, Helmholtz coil.

Mots-clés. DMIA, Pacemaker, Exposition professionnelle, Champ magnétique, Bobines d'Helmholz, CEM.

Note. This article follows the URSI-France workshop held on 21 and 22 March 2023 at Paris-Saclay.

Manuscript received 1 August 2023, revised 24 January 2024 and 30 April 2024, accepted 2 May 2024.

1. Introduction

Cardiac implants are now part of everyday life, with more than one million pacemakers (PMs) implanted each year worldwide [1] and around 67,000 in France [2]. PMs have two main functions: sensing cardiac activity and stimulating the heart muscle if an irregularity is detected. Like every electronic device, they are sensitive to interactions with electromagnetic fields. The principal mechanism of interaction is a perturbation of the measured signals, leading to a lack or inadequate stimulation. Such interference can lead to potentially severe consequences. These Electromagnetic Compatibility (EMC) issues of PMs are the topic of a large number of publications, especially concerning everyday life equipment [3–5]. The patients are generally well informed about the potential risk and they are advised to stand away from some common sources. For example, the device manufacturers specify a minimal distance between the pacemaker and a cell phone, which is usually around 20 cm. Except some studies about power distribution [6], only a few deal with EMC at workplace [7–10]. It is therefore difficult for an occupational physician to correctly assess the risks in the case of an employee equipped with a PM. Furthermore, a worker is likely to be more exposed to electromagnetic fields at work. Indeed, in Europe, occupational exposure limits [11] are generally higher than the general public ones [12]. No major pacemaker malfunction in industrial environment was published, but several articles [7,10] or standards [13] highlight the potential adverse effects using *in vitro* tests. The absence of documented accident at workplace could be explained by various suggestions: malfunctions are generally reversible and do not directly threaten patient safety, this type of malfunction is not reported by the cardiologist and high-risk workers are generally properly protected from electromagnetic sources.

Cardiac implants are more sensitive to low-frequency (LF) magnetic fields. Indeed, these devices are designed to pick up cardiac signals which are LF with a frequency range up to 500 Hz [14]. The higher frequencies are generally filtered out at the device input stage. According to an internal study, the industrial sources, such as a spot welding gun, an induction oven or an arc welding station, generally emit LF magnetic field.

In order to comply with European directives, implant manufacturers perform EMC tests according to international standards [14, 15]. These standards combine different approaches: injection tests for which the signals are directly injected at the pacemaker input stage through a "tissue-equivalent interface circuit" and a radiative test using a simple coil for magnetic field exposure. Some magnetic field thresholds between 0 Hz and 3 GHz are defined to guarantee the implant functioning during daily life situation, that's why they follow or generally exceed the public exposure limits. For information, these limits reach 100 μT (RMS) at 50 Hz, then decrease in inverse proportion to frequency up to 800 Hz and remain constant at 6.25 μT (RMS) up to 150 kHz. To determine the voltage amplitude required for injection tests from the magnetic field thresholds, the standards consider the induced voltage through the inductive loop formed by the pacemaker and its leads. A "worst case" loop dimension, taking into account the length of the leads and the clinical implantation, is considered for the calculation, which tends to maximise the test voltages. This inductive loop consideration is only valid for unipolar (single electrode) mode leads, however almost all PMs implanted in Europe nowadays operate in bipolar (two electrodes) mode [1], which is only partially considered by the literature or international standards [14, 15]. Historically the lead polarity was only unipolar, in this mode the sensing and the pacing are made between an electrode at the lead extremity and the pacemaker case itself which is metallic. Electrical continuity is ensured by the conductivity of the intermediate tissues. In bipolar mode, the electrocardiogram (ECG) monitoring and the pacing are made between two electrodes at the lead extremity. In this case, there is no inductive loop formed by the leads. The differences between these two lead configurations are illustrated in Figure 1. Bipolar probes are thus reputed to be less sensitive to electromagnetic interference, that is why standards EMC tests consider an injected voltage for this mode ten times lower than for unipolar mode [14, 15]. Considering that, the tests proposed by the international standards are limited in some aspects: the considered mechanism of interaction only concerns the case of unipolar leads, the magnetic field exposure test does not consider the PM's leads and the magnetic field is only applied along three mutually perpendicular directions, no signal corresponding to real exposure situations is tested, etc.

According to the previous considerations, there is a need to develop a new test method for estimating the EMC of PMs to occupational LF magnetic fields. The method proposed here is based on an experimental approach using a test bench. It makes it possible to determine the impact of different parameters on the implant behaviour. In our case, the study focused on the impact of the magnetic field direction on the PM with bipolar leads.

2. Material and method

A test bench was designed using the numerical simulation software CST studio suite. A frequency domain solver for LF applications based on the finite element method (FEM) was used. As the system dimensions are significantly smaller than the wavelength at the considered frequencies, the magneto-quasistatic approximation was made, i.e. the displacement current is neglected compared to the conduction current in Maxwell–Ampere equation. Like the human body, the saline solution used to test the PMs has a relatively low electrical conductivity, which implies—considering the system's dimensions—an induced current too low to generate a significant magnetic field. In these conditions and with a test setup made of non-magnetic material ($\mu_r \approx 1$),

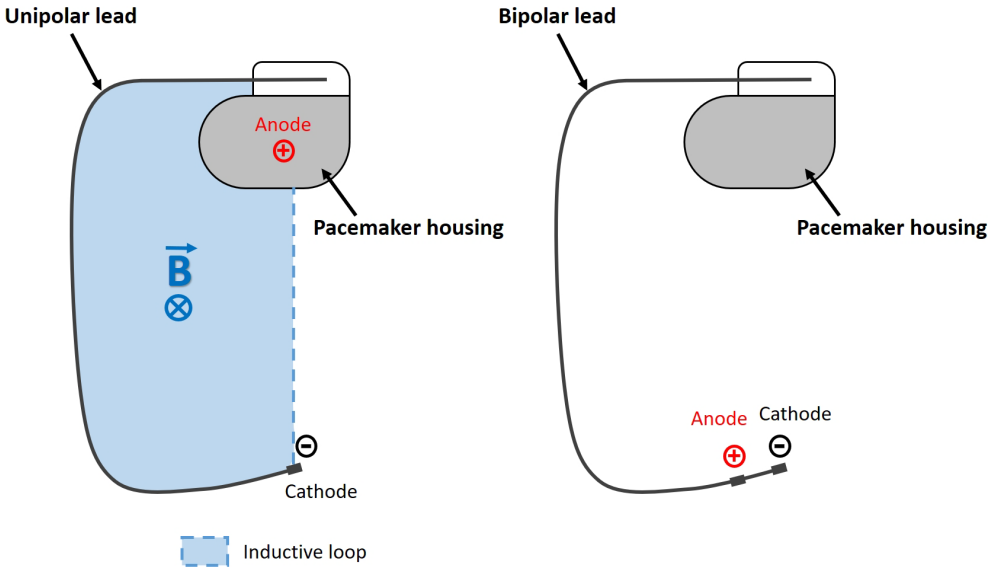

Figure 1. Differences between unipolar and bipolar lead configurations. The unipolar lead has a single electrode (cathode) at its extremity, detection and stimulation are made between it and the pacemaker housing (anode). The bipolar lead has two electrodes at its extremity, detection and stimulation are made between them.

the magnetic field distribution is not impacted by its presence. Also, considering the range of frequencies and the type of biological tissues around the pacemaker, using an equivalent homogeneous solution is a standard experimental approach widely used in the literature [6, 7, 10, 16]. The aim of the test bench is to generate a homogeneous and controlled LF magnetic field over a volume that can encompass an implant with its leads in a configuration approaching a clinical implantation. In order to take into account the high variability of the implant's position relatively to the source, the field can be generated in every space direction. In order to cover a wide range of industrial sources, the test bench was designed to operate between 50 Hz and 3 kHz. In terms of magnitude, the magnetic field is able to reach the high occupational exposure limits over the frequency range, which is theoretically the maximum level that an implant can be exposed. For information, these limits reach 6 mT (RMS) at 50 Hz and decrease in inverse proportion to frequency up to 3 kHz. Concerning the field homogeneity, a maximal variation of ±5% over a volume that encompasses the pacemaker and its leads is researched. The test bench is also able to reproduce a non-sinusoidal magnetic field representative of a real exposure at workplace.

The solution adopted to ensure the technical specifications mentioned above was to combine 3 Helmholtz coil systems in three orthogonal spatial directions (see Figure 2). Numerical simulation was particularly useful to characterise the field homogeneity inside the test bench and to determine the coil inductances, which is essential for selecting the power supply solution. The coils are thus supplied by 5 power amplifiers (model 7548 from AETechron). The geometrical characteristics of the coils are given in Table 1. The high-voltage supply generates unwanted electric fields that can interfere with implants. To avoid these parasitic fields and obtain a source of magnetic field only, the coils are shielded with a conductive layer (see Figure 3). Aluminium was used due to its relative magnetic permeability close to unity, which does not significantly affect the magnetic field distribution.

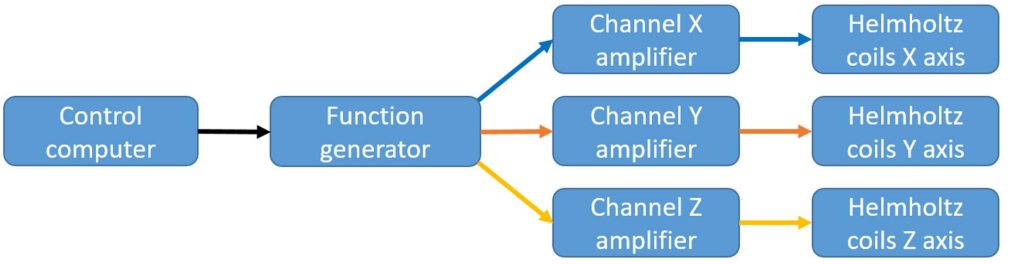

Figure 2. Test bench functional block diagram.

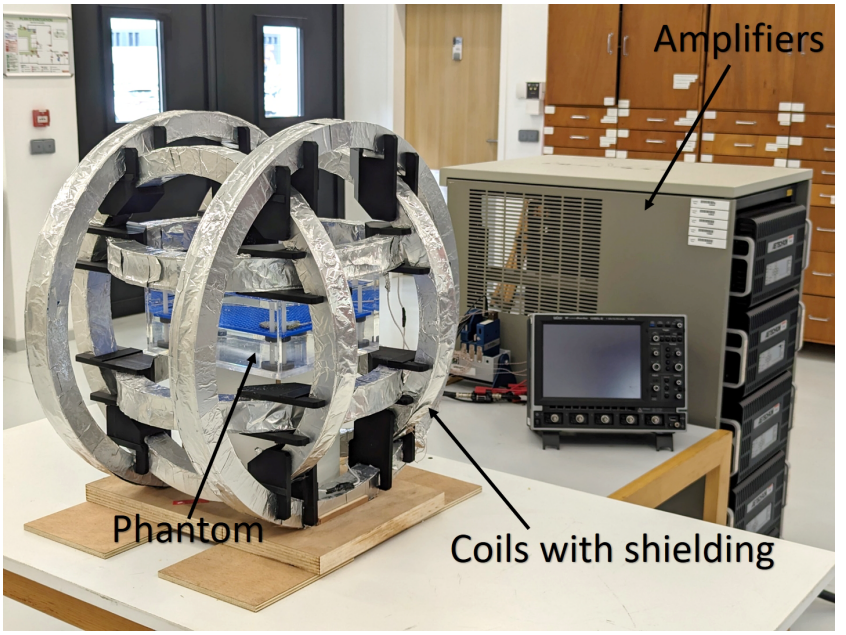

Figure 3. Test bench composed of the set of coils with shielding, the phantom and 5 power amplifiers: 2 in series for the x and y axes and only one for the z-axis, which requires less power.

Table 1. Coil geometrical characteristics

	Average diameter (cm)	N* for LF test bench
X coils	62	148
Y coils	53	127
Z coils	44	105

* Number of turns.

The test bench was characterised and complies with the specifications detailed above. The simulated magnetic field distribution presents, in the centre of the test bench when the 3 axes generate a same field intensity, a maximum variation in intensity of ±5% and a variation of field direction below 8° over a volume of $24 \times 22 \times 3$ cm^3 that can encompass the pacemaker

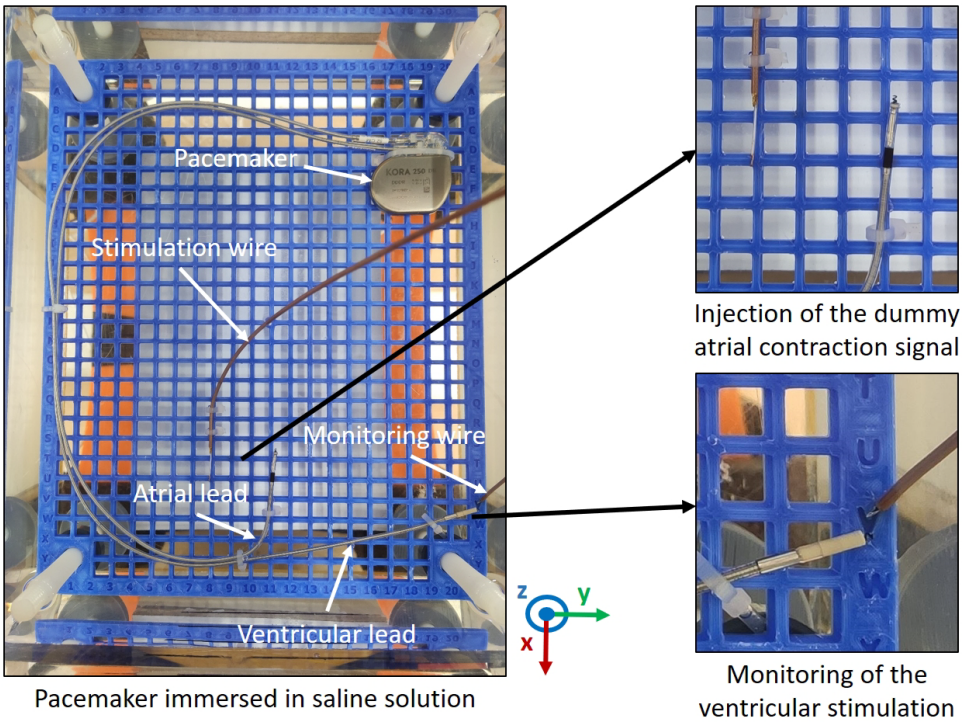

Figure 4. Test setup: monitoring and positioning of the pacemaker inside the phantom.

implantation. A good agreement of the generated magnetic field for a given voltage excitation was observed between the numerical simulation and the experimental measurements, with less than 1% difference.

For more information about the test bench, a related conference paper details its functioning, design and characterisation [17].

To test the implant's behaviour to magnetic field, it is immersed in a saline solution that simulates the electromagnetic properties of the human body. The solution conductivity is around 0.54 S/m, which corresponds to the average conductivity of human blood [18]. The whole system—composed of a plexiglass container with the saline solution, the PM under test and a plastic grid to support it—is placed at the middle of the Helmholtz coils as illustrated in Figure 4. The implant's functioning is monitored during the magnetic field exposure.

Concerning the pacemaker's settings, the tested device is configured in bipolar mode and operates in DDD mode corresponding to the standard setting for a dual-chamber pacemaker, which is the most implanted device configuration in Europe [1]. According to the international nomenclature, these three letters indicate that sensing and stimulation can be carried out on the atrium and on the ventricle, and that the device can either compensate cardiac stimulation irregularities or be inhibited if spontaneous cardiac activity is detected. This configuration permits to test the PM's sensing function as well as its stimulation function. The detection sensitivity is set to the most sensitive case, i.e. the lowest value: 0.1 mV. It corresponds to a worst-case situation. Indeed, the more the detection is sensitive, the more the PM is subject to electromagnetic interference. The PM with its leads is placed inside the container in a position approaching a typical left-sided pectoral implantation, which is the most common implantation (see Figure 3).

Table 2. Unit vectors associated with the 8 considered field directions

Orientation	Coordinates		
	x	y	z
1	0	0	1
2	−0.74	0.59	0.32
3	−0.60	−0.05	−0.80
4	0.88	0.34	0.32
5	−0.70	−0.70	0.16
6	0.45	−0.88	0.16
7	0.14	0.92	−0.35
8	0.55	−0.22	−0.80

In our case, the study focused on the effect of the magnetic field direction, the other parameters are fixed. Eight different directions equi-distributed in space are considered (see Figure 7(a)). The frequency is set to 50 Hz which corresponds to many industrial applications in Europe. The different magnetic field amplitudes applied are between 0 μT and 400 μT with a step size of 10 μT.

The implant monitoring is made with two coaxial wires immersed in the saline solution; the stimulation wire is used to send an ECG signal which simulates the atrial contraction and the monitoring wire is used to detect the ventricular stimulation response generated by the PM (see Figure 4).

In "normal" operating mode, the PM detects the dummy atrial contraction signal and the absence of ventricular contraction, and thus generates a stimulation pulse on the ventricular lead after a pre-programmed delay. During the magnetic field exposure, if a decrease of 50% of the pulse amplitude or a variation of more than 20% on the delay between the atrial contraction and the ventricular stimulation is observed, it is considered as a malfunction [16]. A comparison between a normal operating mode and a malfunctioning situation is presented in Figure 5. The limits considered for proper operation are defined from a reference measurement made without magnetic field (see Figure 6). For each considered magnetic field amplitude, a sequence of 100 cardiac cycles is played at a rate of 60 bpm and the number of malfunctions is recorded. It is then possible to plot the percentage of malfunctions versus the applied magnetic field for each considered direction.

3. Results

The spatial orientations of the eight considered field directions relative to the PM (numbered from 1 to 8) are illustrated in Figure 7(a), the coordinates of the associated unit vectors are given in Table 2. The percentage of malfunction versus the magnetic field amplitude is given for these eight directions in Figure 7(b). In order to better visualise and compare the results in Figure 7(b), the measurements for each direction are fitted by a power function which matches well to the observed trend.

The direction of the magnetic field has a significant impact on the operation of the pacemaker in bipolar mode.

No malfunctioning was observed between 0 and 400 μT for the 6th direction. However it occurs for higher magnetic field amplitudes.

After exposure to the magnetic field, the PM resumes a normal activity. No long-term effect of the magnetic field on the PM is observed. These intermittent malfunctions imply a desynchronisation of the atrial and ventricular contractions which may lead to discomfort. This situation

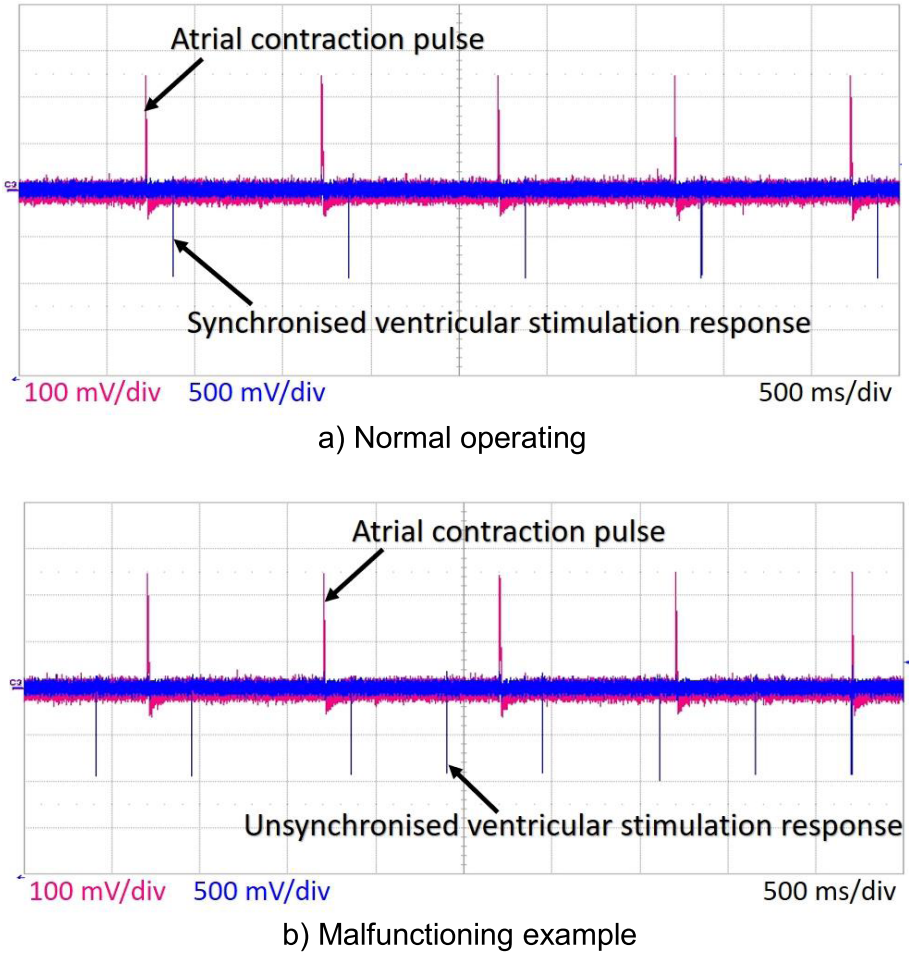

Figure 5. Comparison between a normal operating mode and a malfunctioning situation.

is not suitable especially at workplace—where exposure is repeated and prolonged—and should be avoided. However, this is not life-threatening for the PM holder, except for patients who are entirely PM-dependant.

4. Discussion

The magnetic field direction has an impact on the PM's functioning in bipolar mode. The direction with the highest malfunction rate doesn't correspond to the direction considered as the reference for EMC testing by international standards [14, 15] and the literature [16, 19]. This reference direction corresponds to orientation 1, i.e. the magnetic field perpendicular to the plane formed by the PM and its leads, a situation where a unipolar PM senses the maximum of magnetic flux.

The rational given by international standards and literature, based on an inductive area formed by the electrodes, seems inadequate for a bipolar PM. Indeed for this latter one, the highest malfunction rate doesn't correspond to the highest magnetic flux through an inductive area. Our hypothesis, based on this observation and others, is that the lead in bipolar mode

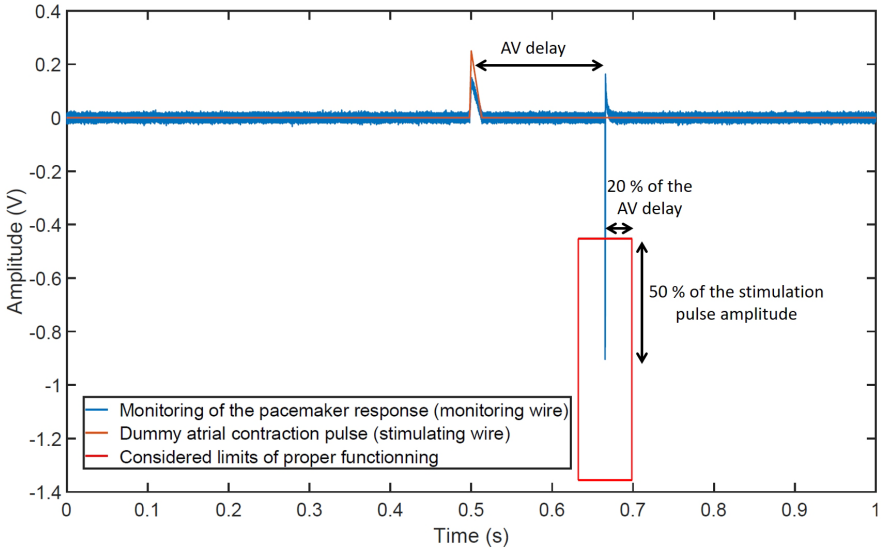

Figure 6. Determination of the proper functioning limits.

is more sensitive to electric field than magnetic field. Indeed, in bipolar mode the induced voltage cannot be derived easily from the evaluation of a magnetic flux through a given surface, but it can be expressed directly as a line integral of the electric field along a path between the two electrodes. In bipolar polarity mode, the lead seems to interact more like a short monopole antenna. In our case, the interfering electric field inside the phantom derives from the time-varying magnetic field (Maxwell–Faraday). Unlike the magnetic field, the electric field distribution over the phantom, obtained by numerical simulation, is inhomogeneous. Indeed, its distribution principally depends on the phantom geometry, the magnetic field direction and the material inside the container, such as the grid or the PM itself. It's therefore relatively complex to accurately predict the electric field distribution over the phantom. However, the fact that the electric field distribution varies according to the magnetic field direction could explain its impact on the PM's functioning.

No long-term effect on the PM is observed, which is in accordance with the requirements of the international standards. However, a relatively high malfunction rate is observed for magnetic field, even below the general public exposure limits. This could be explain by a detection sensitivity of 0.1 mV, which is outside the scope of international standards. It is indeed a key parameter regarding to electromagnetic interference.

5. Conclusion

A new method for assessing the EMC of AIMDs was developed and characterised, then applied to PMs. The first tests showed that the direction of the magnetic field is a relevant parameter for the EMC study of PMs in bipolar mode. Furthermore, the induced voltage cannot be derived easily from the evaluation of a flux through an inductive surface. These observations led us to the hypothesis that the leads in bipolar mode are more sensitive to electric field than magnetic field. This assumption remains to be confirmed by further studies.

The impact of other parameters on the PM's functioning such as the saline solution conductivity, the field frequency or the device positioning is tested using the test bench. A comparative study between different PMs from different manufacturers is also carried out.

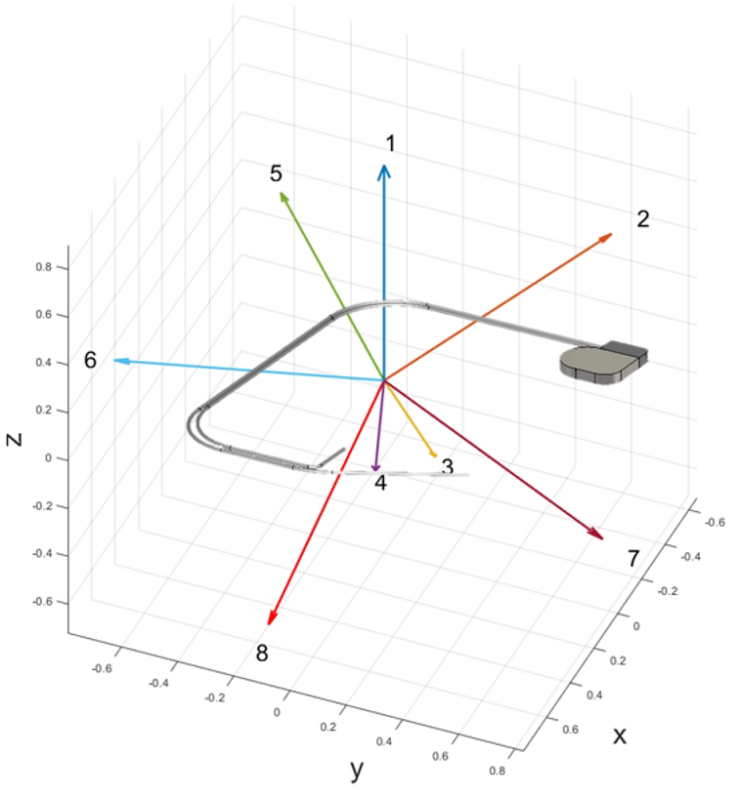

(a)

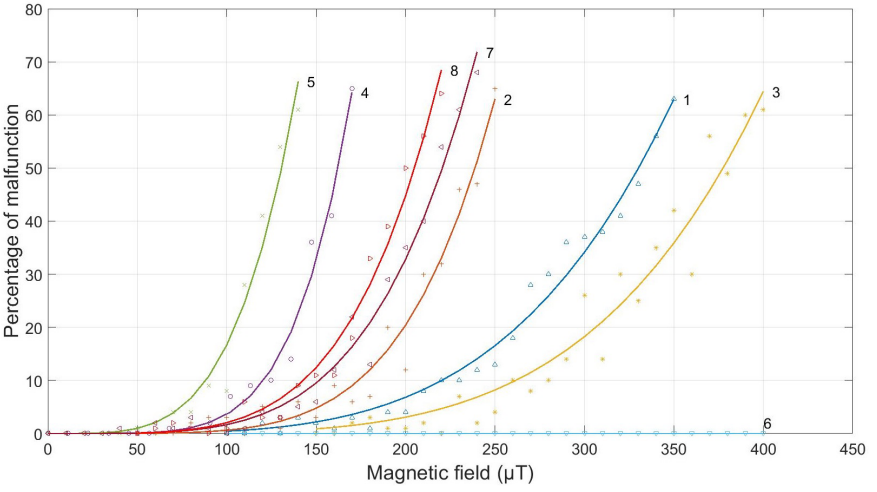

(b)

Figure 7. (a) Visualisation of the unit vectors associated with the 8 considered field directions (the pacemaker and its leads are in the xy-plane). (b) Percentage of malfunction in function of the magnetic field amplitude for the 8 considered field directions when exposed to a 50 Hz sinusoidal magnetic field.

This test method could be applied or adapted to other AIMDs such as implantable cardioverter defibrillators or neurostimulators.

Declaration of interests

The authors do not work for, advise, own shares in, or receive funds from any organization that could benefit from this article, and have declared no affiliations other than their research organizations.

Acknowledgement

The authors would like to thank Dr. Mathieu Echivard, cardiologist from the CHRU of Nancy (F), for his valuable help.

References

[1] H. G. Mond, A. Proclemer, "The 11th world survey of cardiac pacing and implantable cardioverter-defibrillators: calendar year 2009-a world society of Arrhythmia's project: 2009 SURVEY CARDIAC PACEMAKERS AND ICDS", *Pacing Clin. Electrophysiol.* **34** (2011), no. 8, p. 1013-1027.

[2] M. J. P. Raatikainen, D. O. Arnar, K. Zeppenfeld, J. L. Merino, K.-H. Kuck, G. Hindricks, "Current trends in the use of cardiac implantable electronic devices and interventional electrophysiological procedures in the European Society of Cardiology member countries: 2015 report from the European Heart Rhythm Association", *Europace* **17** (2015), no. suppl 4, p. iv1-iv72.

[3] I. Tandogan *et al.*, "The effects of mobile phones on pacemaker function", *Int. J. Cardiol.* **103** (2005), no. 1, p. 51-58.

[4] Y. Endo, K. Saito, S. Watanabe, M. Takahashi, K. Ito, "Study of interference voltage of an implanted pacemaker by mobile terminals", *IEEE Trans. Electromagn. Compat.* **58** (2016), no. 1, p. 30-39.

[5] W. Irnich, A. D. Bernstein, "Do induction cooktops interfere with cardiac pacemakers?", *EP Eur.* **8** (2006), no. 5, p. 377-384.

[6] M. Zhou *et al.*, "Interference thresholds for active implantable cardiovascular devices in occupational low-frequency electric and magnetic fields: a numerical and in vitro study", *Med. Eng. Phys.* **104** (2022), article no. 103799.

[7] E. Mattei, G. Calcagnini, F. Censi, I. Pinto, A. Bogi, R. Falsaperla, "Workers with active implantable medical devices exposed to EMF: in vitro test for the risk assessment", *Environments* **6** (2019), no. 11, article no. 119.

[8] P. Zradziński, J. Karpowicz, K. Gryz, W. Leszko, "Evaluation of the safety of users of active implantable medical devices (AIMD)in the working environment in terms of exposure to electromagnetic fields—practical approach to the requirements of European Directive 2013/35/EU", *Int. J. Occup. Med. Environ. Health* **31** (2018), no. 6, p. 795-808.

[9] M. Tiikkaja *et al.*, "Electromagnetic interference with cardiac pacemakers and implantable cardioverter-defibrillators from low-frequency electromagnetic fields in vivo", *EP Eur.* **15** (2013), no. 3, p. 388-394.

[10] M. Tiikkaja, T. Alanko, H. Lindholm, M. Hietanen, J. Hartikainen, L. Toivonen, "Experimental study on malfunction of pacemakers due to exposure to different external magnetic fields", *J. Interv. Card. Electrophysiol.* **34** (2012), no. 1, p. 19-27.

[11] The European Parliament and the Council of the European Union, Directive 2013/35/EU of the European Parliament and of the Council of 26 June 2013 on the minimum health and safety requirements regarding the exposure of workers to the risks arising from physical agents (electromagnetic fields) (20th individual Directive within the meaning of Article 16(1 of Directive 89/391/EEC) and repealing Directive 2004/40/EC, Official Journal of the European Union L 179, 29.6.13, p. 1.

[12] P. O. of the E. Union, "Recommendation of 12 July 1999 on the limitation of exposure of the general public to electromagnetic fields (0 Hz to 300 GHz)", 1999, Publications Office of the European Union.

[13] NF EN 50527-1, "Procedure for the assessment of the exposure to electromagnetic fields of workers bearing active implantable medical devices - Part 1 : general", February 2017, AFNOR.

[14] ISO 14117:2019, "Active implantable medical devices—Electromagnetic compatibility—EMC test protocols for implantable cardiac pacemakers, implantable cardioverter defibrillators and cardiac resynchronization devices", January 2019.

[15] NF EN 45502-2-1, "Active implantable medical devices Part 2-1: Particular requirements for active implantable medical devices intended to treat bradyarrhythmia (cardiac pacemakers)", May 2004, AFNOR.

[16] V. Buzduga, D. M. Witters, J. P. Casamento, W. Kainz, "Testing the immunity of active implantable medical devices to CW magnetic fields up to 1 MHz by an immersion method", *IEEE Trans. Biomed. Eng.* **54** (2007), no. 9, p. 1679-1686.

[17] L. Hammen, L. Pichon, Y. Le Bihan, M. Bensetti, G. Fleury, "Testing immunity of active implantable medical devices to industrial magnetic field environments", in *International Symposium and Exhibition on Electromagnetic Compatibility - EMC Europe, Göteborg, Sweden*, 2022.

[18] N. Ištuk, A. L. Gioia, H. Benchakroun, D. O'Loughlin, A. Lowery, M. O'Halloran, "Measurement of electrical conductivity of human blood at frequencies below 100 kHz with four-electrode probe method", in *021 XXXIVth General Assembly and Scientific Symposium of the International Union of Radio Science (URSI GASS), Rome, Italy*, 2021, p. 1-4.

[19] A. Augello, G. D. Chiara, V. M. Primiani, F. Moglie, "Immunity tests of implantable cardiac pacemaker against CW and pulsed ELF fields: experimental and numerical results", *IEEE Trans. Electromagn. Compat.* **48** (2006), no. 3, p. 502-515.

ACADÉMIE DES SCIENCES
INSTITUT DE FRANCE

Comptes Rendus. Physique
2024, Vol. 25, Special issue S1, p. 87-108
https://doi.org/10.5802/crphys.189

Research article / *Article de recherche*

Energy in the heart of EM waves: modelling, measurements and management / *L'énergie au cœur des ondes électromagnétiques : modélisation, mesures et gestion*

3D Computation of Lightning Leader Stepped Propagation Inside a Realistic Cloud

Calcul en 3D de la propagation par étape d'un éclair à l'intérieur d'un nuage réaliste

Philippe Dessante [a, b]

[a] Université Paris-Saclay, CentraleSupélec, CNRS, Laboratoire de Génie Electrique et Electronique de Paris, 91192, Gif-sur-Yvette, France

[b] Sorbonne Université, CNRS, Laboratoire de Génie Electrique et Electronique de Paris, 75252, Paris, France

Abstract. The simulation of lightning propagation is a complex problem studied for years. Here we propose to use the information from the electric potential created from a real cloud structure to study the propagation. The electric potential and field are calculated using a realistic thundercloud structure: the typical three layers cloud structure is constructed using a real cloud photograph. The different altitudes and separations of each layer are calculated from the luminosity of the picture and the space charge values are taken from data in the literature. A model of stepped leader propagation is proposed. It consists in finding by steps the path which maximises the potential difference taking into account the cloud and leader space charge. After each step, the electric potential is recalculated, and a new iteration gives a new direction. This framework permits us to analyse diverse cloud configurations. Only positive leaders from the base layer can reach the ground if the three layers are complete. Only negative lightning reaches the ground when the bottom positive layer is reduced (typical of the middle of a storm). Finally, when the two bottom layers are reduced in size (typical of the storm's end), positive lightning from the upper positive layer can make its way into the cloud toward the ground. These simulated observations agree with the hypotheses made previously by Nag and Rakov.

Résumé. La simulation de la propagation de la foudre est un problème complexe étudié depuis plusieurs années. Nous proposons ici d'utiliser les informations du potentiel électrique créé à partir d'une structure de nuage afin d'étudier la propagation. Le potentiel électrique et le champ sont calculés en utilisant une structure de nuage d'orage réaliste : la structure de nuage typique à trois couches est construite à partir d'une photographie de nuage réel. Le modèle de propagation consiste à trouver par étapes le chemin qui maximise la différence de potentiel en tenant compte de la charge spatiale du nuage et du leader. Ce cadre nous permet d'analyser diverses configurations de nuages qui sont présentées dans cet article.

Keywords. lightning, electrical discharge, simulation, modelling, lightning propagation, electric field, cloud.

Mots-clés. foudre, décharge électrique, simulation, modélisation, propagation de la foudre, champ électrique, nuage.

Note. This article follows the URSI-France workshop held on 21 and 22 March 2023 at Paris-Saclay.

Manuscript received 12 June 2023, revised 21 March 2024, accepted 21 May 2024.

1. Introduction

Lightning is a research domain that has largely been studied for years. As the reproduction in the laboratory of lightning phenomena are difficult [1–3], more and more studies use computer modelling and simulation to understand the propagation of leaders in clouds or toward the ground and structures [4]. They use a mix of macro modelling [5–8] and heuristic like fractals [9, 10] to simulate the stepped leader formation and propagation.

In this article, we use a macro model and a heuristic based on the electric potential's maximisation to find a leader's direction. This type of model has already been used in the article by Lalande et al. [11], but with a cylindrical cloud structure. Here we use the same type of cloud structure (3 layers cloud) but based on a real cloud space charge repartition.

This research article aims to verify the different hypotheses made by the authors in [12, 13]. They try to explain, based on theoretical study and measurement, the different possibilities for the leader propagation toward the ground (cloud to ground or CTG) or in the cloud (intra-cloud: cloud to cloud CTC) based on their polarity and the cloud structure.

A typical cloud charge structure is based on three different layers: on top of the cloud, a positive charge; in the middle, a negative charge; and at the bottom a limited positive charge [14]. Several simulations have been made based on heuristic rules for leader propagation [7, 15, 16], but to our knowledge, none take into account a realistic cloud.

The different cloud layers may impact the propagation of the leader as proposed by Nag and Rakov [2, 12, 13]: the positive base layer can, in one part, accelerate the development of cloud-to-ground lightning, but it can also shield the bottom part of the cloud from upper lightning, favouring the development of cloud-to-cloud lightning, depending on the origin point of the leader's inception.

This research uses three kinds of cloud structures: a full three layers cloud structure, a reduced base layer, and then the two bottom layers reduced. These structures can mimic the accurate distribution of electrical charges at different storm moments.

This space charge repartition is used to calculate an electrical potential distribution above the ground. A leader propagation modelling is then proposed: The leader propagates in the direction of the maximum difference in terms of electrical potential. Different altitudes for the leader inception are tested. The simulations tend to validate the hypothesis that positive cloud-to-ground lightning comes from the base layer. This positive base layer form also a shield for the negative lightning which tends to be intracloud. Negative lightning must benefit from weaknesses or holes in the positive base layer to propagate toward the ground.

A definition of the cloud model will be presented in Section 2, and then the stepped leader macro-model will be introduced in Section 3. Section 4 will explain how we compute the electric potential of the cloud and the leader. The results will be shown in Section 5, and a conclusion and perspective will close this paper.

2. Cloud Model

We will start from a real cloud to better model the structure. Figure 1 shows photography of thunderstorm clouds above Paris. We will use the information in this photograph to construct the geometrical structure of the cloud. The photography is cropped to take only the cloud part (Figure 2a). The resulting image is then converted into black and white, and smoothing based on a Gaussian filter is applied (Figure 2b).

The image luminosity is then analysed, and its level is stored in a two dimension array. These levels are converted into altitude (more light means less altitude) to form the cloud base layer (Figure 2c).

Figure 1. Photography of thunderclouds over Paris (Ph. Dessante)

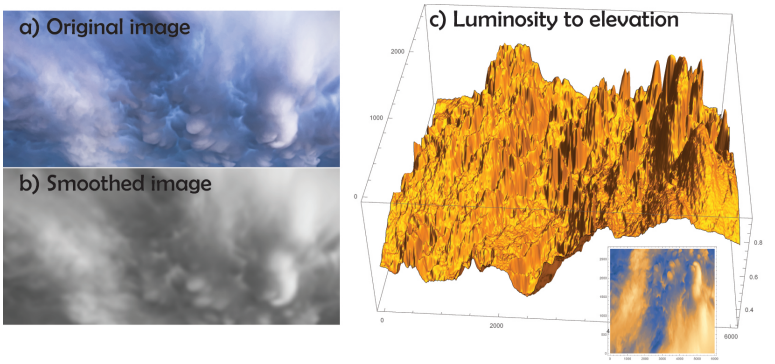

Figure 2. Photography of thunderclouds over Paris (Ph. Dessante) (a), black and white and smoothed version (b), elevation calculation based on luminosity (c).

A typical cloud structure [14] is based on three different layers: on top of the cloud a large positive charge, in the middle a negative charge, and at the bottom a limited positive charge. In previous studies, [11], clouds are in general modelled in 3D by cylindrical zones like in Figure 3.

The generated altitude map is repeated at each charge separation altitude: see Figure 4, where the colour represents the sign of the space charge (red for positive and blue for negative charge). The different altitude are taken in the literature [11, 14]. For the longitudinal and lateral dimension of the cloud, the dimensions are arbitrarily chosen based on the picture but also to have a sufficiently large space dimension for the leader propagation.

Based on the literature [11, 14], we have taken a positive space charge density of $c_1 = 0.21 \times 10^{-9}$ C/m^3 for the positive bottom layer, a negative space charge density of $c_2 = -0.18 \times 10^{-9}$ C/m^3 in the middle layer and a positive space charge density of $c3 = 1.3 \times 10^{-9}$ C/m^3 for the upper layer.

When calculating the electric potential using the finite element method, it is advisable to prevent discontinuities between the layers of the cloud. Utilising a Gaussian distribution is

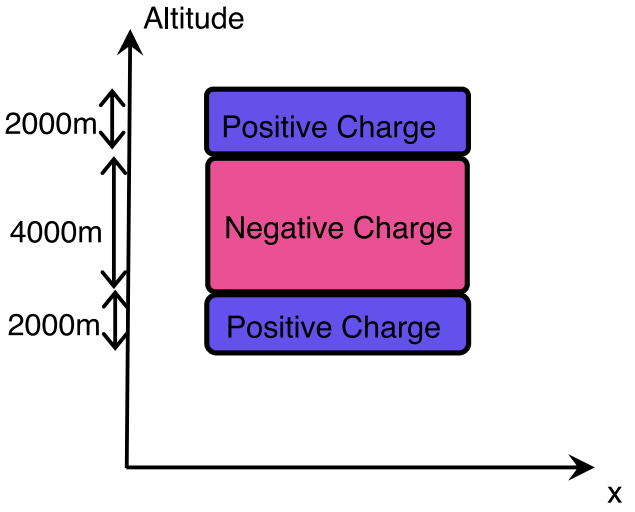

Figure 3. Typical cloud structure [11, 14], in blue the positive upper and bottom layers, in red the middle negative layer.

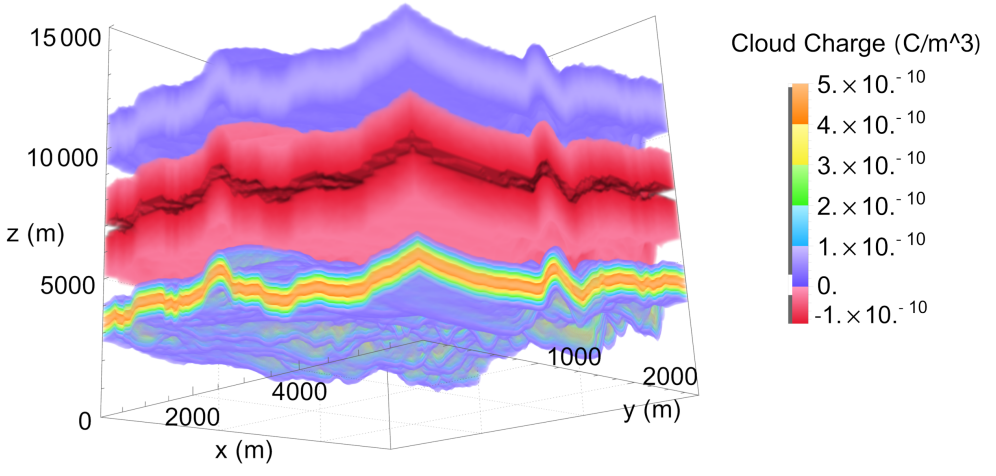

Figure 4. *Cloud structure modelling: red negative space charge, blue to orange positive space charge.*

one straightforward approach to achieving this; however, an error function (erf) or hyperbolic tangent (tanh) function could have also been used for the transition. Nevertheless, owing to the difficulty in measuring experimentally this transition, it cannot be definitively determined which

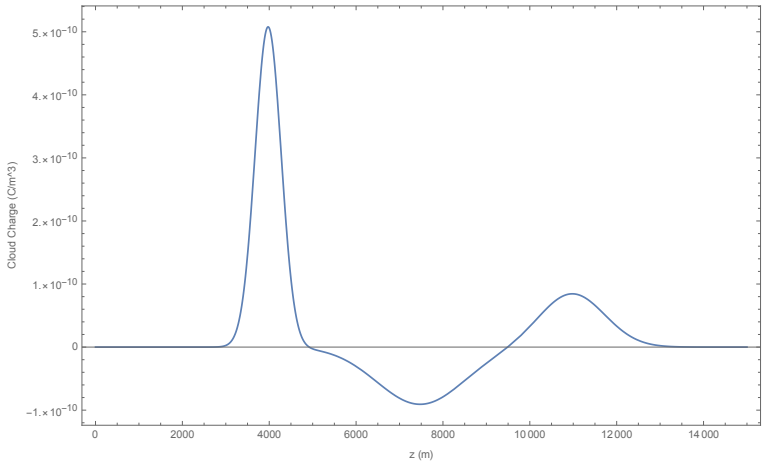

Figure 5. Space Charge along the line in the middle of the cloud between the ground ($z = 0$) and the upper part of the cloud.

option is most effective. Future studies may benefit from exploring various transition types and implementing different ones in distinct parts of the cloud, potentially to examine layer-specific properties.

The cloud space charge density vertical distribution is represented in Figure 5, the separation into three different layers is done by smoothing the transitions by three different Gaussian distributions:

$$\begin{aligned}\rho(x,y,z) = &\frac{c_1}{\sqrt{2\pi}} \times \exp\left[\frac{-(z-m_1(x,y))^2}{2\sigma_1^2}\right] \\ &+\frac{c_2}{\sqrt{2\pi}} \times \exp\left[\frac{-(z-m_2(x,y))^2}{2\sigma_2^2}\right] \\ &+\frac{c_3}{\sqrt{2\pi}} \times \exp\left[\frac{-(z-m_3(x,y))^2}{2\sigma_3^2}\right]\end{aligned} \tag{1}$$

where $\sigma_{1,2,3}$ are respectively the standard deviation of each Gaussian's (300m, 2000m and 750m), they are chosen arbitrarily to ensure a smooth transition between the positive and negative layers. $m_{1,2,3}$ are the middle of each cloud layers (4000m, 7500m and 11000m).

3. Stepped Leader Propagation Model

A start point X_0 for the leader propagation is chosen in the cloud. For each iteration n of the propagation, we first find with the help of a deterministic gradient optimisation algorithm the maximal potential difference in a sphere of $r_c = 50m$ radius around the leader's head. For this search radius the leader step should be less than 50m, which is consistent with the literature review in [17]. In the case of a positive leader, this leads to the problem:

$$\begin{aligned}\underset{X}{\text{maximize}} \quad & V(X_n) - V(X) \\ \text{subject to} \quad & |X - X_n| < r_c\end{aligned} \tag{2}$$

and in the case of a negative leader to the optimisation problem:

$$\begin{aligned}\underset{X}{\text{maximize}} \quad & V(X) - V(X_n) \\ \text{subject to} \quad & |X - X_n| < r_c\end{aligned} \tag{3}$$

These two formulations can be reformulated respectively as:

$$\begin{array}{ll} \underset{X}{\text{minimize}} & V(X) \\ \text{subject to} & |X - X_n| < r_c \end{array} \tag{4}$$

and:

$$\begin{array}{ll} \underset{X}{\text{maximize}} & V(X) \\ \text{subject to} & |X - X_n| < r_c \end{array} \tag{5}$$

To represent the stochastic behaviour of the leader propagation, a random point is chosen around this maximum (in a sphere of 10m radius) which becomes the new leader's head. The leader is propagated with a constant radius $r_l = 5m$ and a space charge density equals to $50 \times 10^{-6}/(\pi r_l^2)$ C/m^3 if the leader originates from a positive region and $-150 \times 10^{-6}/(\pi r_l^2)$ if it originates from a negative region [11, 18]. With $r_l = 5$m the radius of the leader is somewhat overestimated due to mathematical constraints for the Poisson equation (8) resolution). This process is illustrated in Figure 6 for a negative leader in a two dimensions case for better clarity. The blue spheres represent the area where the optimisation is conducted (constraint $|X - X_n| < r_c$). The centre of the red sphere is the optimum found by equations (4) or (5), and the red spheres represent the area where the new point X_{n+1} is chosen randomly. The grey segments are two stepped leader iterations.

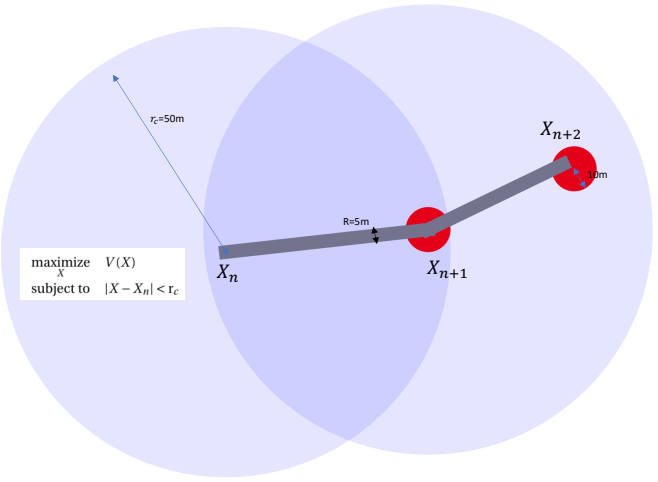

Figure 6. Two iterations of a negative leader propagation.The blue spheres represent the area where the optimisation is conducted (constraint $|X - X_n| < r_c$). The centre of the red sphere is the optimum found by equations (4) or (5), and the red sphere represents the area where the new point X_{n+1} is chosen randomly.The grey segments are two stepped leader iterations.

The potential is then finally recalculated by the equation (8) taking into account the new space charge and a new refined mesh.

4. Electric potential evaluation

The formation and propagation of lightning are mainly due to electrostatic phenomena [14], that are caused by the electric field. To compute the electric field E, one needs to solve the Poisson equation:

$$\nabla \vec{E} = \frac{\rho}{\varepsilon_0} \tag{6}$$

where ρ is the space charge, and ε_0 is the dielectric constant in vacuum.
With the introduction of the potential distribution V:

$$\vec{E} = -\nabla V \tag{7}$$

The Poisson equation can be writen as:

$$\Delta V(x,y,z) = -\frac{\rho(x,y,z)}{\varepsilon_0} \tag{8}$$

The boundary conditions are defined by a Dirichlet condition on the earth's surface:

$$V(x,y,0) = 0 \tag{9}$$

and Neumann conditions on the others borders $\partial\Omega$:

$$\left.\frac{\partial V}{\partial n}\right|_{\partial\Omega} = 0 \tag{10}$$

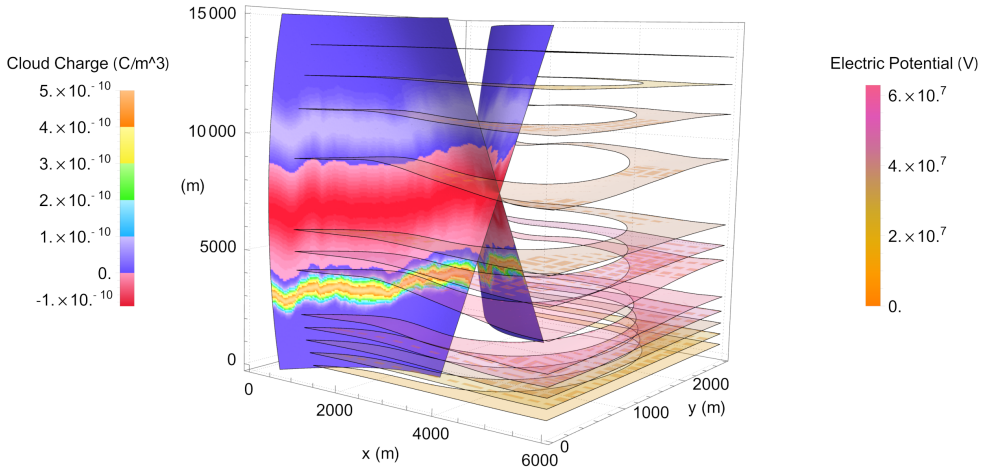

Figure 7. *Electric Potential (iso planes), space charge (left plotted on a surface) for a full 3 layers cloud structure.*

We use a finite elements method (FEM) with the help of the Wolfram Mathematica software to solve the Poisson equation in three dimensions. FEM are often utilised to calculate electric fields when the geometry or the excitation (here the space charge) are non rectangular. This method discretises the space into a partition called the mesh. This mesh must be fine enough to be able to represent the small space charge variation inside the cloud but also in the leader. In order to solve the Poisson equation with the cloud space charge, a uniform tetrahedral mesh is used; we impose the maximum size of each mesh vertex to be 100m. The total number of hexahedron elements is 724 200, and the total number of degrees of freedom (DOF) is 2 987 552 for an order 2 formulation.

The calculation time of such a resolution is about 30 minutes on a 28 cores computer and 128Gb of memory with Mathematica (a maximum of 16 cores are used).

The leader is symbolised by a 3D cylindrical shape with spherical endpoints, and its entire volume is populated with either positive or negative space charge depending on its origin point. Neglecting the discrepancy in charge density between the leader's head and body is a deliberate choice since the leader advances in large step (50m). Incorporating the difference of space charge exclusively during the recalculation of electric potential lacks realism, as the simulation does not account for it throughout the propagation phase.

One feasible solution to enhance realism in the simulation could be diminishing the step size for each leader stride. This modification might enable a more accurate representation of space charge differences during the leader's propagation but at the expense of computation time (the mesh needed for representing the space charge should be largely refined).

When the leader propagates, it deposes a certain number of space charges along its passage. The leader radius is 5m, and it is necessary to have a minimum of two mesh elements inside the leader channel, leading to a finer mesh. It is not possible to use a uniform mesh anymore, but it is possible to refine the mesh around the leader's shape. The superposition of this super fine mesh and the cloud mesh induces a mesh of 12 452 745 elements and 16 541 562 DOF for one step of the leader's propagation, which tends to be largely challenging to solve on a desktop computer. This computation must be realised at each leader propagation step; it leads to long and unpractical computing time. When the leader has several steps, the memory necessary to solve the Poisson problem exceeds the 128Gb available.

That is why we have used the superposition principle to solve the potential calculation. We separate the cloud space charge and each leader step (each grey segment in the Figure 6). The electrical potential distribution V_0 due to the cloud space charge is firstly calculated on the 100m fine mesh. Then at each step, the electrical potential V_i due to the sole leader step i (only the space charge of the last grey segment in the Figure 6) is calculated.

This could be done on a fine mesh around the leader tip and a broad mesh outside a circle twice the size of the leader step. The superposition principle gives the total electrical potential V_n for the leader propagation at iteration n:

$$V_n = \sum_{i=0}^{n} V(i) \tag{11}$$

This method helps us to only use a finer mesh around the leader step (mesh size of 2m in a distance of 100m around the leader) and a broad mesh (maximum of 1000m size) elsewhere. Tests have been realised to verify the effectiveness of this technic.

The electric potential V_0 due to the cloud space charge is given in the Figure 7, the resulting electric field is shown in Figure 8 and the Figure 9 gives a representation of the electric field (arrows and line plot), the electric potential as surface levels and the cloud space charge as a truncated volume (on the figure's left).

5. Results

5.1. *Three layers cloud*

Before presenting the results, we give a flowchart of the complete simulation procedure in Figure 10. Firstly the cloud structure is defined from a picture and a complete space charge model is computed. The electric potential due to this space charge is then calculated. The inception altitude is chosen, defining if it's a positive or negative leader. After that the simulation enter its main loop where the next leader step is found as the optimum location of equation (4) or (5).

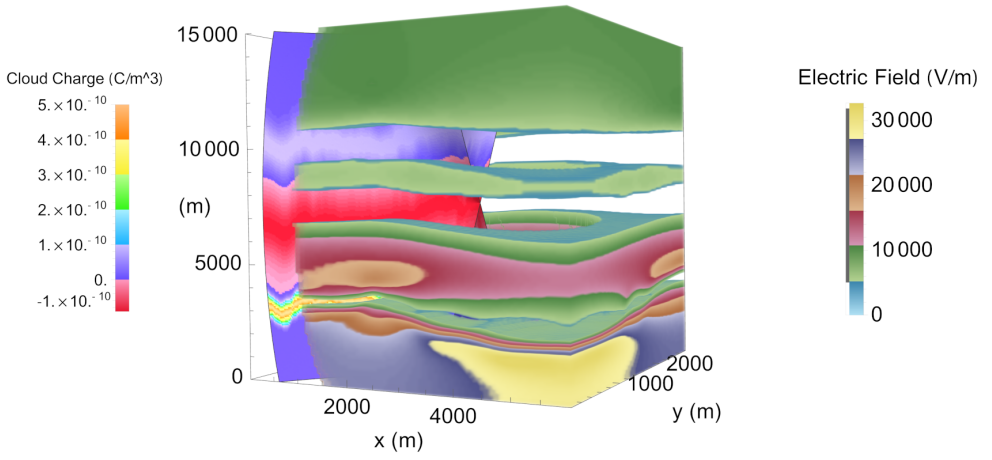

Figure 8. *Electric Field (volume) and space charge on the cut surface for a full 3 layers cloud structure.*

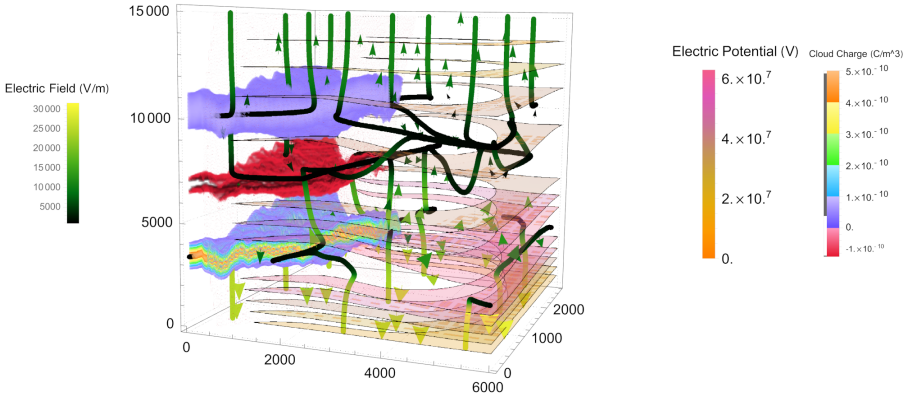

Figure 9. *Electric Field (vector and line plot), Electric Potential (surface levels), space charge (volume on left) for a full 3 layers cloud structure.*

The leader deposes a space charge, and the electric potential $V(i)$ induced by this leader step is computed. The loop closes after the summation of all the electric potential (leader steps and cloud) or terminates if the leader reaches a border.

The first set of results is presented in figure 11. The whole cloud structure in three complete layers is taken into account. Ten starting points are considered, they take inception in the middle of the cloud in lateral and longitudinal coordinates and altitudes from 3000m to 12000m above

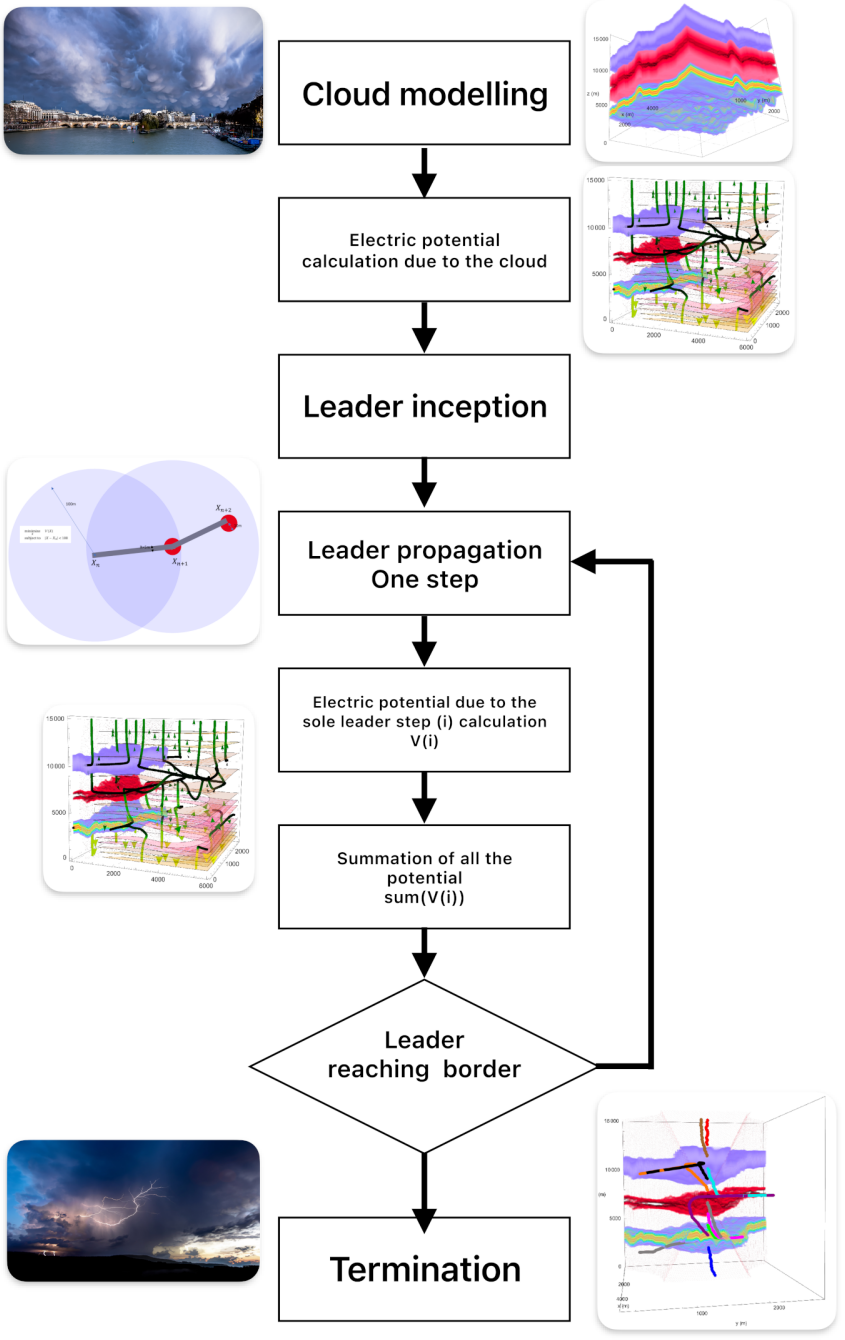

Figure 10. *Flow chart of the complete simulation.*

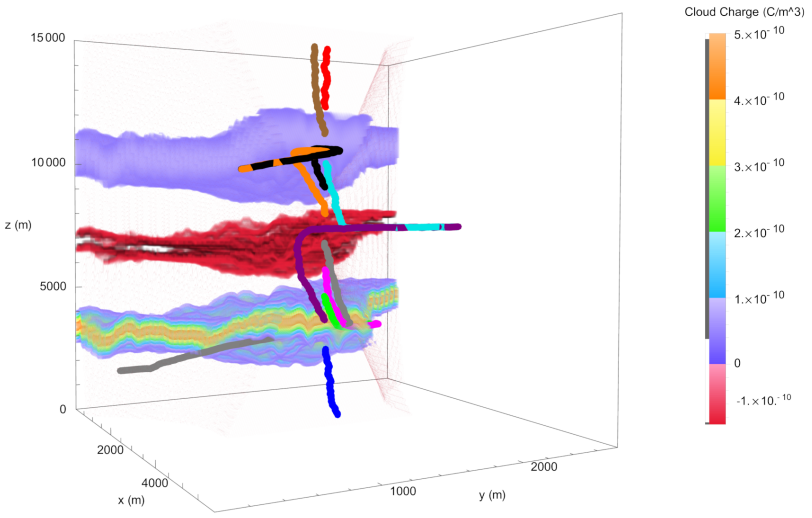

Figure 11. *Propagation of lightning in a full cloud structure, see Table 1 for initialisation data, volume on back: cloud space charge.*

Table 1. Initial conditions and results for the three layers cloud structure.

Alitude (m)	Color	Charge	Direction	Type
3000	Blue	+	↓	CTG
4000	Purple	+	↑	CTC
5000	Green	-	↓	CTC
6000	Magenta	-	↓	CTC
7000	Gray	-	↓	CTC
8000	Orange	-	↑	CTC
9000	Black	-	↑	CTC
10000	Cyan	+	↓	CTC
11000	Brown	+	↑	CTC
12000	Red	+	↑	CTC

the ground level with 1000m steps. The results are summarised in the Table 1, which indicates the inception altitude, the colour of the leaders in Figure 11, the leader's initial charge, the general upward or downward direction, and if they are cloud-to-ground (CTG) or cloud-to-cloud (CTC) leaders.

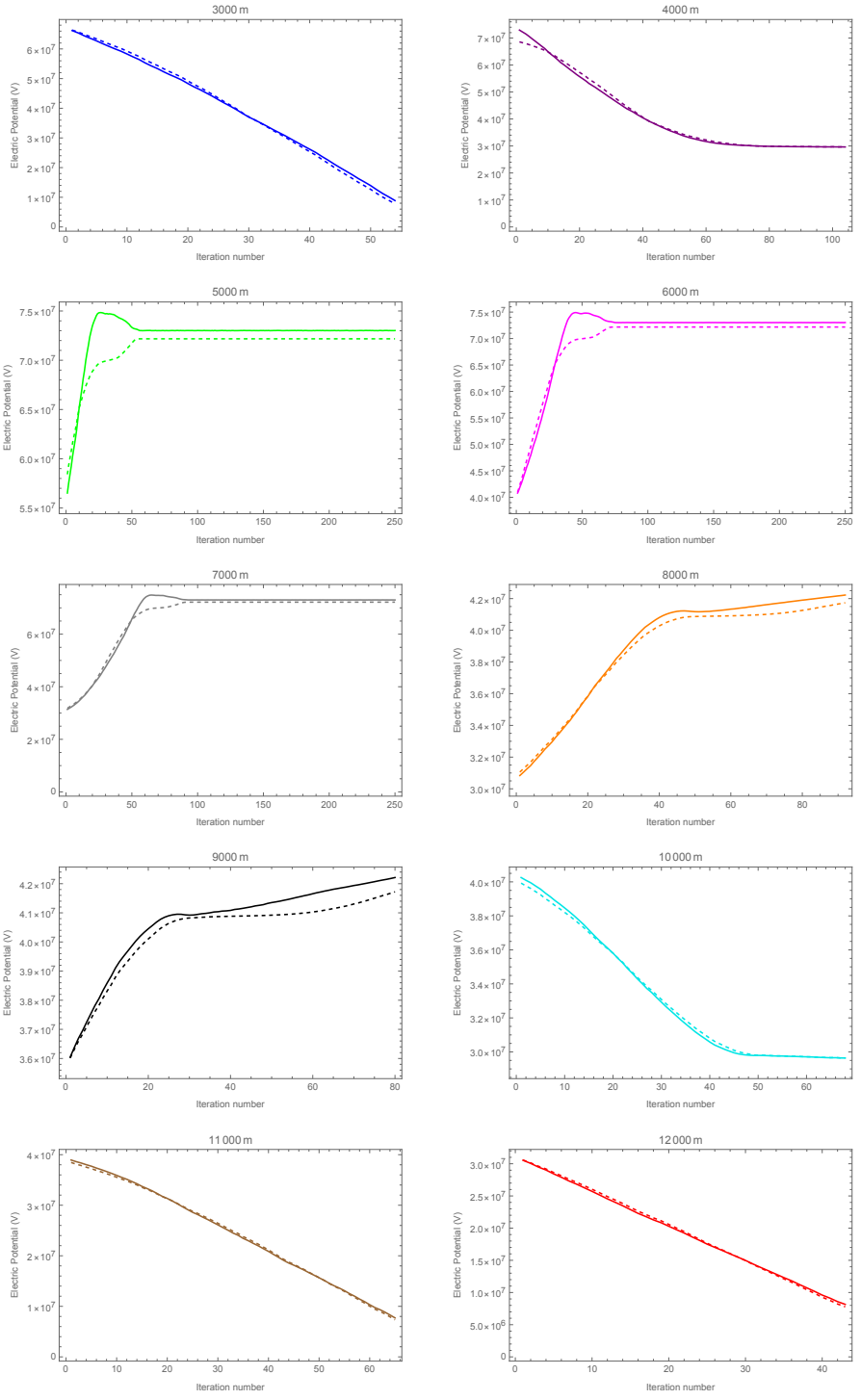

Figure 12. Value of the Electric Potential in front of the leader for the different inception altitudes. Plain: electric potential due to the cloud, Dashed: electric potential induced by the cloud space charge and the leader charge deposition.

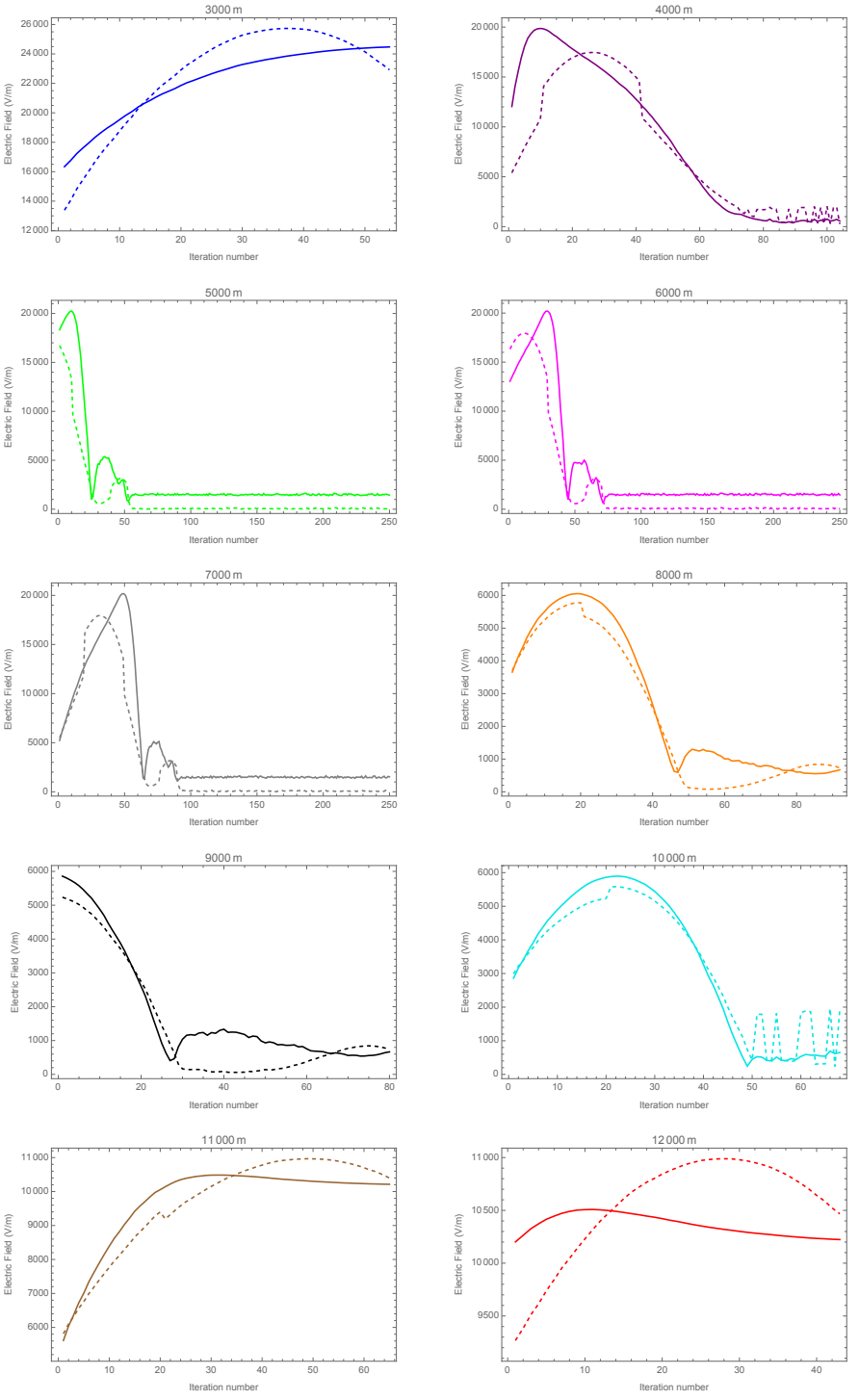

Figure 13. Value of the Electric Field norm in front of the leader for the different inception altitudes. Plain: electric field due to the cloud, Dashed: electric field induced by the cloud space charge and the leader charge deposition.

The only leader who connects to the ground is the positive one coming from the bottom part of the base positive layer (inception at 3000m in blue). The negative leaders from the negative middle part of the cloud (between 5000m to 9000m) are trapped between the two (bottom and top) positive layers. They reach the separation altitude (either up or down) between the layers and then cannot propagate vertically anymore. These negative leaders cannot reach the ground, which is blinded and *protected* from the bottom positive layer as shown theoretically by Nag and Rakov [12].

One must note that no positive lightning coming from the upper part of the ground (inception from 10000m to 12000m) can reach the ground, the middle negative leader forms a shield toward the ground and stops the leaders to descend further.

The electric potential variation at the leader's front is shown in Figure 12 as a function of the step number. Positive leaders tend to follow decreasing potential values, and negative leaders tend to follow increasing potential values. One must note that taking into account the leader space charge (dashed curves in the figure) seems to be relatively important for intra-cloud lightning (inception points of 5000m to 10000m). There is an increase in the electric potential difference between the two cases when the leader reaches the layer separation as can be seen in Figure 11.

The electric field variation at the leader's front is shown in Figure 13 as a function of the step number. One must note that the value of the electric field in front of the leader should be treated with care and used in qualitative terms only. The radius of the leader is too high (5m) to have a good estimation of the electric field induced by the leader space charge, even if the charge density is correct; the leader's shape in our calculation is too smooth. Another caution must be taken as we use a finite elements scheme to solve the Poisson equation: even if we have taken elements of order two, the electric field derivates from the electric potential, and a loss in precision is always present.

The general pattern of the electric field variation during the leader propagation is an increase in value followed by a decrease. When a leader connects to an opposite part of the cloud they would normally extinct themselves, this is correlated with the decreasing value of the electric field norm largely under their starting values. For further simulations, this could be implemented as a stopping condition in addition to the leader reaching one of the domain borders.

This is not true for the leader connecting to the ground (3000m) or the upper part of the simulation domain (11000m and 12000m) because the external electric field is almost constant in these areas and because the simulation stops when a leader reaches a border.

These results are reproducible with some variations on several runs.

5.2. *Two full layers cloud, reduced bottom layer*

To verify the hypothesis of Nag and Rakov [12, 13] in their articles, we have reduced the positive base layer around the middle of the cloud. The new cloud space charge is shown in Figure 14. One must note that as for the original cloud model, the transition to either neutral space charge or to other layers is smoothed by Gaussian functions to ensure a proper FEM resolution.

The new 3D potential (iso-potential surfaces) of the cloud space charge is shown in Figure 15 along the electric field (arrows and streamlines). The same inception conditions as in the previous section are taken as shown in Table 2.

The leader's propagations are shown in Figure 16. This time the negative pink leader coming from the inception point at 6000m inside the negative layer can turn around the reduced base layer and reach the ground. This simulation validates the theoretical hypothesis of Nag and Rakov [12] and shows that negative lightning must profit some weaknesses or holes in the base positive layer to propagate towards the ground.

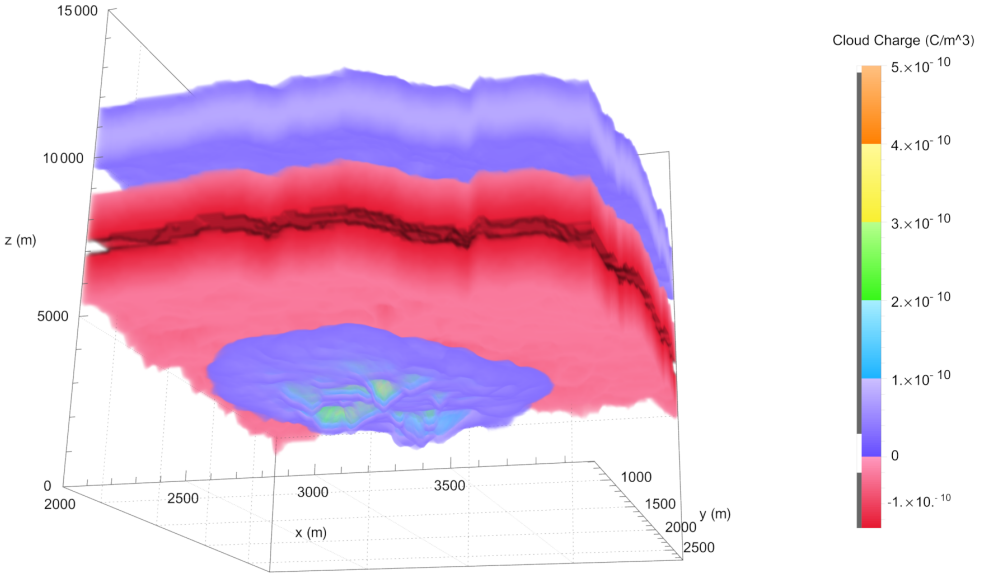

Figure 14. Cloud structure and space charge for a reduced bottom layer.

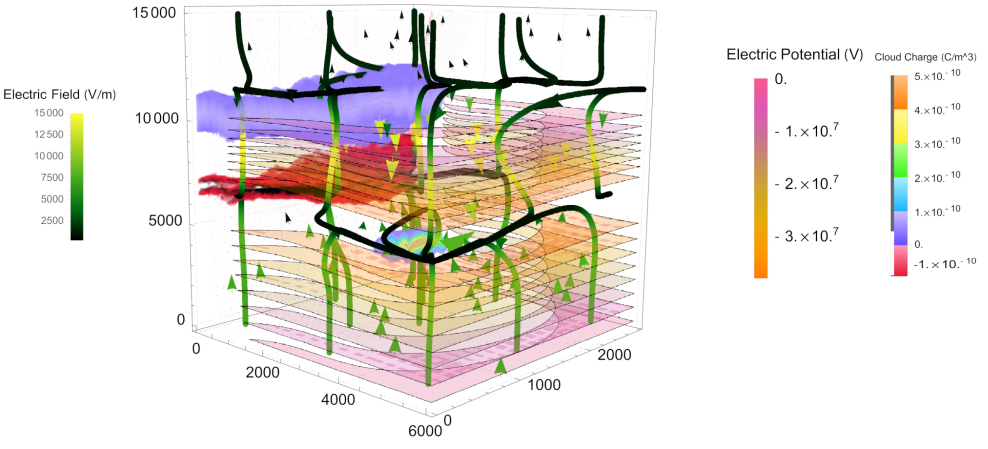

Figure 15. Electric Field (vector and line plot), Electric Potential (surface levels), space charge (volume on left) for a reduced bottom layer cloud structure.

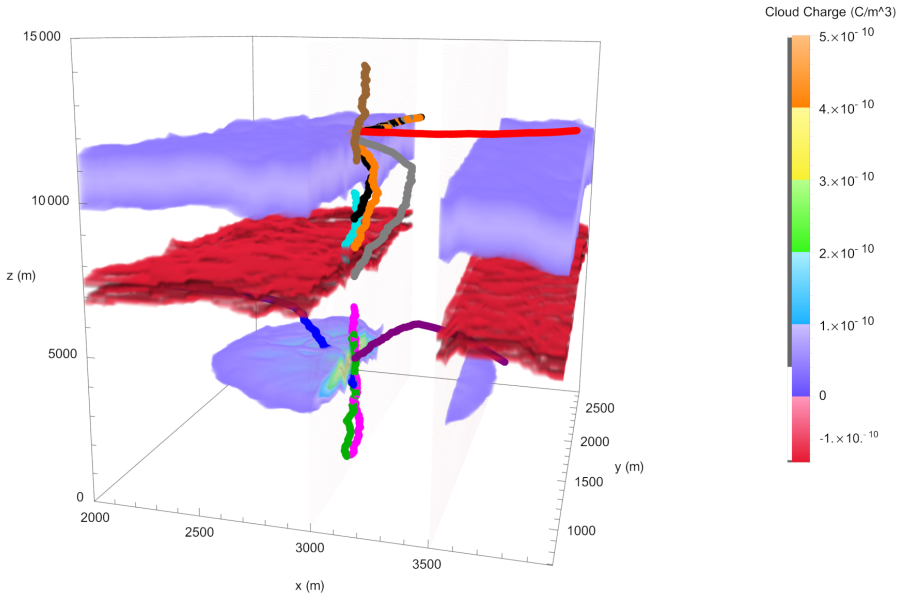

Figure 16. Propagation of lightning in a reduced bottom layer cloud structure, see Table 2 for initialisation data, volume: cloud space charge (cut for clarity.

Table 2. Initial conditions and results for the two layers cloud structure.

Alitude (m)	Color	Charge	Direction	Type
3000	Blue	+	↑	CTC
4000	Purple	+	↑	CTC
5000	Green	-	↓	CTG
6000	Magenta	-	↓	CTG
7000	Gray	-	↑	CTC
8000	Orange	-	↑	CTC
9000	Black	-	↑	CTC
10000	Cyan	+	↓	CTC
11000	Brown	+	↑	CTC
12000	Red	+	↑	CTC

In this configuration, the positive leaders coming from the base layer are attracted to the middle negative layer, and none of them can reach the ground. This is also the case for the upper part of the clouds, as in the previous simulation.

During normal storms, the vast majority of lightning strikes reaching the ground are negative. The common model of the cloud space charge also agrees with this type of repartition [14], where the positive bottom layer is largely reduced in size or thickness.

5.3. *One full layer cloud and two reduced bottom layers*

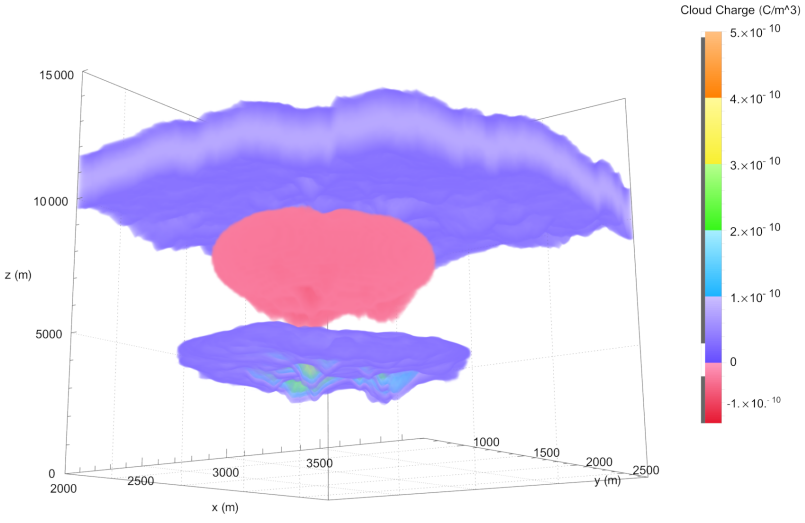

Figure 17. Cloud structure and space charge for a reduced bottom and middle layers.

Table 3. Initial conditions and results for the one layer cloud structure.

Alitude (m)	Color	Charge	Direction	Type
3000	Blue	+	↓	CTG
4000	Purple	+	↓	CTG
5000	Green	-	↑	CTC
6000	Magenta	-	↑	CTC
7000	Gray	-	↑	CTC
8000	Orange	-	↑	CTC
9000	Black	-	↑	CTC
10000	Cyan	+	↓	CTG
11000	Brown	+	↑	CTC
12000	Red	+	↑	CTC

Finally, we treat the representative case of the final moments of the storm. Under the effect of the different wind speeds in altitude and the horizontal development of the cloud, the upper positive layer expands laterally and becomes much larger than the bottom layers [14].

The space charge resulting from this deformation is modelled and shown in Figure 17. The positive and negative bottom layers are laterally reduced with the help of a 3D gaussian centred in the middle of the cloud, ensuring that no high gradient can perturbate the Poisson equation resolution. The electrical potential (iso-potential surface) for this calculation is shown in Figure 18 along the electric field (arrows and streamlines). The same inception altitudes as in the previous section are taken, as shown in the Table 3.

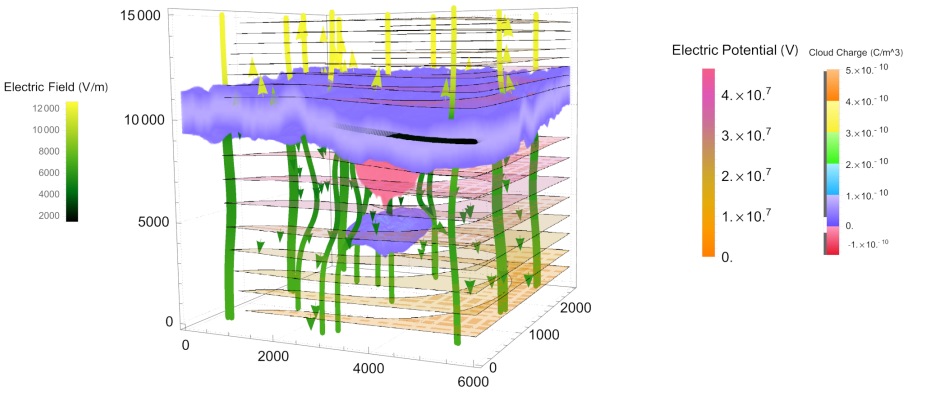

Figure 18. Electric Field (vector and line plot), Electric Potential (surface levels), space charge (volume on left, for a reduced bottom and middle layers cloud structure.

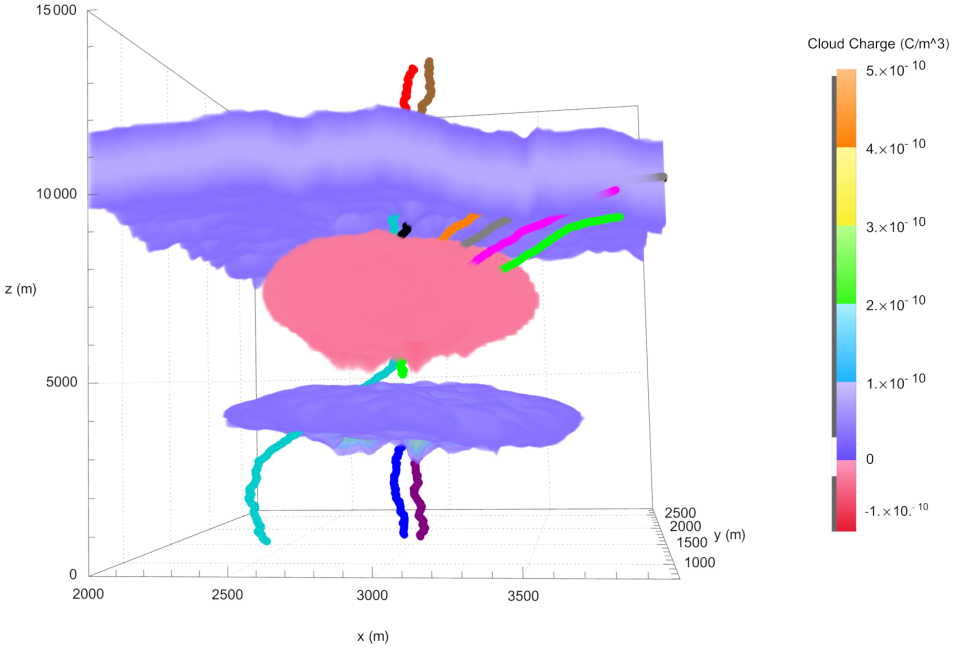

Figure 19. Propagation of lightning in a reduced bottom and middle layers cloud structure, see Table 3 for initialisation data.

The propagation of the various leaders is shown in Figure 19. In this situation, the only leaders connecting to the ground are those from the cloud's positive upper and bottom parts. The upper positive charge space attracts the leaders from the negative middle part.

The two leaders coming from the bottom positive layer (blue and magenta) are attracted as in the first case (3 layers scenario) by the ground: the potential difference given by equation (2) is more important in this direction as can be seen in Figure 20.

The electric potential variation at the leader's front is shown in Figure 20 as a function of the step number. Positive leaders tend to follow decreasing potential values, and negative leaders tend to follow increasing potential values. Again, this figure shows that taking into account the leader space charge is necessary for a proper calculation of the electric potential during the propagation of intraclouds lightning.

The leader coming from the positive top layer (cyan) is attracted firstly toward the negative middle cloud, but it can pass through it as it is reduced. The bottom positive layer bends the field lines and repulses the leader toward its border. At last, it can find a path around this positive layer toward the ground. This is corroborated by the Figure 20 where the leader coming from the inception point 10000m (cyan) follows a potential always decreasing but with a little inflexion point at the moment of the leader bypassing the bottom positive layer.

This scenario aim at modelling the last moments of the storm. It has been observed [12–14] that during the last stage of the thunderstorm, positive lightning becomes the majority of the lightning that connect to the ground.

6. Conclusions

In this paper, we have used a lightning propagation model aimed at testing the hypotheses made by Nag and Rakov about the different possibilities of cloud-to-ground or cloud-to-cloud leader propagation. We have constructed a new cloud model from a picture of a real thunderstorm cloud for this aim. The space charge inside the cloud is composed of three layers: a positive charge at the bottom and top, and a middle negative charge layer.

This space charge is used to compute an electric potential. Introducing a stepped leader propagation model helps us characterise for different inception altitudes the behaviour of lightning inside the cloud. We have found that when the bottom positive layer covers the whole cloud in latitude and longitude, it protects the ground from negative lightning as it repulses the negative leaders inside the cloud. Only positive leaders from the bottom positive layer reach the ground in this case.

If the bottom positive layer is reduced in size, which is more representative of a typical thunderstorm cloud [14], the only lightning reaching the ground is a negative one that takes inception in the cloud middle layer.

Due to wind gradients, the end of a storm is characterised by reduced bottom and middle layers. In this scenario, as proposed by Nag and Rakov [12, 13], only leaders coming from the two positive layers can reach the ground.

This model associated with this cloud structure has permitted us to validate these hypotheses. The photography presented in the Picture 21, where lightning reaching the ground comes from the bottom part of the cloud, corroborate these hypotheses visually.

We think that this model, associated with other cloud structures, can improve the comprehension of the leader's propagation in different types of clouds (holes or reduction in layer thickness, for example).

In the future, we plan to introduce branching in the propagation model to have a better lightning representation, in this case, one must calculate the electric the potential of each branch, and this will induce interaction between branches.

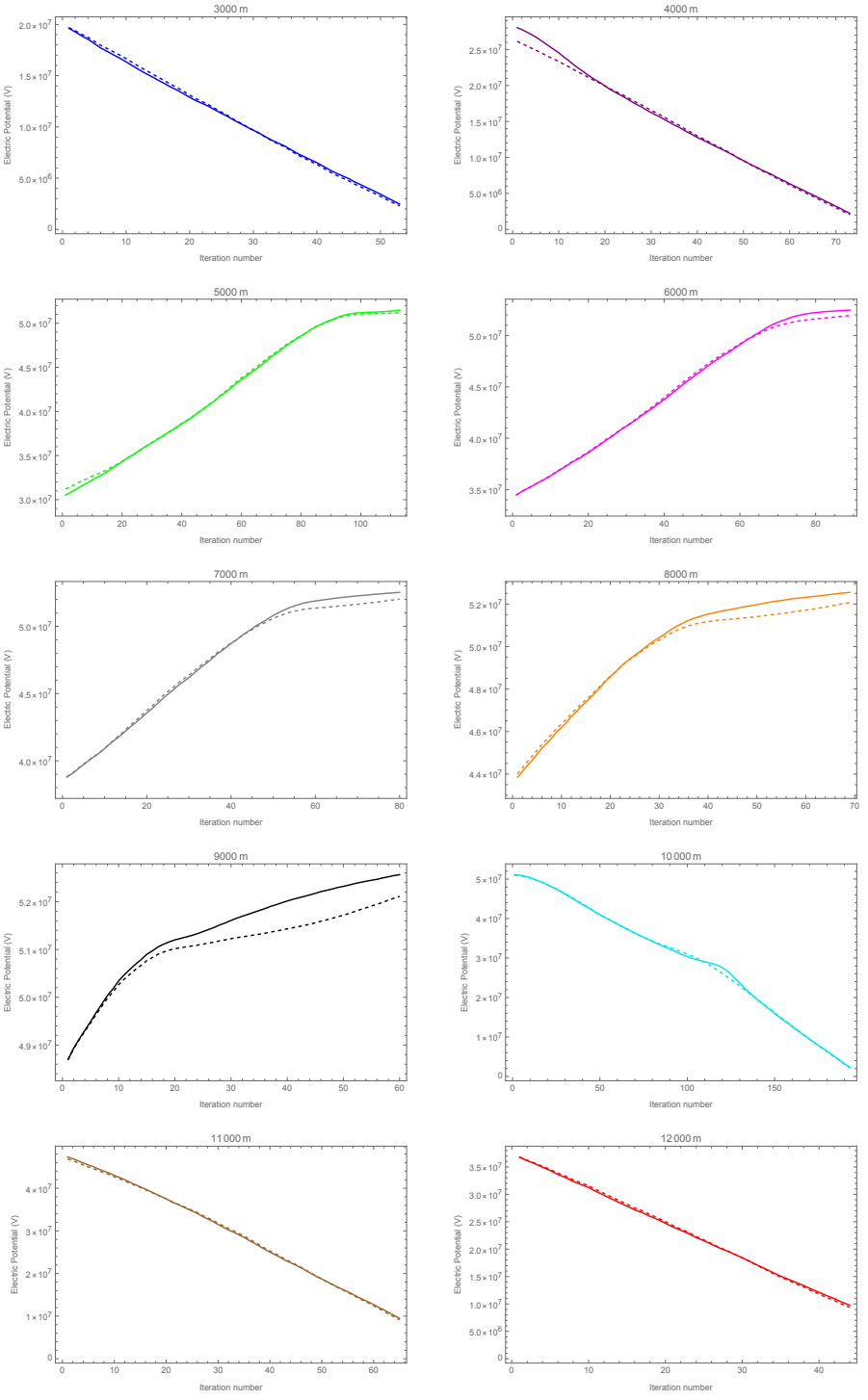

Figure 20. Value of the Electric Potential in front of the leader for the different inception altitudes. Plain: electric potential due to the cloud, Dashed: electric potential induced by the cloud space charge and the leader.

Figure 21. Photo of a storm showing bottom CTG leaders and top CTC leaders (Photography Ph. Dessante).

Another improvement is to reduce the leader's radius to have a better estimation of the electric field. This could lead to a stopping condition for leader propagation.

Declaration of interests

The authors do not work for, advise, own shares in, or receive funds from any organization that could benefit from this article, and have declared no affiliations other than their research organizations.

References

[1] Les Renardières Group and others, "Research on long air gap discharges at Les Renardières", *Electra* **23** (1972), pp. 53–157.

[2] Les Renardières Group and others, "Research on long air gap discharges at les Renardières–1973 results", *Electra* **35** (1974), pp. 49–156.

[3] R. T. Waters, "Positive Discharges in Long Air Gaps at Les Renardières–1975 Results and Conclusions", *Electra* **53** (1977), pp. 31–132.

[4] A. A. Syssoev, D. I. Iudin, A. A. Bulatov and V. A. Rakov, "Numerical Simulation of Stepping and Branching Processes in Negative Lightning Leaders", *J. Geophys. Res. Atmos.* **125** (2020), no. 7, article no. e2019JD031360.

[5] M. Vargas and H. Torres, "On the development of a lightning leader model for tortuous or branched channels – Part II: Model results", *J. Electrost.* **66** (2008), no. 9, pp. 489–495.

[6] Y. Xu and M. Chen, "An improved 3-D self-consistent stochastic stepped leader model", in *2011 7th Asia-Pacific International Conference on Lightning*, 2011, pp. 699–705.

[7] D. Xu et al., "Numerical Simulation on the Effects of the Horizontal Charge Distribution on Lightning Types and Behaviors", *J. Geophys. Res. Atmos.* **126** (2021), no. 18, article no. e2020JD034375.

[8] V. Cooray and L. Arevalo, "Modeling the Stepping Process of Negative Lightning Stepped Leaders", *Atmosphere* **8** (2017), no. 12, article no. 245.

[9] R. Ghaffarpour and S. Zamanian, "Fractal-based lightning model for investigation of lightning direct strokes to the communication towers", *Electr. Eng.* **104** (2022), no. 4, pp. 2543–2551.

[10] A. I. Ioannidis, P. N. Mikropoulos, T. E. Tsovilis and N. D. Kokkinos, "A Fractal-Based Approach to Lightning Protection of Historical Buildings and Monuments: The Parthenon Case Study", *IEEE Ind. Appl. Mag.* **28** (2022), no. 4, pp. 20–28.

[11] P. Lalande and V. Mazur, “A Physical Model of Branching in Upward Leaders”, *AerospaceLab* **5** (2012), article no. AL05-07.

[12] A. Nag and V. A. Rakov, “Some inferences on the role of lower positive charge region in facilitating different types of lightning”, *Geophys. Res. Lett.* **36** (2009), no. 5.

[13] A. Nag and V. A. Rakov, “Positive lightning: An overview, new observations, and inferences”, *J. Geophys. Res. Atmos.* **117** (2012), no. D8, article no. D08109.

[14] *The Lightning Flash*, (V. Cooray, ed.), Institution of Engineering and Technology, London, 2003.

[15] A. A. Dul’zon, V. V. Lopatin, M. D. Noskov and O. I. Pleshkov, “Modeling the development of the stepped leader of a lightning discharge”, *Tech. Phys.* **44** (1999), no. 4, pp. 394–398.

[16] Y. Xu and M. Chen, “A 3-D Self-Organized Leader Propagation Model and Its Engineering Approximation for Lightning Protection Analysis”, *IEEE Trans. Power Deliv.* **28** (2013), no. 4, pp. 2342–2355.

[17] F. A. M. Rizk, “Modeling of Lightning Stepped Leader Characteristics”, *IEEE Trans. Dielectr. Electr. Insul.* (2024).

[18] P. Lalande, A. Bondiou-Clergerie, G. Bacchiega and I. Gallimberti, “Observations and modeling of lightning leaders”, *C. R. Phys.* **3** (2002), no. 10, pp. 1375–1392.

ACADÉMIE DES SCIENCES
INSTITUT DE FRANCE

Comptes Rendus. Physique
2024, Vol. 25, Special issue S1, p. 109-124
https://doi.org/10.5802/crphys.193

Research article / *Article de recherche*

Energy in the heart of EM waves: modelling, measurements and management / *L'énergie au cœur des ondes électromagnétiques : modélisation, mesures et gestion*

Multi-label classification with deep learning techniques applied to the B-Scan images of GPR

Classification multi-label par des techniques d'apprentissage profond appliquées aux images B-Scan de radars à sondage de sol

Soukayna El Karakhi [*,a], **Alain Reineix** [*,a] **and Christophe Guiffaut** [a]

[a] University of Limoges, XLIM Institute, 123 Av. Albert Thomas, 87000 Limoges, France
E-mails: soukaynaelkar@gmail.com (S. El Karakhi), alain.reineix@xlim.fr (A. Reineix), christophe.guiffaut@xlim.fr (C. Guiffaut)

Abstract. The ground penetrating radars (GPR) are now widely used for the detection of buried objects in areas such as: geology, archaeology and civil engineering. It has the advantage of allowing detection by a non-destructive technique. The principle for time domain GPR consists in emitting electromagnetic pulses in the ground, these one are then diffracted by the targets to be detected. A single GPR signal trace captured at a position of the radar is a 1D signal called Ascan. A set of Ascan radar waveforms captured at a certain number of different consecutive positions along a particular direction will form a 2D image called B-scan. They show response shapes of hyperbolic type and their analysis give many characteristics. For example, in the case of buried pipes, a specific processing allows to find their diameter, their nature as well as the electrical characteristics of the ground. However, these approaches often require complex post-processing of the Bscan, which can be time-consuming and therefore makes it difficult to perform real-time characterization at the expense of such methods. With the emergence of deep neural networks and with a learning phase on a large number of Bscan, it becomes possible to extract almost instantaneously the characteristics of GPR radar data. In this study, a multi-label classification (MLC) model based on transfer learning and data augmentation has been developed to generate multiple information elements on the same image and to realize classification. Three deep learning models: VGG-16, ResNet-50 and adapted CNN were used as pre-trained models for transfer learning. The networks were trained on a synthetic dataset created in this study and evaluated on a set of performance metrics.

Résumé. Les radars à pénétration de sol (GPR) sont aujourd'hui largement utilisés pour la détection d'objets enterrés dans des domaines tels que la géologie, l'archéologie et le génie civil. Il présente l'avantage de permettre une détection par une technique non destructive. Le principe du GPR dans le domaine temporel consiste à émettre des impulsions électromagnétiques dans le sol, celles-ci étant ensuite diffractées par les

* Corresponding authors

cibles à détecter. Une seule trace de signal GPR capturée à une position du radar est un signal 1D appelé Ascan. Un ensemble de formes d'ondes radar Ascan capturées à un certain nombre de positions consécutives différentes le long d'une direction particulière formera une image 2D appelée B-scan dans le cas d'un déplacement rectiligne. Elles montrent des formes de réponse de type hyperbolique et leur analyse donne de nombreuses caractéristiques. Par exemple, dans le cas de canalisations enterrées, un traitement spécifique permet de connaître leur diamètre, leur nature ainsi que les caractéristiques électriques du sol. Cependant, ces approches nécessitent souvent un post-traitement complexe du Bscan, ce qui peut être chronophage et rend donc difficile la caractérisation en temps réel au détriment de ces méthodes. Avec l'émergence des réseaux neuronaux profonds et avec une phase d'apprentissage sur un grand nombre de Bscan, il devient possible d'extraire presque instantanément les caractéristiques des données radar GPR. Dans cette étude, un modèle de classification multi-label (MLC) basé sur l'apprentissage par transfert et l'augmentation des données a été développé pour générer des éléments d'information multiples sur la même image et réaliser la classification. Trois modèles d'apprentissage profond : VGG-16, ResNet-50 et CNN adapté ont été utilisés comme modèles pré-entraînés pour l'apprentissage par transfert. Les réseaux ont été formés sur un ensemble de données synthétiques créé dans cette étude et évalués sur un ensemble de mesures de performance.

Keywords. Ground Penetrating Radar, Image processing, Detection of Buried objects, Deep learning.

Mots-clés. Radar à sondage de sol, traitement d'images, détection d'objets enfouis, apprentissage profond.

Note. This article follows the URSI-France workshop held on 21 and 22 March 2023 at Paris-Saclay.

Manuscript received 27 June 2023, revised 13 March 2024 and 21 June 2024, accepted 26 June 2024.

1. Introduction

Ground Penetrating Radar (GPR) [1] has become an increasingly significant and effective tool for non-destructive engineering investigations. Over an extended period, GPR has found extensive applications in geological research, civil engineering, agriculture, and environmental studies. In recent years, various approaches have been proposed by researchers to enhance the processing of GPR data. Notably, T. Noreen [2] has suggested a machine learning-based approach for hyperbolic signature identification using a Support Vector Machine (SVM) with Histogram of Oriented Gradient (HOG) features. E. Temlio [3] has explored diverse techniques for landmine detection, including Binary Robust Independent Elementary Features (BRIEF), Edge Histogram Descriptor (EHD), Histogram of Oriented Gradients (HOG), Scale Invariant Feature Transform (SIFT), and Speeded Up Robust Features (SURF). Additionally, in a separate study, W. A. Wahab [4] introduced an innovative hyperbola fitting technique for estimating the radius of buried utilities such as pipes and cables, conducting experiments on pipes with nine different diameter values. Furthermore, B. Walker and L. Ray [5] have implemented a feature-based machine learning approach to process GPR data, utilizing feature vectors derived from the Histogram of Oriented Gradients (HOG) in conjunction with a Support Vector Machine (SVM) for the detection of deep and shallow crevices. These methods often involve additional characteristic operators as a preprocessing step, including Sobel's, Wavelet Edge Detection [6], and Canny's operators. While these methods yield precise results, they are computationally intensive. In recent years, several researchers have proposed novel approaches for the automatic identification and localization of buried objects using deep learning models. This has underscored the numerous advantages of deep learning technologies. With the growing volume of GPR data, traditional machine learning techniques are showing limitations in digital image processing. Researchers have increasingly turned to Convolutional Neural Network (CNN)-based methods to learn hyperbolic shapes for classifying and identifying buried objects. Most of the methods mentioned have focused on the identification and positioning of buried objects, classifying them based on a single characteristic. Notably, limited studies have explored multi-label classification models, aiming to extract multiple pieces of information from a single image. It is also crucial to highlight that recent studies in

this field have advanced the capabilities of GPR data analysis. For instance, Nairit Barkataki [7] introduced a deep Convolutional Neural Network (CNN) model for the automatic classification of soil types based on GPR B-Scan images. Mehmet Sezgin [8] achieved nearly 100 % classification accuracy for the two-class identification of buried objects, distinguishing clutter from surrogate mines, using real GPR datasets. Enver Aydin demonstrated the advantages of deep learning in detecting buried targets considered by GprMax simulation. These recent advancements underscore the potential of deep learning in GPR data analysis. Our paper's contributions are synthesized as follows: we have created a database using the Finite Difference Time Domain (FDTD) simulation, employed gradient operators for edge region detection (Sobel, Canny, and Prewitt) for image processing, and developed a multi-label model for the identification of the diameter of buried pipes, the characterization of their internal spaces, and the determination of the soil medium's composition. The originality of our work primarily lies in the development of deep learning model architectures and the approach to model prediction and analysis for the three models we have developed. What distinguishes our work from existing studies is our innovative approach to multi-label classification in the context of GPR data analysis. While prior research has predominantly focused on single-class or binary-class classification of GPR data, our study takes a significant step forward by simultaneously extracting multiple facets of information from a single GPR image. Unlike the conventional approach that classifies objects based on a single characteristic, our model is designed to identify various attributes concurrently, such as the diameter of buried pipes, the characteristics of their internal spaces, and the composition of the surrounding soil medium. This multi-label approach introduces a new dimension to GPR image classification, allowing for a more comprehensive exploration of the data and providing rich and detailed insights into the subterranean environment. As a result, our research represents a significant advancement in the field of non-destructive engineering investigations, opening up exciting possibilities for applications in geology, civil engineering, and other related fields. In addition to the multi-label approach, our research stands out due to our novel methodology for creating a synthetic database using the Finite Difference Time Domain (FDTD) simulation model. We have further enhanced the quality of our data by implementing gradient operators, such as Sobel [9], Canny, and Prewitt, for edge region detection. To classify the GPR images, we have developed and employed three distinct deep learning models: VGG 16, Resnet 50, and a custom-designed CNN. The subsequent sections of this paper will provide detailed explanations of our methodology, including the creation of the database and the evaluation of our multi-label model. In summary, our work signifies a new era in non-destructive engineering investigations by extending the boundaries of GPR image classification and offering fresh insights into data analysis, with implications spanning from geology to construction.

2. The creation of the synthetic dataset

In order to generate our dataset, we will use the TEMSI-FD software [10] developed within the EMC team of the XLIM Institute. It consists of a FDTD-based method software [11] designed to simulate the propagation of electromagnetic waves in complex media. For the GPR study, the time domain signal emitted, propagating and received by antennas can be calculated. It is useful to represent these recordings in two forms: the A-scan (1D response), the B-scan (2D image resulting of multiple consecutive A-scan).To create a simulation model, a number of settings are required. First, the entire scene has to be designed. The scene is characterized by the propagation medium of the electromagnetic waves. The model of the ground is based on the fractal model [10], but also on homogeneous medium such as dry clay, dry sand and concrete. The dimensions of the scene is 1000 mm x 800 mm x 1200 mm (X x Y x Z), the cell size being 4 mm in each cartesian direction. The soil layer depth is 1 meter. It is the maximum depth value

to be probed by the GPR, and consequently, it determines the estimation of the maximum time of observation/simulation, which is 20 ns for this volume. The waveform generated by the Wu-King antenna is a sinusoidal Gaussian, and this pulse is centered at the frequency of 1GHz with a bandwidth of 500 MHz. This duration was calculated for the case of the concrete layer which has the smallest value for the propagation velocity among the media considered: $v_p = \frac{c}{\sqrt{\epsilon_r}}$ with c the velocity of light in vacuum. The GPR antennas system is composed of a fixed emitter and 10 receiving antennas. The receivers are also spaced 20 mm apart and moved in groups of 200 mm along the horizontal scan line on the soil, resulting in a 10-fold reduction in the number of simulations compared to considering the receivers individually throughout the computational volume. The multi-receiver bistatic GPR is illustrated in the Figure 1. A set of 5400 GPR B-scans database concerning 4 soil types, 50 depth values and 9 different pipe diameters is generated; the current diameters for the simulation data are 16, 24, 32, 40, 48, 64, 72, 80 and 100 mm. The depth values range from 204 mm to 400 mm below the soil surface. Three types of pipes were chosen during the simulation: a perfectly conductive metal pipe, an air-filled pipe, and a water-filled pipe. For the second one, the pipe is not modeled, the sheath dielectric is then neglected. That is also the case for the water-filled configuration.

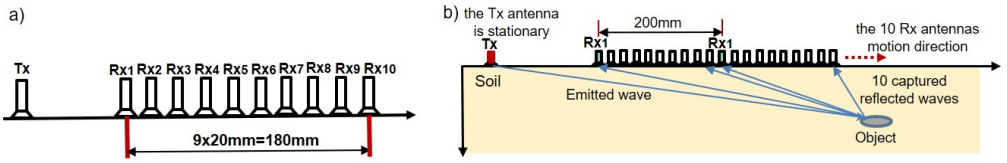

Figure 1. a) The multi-receiver 10 Rx antennas bistatic GPR with one Tx antenna emitter architecture, b) The way the 10 Rx antennas are moved in one direction during the exploration on the soil.

2.1. *A-Scan*

An A-scan is a one-dimensional (1D) representation of the amplitude of the collected signal as a function of time after placing the receiving sensor antenna above the point of interest. An example of an A-scan is shown in Figure 2. It represents the signal captured by the receiving sensor antenna R_{x1} from the group of 10 low coupled receiving antennas. The first reflection generally corresponds to a combination of direct coupling between the antennas (Tx, R_{x1}) and reflection off the surface of the ground. The second reflection (at t = 8.5 ns), with a lower amplitude, corresponds to the response of the object of interest.

To improve the quality of the recordings, it is often essential to eliminate both surface echoes and direct antenna coupling, retaining only the relevant signal. This operation can be performed using two methods during the simulation. Firstly, by taking a measurement without any objects present and subtracting it from the recording obtained with objects in the scene, effectively removing the various couplings. Alternatively, this can be achieved by disregarding the initial moments of the recording.

2.2. *B-Scan*

The 2D image of the B-scan represents a vertical cross-sectional view of the subsurface. The horizontal axis of this section represents the position on the ground surface, while the vertical

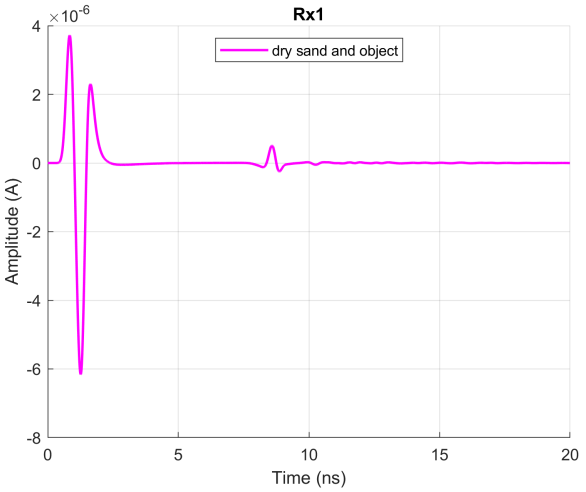

Figure 2. Example of the waveform of an A-scan captured by the receiving antenna R_{x1}.

axis represents the round-trip time of the EM wave propagation. By combining all the A-scans that make up the B-scan, a matrix is created where each row represents a time sample and each column represents an A-scan trace. Each element of this matrix has a value corresponding to the amplitude of the field for the associated A-scan trace and time sample. Buried objects appear as hyperbolic shapes in the B-scan images. Recordings taken from different positions on the ground are combined in the B-scan image, thus creating these specific hyperbolic shapes. The Figure 4 is illustrating the resulting treatment of B-scan.

2.3. *Relevant parameter values*

The parameter values employed in the simulation can be found in Table 1, while Table displays the dielectric parameters corresponding to the soil types.

Table 1. The parameter values of simulations.

Parameters of simulations	**Values**
Source frequency	1.00 GHz
Bandwidth	500 MHz
Source waveform	Sino-Gaussian pulse
Source pulse duration	1 ns
A-scans intervals	20 mm
No of A-scans	40
Spatial resolution	4 mm

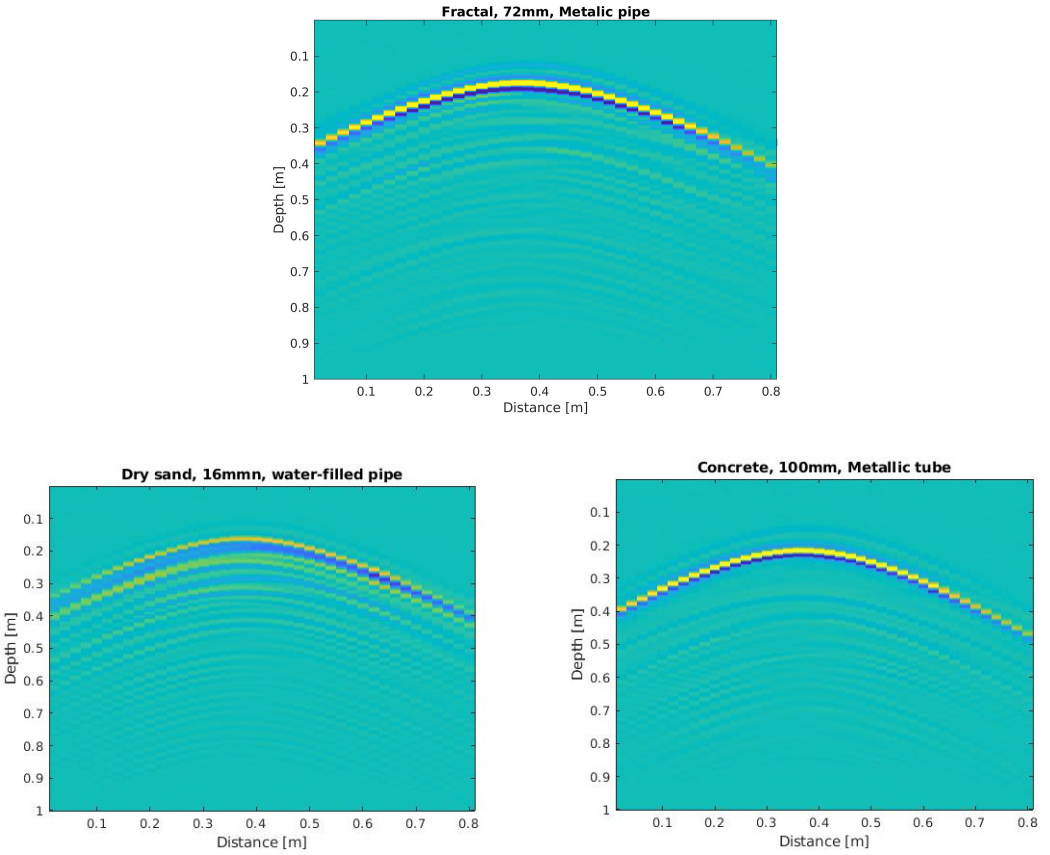

Figure 3. An example of B-scan images obtained using various propagation mediums, different diameters, and types of pipes.

The Table 2 provides information on different soil types along with their respective conductivity and relative permittivity values. The fractal model illustrates that soils are present in distinct layers or geological formations, which are separated by rough interfaces. These layers demonstrate a wide range of characteristics [12].

Table 2. Soil Conductivity and Relative Permittivity.

SI. No	Soil type	Conductivity (S/m)	Relative permittivity (ε_r)
1	Dry sand	0.002	10.00
2	Dry clay	0.001	5.53
3	Concrete	0.001	8.00
4	Fractal	0.001	6.00

3. Proposed Deep Learning architecture

Now, the CNN and the procedure used to apply deep learning for retrieving the soil and pipes characteristics will be described. First, the global GPR data handling workflow in this study involves feature extraction, splitting the dataset into training and test sets. This allows respectively CNN model training and prediction efficiency. The feature extraction pipeline for B-Scan images consists of testing several approaches to edge detection. The goal of this technique is to significantly reduce the amount of data while retaining information that can be considered more relevant. The objective is to focus on regions of the hyperbola where there is a distinct intensity variation. The hyperbola region is detected by a bounding box, the image is cropped to extract the region of interest from each frame. For this purpose, we have focused on Canny's operators. Canny is a multi-step edge detection algorithm developed by John F. Canny in 2001 [13], which proceeds through the following steps:

(1) noise reduction: Noise is removed from the image with a 5x5 Gaussian filter [14].
(2) Determine the gradient intensity of the image using the Canny operator.
(3) Non-maximum Suppression: this step consists of eliminating those undesirable pixels that may not be edges.
(4) Hysteresis Thresholding.

The objective of this work is to implement Deep Learning models for extracting features like buried pipes diameters or type of soil layer from B-scan images. We will implement three different architectures: VGG-16, Resnet-50 through learning transfer and a custom CNN model. The proposed architecture is a multi-label model classification in which individual objects can be classified into multiple classes at one time, compared to traditional one-label classification cases involving a single class of objects. Multi-label classification approaches are becoming unavoidable in advanced technology. In this work, in the classification of B-Scan images, each image can belong to several distinct categories. For example, we classify the type of pipe (metal pipe, water-filled pipe and empty pipe), 9 different diameters, so that we distinguish four different mediums. As seen above, the dataset contains 5400 B-Scans, it will be divided in such a way that 80 % is reserved for model training, and 20 % for test data. Now we will describe the different topologies.

3.1. *Transfer learning using VGG 16 and Resnet 50*

Residual neural networks, commonly known as ResNet, have revolutionized the field of computer vision by serving as a fundamental architecture for various tasks. The term "Residual" refers to the key concept behind ResNet's [15] success. Prior to ResNet, training deep neural networks with over 50 layers was challenging due to the problem of gradient backpropagation [16]. However, ResNet overcame this obstacle. The strength of ResNet lies in its implementation of skip connections, which are illustrated in Figure 5. On the left of Figure 5 we stack the convolution layers successively. On the right, we stack the convolution layers as before, but we connect the original input to the output of the convolution block. This connection, known as a skip connection, plays a crucial role in retaining important information from earlier layers. It enables the network to effectively train deep networks by mitigating the vanishing gradient problem.The skip connection in ResNet facilitates the flow of gradients throughout the network during training. This means that the gradients can propagate back to earlier layers more easily, allowing for smoother and more efficient learning. By incorporating these skip connections, ResNet has achieved remarkable performance in various computer vision tasks and has become a state-of-the-art model for deep neural network training.

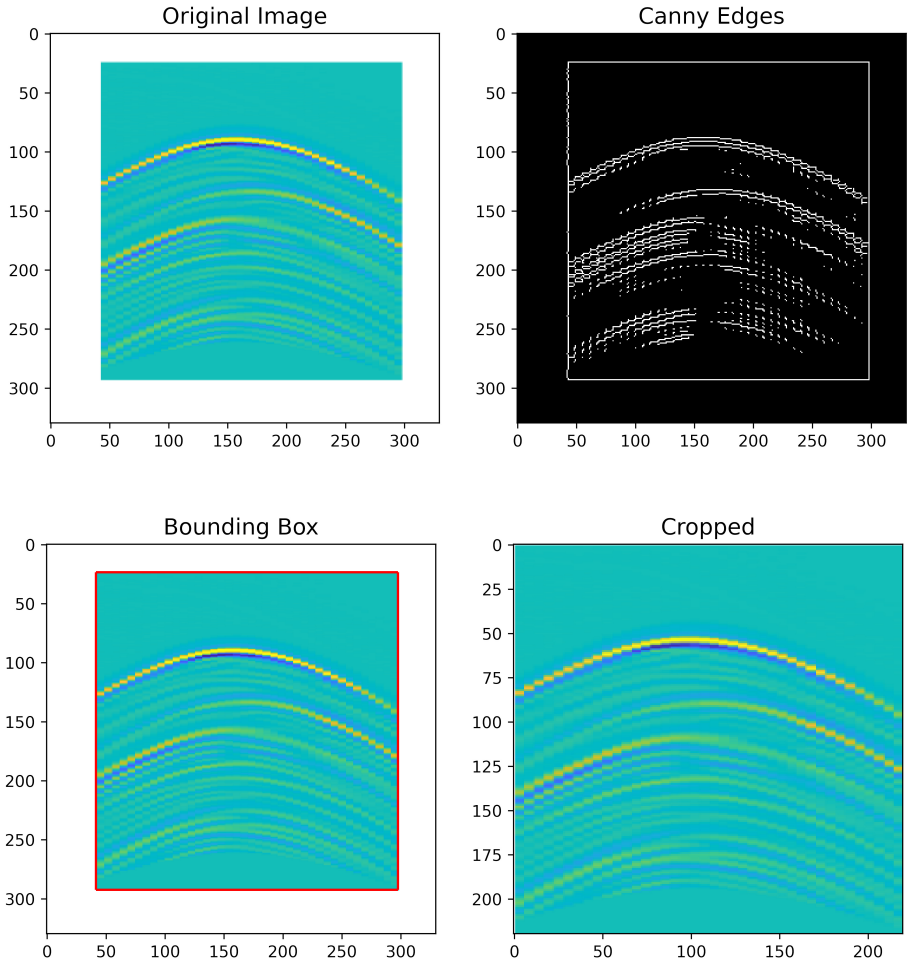

Figure 4. Example of Output from the Canny Edge Detection Operator.

The Visual Geometry Group **(VGG-16)** [17] is a widely recognized deep Convolutional Neural Network (CNN) architecture developed by the Visual Geometry Group. The key contribution of VGG-16 lies in its design, which utilizes a stack of 3x3 filters. This approach demonstrated that using multiple small kernel size filters can achieve the same effect as using larger filters, while also providing the flexibility to increase the depth of the network. VGG models introduced the notion of depth as a crucial factor in the success of convolutional neural networks. By employing smaller filter sizes, VGG models are able of learning a larger number of filters, leading to a more complex representation of the input data. This approach marked a significant departure from earlier models that heavily relied on larger filters to capture low-level features. One of the notable achievements of VGG models is their ability to effectively capture both high-level and low-level features using smaller filters. This demonstrated that the depth of the network combined with smaller filters can produce powerful representations. This insight paved the way for subsequent advancements in deep learning architectures. In the case of VGG-16, the network comprises 16 trainable layers, as depicted in Figure 6. The VGG-16 model has been widely adopted in various computer vision tasks and has achieved state-of-the-art performance on benchmark datasets. Its success has inspired further research and the development of more advanced CNN architectures.

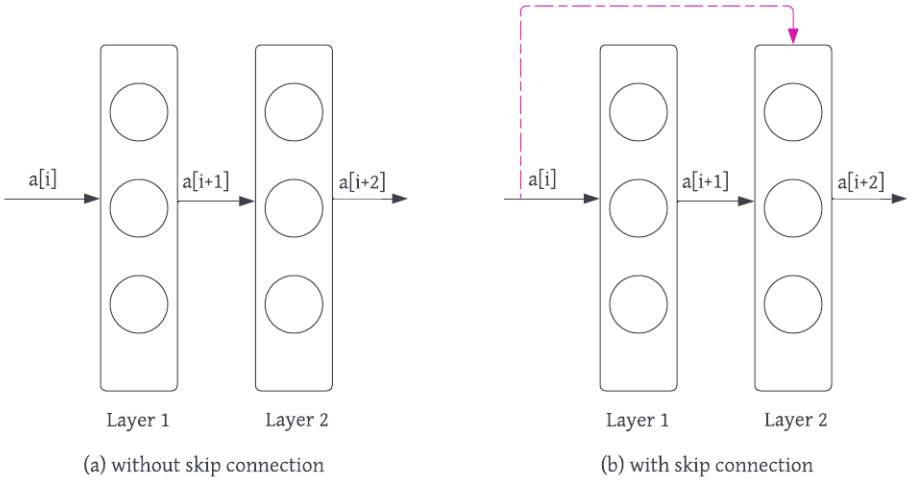

Figure 5. Residual learning: a building block.

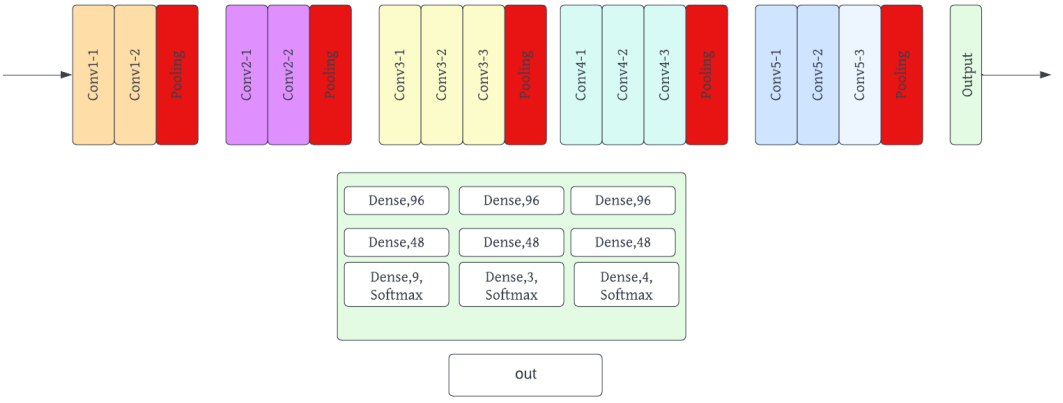

Figure 6. VGG16 architecture with building block of last layers.

The pre-trained models VGG16 and Wide ResNet-50 are used in this study. Normalized input images in mini-batches, with RGB images having three channel dimensions ($3 \times H \times W$), where H and W are assumed to be 224, are required by these models. In our approach, the final classification layers are substituted with fully connected layers. Specifically, three separate layers replace the last layer. Diameter classification, pipe type classification, and differentiation of propagation mediums are handled by the first, second, and third layers, respectively. ReLU and softmax activation functions are employed. The initial training layers are frozen, and the modified layer is trained using the B-Scans dataset. A training duration of 30 epochs with a batch size of 32 is used. Adam [18, 19] serves as the model optimizer, and categorical cross-entropy is employed for loss calculation. To enhance computational efficiency and performance, techniques such as early stopping, data augmentation, and adaptive learning rates are employed.

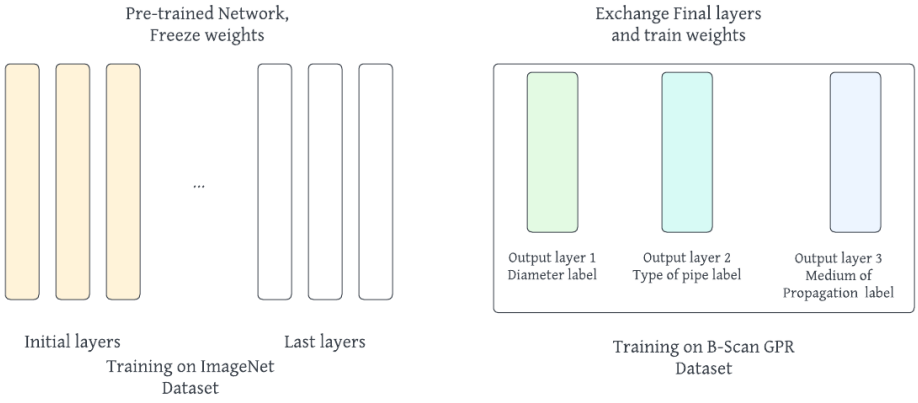

Figure 7. Transfer learning strategy.

These techniques aim to improve both the speed of computation and the overall performance of the model.

3.2. *Custom Model*

In this work, a deep convolutional neural network is developed for multi-label classification to classify 9 different diameters, 3 different pipe types, and 4 different propagation media. The custom CNN model is inspired by the inception network [20], it is a model developed by google. The main difference between the inception model and the ordinary CNNs [21] are the inception blocks. These consist in convoluting the same input with several filters and concatenating their results. The aim of this model is to introduce the concept of multipathing, which allows different characteristics to be simultaneously captured and extracted. The building block is illustrated in Figure 8, this block contains different convolution layers of different filter sizes $(1x1)$, $(5x5)$, $(7x7)$. The diversity of the kernel size will increase the capacity of the network to extract the most complex features. In the input layer, 32 filters of size 3×3 are used, followed by a MaxPool layer and then a batch normalization layer to increase the speed and stability of learning. After that, a convolution layer with 64 filters of size $3x3$ is applied, followed by a max pooling layer. Two inception building blocks are then defined, each containing convolution layers with 128 and 16 filters of size $(1x1)$, $(5x5)$, $(7x7)$, respectively. At the end of each inception block, all feature maps are concatenated. The activation function employed in all convolutional layers is the rectified linear unit (ReLU) defined as: the output of ReLU is equal to 0 if the input value is less than 0 and equal to the input value if the input is positive. Then, all the feature maps are transformed into a 1D vector using a flattened layer. A set of 3 dense layers has been defined, containing 256, 512, and 256 neurons respectively. Each layer is followed by an activation function ReLU. Finally, 3 branches were defined for each output, each branch includes upstream a set of three dense layers respectively consisting of 96, 48 and 48 neurons, each output layer has 9 neurons to recognize the diameter size, 4 neurons to specify the propagation medium, and 3 neurons to distinguish the pipe type. The output layers are followed by a softmax layer mainly used for multi-label classification [22] problems to predict the probability of each label. As in most CNN, the data split between the training and validation data is 80 per cent and 20 per cent respectively. The ADAM optimizer has been used in the present case.

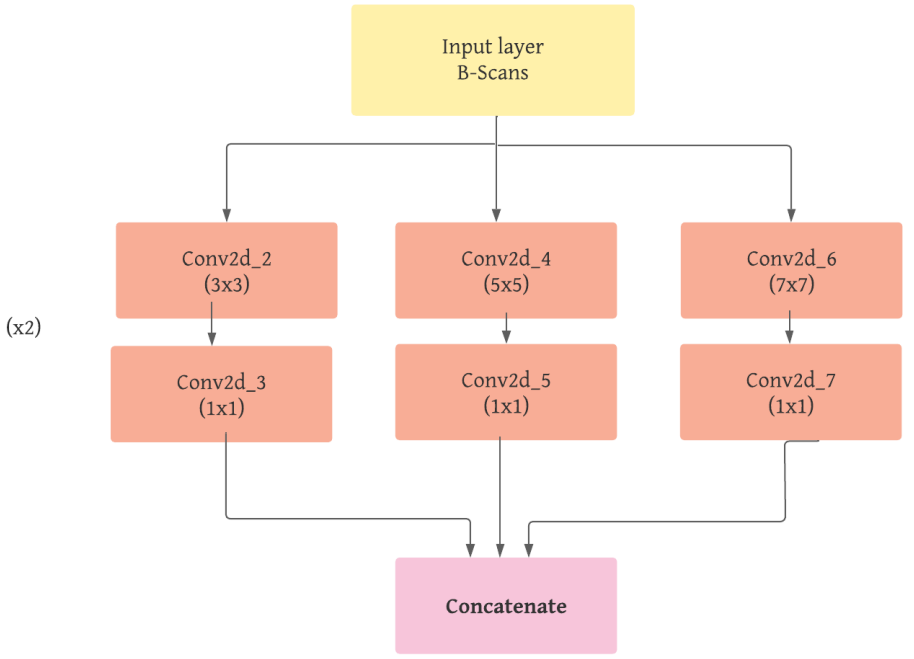

Figure 8. Custom CNN Model - building block.

4. Results

The simulation dataset consists of nine different diameter values, three types of pipes, and four different propagation mediums. The dataset includes 50 different depths for each simulation scenario. Each simulation scenario generates a B-scan image, resulting in a total of 5,400 B-scan images. Each image is constituted by $224x224$ pixels. To further enhance the dataset, data augmentation techniques were applied, resulting in a total of 10,800 B-scan images. The data augmentation process involved key transformations, including no rotation of the images, zooming up to 10 % of their original size, horizontal movement up to 10 % of their width, and vertical movement up to 10 % of their height.

4.1. *Data augmentation*

Enhancing model performance is a comprehensive process that involves employing various techniques to improve the accuracy, efficiency, and robustness of the model. This includes the use of advanced algorithms, preprocessing data, selecting relevant features, and tuning hyperparameters. By optimizing these factors, significant improvements can be achieved in the model's performance. The effectiveness and reliability of a deep learning model greatly depend on the quantity and diversity of the training data. To enhance data diversity and improve the model's interpretation of information, basic data augmentation techniques as described in reference [23–25] are employed. These techniques introduce visual variability to the data, leading to enhanced accuracy. For the B-Scans GPR dataset, the applied data augmentation techniques involve the use of Horizontal and Vertical shifts, as well as Resizing.

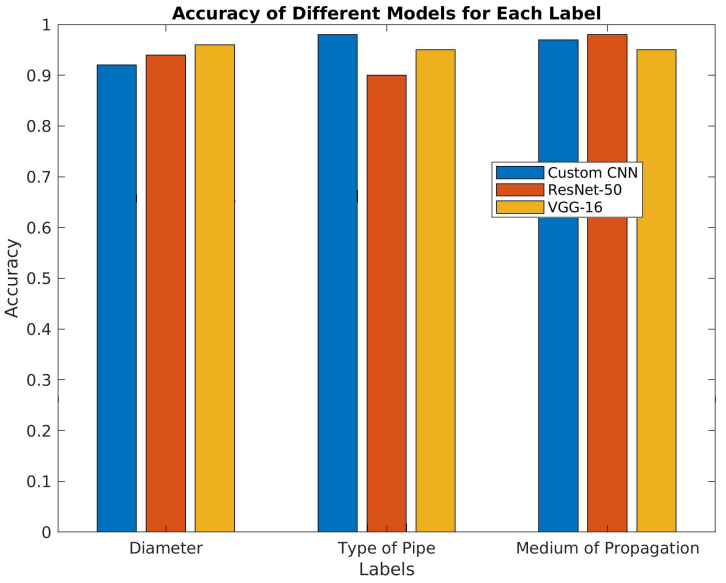

Figure 9. Accuracy of the three developed models with Canny's operators.

4.2. *Early stopping techniques*

Early stopping [26, 27] is a regularization technique commonly used in deep neural networks. It involves monitoring the model's performance on a validation dataset during training and stopping the training process after a certain number of epochs if the model's performance does not improve. The weights of the model are saved and updated throughout training. When further updates no longer result in performance improvement, training is halted, and the most recent optimal parameters are kept.

4.3. *Evaluation metrics*

Three indicators were used to evaluate the three Deep Learning models: Precision, Recall, and F1-score, the accuracy is the simplest indicator, it measures the percentage of correct predictions. It is defined as follows:

$$\text{accuracy} = \frac{TP + TN}{TN + TP + FP + FN} \tag{1}$$

Based on the results presented in Figure 9, a higher accuracy of 96 % is observed for the diameter identification using the VGG16 mode, and an efficiency of 98 % for the pipe type identification achieved by the Resnet-50 model. We also reach a higher level of sensitivity for the identification of the propagation medium, which achieves 98 % for both the VGG16 model and the customized CNN model.

TP (True positive) stands for the number of accurate diameter, pipe type and medium identifications, FP (False Positives) represents the number of incorrect identifications and FN (False negative) represents the number of failed recognitions. In GPR, accurate identifications mean that the target is well located and accurately classified. Incorrect identifications are indicative of a well-located target, but its geometry, as well as its type and medium, are not properly classified. The missed identifications reflect the target not being located. The Table 3 shows the

performance of the model Resnet-50 based on the 9 classes for the identification of diameters. The overall accuracy is 96 %. Table 3 shows the classification report for the 9 diameter values, we find the precision that indicates the performance or the positive prediction given by the model, recall is a statistical metric that shows how many positive cases actually correspond to the predicted class. The F1 score provides the information about the incorrect predictions of the model meaning that 1 is the best and 0 is the worst. The F1 score is obtained by calculating the precision and recall of the model. From Figure 10, out of 86 images it is seen that 80 are correctly predicted as having a diameter of 80mm and remaining 6 incorrectly assigned to other classes. So the precision of the diameter 80 mm class shown in Table 3, can be calculated as:

$$\text{Precision} = \frac{80}{86} = 0.93 \tag{2}$$

In Figure 10, out of a total of 86 images labeled as 80 mm diameter, 80 images were correctly predicted, resulting in a recall of approximately 93.00 % for the class "diam80".

$$\text{Precision} = \frac{80}{82} = 0.98 \tag{3}$$

The F1-score can be calculated as follows:

$$\text{F1-score} = \frac{2 \cdot \text{Precision} \cdot \text{recall}}{\text{Precision} + \text{recall}} = 0.95 \tag{4}$$

Table 3. Results of the ResNet-50 Classification Report: Diameter Identification on the Test Set.

Labels	Precision	Recall	F1-Score
Diameter 16mm	0.96	0.98	0.99
Diameter 24mm	1.00	0.98	0.99
Diameter 32mm	1.00	0.98	1.00
Diameter 40mm	1.00	0.95	0.98
Diameter 48mm	0.95	0.97	0.96
Diameter 64mm	0.85	0.98	0.96
Diameter 72mm	0.95	0.84	0.89
Diameter 80mm	0.93	0.98	0.99
Diameter 100mm	1.00	0.98	0.99

In Figure 10, the confusion matrix provides insights into the model's accuracy in predicting diameters. It excelled in predicting diam16, diam32, and diam80, but misclassified diam72 as diam80 or diam64. The matrix depicts actual class labels on the vertical axis and predicted class labels on the horizontal axis. It showcases precise classification for all four categories (clay, concrete, fractal, sand) with no misclassifications. However, some instances of "Water-filled pipe" were misclassified as "Vaccum" while the model performed well in classifying "Metallic" and "Vaccum" categories.

5. Discussion and conclusions

In this study, the focal point was on developing a multi-label classification (MLC) model using transfer learning and data augmentation techniques. Three deep learning models, namely VGG-16, ResNet-50, and an adapted CNN, were utilized as pre-trained models for transfer learning. These models were trained on a synthetic dataset created using the TEMSI-FD software, which simulates the propagation of electromagnetic waves in complex media. To enhance the model's

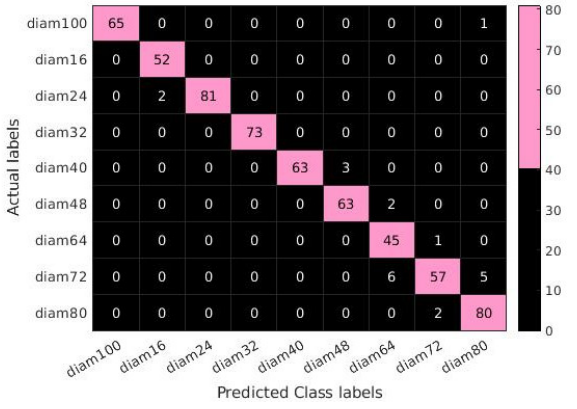

(a)

(b)

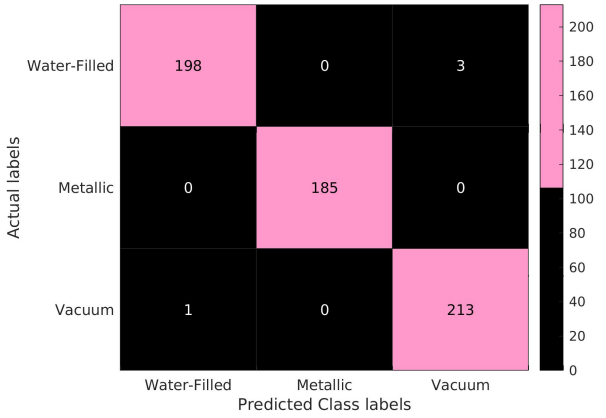

(c)

Figure 10. Matrix-confusion of diameter identification - Medium of propagation and type of pipe classification with Resnet-50 Model.

performance, various techniques were employed, including advanced algorithms, data preprocessing, feature selection, and hyperparameter tuning. Data augmentation techniques, such as Horizontal and Vertical shift, as well as Resizing, were used to improve data diversity and the model's interpretation of information. The regularization technique of early stopping was applied to the training process. This technique involves monitoring the model's performance on a validation dataset and stopping the training after a certain number of epochs if no improvement is observed. The weights of the model are saved and updated throughout training, and the most recent optimal parameters are used when further updates no longer improve performance. Based on the results presented the VGG16 model achieved a better accuracy of 96 % in diameter identification, while the Resnet-50 model achieved an efficiency of 98 % in pipe type identification. Both the VGG16 model and the customized CNN model achieved a higher level of sensitivity (98 %) in the identification of the propagation medium. To evaluate the performance of the network in the presence of various underground objects, B-Scan images were created with up to 2 objects of different diameters, depths, and pipe types. In conclusion, this study successfully developed a multi-label classification model using deep learning techniques, transfer learning, and data augmentation. The models demonstrated high accuracy and sensitivity in identifying diameters, pipe types, and propagation mediums. The use of synthetic datasets, advanced algorithms, and regularization techniques contributed to the model's improved performance and reliability. Future work will focus on generating noisy data to assess the robustness of our models. As well as the development of a new algorithm based on transformers for extracting characteristics from Radar signals while combining A-Scan and B-Scan.

Declaration of interests

The authors do not work for, advise, own shares in, or receive funds from any organization that could benefit from this article, and have declared no affiliations other than their research organizations.

References

[1] H. M. Jol, *Ground penetrating radar theory and applications*, Elsevier, 2008.

[2] T. Noreen and U. S. Khan, "Using pattern recognition with HOG to automatically detect reflection hyperbolas in ground penetrating radar data", in *2017 International Conference on Electrical and Computing Technologies and Applications (ICECTA)*, 2017, pp. 1–6.

[3] E. Temlioğlu, M. Dağ and R. Gürcan, "Comparison of feature extraction methods for landmine detection using ground penetrating radar", in *2016 24th Signal Processing and Communication Application Conference (SIU)*, 2016, pp. 665–668.

[4] W. A. Wahab, J. Jaafar, I. M. Yassin and M. R. Ibrahim, "Interpretation of Ground Penetrating Radar (GPR) image for detecting and estimating buried pipes and cables", in *2013 IEEE International Conference on Control System, Computing and Engineering*, 2013, pp. 361–364.

[5] B. Walker and L. Ray, "Multi-class crevasse detection using ground penetrating radar and feature-based machine learning", in *IGARSS 2019-2019 IEEE International Geoscience and Remote Sensing Symposium*, 2019, pp. 3578–3581.

[6] I. Giannakis, A. Giannopoulos and C. Warren, "A machine learning scheme for estimating the diameter of reinforcing bars using ground penetrating radar", *IEEE Geosci. Rem. Sens. Lett.* **18** (2020), no. 3, pp. 461–465.

[7] N. Barkataki, S. Mazumdar, P. B. Devi Singha, J. Kumari, B. Tiru and U. Sarma, "Classification of soil types from GPR B scans using deep learning techniques", in *2021 International Conference on Recent Trends on Electronics, Information, Communication & Technology (RTEICT)*, 2021, pp. 840–844.

[8] M. Sezgin and M. N. Alpdemir, "Classification of Buried Objects Using Deep Learning on GPR Data", in *2023 IEEE International Conference on Advanced Systems and Emergent Technologies (IC_ASET)*, 2023, pp. 01–05.

[9] C. Maas and J. Schmalzl, "Using pattern recognition to automatically localize reflection hyperbolas in data from ground penetrating radar", *Comput. Geosci.* **58** (2013), pp. 116–125.

[10] XLIM Institute, *Time Electromagnetic Simulator - Finite Difference Time Domain*. Software Developed in Limoges, France.

[11] A. Taflove, S. C. Hagness and M. Piket-May, "Computational electromagnetics: the finite-difference time-domain method", in *The Electrical Engineering Handbook*, Academic Press, Burlington, 2005, pp. 629–670.

[12] V. Ciarletti, A. Herique, J. Lasue, et al., "CONSERT constrains the internal structure of 67P at a few metres size scale", *Mon. Not. Roy. Astron. Soc.* **469** (2017), no. Suppl_2, S805–S817.

[13] R. P. K. Reddy, C. Nagaraju and I. R. Reddy, *Canny scale edge detection*, 2015. https://www.researchgate.net/publication/319701466_Canny_Scale_Edge_Detection.

[14] N. Barkataki, B. Tiru and U. Sarma, "A CNN model for predicting size of buried objects from GPR B-Scans", *J. Appl. Geophys.* **200** (2022), article no. 104620.

[15] D. Sarwinda, R. H. Paradisa, A. Bustamam and P. Anggia, "Deep learning in image classification using residual network (ResNet) variants for detection of colorectal cancer", *Procedia Comput. Sci.* **179** (2021), pp. 423–431.

[16] H. H. Tan and K. H. Lim, "Vanishing gradient mitigation with deep learning neural network optimization", in *2019 7th international conference on smart computing & communications (ICSCC)*, 2019, pp. 1–4.

[17] K. Simonyan and A. Zisserman, "Very deep convolutional networks for large-scale image recognition", 2014. *preprint* arXiv:1409.1556.

[18] Z. Zhang, "Improved adam optimizer for deep neural networks", in *2018 IEEE/ACM 26th international symposium on quality of service (IWQoS)*, 2018, pp. 1–2.

[19] A. Tato and R. Nkambou, *Improving adam optimizer*, 2018. https://openreview.net/forum?id=HJfpZq1DM.

[20] Y.-J. Cao, L.-L. Jia, Y.-X. Chen, et al., "Recent advances of generative adversarial networks in computer vision", *IEEE Access* **7** (2018), pp. 14985–15006.

[21] N. Jmour, S. Zayen and A. Abdelkrim, "Convolutional neural networks for image classification", in *2018 international conference on advanced systems and electric technologies (IC_ASET)*, 2018, pp. 397–402.

[22] J. Read and F. Perez-Cruz, "Deep learning for multi-label classification", 2014. *preprint* arXiv:1502.05988.

[23] D. A. Van Dyk and X.-L. Meng, "The art of data augmentation", *J. Comput. Graph. Stat.* **10** (2001), no. 1, pp. 1–50.

[24] C. Shorten and T. M. Khoshgoftaar, "A survey on image data augmentation for deep learning", *J. Big Data* **6** (2019), no. 1, article no. 60.

[25] B. Hu, C. Lei, D. Wang, S. Zhang and Z. Chen, "A preliminary study on data augmentation of deep learning for image classification", 2019. *preprint* arXiv:1906.11887.

[26] Y. Bai, E. Yang, B. Han, et al., "Understanding and improving early stopping for learning with noisy labels", in *NIPS'21: Proceedings of the 35th International Conference on Neural Information Processing Systems*, Curran Associates, Inc., 2021, pp. 24392–24403.

[27] M. Mahsereci, L. Balles, C. Lassner and P. Hennig, "Early stopping without a validation set", 2017. *preprint* arXiv:1703.09580.

ACADÉMIE DES SCIENCES
INSTITUT DE FRANCE

Comptes Rendus. Physique
2024, Vol. 25, Special issue S1, p. 125-139
https://doi.org/10.5802/crphys.188

Research article / *Article de recherche*

Energy in the heart of EM waves: modelling, measurements and management / *L'énergie au cœur des ondes électromagnétiques : modélisation, mesures et gestion*

Analysis of inductive power transfer systems by metamodeling techniques

Analyse de systèmes de transfert de puissance inductifs par des techniques de métamodélisation

Yao Pei [a, *, a, b], **Lionel Pichon** [a, b], **Mohamed Bensetti** [a, b] **and Yann Le Bihan** [a, b]

[a] Université Paris-Saclay, CentraleSupélec, CNRS, Laboratoire de Génie Electrique et Electronique de Paris, 91192, Gif-sur-Yvette, France

[b] Sorbonne Université, CNRS, Laboratoire de Génie Electrique et Electronique de Paris, 75252, Paris, France

E-mail: yao.pei@centralesupelec.fr (Y. Pei)

Abstract. This paper presents some metamodeling techniques to analyze the variability of the performances of an inductive power transfer (IPT) system, considering the sources of uncertainty (misalignment between the coils, the variation in air gap, and the rotation on the receiver). For IPT systems, one of the key issues is transmission efficiency, which is greatly influenced by many sources of uncertainty. So, it is meaningful to find a metamodeling technique to quickly evaluate the system's performances. According to the comparison of Support Vector Regression, Multigene Genetic Programming Algorithm, and sparse Polynomial Chaos Expansions (PCE), sparse PCE is recommended for the analysis due to the tradeoff between the computational time and the accuracy of the metamodel.

Résumé. Ce papier présente différentes techniques de métamodélisation afin d'analyser la variabilité des performances d'un système de transfert de puissance par induction (IPT), en tenant compte des sources d'incertitude (décentrage des bobines, la variation de l'entrefer et la rotation du récepteur). Pour les systèmes IPT, l'une des questions clés est l'efficacité de la transmission, qui est fortement influencée par les nombreuses sources d'incertitude. Il est donc important de déterminer une technique de métamodélisation susceptible d'évaluer rapidement les performances du système. Trois techniques de métamodélisation sont comparées : la régression à vecteurs de support, l'algorithme de programmation génétique multigénique et les développements du chaos polynomial (PCE), il ressort que la technique PCE est recommandée pour une telle analyse en raison du compromis entre le temps de calcul et la précision du métamodèle.

Keywords. Wireless power transfer, Metamodels, Polynomial chaos expansions, Support vector regression, Multigene genetic programming algorithm.

Mots-clés. Transfert d'énergie sans contact, Métamodèles, Développements du chaos polynomial, Régression à vecteurs de support, L'algorithme de programmation génétique multigénique.

Note. This article follows the URSI-France workshop held on 21 and 22 March 2023 at Paris-Saclay.

Manuscript received 18 July 2023, revised 19 February 2024 and 14 May 2024, accepted 15 May 2024.

* Corresponding author

1. Introduction

Around 800 million vehicles with internal combustion engines (ICEs) are used worldwide [1]. These vehicles are a major source of greenhouse gases, especially CO_2. Thus, a practical way of dealing with the global warming problem is to replace ICE-powered vehicles with electric vehicles (EVs) [1–3]. The use of electric cars also improves the quality of air around major cities. To replace ICEs, many vehicle companies are developing "plug-in" EVs, which use lithium-ion (or polymer) batteries that can be recharged at home or at charging stations [2,3]. But the promotion and adoption of plug-in EVs raise many questions. First, the cost of lithium batteries is high. Second, the batteries are heavy. Third, to decrease the charging time for the battery, it requires an expensive infrastructure for charging stations [2–7]. Finally, mishandling the high-power cables will lead to security problems [3, 4, 8, 9]. So, due to these problems, inductive power transfer (IPT) has been introduced as an alternative technology, allowing power flow in a contactless manner. Using a resonant IPT system seems to be an effective technology for the growth of the EVs market [10]. Moreover, its application for the charge during the vehicle's motion is promising to overcome the barriers of heavy onboard battery storage and the long recharging time [3,4,8,9]. IPT is essentially based on the resonance of two magnetically coupled inductors (constituting the coupler): the transmitter, placed on the ground, and the receiver, placed under the vehicle floor.

In a real IPT system scenario, various receiver positions may happen during the park or driving [9]. A careful design process of IPT systems requires considering multiple parameters (misalignment, relative rotation of the receiver, air gap, etc.). So, when using simulation tools, multiple 3D numerical computations are needed to assess the performance of the IPT system when these situations happen. Nevertheless, using complex simulation tools (such as the finite element method) leads to high computational costs for wide parametric analysis. In this case, a standard Monte Carlo (MC) analysis becomes challenging regarding computer resources and simulation time [11, 12].

To solve this problem, "metamodeling techniques" for the parametric and statistical analysis in complex nonlinear problems have been developed. These approaches can reduce the computational cost by substituting an expensive computational model with a so-called metamodel, an analytical approximation of the original model that is much faster to evaluate [11–15]. The metamodels are constructed by learning the varying trend from input parameters and their corresponding model responses, for example, generated from running 3D FEM computations. Because it is faster to evaluate, a metamodel allows more sophisticated analyses, such as sensitivity analysis [16, 17]. In recent literature, several metamodeling techniques have been applied to generate some metamodels trained with a limited set of simulation results, such as Support Vector Regression (SVR) [18], Multigene Genetic Programming Algorithm (MGPA) [19], Polynomial Chaos Expansions (PCE) [20], and so on. Reference [14] focuses on applying the SVR with polynomial kernels to the uncertainty quantification and the parametric modeling of structures. Then, references [14, 15] compare the accuracy and robustness to noise among the SVR, the least squares SVR [21], and the sparse PCE. In the domain of inductive power transfer, a MGPA metamodel is investigated to express the self-inductance and the mutual inductance of the IPT system versus geometrical parameters of the ferrite and coils, so new equations are proposed for evaluating these values of the inductances [22–24]. In [25], sources of uncertainties have been analyzed with different shapes of small-scale couplers by the sparse PCE. Reference [26] has compared the MGPA and sparse PCE metamodeling techniques for the design of IPT systems. Since the design of realistic IPT systems involves complex configurations including many parameters, choosing a fast metamodel is a key point. Comparing different metamodeling techniques in the real-scale couplers for IPT systems is required, and it is important to prove the efficiency in a realistic experiment.

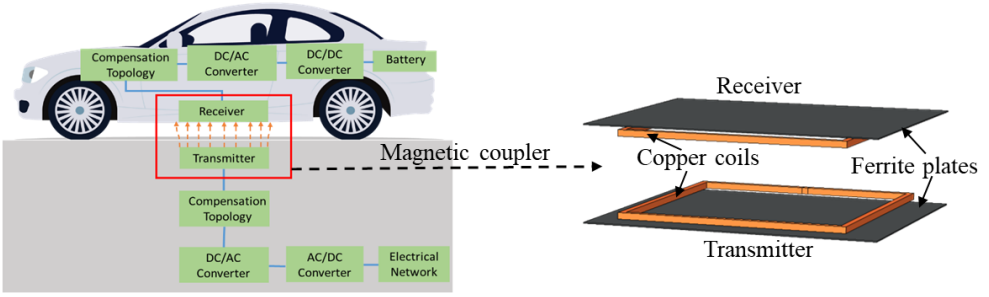

Figure 1. Block diagram of an IPT system.

Therefore, the paper aims to compare several metamodeling techniques for analyzing the mutual inductance of IPT systems, considering the sources of uncertainty (misalignment along the X/Y-axis, variation in air gap, and receiver rotation). First, in Section 2, a 3D model of a practical IPT system is built and numerical predictions related to the electrical parameters and stray magnetic field are validated against experimental measurements. Then, different metamodeling techniques about SVR with the Gaussian radial base function (RBF) kernel, MGPA, and PCE are introduced in Section 3. After, in Section 4, a comparison is presented among these different metamodels for the analysis of square couplers, considering the sources of uncertainty. Finally, the conclusion is given in Section 5.

2. IPT system

2.1. *IPT system introduction*

Figure 1 shows the block diagram of an IPT system for EVs. The system consists of a transmitter, a receiver, converters, and compensation networks for the transmitter and the receiver. The electrical network provides a voltage through the AC/DC converter. The magnetic field produced by the transmitter induces an alternating magnetic field in the receiver. The converters then rectify the AC power to charge the battery. Due to the dimensions of the coils, the parasitic capacitance is insufficient to ensure the resonance in the operational frequency range. Consequently, compensation networks (such as capacitors) are connected to the transmitter and receiver (the self-inductance of the transmitter and the receiver) to adjust the operational frequency and create the resonant state [3,4,8,9,27–30]. It minimizes the reactive power supply and improves both the transmission efficiency and the power transfer capability.

In the system, the magnetic coupler (indicated in the red line frame) is the key part, which normally includes a pair of coils, ferrite plates, and shielding [3,4,8,9,27–30]. The geometry and configuration of the coils are crucial for determining the magnetic field of the IPT system and its efficiency. The ferrite plates influence the efficiency and prevent magnetic flux leakage. The shielding is used to prevent magnetic flux leakage, which is usually placed above the receiver to minimize the flux leakage around the system. Some of the IPT systems take the vehicle chassis as conductive material for shielding [31]. For the IPT system transmission efficiency, circuit models with lumped parameters are often used, and the compensation networks are designed to minimize the reactive component of the power supply. Following [3, 4, 8, 9, 27, 29–34], the series–series (SS) compensation network is taken into account to analyze the power transmission efficiency of the system, as shown in Figure 2. Indeed, according to [3, 4, 8, 9, 27, 29–34], it is suitable for the IPT systems, and the condition of resonance in the SS compensation remains

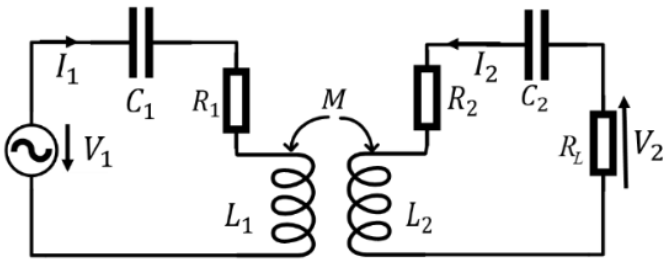

Figure 2. Equivalent electrical circuit in the SS compensation topology [3,4,8,9,27,29–34].

Table 1. Parameters of the magnetic coupler

Parameter	Value (Unit)
Exterior length of the coils l_{ex}	468 (mm)
Interior length of the coils l_{in}	442 (mm)
Coil thickness d_c	13 (mm)
Ferrite length l_f	600 (mm)
Ferrite width w_f	500 (mm)
Ferrite thickness t_f	2 (mm)
Distance between the coils and the ferrite	8 (mm)
Ferrite relative permeability μ_r	2000
Cross-sectional area of the wires S	9.82 (mm^2)
Air gap	150 (mm)

constant, independently of the variations of the mutual inductance and the load R_L. L_1 and L_2 represent the self-inductances of the transmitter and the receiver, respectively; R_1 and R_2 represent the resistances of the transmitter and the receiver, respectively; C_1 and C_2 are the resonant capacitors; M is the mutual inductance between the transmitter and the receiver.

So, the equation to calculate the maximum transmission efficiency η_{max} of the system in Figure 2 can be achieved as below when the transmitter and the receiver are identical [32–34]:

$$\eta_{max} \approx 1 - \frac{2}{kQ} = 1 - \frac{2\sqrt{R_1 R_2}}{w_0 M} = 1 - \frac{R_1}{\pi f_0 M} \tag{1}$$

where the coupling coefficient $k = M/\sqrt{L_1 L_2}$; the system quality factor $Q = 2\pi f_0 \sqrt{L_1 L_2 / R_1 R_2}$ [35–37]; f_0 is the resonant frequency.

2.2. *IPT system experimental validation*

In this work, a square coupler was built in the GeePs laboratory, and shown in Figure 3. The square shape is proven in [33,34] to be well-suited for IPT systems. The parameters of the coupler are summarized in Table 1 [33,34]. The square coupler has six turns arranged in two layers. These turns are made with litz wires composed of 1250 strands, and the strand's diameter is 0.1 mm, so it is smaller than the skin depth at the operating frequency [34]. The operating frequency of the IPT system is around 85 kHz [33–36,38].

Then, the magnetic parameters of the square coupler are simulated in COMSOL 6.1 [39] and measured by a RLC meter (Wayne Kerr 4300), and the results are given in Table 2. The relative errors between the measurement and the simulation are around 10%, which may be caused by the real coil shape that is not exactly the same as defined in the simulation. Also,

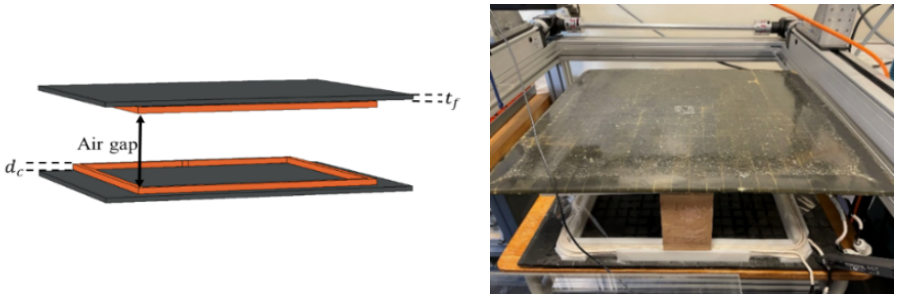

(a) Square magnetic coupler

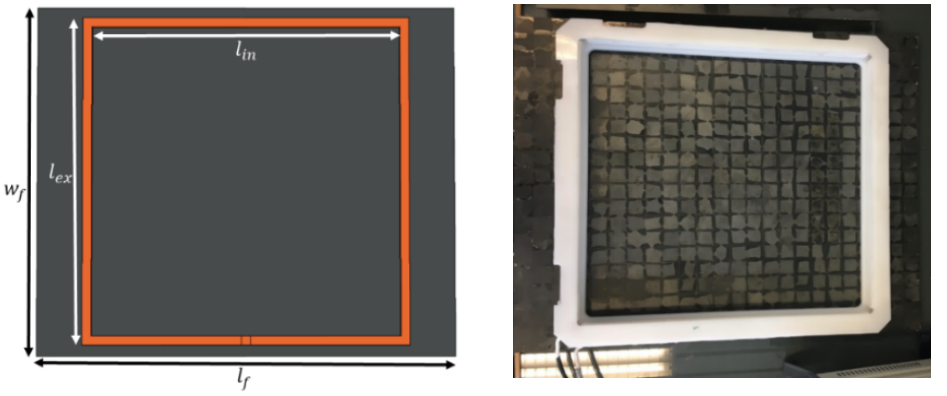

(b) Size of the square magnetic coupler

Figure 3. Simulation model and experimental model of the square magnetic coupler.

Table 2. Comparison of the magnetic parameters in the simulation and the measurement

Frequency = 85 (kHz)	Self-inductance L (μH)	Mutual inductance M (μH)	Coupling coefficient k
Simulation	63.7	13.4	0.21
Measurement	58.5	12.1	0.20
Relative error of the experiment (%)	8.1%	9.7%	4.8%

some uncertainty exists about the winding arrangement in the real coil, which may not be well positioned in two layers.

The magnetic flux density distribution is measured at 150 mm above the receiver as shown in Figure 4. The method to do the measurement in the near-field test bench is presented in [34]. The magnetic probe measures the magnetic field and the robot moves the magnetic probe automatically for different measurement positions.

Figure 5 compares the measured and simulated B_{norm} (the norm of the magnetic flux density) on the measurement line as depicted in Figure 4. The relative error between the measured and simulated B_{norm} is around 10%. There exist differences in the position and the amplitude of the magnetic flux density, probably because the coils of the coupler are made by hand. Hence, they are not exactly the same as those defined in the simulation. Moreover, the ferrite plate in the experiment is not as flat as it is in the simulation. Consequently, the magnetic flux density values of the measurement line are not the same as those in the simulation.

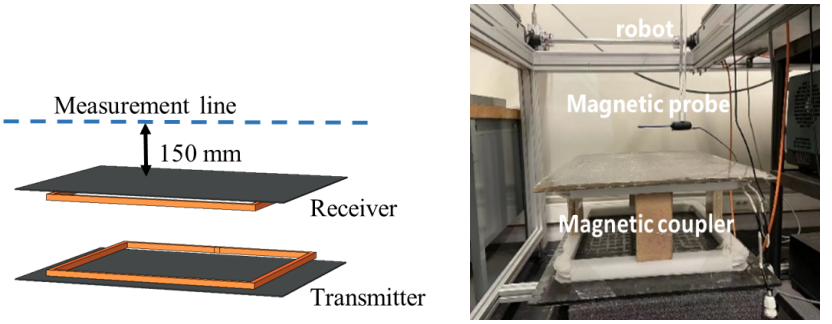

Figure 4. Measurement line of the magnetic flux density above the receiver.

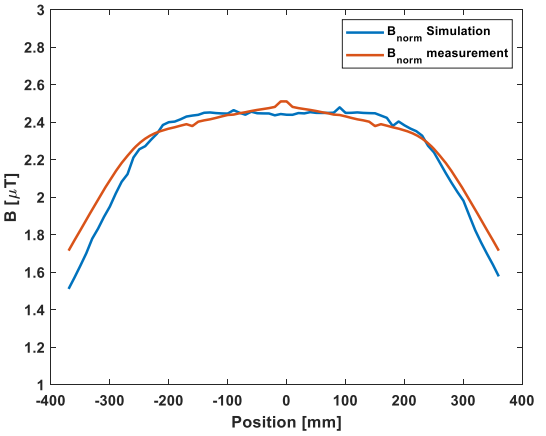

Figure 5. Comparison of the magnetic flux density B_{norm} obtained by the simulation and measurement.

From the results presented above, the reliability of the 3D coupler model has been confirmed through the comparison between the simulated values and the measurement values both for the mutual inductance and the magnetic flux density.

2.3. *Uncertain parameters in the IPT System*

To investigate the efficiency of the IPT system, it is mandatory to consider the sources of uncertainty, such as variations in the misalignment of the receiver due to imperfect parking alignment and variations in the air gap due to loading or unloading the vehicle. Figure 6 shows the rotation angle along the Z-axis α, the misalignment along the X-axis Δx, the misalignment along the Y-axis Δy, and the air gap between two coils Δz for the couplers.

Before performing the uncertainty analysis, it is necessary to assume a probability distribution for the sources of uncertainty. Here, a Gaussian distribution is chosen for these influencing factors, which conforms to the probability that may happen in reality. The statistical parameters of the influencing factors are displayed in Table 3. The range of the air gap and the rotation angle along the Z-axis are referred to [38]. Meanwhile, the range for the misalignment along the X/Y-axis is considered reasonable due to the size of the parking space and the size of the EV chassis.

A parametric sweep for all these influencing factors is very time-consuming. So, it is relevant to build a metamodel using the COMSOl simulation results, which will help save computational

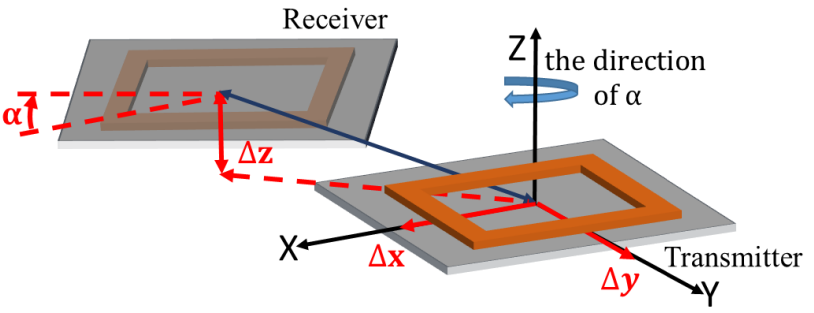

Figure 6. Influencing factors for the square couplers.

Table 3. Properties of the influencing factors

Parameters	Symbol	Distribution	Mean value	Standard deviation
Misalignment along X-axis (mm)	Δx	Gaussian	0	150
Misalignment along Y-axis (mm)	Δy	Gaussian	0	150
Air gap between two coils (mm)	Δz	Gaussian	150	20
Rotation angle along Z-axis (deg)	α	Gaussian	0	3

time. The following section presents a detailed study of the metamodels of the mutual inductance M, considering sources of uncertainty.

3. Metamodeling techniques introduction

This section provides an overview of the mathematical framework behind three metamodeling techniques:

- Support Vector Regression (SVR) with RBF kernel;
- Multigene Genetic Programming Algorithm (MGPA);
- Sparse Polynomial Chaos Expansions (sparse PCE).

They are considered promising techniques which allow building metamodels for the nonlinear system responses with several variables [14, 15, 20–26].

3.1. *Support vector regression metamodeling*

Support vector regression (SVR) is a metamodeling technique approximating an unknown or expensive-to-evaluate model. It represents a class of learning techniques for regression tasks developed by Vapnik [40]. This method provides significant generalization capabilities, thus making it less likely to overfit data.

SVR attempts to approximate the relationship between the input variables $x = [x_1, \ldots, x_d] \in \mathbb{R}^d$ and the output $y \in \mathbb{R}$ given a training data set of N samples $\{(\boldsymbol{x}_i, y_i)\}_{i=1}^N$ ($y = M(\boldsymbol{x})$ is the model response of the system supposed to be a scalar quantity with a finite variance, where M is a numerical model presenting the observed phenomenon). It achieves this through the equation [14, 18, 21]:

$$\mathscr{M}^{\mathrm{SVR}}(\boldsymbol{x}) = \boldsymbol{w}^T \Phi(\boldsymbol{x}) + b \tag{2}$$

where $\Phi(\boldsymbol{x}) = [\phi_1(\boldsymbol{x}), \ldots, \phi_D(\boldsymbol{x})]$ is a nonlinear mapping function $\Phi(\cdot)$: $\mathbb{R}^d \to \mathbb{R}^D$ which maps the parameter space of dimension d into the corresponding *feature space* of dimension D; $\boldsymbol{w} \in \mathbb{R}^D$ is

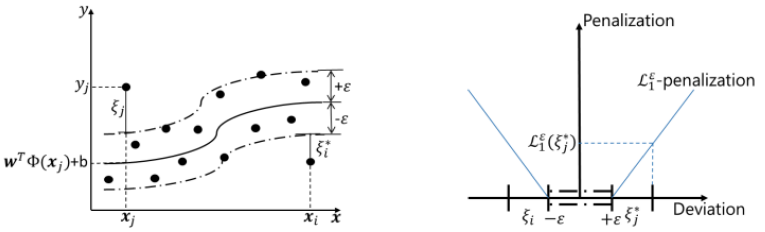

Figure 7. (a) Only the vectors outside the ε -insensitive tube (dotted line area) are penalized; (b) Penalization of deviations larger than ε for $\mathscr{L}^\varepsilon$ loss function [14, 15, 18].

a vector collecting the unknown coefficients of the nonlinear regression; $b \in \mathbb{R}$ is a bias term that is retrieved as a by-product of the solution in [14, 15, 18]; $\boldsymbol{w}^T\Phi(\boldsymbol{x})$ is defined as the inner product in $\mathbb{R}^D$ [18]. The dimensionality of the *feature space* D is defined by the nonlinear map $\Phi(\boldsymbol{x})$.

Assuming that we can tolerate a deviation of at most ε between $\mathscr{M}^{\text{SVR}}(\boldsymbol{x})$ and y, so only when the absolute value of the difference between $\mathscr{M}^{\text{SVR}}(\boldsymbol{x})$ and y is greater than ε, it needs to reduce this deviation. Then, the SVR model expression can be formalized to find $\boldsymbol{w}$ following the minimization equation [18]:

$$\min_{\boldsymbol{w}} \frac{1}{2}\|\boldsymbol{w}\|^2 + C\sum_{i=1}^{N} \mathscr{L}^\varepsilon(\mathscr{M}^{\text{SVR}}(\boldsymbol{x}_i), y_i) \tag{3}$$

where $C \in \mathbb{R}^+$ is a regularization parameter, chosen by cross-validation, which provides a trade-off between the accuracy of the model on the training data set and its flatness to avoid overfitting leading to an oscillating behavior [18]; $\mathscr{L}^\varepsilon$ is the ε-insensitive loss function, which is most widely used as follows (called: $\mathscr{L}_1$-penalization) [14, 15, 18]:

$$\mathscr{L}_1^\varepsilon(\boldsymbol{x}; y) = \begin{cases} 0 & \text{if } |\mathscr{M}^{\text{SVR}}(\boldsymbol{x}) - y| < \varepsilon, \\ (|\mathscr{M}^{\text{SVR}}(\boldsymbol{x}) - y| - \varepsilon) & \text{otherwise.} \end{cases} \tag{4}$$

A nonlinear regressor considering this loss function is illustrated in Figure 7(a). Any point that is outside the ε-insensitive tube needs to be penalized, illustrated in Figure 7(b). The best combination of the parameters $(\boldsymbol{w}, b)$ minimizes the deviation of the model predictions from the training samples outside the ε-intensive zone.

The parameters for building an SVR metamodel in this chapter are shown below, implemented within UQLAB version 2.0 [18, 41], which is fully compatible with the MATLAB environment. UQLAB is a general purpose Uncertainty Quantification framework developed at ETH Zurich (Switzerland), which is made of open-source scientific modules.

- Loss function: L_1 ε-insensitive.
- Kernel function: Gaussian radial basis function (RBF)

$$k_{\text{Gaussian}}(\boldsymbol{x}_i, \boldsymbol{x}_j) = \exp\left(-\frac{\|\boldsymbol{x}_i - \boldsymbol{x}_j\|^2}{2\sigma^2}\right) \tag{5}$$

where $\|\boldsymbol{x}_i - \boldsymbol{x}_j\|$ is the Euclidean distance between $\boldsymbol{x}_i$ and $\boldsymbol{x}_j$. The larger this distance, the smaller the value of RBF. $\sigma > 0$ is the width of the RBF. The smoothness of the Gaussian RBF is controlled by the magnitude of σ (the higher σ, the smoother the Gaussian RBF).

3.2. *Multigene genetic programming algorithm metamodeling*

In MGPA, each prediction M^{MGPA} of the model output is formed by the weighted output of the genes plus a bias term. Each gene is a function of the d input variables $\boldsymbol{x} = \{x_1, \ldots, x_d\}$ of the system. Given a training data set of N samples $\{(\boldsymbol{x}_i, y_i)\}_{i=1}^{N}$ ($y = M(\boldsymbol{x})$ is the model response of the system supposed to be a scalar quantity with a finite variance, where M is a numerical model presenting the observed phenomenon), the MGPA metamodel can be expressed as [19]:

$$M^{\mathrm{MGPA}}(\boldsymbol{x}) = d_0 + d_1 \times \text{gene } 1 + \cdots + d_Q \times \text{gene } Q$$
$$= d_0 + d_1 \times \quad + d_2 \times \quad + \cdots + d_Q \times \quad \tag{6}$$

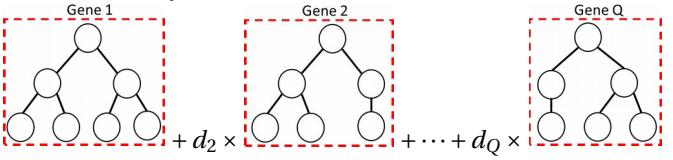

where d_0 is the bias term, $d_1, \ldots, d_Q$ are the gene weights and Q is the number of genes. The weights $\boldsymbol{d}(\boldsymbol{d} = [d_0 d_1 \cdots d_Q])$ for the genes are automatically determined by using an ordinary least square method to regress the genes against a training data set [19]. Each gene combines a set of elementary functions with the input variables (such as sum, multiplication, division, logarithm, arctangent, hyperbolic tangent, sine, exponential, power function, etc.), and the gene depth is the number of levels in the gene structure. The expression of the MGPA metamodel is evolved automatically by using the training data set [19, 22, 23].

The process of building a metamodel with the MGPA method is [19]:

(1) Load the training data set (a set of existing input values and corresponding model response values);

(2) The genetic algorithm works on a population of metamodels, each one representing a potential solution for expressing the relationship between the input variables and the model response. The initial population of the metamodels is evolved automatically by using the training data set. During its evolution, this algorithm transforms the current population of metamodels into a new population by applying the classical genetic operations (selections, cross over, mutation, etc.) [42]. When it achieves the maximum generation, the MGPA metamodel will be picked out in terms of high coefficient of determination (R^2) and low model complexity [19]. The model complexity is computed as the simple sum of the number of nodes (the number of elementary functions plus the number of occurrences of the input variables) inside its constituent genes [43], and R^2 is calculated as below [19]:

$$R^2 = 1 - \frac{\sum_{i=1}^{N} (M(\boldsymbol{x}_i) - M^{\mathrm{MGPA}}(\boldsymbol{x}_i))^2}{\sum_{i=1}^{N} \left(M(\boldsymbol{x}_i) - \frac{1}{N}\sum_{i=1}^{N} M(\boldsymbol{x}_i)\right)^2} \tag{7}$$

where $M(\boldsymbol{x}_i)$ is the ith value from the studied system, $M^{\mathrm{MGPA}}(\boldsymbol{x}_i)$ is the predicted value on the MGPA metamodel, and N is the number of samples in the training data set. This value ranges from 0 to 1.

The MGPA toolbox is provided by GPTIPS, which is a free, open-source MATLAB-based software platform [19]. It can automatically evolve both the structure and the parameters of the mathematical model from the training data set. However, how to appropriately define the maximum number of genes and the maximum gene depth for an accurate MGPA metamodel needs to be carefully considered.

3.3. *Sparse polynomial chaos expansions metamodeling*

Polynomial Chaos Expansions (PCE) is a metamodeling technique that provides a functional approximation for the relationship between the input variables and model output in a non-intrusive way [20, 44]. It means that it focuses only on the one-to-one mapping relationship between input and output. Furthermore, the post-process of the PCE metamodel can also help to find the most influential input variable to the model output.

It starts by considering the vector $\boldsymbol{x} \in \mathbb{R}^d$ collecting d independent input variables $\{x_1, \ldots, x_d\}$ with a joint probability density function (PDF) $f_{\boldsymbol{X}}(x)$, representing the input variables of the physic system. Given a training data set of N samples $\{(\boldsymbol{x}_i, y_i)\}_{i=1}^N$ ($y = M(\boldsymbol{x})$ is the model response of the system supposed to be a scalar quantity with a finite variance, where M is a numerical model presenting the observed phenomenon), the PCE metamodel is established to simulate the varying trend of the model response [20, 44]:

$$M^{\mathrm{PCE}}(\boldsymbol{x}) = \sum_{\alpha \in \mathbb{N}^d} \hat{c}_\alpha \Phi_\alpha(\boldsymbol{x}) \tag{8}$$

where $\hat{c}_\alpha$ are the unknown deterministic coefficients, and $\Phi_\alpha(\boldsymbol{x})$ are multivariate polynomials basis functions which are orthonormal with respect to the joint PDF $f_{\boldsymbol{x}}(x)$. $\alpha \in \mathbb{N}^d$ is a multi-index that identifies the components of the multivariate polynomials Φ_α. If the input variables have a uniform distribution, the orthogonal polynomial is Legendre; while if the input variables have a Gaussian distribution, the orthogonal polynomial is Hermite [44].

The coefficients $\hat{c}_\alpha$ are obtained by post-processing the experimental design $\{(\boldsymbol{x}_i, y_i)\}_{i=1}^N$, a training data set consisting of N samples of the input variables and the corresponding model responses y. From the set of model responses, the coefficients can be estimated by the ordinary least square regression method [16, 20, 44]. For this, the infinite series in Equation (9) has to be truncated. Choosing a maximum polynomial degree p, the usual truncation scheme preserves all polynomials associated with the set [16, 20, 44]:

$$\mathscr{A}^{d,p} = \left\{ \alpha \in \mathbb{N}^d : \|\alpha\|_1 = \sum_{i=1}^{d} \alpha_i \leq p \right\}. \tag{9}$$

Thus, the cardinal of the set $\mathscr{A}^{d,p}$ denoted $L = (d+p)!/d!p!$ increases quickly with the number of input variables d and the degree p of the polynomials [16, 20]. This leads that the size of the PCE retained in the set $\mathscr{A}^{d,p}$ will be too large when dealing with high-dimensional problems.

In order to overcome this limitation, a hyperbolic truncation strategy $\mathscr{A}_q^{d,p}$ based on the total degree p and a parameter q, with $0 < q < 1$, allowing for reduction of the size of the PCE basis is then defined as follows [16, 20, 44]:

$$\mathscr{A}_q^{d,p} = \left\{ \alpha \in \mathbb{N}^d : \|\alpha\|_q = \left(\sum_{i=1}^{d} \alpha_i^q \right)^{1/q} \leq p \right\}. \tag{10}$$

This favors the most relevant effects and low-order interactions, which are known to have the largest impact on the variability of the model response according to the sparsity-of-effects principle [44]. It is important to point out that lower values of q imply a larger number of neglected high-rank interactions. In addition, when $q = 1$, this scheme is equivalent to the standard PCE. When $q < 1$, the retained terms of the polynomial basis can be substantially reduced [20, 44].

3.4. *Error estimates of a metamodel*

After the metamodel is constructed, its accuracy can be quantified by estimating the Root Mean Square Error (RMSE) obtained with the metamodel on the training data set. It is defined as:

$$\varepsilon_{\mathrm{RMSE}} = \sqrt{\frac{\sum_{i=1}^{\mathrm{N}} (M^{\mathrm{metamodel}}(\boldsymbol{x}_i) - M(\boldsymbol{x}_i))^2}{N}} \tag{11}$$

where $M(\boldsymbol{x}_i)$ is the model response of the training data set, $M^{\mathrm{metamodel}}(\boldsymbol{x}_i)$ is the prediction value from the metamodels above, and N is the number of samples in the training data set.

Except for the training data set used to construct the metamodel, a test data set different from the training samples, can be used to validate the predictive performance. The test error between the test data set and the predictive values on the metamodel can also be calculated by RMSE.

4. Metamodeling techniques for square couplers taking into account sources of uncertainty

Here, the SVR with RBF kernel, MGPA, and the sparse PCE metamodeling techniques are implemented to build a metamodel for small-scale square couplers and are compared below. The results given in this section were done with a XEON E5-1620, 8-core processor, working at 3.70 GHz. The 3D model of the couplers is obtained by COMSOL 5.6, and the SVR and PCE metamodels are calculated in MATLAB 2019b with the UQLAB Framework, while the MGPA metamodel is calculated in MATLAB 2017b due to the limitation of the GPTIPS toolbox functions.

The SVR with RBF kernel, MGPA, and the sparse PCE methods have been adopted to quantify the impact of these uncertainty parameters on the mutual inductance M of small-scale square couplers. In addition, the parameters on MGPA and sparse PCE methods are chosen considering the metamodel accuracy and the computational time to build an accurate metamodel. The SVR with RBF kernel builds a metamodel in light of the L_1 ε-insensitive loss function. The MGPA metamodel is performed with the following settings: Population size = 300, Number of generations = 100, Maximum number of genes = 6, and Maximum gene depth = 4. The sparse PCE metamodel is constructed by the adaptive degree method [20, 44], in which the degree of PCE metamodel varies from 3 to 15 to select the most accurate one. The hyperbolic scheme in Equation (10) is set to $q = 0.75$ to reduce the size of the polynomial basis.

1000 samples are chosen by the Latin hypercube sampling (LHS) method [45] and formed as the database. All metamodels have been trained from the same training dataset containing around one-third of the samples of the database. This data set results from COMSOL simulations with a computational cost of 6 h (one simulation with the full solver takes about 50 s). To investigate the performance of the obtained metamodels, their predictions are then compared with a test data set containing the remaining database samples. Table 4 provides a detailed comparison of the accuracy and the computational cost of the proposed metamodeling techniques by collecting the RMSE on the training data set and the test data set, along with the corresponding computational time t_{training} and the predictive time $t_{\mathrm{predictive}}$ (to predict one output) respectively. It also shows that the sparse PCE metamodel turns out to use the least computational time and to be the most accurate metamodel with a training RMSE and a test RMSE, which is better than the accuracies obtained by the SVR and MPGA metamodels.

Furthermore, another 1000 samples selected by the MC method are computed in COMSOL to form a new data set. Figure 8 provides the scatter plots for the metamodels of the mutual inductance on the SVR, MGPA, and sparse PCE methods. These plots emphasize a good agreement between these metamodels and this data set because the samples are very close to the solid lines.

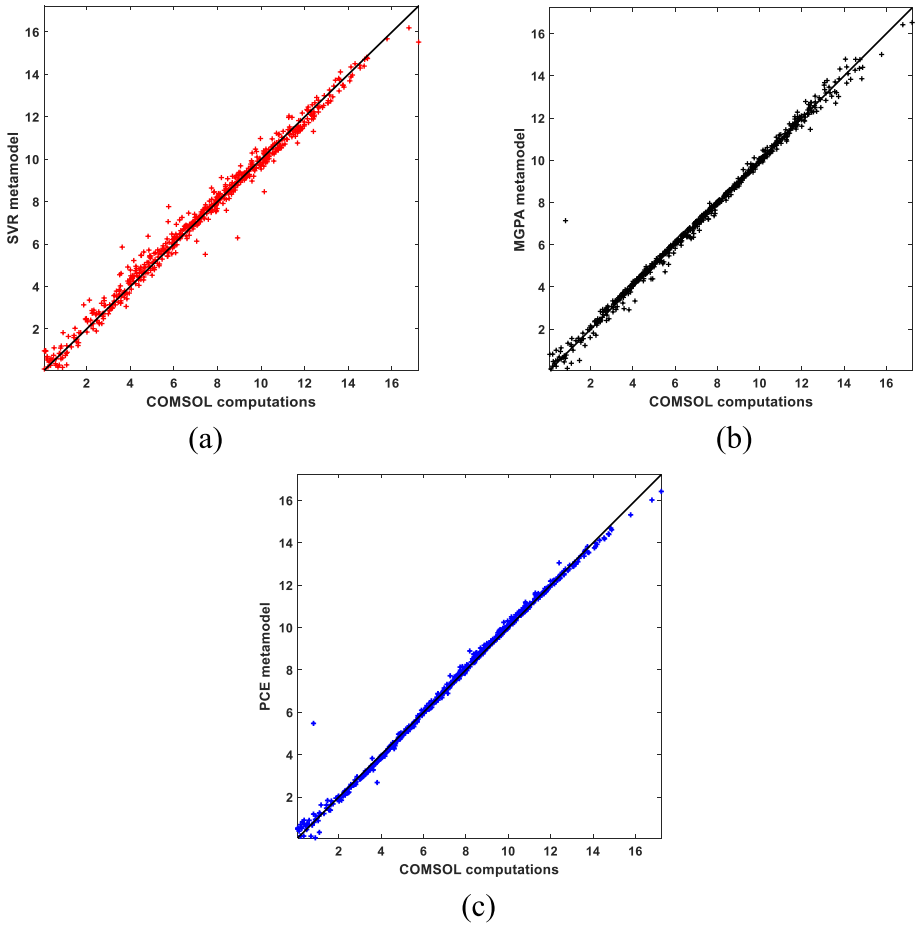

Figure 8. Scatter plots of the mutual inductance providing a comparison among the predictions of the SVR metamodel with RBF kernel (red marker in (a)), the MGPA metamodel (black marker in (b)), the sparse PCE metamodel (blue marker in (c)) and the results of COMSOL computations.

Table 4. Comparison of the accuracy and the computational cost of the SVM, MPGA, and PCE metamodels computed for the square couplers

Method	Training RMSE	Test RMSE	t_{training}	$t_{\text{predictive}}$
COMSOL computations	-	-	6.45 h	60 s
SVR (RBF)	0.0266	0.0420	2.48 s	<1 s
MGPA	0.0233	0.0475	313.54 s	<1 s
Sparse PCE	0.0158	0.0270	0.357 s	<1 s

Then, the impact of the influencing factors on the mutual inductance is illustrated in Figure 9, where the probability density functions (PDFs) of the mutual inductance estimated via the SVR, MGPA, and sparse PCE metamodels are compared with the PDF of the COMSOL computations. It can be seen that the variability of the mutual inductance is well captured by these metamodels, which confirms a good estimation of the PDF of the mutual inductance with these metamodels and highlights a similar level of accuracy. In terms of computational cost, this data set, including

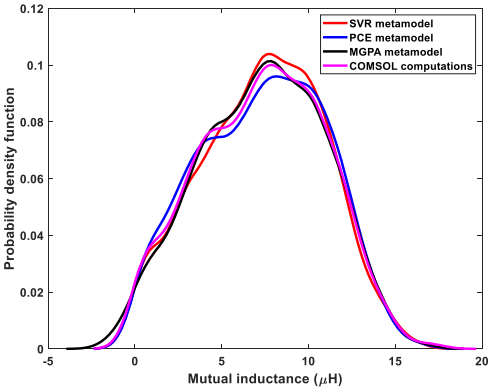

Figure 9. PDFs of the mutual inductance obtained from the SVR (solid red curve), MGPA (solid black curve) and sparse PCE metamodels (solid blue curve) compared with the PDF of COMSOL computations (solid magenta curve).

1000 samples, required about 14 h to compute in COMSOL, while the metamodels on the SVR, MGPA, and sparse PCE need less than 1 minute. It is worth noting that this computational cost does not include the time to generate the training samples from LHS in COMSOL, which were needed for constructing the metamodels.

Compared to the other metamodeling techniques based on the same dataset, the sparse PCE metamodeling technique uses less time to build a metamodel and provides more accurate results. So, it is meaningful to choose such an approach to analyse the performances of the coupler, taking into account the sources of uncertainty.

5. Conclusion

This paper provides an overview of SVR with RBF kernel, MGPA, and PCE metamodeling techniques and their application in case of analyzing an IPT system. When the metamodels are built by these techniques, the ways to evaluate the accuracy and build the PDF are also summarized. Some metamodeling techniques (SVR with RBF kernel, MGPA, and sparse PCE) are built and compared for analyzing the mutual inductance M of the magnetic couplers considering sources of uncertainty. Due to the tradeoff between the computational time and the accuracy of the metamodel, the sparse PCE metamodeling technique appears to be a very useful tool in the analysis of IPT systems. Then, it will be used in the next step to address the magnetic and thermal coupled field analysis. Indeed, when a high-power IPT system works for a long time, the heating of the magnetic coupler brings adverse effects on the efficiency and stability of the system. An accurate prediction of such a phenomenon will improve the assessment of IPT performances.

Declaration of interests

The authors do not work for, advise, own shares in, or receive funds from any organization that could benefit from this article, and have declared no affiliations other than their research organizations.

References

[1] M. Eshani *et al.*, "Modern electric, hybrid electric and fuel cell vehicles", in *Fundamentals, Theory, and Design*, CRC Press, Boca Raton, FL, 2005.

[2] M. Yilmaz, P. T. Krein, "Review of battery charger topologies, charging power levels, and infrastructure for plug-in electric and hybrid vehicles", *IEEE Trans. Power Electron.* **28** (2013), no. 5, p. 2151-2169.
[3] C. T. Rim, C. Mi, "Wireless Power Transfer for Electric Vehicles and Mobile Devices | IEEE eBooks | IEEE Xplore", Accessed: July 10, 2024. [Online]. Available: https://ieeexplore.ieee.org/book/7953908.
[4] T. M. Fisher *et al.*, "Electric vehicle wireless charging technology: a state-of-the-art review of magnetic coupling systems", *Wireless Power Transf.* **1** (2014), no. 2, p. 87-96.
[5] "J1772_202401 : SAE Electric Vehicle and Plug-in Hybrid Electric Vehicle, Conductive Charge Coupler - SAE International", Accessed: July 10, 2024. [Online]. Available: https://www.sae.org/standards/content/j1772_202401/.
[6] "Charger Types and Speeds | US Department of Transportation", Accessed: July 10, 2024. [Online]. Available: https://www.transportation.gov/rural/ev/toolkit/ev-basics/charging-speeds.
[7] Z. J. Lee, J. Z. Pang, S. H. Low, "Pricing EV charging service with demand charge", *Electr. Power Syst. Res.* **189** (2020), article no. 106694.
[8] A. Mahesh, B. Chokkalingam, L. Mihet-Popa, "Inductive wireless power transfer charging for electric vehicles—a review", *IEEE Access* **9** (2021), p. 137667-137713, https://10.1109/ACCESS.2021.3116678.
[9] C. Panchal, S. Stegen, J. Lu, "Review of static and dynamic wireless electric vehicle charging system", *Eng. Sci. Technol. Int. J.* **21** (2018), no. 5, p. 922-937, https://10.1016/j.jestch.2018.06.015.
[10] "Electric Vehicles - Worldwide – Statista Market Forecast", Statista. Accessed: July 10, 2024. [Online]. Available: https://www.statista.com/outlook/mmo/electric-vehicles/worldwide.
[11] M. Larbi *et al.*, "Variability impact of many design parameters: the case of a realistic electronic link", *IEEE Trans. Electromagn. Compat.* **60** (2018), no. 1, p. 34-41.
[12] S. De Ridder *et al.*, "A generative modeling framework for statistical link analysis based on sparse data", *IEEE Trans. Compon. Packag. Manuf. Technol.* **8** (2018), no. 1, p. 21-31.
[13] V. Cirimele *et al.*, "Uncertainty quantification for SAE J2954 compliant static wireless charge components", *IEEE Access* **8** (2020), p. 171489-171501.
[14] R. Trinchero *et al.*, "Machine learning and uncertainty quantification for surrogate models of integrated devices with a large number of parameters", *IEEE Access* **7** (2019), p. 4056-4066.
[15] R. Trinchero *et al.*, "Machine learning for the performance assessment of high-speed links", *IEEE Trans. Electromagn. Compat.* **60** (2018), no. 6, p. 1627-1634.
[16] B. Sudret, "Global sensitivity analysis using polynomial chaos expansions", *Rel. Eng. Syst. Saf.* **93** (2008), no. 7, p. 964-979.
[17] I. M. Sobol, "Sensitivity estimates for nonlinear mathematical models", *Math. Model. Comput. Exp.* **1** (1990), no. 4, p. 407-414.
[18] M. Moustapha *et al.*, "UQLab user manual – Support vector machines for regression", in *Report UQLab-V2.0-111, Chair of Risk, Safety and Uncertainty Quantification*, ETH Zurich, Switzerland, 2022.
[19] D. P. Searson, "GPTIPS 2: an open-source software platform for symbolic data mining", in *Handbook of Genetic Programming Applications* (A. H. Gandomi, A. H. Alavi, C. Ryan, eds.), Springer International Publishing, Cham, 2015, p. 551-573.
[20] G. Blatman, B. Sudret, "Adaptive sparse polynomial chaos expansion based on least angle regression", *J. Comput. Phys.* **230** (2011), no. 6, p. 2345-2367.
[21] J. A. K. Suykens *et al.*, *Least Squares Support Vector Machines*, World Scientific, Singapore, 2002.
[22] G. D. Capua *et al.*, "Mutual inductance behavioral modeling for wireless power transfer system coils", *IEEE Trans. Ind. Electron.* **68** (2021), no. 3, p. 2196-2206.
[23] A. Delgado *et al.*, "Self and mutual inductance behavioral modeling of square-shaped IPT coils with air gap and ferrite core plates", *IEEE Access* **10** (2022), p. 7476-7488.
[24] G. Di Capua *et al.*, "Analysis of dynamic wireless power transfer systems based on behavioral modeling of mutual inductance", *Sustainability* **13** (2021), no. 5, article no. 2556.
[25] Y. Pei *et al.*, "Comparison of coupling coils for static inductive power-transfer systems taking into account sources of uncertainty", *Sustainability* **13** (2021), no. 11, article no. 6324.
[26] Y. Pei *et al.*, "Fast shielding optimization of an inductive power transfer system for electric vehicles", *IEEE Access* **10** (2022), p. 91227-91234.
[27] A. Triviō-Cabrera, J. M. González-González *et al.*, "Wireless Power Transfer for Electric Vehicles: Foundations and Design Approach", Accessed: July 10, 2024. [Online]. Available: https://link.springer.com/book/10.1007/978-3-030-26706-3.
[28] "Vehicle Initiative Consortium for Transport Operation and Road Inductive Applications", Victoria Project, April 25, 2017. http://greentechlatvia.eu/wp-content/uploads/bsk-pdf-manager/1-8_Project_Victoria_(Bludszuweit)_8.pdf (accessed September 19, 2022).
[29] V. Cirimele, M. Diana, F. Freschi, M. Mitolo, "Inductive power transfer for automotive applications: state-of-the-art and future trends", *IEEE Trans. Indus. Appl.* **54** (2018), no. 5, p. 4069-4079.

[30] G. A. Covic, J. T. Boys, "Modern trends in inductive power transfer for transportation applications", *IEEE J. Emerging Sel. Top.n Power Electron.* **1** (2013), no. 1, p. 28-41.

[31] M. Ibrahim, *Wireless Inductive Charging for Electrical Vehicules: Electromagnetic Modelling and Interoperability Analysis*, Phd thesis, 2014, Université Paris Sud – Paris XI. Accessed February 11, 2024. [Online]. Available: https://tel.archives-ouvertes.fr/tel-01127163.

[32] P. S. R. Nayak, D. Kishan, "Design and analysis of SS resonant IPT system with computed mutual inductance through FEM model", in *2018 International Conference on Power, Instrumentation, Control and Computing (PICC), Thrissur, India, January*, 2018, p. 1-5.

[33] K. Kadem *et al.*, "Optimal coupler topology for dynamic wireless power transfer for electric vehicle", *Energies* **14** (2021), no. 13, article no. 3983.

[34] K. Kadem, *Modélisation et optimisation d'un coupleur magnétique pour la recharge par induction dynamique des véhicules électriques*, Theses, Centralesupelec, 2020, Accessed August 29, 2022. [Online]. Available: https://hal.archives-ouvertes.fr/tel-03253967.

[35] R. Bosshard, J. Mühlethaler, J. W. Kolar, I. Stevanović, "Optimized magnetic design for inductive power transfer coils", in *2013 Twenty-Eighth Annual IEEE Applied Power Electronics Conference and Exposition (APEC), Long Beach, CA, USA, March*, 2013, p. 1812-1819.

[36] R. Bosshard, J. W. Kolar, J. Mühlethaler, I. Stevanović, B. Wunsch, F. Canales, "Modeling and η - α -pareto optimization of inductive power transfer coils for electric vehicles", *IEEE J. Emerging Sel. Top. Power Electron.* **3** (2015), no. 1, p. 50-64.

[37] R. W. Erickson, D. Maksimović, "Inductor design", in *Fundamentals of Power Electronics* (R. W. Erickson, D. Maksimović, eds.), Springer US, Boston, MA, 2001, p. 539-564.

[38] "J2954 : wireless power transfer for light-duty plug-in/electric vehicles and alignment methodology - SAE International", Accessed: July 10, 2024. [Online]. https://www.sae.org/standards/content/j2954_202010/.

[39] "Software for Simulating Static and Low-Frequency Electromagnetics", COMSOL. Accessed: July 10, 2024. https://www.comsol.com/acdc-module.

[40] V. N. Vapnik, *The Nature of Statistical Learning Theory*, Springer, New York, NY, 2000, Accessed: July 10, 2024. [Online]. Available: https://link-springer-com.ezproxy.universite-paris-saclay.fr/book/10.1007/978-1-4757-3264-1.

[41] S. Marelli, B. Sudret, "UQLab: a framework for uncertainty quantification in Matlab", in *Proceedings of the 2nd International Conference on Vulnerability, Risk Analysis and Management (ICVRAM2014), Liverpool, United Kingdom*, 2014, p. 2554-2563.

[42] M. Mitchell, *An Introduction to Genetic Algorithms*, The MIT Press, Cambridge, MA, 1998, Accessed: July 10, 2024. [Online]. Available: https://mitpress.mit.edu/books/introduction-genetic-algorithms.

[43] G. F. Smits, M. Kotanchek, "Pareto-front exploitation in symbolic regression", in *Genetic Programming Theory and Practice II* (U.-M. O'Reilly, T. Yu, R. Riolo, B. Worzel, eds.), Springer US, Boston, MA, 2005, p. 283-299.

[44] S. Marelli, N. Luthen, B. Sudret, *UQLab user manual – Polynomial chaos expansions, Report UQLab-V2.0-104, Chair of Risk, Safety and Uncertainty Quantification*, ETH Zurich, Switzerland, 2022.

[45] C. Lataniotis *et al.*, *UQLab user manual – The Input module, Report UQLab-V2.0-102, Chair of Risk, Safety and Uncertainty Quantification*, ETH Zurich, Switzerland, 2022.

ACADÉMIE DES SCIENCES
INSTITUT DE FRANCE

Comptes Rendus. Physique
2024, Vol. 25, Special issue S1, p. 141-156
https://doi.org/10.5802/crphys.184

Review article / *Article de synthèse*

Energy in the heart of EM waves: modelling, measurements and management / *L'énergie au cœur des ondes électromagnétiques : modélisation, mesures et gestion*

Matching of an observed event and its virtual model in relation to smart theories, coupled models and supervision of complex procedures—A review

Appariement d'un évènement observé et de son modèle virtuel en relation aux théories intelligentes, aux modèles couplés et à la supervision de procédures complexes — Bilan

Adel Razek [a]

[a] Group of Electrical Engineering – Paris (GeePs), CNRS, University of Paris-Saclay and Sorbonne University, F91190 Gif sur Yvette, France

E-mail: adel.razek@centralesupelec.fr

Abstract. This contribution aims to illustrate the nature of the observation–modeling (or real–virtual) link, the importance of the exact model (or coupled model) in the matching involved in this link and the use of this link in the supervision of complex procedures. This involves offline and real-time matching practices. The offline case is mainly about the management and ruling of elegant theories and computational tools mimicking physical paradigms. Real-time pairing notably concerns natural phenomena, autonomous automated systems and complex procedures. The paper assesses, analyzes and discusses the different elements mentioned. This is aided by a literature review.

Résumé. Cette contribution vise à illustrer la nature du lien observation–modélisation (ou réel–virtuel), l'importance du modèle exact (ou modèle couplé) dans l'appariement impliqué dans ce lien et l'utilisation de ce lien dans la supervision de procédures complexes. Cela implique des pratiques de mise en correspondance hors ligne et en temps réel. Le cas hors ligne concerne principalement la gestion de théories élégantes et d'outils informatiques imitant des paradigmes physiques. L'appariement en temps réel concerne notamment les phénomènes naturels, les systèmes automatisés autonomes et les procédures complexes. Le document évalue, analyse et discute les différents éléments mentionnés. Cela est assisté par une revue de la littérature.

Keywords. Matching, Coupled models, Electromagnetic systems, Complex producers, Supervision.

Mots-clés. Appariement, Modèles couplés, Systèmes électromagnétiques, Producteurs complexes, Supervision.

Note. This article follows the URSI-France workshop held on 21 and 22 March 2023 at Paris-Saclay.

Manuscript received 26 May 2023, revised 17 January 2024, accepted 19 March 2024.

1. Introduction

Cognitive inference or virtual modeling can account for the observation of an object, phenomenon or procedure. Pairing or mirroring an observable and its virtual image has been, and still is done in many natural and man-made situations. Humankind, other creatures and natural elements often exercise the practice of observation, experience or sensory manipulation. At the same time, from this practice, they will eventually use deductive (or mimesis) skills to manage their evolution, self-protection, comfort, and survival. The activity of deduction associated with observation is one of the first natural duties born in the world. Deduction, prediction, or reasoning (modeling) associated with observation may be encountered in inherent natural events or manufactured procedures. Such a couple often works according to a process of pairing or imitation. For example, in nature, based on observation, cases of mimetic simulation (imitation strategy) are very frequent allowing camouflage [1]. This permits creatures to blend into their surroundings. This could involve simple matching or dynamic (adaptive) matching.

Both cases of link observation–modeling involving offline and online matching can be used in distinct matching categories. The offline one can be practiced in managing universal elegant theories involving their validation, explanation and unification. The online matching procedures of the link observation–modeling are practiced in various natural processes and artificial modern applications related to the supervision of automated and complex systems. In these applications, we need to reduce the involved uncertainties to achieve an optimized supervision. Such reduction is mostly needed in the virtual side of the link. Thus, we need accurate realistic system models, which can be obtained by reintegrating neglected items committed in idealizing for elegance of theories. Such coupled models permit optimized matching of the link observation–modeling. We see that the matching in the link is closely associated to elegant theories and coupled models, respectively for offline theories managing and online systems supervision.

Indeed, the foundation of basic research is built on elegant and consistent theories, which is essential for science. Let us illustrate the notion of elegance in the theories that belong to fundamental science. When a theory or model clearly and directly describes a phenomenon, it is said to be elegant. Additionally, an easy-to-understand enterprise can capture a lot of information and answer many questions. Therefore, the definition of elegance as simplicity plus greater capacity seems fair. Note that this last statement is valid only when the theory is applied in its strict scope. One of the most famous elegant unified theories is Maxwell's set of equations [2]. The case of Maxwell's equations illustrated the interest of the concept of elegance. However, later in this article in the application to electromagnetic systems, we will see that in real systems, Maxwell's equations could not always be applied immediately and such elegance could conflict with real applications. In such cases, one must make a volte-face from elegance to reality by reconsidering the corresponding committed approximations. We are therefore inclined to modify the model based on the theory of the main field, by combining the secondary fields in a modified coupled model [3]. Such a modified model resulting from "retrograde postulations" paradoxically seems to represent the real context. Note that coupled models belong to applied science.

Many recent innovative technological processes use the concept of matching physical (observable) operations with their (virtual) mirror models. Matching depth is closely related to the fidelity of the virtual model to the real physical object. Such consistency implies the nature and ability of the model to take into account the variation of the physical element due to its operational and environmental conditions [4]. Therefore, a complete model taking into account all the phenomena governing these conditions becomes necessary and the model uncertainty involved in such a circumstance will be of knowledge type. Currently, in very promising fields, where the large number of creations and the growing importance of digital components in automated

assemblies offer an opportunity to reach higher levels of production [5]. The practice of digital technologies allows the virtual projection of products and processes [6]. The combination of physical and virtual elements can be achieved through the concept of matching physical operations with their mirror models—digital twin (DT). DT is gradually being studied as a means of improving the functioning of physical units by taking advantage of the computational practices made possible by those of virtual pairing. Bidirectional links feed data from the physical element to its virtual image, and process it from the latter to the physical element [7]. This matching sequence (pairing) is a kind of mirroring of real and virtual elements. The virtual one allows various specific tasks of simulation, test, optimization... [8]. Since Michael Grieves introduced the concept of digital twins in 2002, which has quickly taken hold in various fields; the number of publications on its applications has increased significantly.

This contribution aims to illustrate the nature of the observation–modeling link and its relation with elegant theories and coupled models. First, we analyze the role of this link in the managing of elegant universal theories. Then we discuss the relation of these smart theories and coupled models. At the last part of the paper, we illustrate the importance of coupled models in the real-time matching involved in this link and its use in the supervision of complex procedures.

2. Characteristics of the link observation–modeling

This section aims to examine how the two elements of observation and theory each support and mutually form a duo. Thus, we examine how they are complementary and evaluate their actions in the management of universal theories involving validation, explanation and unifying capacities. Finally, we discuss advanced computational tools mimicking the physical paradigms ruled by the duo. All the observation–theory duo activities discussed in this section fall under offline matching practices.

2.1. *Managing of smart theories*

2.1.1. *Observation and theory complementarity*

Observation or theoretical modeling can be self-ruling in areas of investigation that are consistently seen as standards. However, in widespread cases, we use the two items in a complementary way. Therefore, yet in a domain that customarily necessitates observation, it is generally not autonomous and it requires modeling for further investigation. Structural research in social sciences is a typical example in this category; see e.g. [9], in addition, in a field currently requiring theoretical modeling, it is not regularly either autonomous and it requires to be validated by observation, simply to be reliable [10], as we will see in the next lines.

2.1.2. *Validating or invalidating a theory by observation*

In general, a theory is only thought to be established after it has been verified by observation. Furthermore, such a theory stays true until inconsistency with another observation.

Validation of the theory of superposition states in quantum mechanics. Considering the case of the "theory of superposition states" in quantum mechanics proposed by Schrödinger in 1926 [11], (Nobel 1933). In this theory, the wave function provides the probability of locating a particle at a specific position. Wineland's ion traps [12] and the cavity quantum electrodynamics of Haroche [13] validated this theory a little before 2000 (Nobel 2012: for revolutionary experimental methods, which make it possible to measure and manipulate individual quantum systems). It was only after such validation that this theory was established until a possible future invalidation.

Partial invalidation of the treatise of JC Maxwell by the Hall effect. Concerning the "Hall Effect" proposed by Hall in 1879 that resulting from an experiment; it concerns the relation between the force and the current in a conductor. It invalidates part of the "treatise on electricity and magnetism" proposed by Maxwell in 1873 [14]. Hall revealed and experimentally confirmed in his thesis work, the effect of force on current (distribution) in a conductor immersed in a magnetic field [15]. Maxwell thought there was no such effect.

2.1.3. *Observation confirmed and explained later by theory*

One can meet the situation of first reaching a finding from experiments and then establishing the theory explaining and confirming such discovery. Generally, we come across such a situation in a "serendipity condition": we find something while looking for another. A typical illustration is the revealing of the superconductivity phenomenon by Kamerlingh Onnes (1853–1926), (Nobel 1913: for his investigations on the properties of matter at low temperatures which led, inter alia, to the production of liquid helium) [16]. In this context, he was studying the problems connecting to the effects of low temperatures on electronics. He could not imagine the phenomenon he observed. All the theories confirming and explaining the superconductivity phenomenon followed his discovery.

2.1.4. *Generalizing and amalgamating observations by a theory*

Several characteristics can distinguish intelligence of theories such as enhancement, generalization, and fusion. An example of such intelligence can be seen in Maxwell's equations, which are an illustration of the highest elegant composite theories. These equations originated by James Clerk Maxwell (1831–1879) incorporate an association of three laws that are obtained experimentally, discovered by three of his predecessors. They are Carl Friedrich Gauss (1777–1855), André-Marie Ampère (1775–1836) and Michael Faraday (1791–1867). The unification of Maxwell's equations was possible only because Maxwell remarked how to progress from the three experimental laws, introducing into one equation a missing link, the announced displacement current, the occurrence of which guarantees the consistency of the integrated organization [2, 14].

2.2. *Innovative computing tools imitating physical paradigms*

Neuromorphic and quantum computing technologies are two constructed tools based on imitations of physical systems. These two modeling tools originate straight from two paradigms belong to neurosciences and quantum physics.

2.2.1. *Neuromorphic computing*

The brain is an exceptionally intricate organization that performs tasks much quicker than the swiftest digital computers. Neuromorphic computing uses inspired models of the brain built on biologically replicated or artificial neural networks. Neuromorphic computers can perform complex calculations quicker, with greater power efficiency and lesser size than traditional architectures. They have the capacity to expand trained real-time learning algorithms to work online like real brains. This showed potential due to the similarities of biological and artificial neural networks (BNN and ANN) [17]. The rising request of deep learning and neural networks has stimulated a sprint to advance artificial intelligence (AI) hardware devoted to neural network calculations [18]. These tools are broadly operated in optimization, diagnostics, images, machine learning, AI, etc.

2.2.2. *Quantum computing*

The notion of states in quantum mechanics is the base of "quantum computers", a term created by Richard Feynman [19]. A typical computer uses transistors to process information in sequences of zeros and ones (binary mode). A quantum computer uses qubits according to the rules of quantum mechanics connecting to particle states. For a qubit, a particle can be in several states simultaneously, as well, a different phenomenon affects particle states called entanglement. This means that when two qubits in a superposition meet; signifying the state of one depends on the state of the other. Due to these phenomena, a quantum computer can achieve 0, 1, or both states at the same time for a qubit or a qubit entanglement. Thus, an n-qubit quantum computer can work instantaneously on the 2n possibilities; however, a standard computer with n bits can only operate on one of these 2n possibilities at a time. Therefore, the former gives us more processing power. Scientists agree that quantum computers are theoretically exponentially faster and much smarter at cracking codes that are apparently unfeasible for classical technology [20, 21].

3. Idealized smart theories and coupled models

This section aims to analyze and discuss the characteristics of elegant theories and realistic coupled models. Often, the notion of elegance belongs to the philosophy of science. On the other hand, in the present article we specify that the use of the term of elegance of theories concern fundamental sciences whereas that of coupled models concerns applied sciences. Let us clarify the notion of elegance in the theories of fundamental sciences. When a theory describes a phenomenon in a clear and direct way, it is said to be elegant. Additionally, an easy-to-understand construct can provide a large amount of information and answer many questions. Therefore, the definition of elegance as simplicity and greater capacity seems right. Note that this last statement is only valid when the theory is employed within its strict scope of application.

3.1. *Smart theories and postulations*

Let us consider a real physical problem which could be represented by the field A, which is the union of the functions B, C, D ... which depend on the variables x, y, z .... Each of these functions relates to a different domain of science. On the other hand, often a domain is more concerned by the problem studied than the others are, let us call it the main domain and represent it by the function B in (1). If we allow that the main domain B can represent the real problem, Equation (2) will give this approximation A_1. Moreover, founding coherent and elegant theories usually requires postulations that compress and idealize the real context resulting in A_2 given by (3).

$$A: \ \mathrm{B(x,y)} \cup \mathrm{C(y)} \cup \mathrm{D(z)} \ldots \tag{1}$$

$$A_1: \ \mathrm{B(x,y)} \tag{2}$$

$$A_2: \ \mathrm{B(x)} \tag{3}$$

Note that the validation of this elegant theory given by A_2, which allows its foundation, must also be done under these postulation conditions.

Therefore, when we model a real problem using the main domain idealized theory, the result would often be erroneous. This is due to committing two approximations. The first is relative to overlooking the other domains influences (replacing A by A_1) and the second is due to the use of idealizing postulations (replacing A_1 by A_2). The more these two approximations are

unfounded vis-à-vis the real setting, the obtained results will be far from the reality. In such a case, in order to adjust this situation, we have to track a reverse procedure that to re-integer in the model, via coupling, all the ignored aspects subsequent to the used approximations. Concerning the reduction from expressions (1)–(3), one can study a given problem from different aspects corresponding to different reductions involving different approximations. This depends, for a multi-domain problem, on the investigated domain. For example, we will consider a problem involving thermal and biological domains. When studying thermal performance, one may tend to introduce biological approximations for reduction and reciprocally.

3.2. *Revised coupled models and solution strategy*

The reverse procedure mentioned in the last section will go through a kind of revised model comprising the main theory associated with the other theories involved and reintegrating into the model all the characteristics ignored in the idealizing action. In general, coupled problem schemes involve the mathematical solution of equations governing different natural or artificial phenomena belonging to distinct branches of the theoretical sphere. The nature of the behaviors of these phenomena and their interdependence as well as the proximity of their temporal evolution (time constants) are directly linked to the approach of solving the corresponding governing equations. Each of these behaviors can be linear or non-linear and have a low or high time evolution. Moreover, these behaviors can be independent or interdependent, which may or may not be linear. At one extreme, we have the case of independent linear behaviors with very distant time constants. In this case, we can solve the governing equations individually. At the other extreme, we have the case of nonlinear and, nonlinearly interdependent, behaviors with very close time constants. In this situation, we need a strongly coupled simultaneous solution of equations. Between these two extremes, the equations can be solved in consecutive progression mode by iteration according to the severity and the degree of complexity of the behaviors.

Moreover, in general, the nature of the source, the behavior of the matter and the geometry concerned in the real problems are more complex than, those envisaged in a smart theory. Therefore, the spatial and temporal behaviors of the different variables in the corresponding equations are also more complicated compared to elegant theories. Such a complex system of equations does not allow analytical solutions. In order to apply the theories correctly, it is often necessary to consider a discretized form in space and time of the equations. In this case, the theories will operate locally in finite discrete domains for which the global assembly solution will operate in the discretized time domain. Spatial local non-linearity is considered by iterative procedures.

3.3. *Case of electromagnetic and energy conversion systems*

For a better understanding of the problem addressed in the last section, we will consider an application in the field of electromagnetic systems (EMS) including energy conversion drives. These are present in many societal applications such as mobility, health, security, communication, etc. In these systems, the intelligent management, conversion and supervision of energy involve the use of an accurate realistic representation of the arrangement concerned. A revised realistic coupled model achieves this goal through its use in system design, optimization, and control. The main field in such a case is electromagnetic (EM), which is governed by Maxwell's equations. However, EMS generally behave in four territories: electrical, magnetic, mechanical and thermal.

3.3.1. *Maxwell equations*

This system of equations can be formulated mathematically in different forms depending on the problem under consideration. One of the most common is the basic full-wave electromagnetic formulation given by:

$$\nabla \times \mathbf{H} = \mathbf{J} \tag{4}$$

$$\mathbf{J} = \sigma \mathbf{E} + \mathrm{j}\omega \mathbf{D} + \mathbf{Je} \tag{5}$$

$$\mathbf{E} = -\nabla \mathrm{V} - \mathrm{j}\omega \mathbf{A} \tag{6}$$

$$\mathbf{B} = \nabla \times \mathbf{A} \tag{7}$$

where **H** and **E** are the magnetic and electric fields, **B** and **D** are the magnetic and electric inductions, **A** and V are the magnetic vector and electric scalar potentials. **J** and **Je** are the total and source current densities, σ is the electric conductivity and ω is the frequency pulsation. The symbol ∇ is a vector of partial derivative operators, and its three possible implications are gradient (product with a scalar field), divergence and curl (dot and cross products respectively with a vector field). The magnetic and electric behavior laws respectively between **B**/**H** and **D**/**E** are characterized respectively by the permeability μ and the permittivity ε.

The solution of Equations (4)–(7) permits to determine in a system the concerns of electromagnetic fields for a frequency pulsation accounting for the magnetic materials behaviors through the permeability, for eddy currents in electric conductors through the electric conductivity and for behavior of dielectrics through the permittivity. Often, EMS involve other fields than EM. In some cases, the influence of these other fields could be negligible and it will be then possible to solve the problem correctly with only the Maxwell's equations. In general, to model an EMS we need to account for other fields in addition to EM field through the coupling of the corresponding governing equations. As mentioned before, EMS behave under four phenomena: electrical, magnetic, mechanical, and thermal. The first three have small and relatively near-time constants while the thermal phenomenon has a relatively higher time constant. The different mixtures of these phenomena can be classified into causal (system behavior), integrated (electrical and magnetic) and intrinsic material (functional). The last mainly concerns intelligent materials such as magnetostrictive, electrostrictive, shape-memory, thermoelectric ....

3.3.2. *Coupling and solution of equations in EMS*

The solution of the equations of the events involved must take into account different specifications. The nature of the behavior of the system concerned, involves analyses either in the frequency domain or in the time domain. The fact that EMS often have complex geometries and involve materials with nonlinear laws of behavior implies going through a local distribution of variables such as, fields, potentials .... For this purpose, we use 2D or 3D discretized geometric cells, with conditions defined on the boundaries of the discretized domains, see e.g. [22, 23]. The above-mentioned categories of couplings are detailed as follows.

Integrated coupling. Generally, in EMS the current is delivered by a voltage source through an external electric circuit. The general relation between the voltage v and the current i in the circuit is given by:

$$v = 1/C \cdot \int i \, \mathrm{d}t + r\, i + L \cdot \mathrm{d}i/\mathrm{d}t + \mathrm{d}\Psi/\mathrm{d}t + \eth \tag{8}$$

In this expression r is the total resistance of the circuit, L a linear inductance, C a capacitance, $\eth$ a non-linear voltage drop (e.g., a diode) in the electrical circuit and Ψ the implied flux linkage.

This circuit equation should be solved coupled with the EM equations. Therefore, the equations to solve are (4)–(8). This coupling between the EM domain and the external electric circuit is particular regarding other couplings with other domains than EM because it represents a

"correction" inside the EM domain. We call it integrated coupling. Generally, the coupling of EM domain with the external electric domain needs simultaneous strong solution of the equations due to non-linearity of behaviors and closeness of the magnetic and electric time constants, see e.g. [24].

Causal couplings. This class of couplings is related to system behavior. Typical situations in this category are the EMS that governed by EM domain, where the operation, the source or the outcome is directly related to another domain. Most EMS related to energy conversion stand in this category; for instance, the mechanical source or outcome respectively in electric generators, e.g. [25] or motors e.g. [26]. These cases may involve behavioral alterations in the EM and other areas modified by each other. This happens when the behaviors are interdependent. The solution of the equations for a given EMS would be separate, iterative or strongly coupled, as mentioned before, depending on the severity of the behaviors.

EM and mechanical coupled problem. We consider the case of an EMS where beside EM the mechanical domain is involved in forms of displacement or deformation. Let us consider the example of the typical electromagnet given in Figure 1, which is a characteristic EMS involving electro–magneto–mechanical aspects permitting to illustrate the consideration of these different domains [27]. It consists of a stationary part constituted of non-conducting magnetic material (μ) and a mobile armature made of conducting magnetic material (μ, σ). A coil fed by a voltage source excites the stationary part. The mobile armature is connected to a spring, a damper and an external force. The equations governing such a system are:

$$m \cdot \mathrm{d}^2X/\mathrm{d}t^2 + c \cdot \mathrm{d}X/\mathrm{d}t + kX = F_{\mathrm{mag}} + F_{\mathrm{ext}} \tag{9}$$

$$\mathrm{d}\Psi/\mathrm{d}t + rI = U \tag{10}$$

In these equations, U is the source voltage and I the current in the exciting coil. X is the displacement, F_{mag} and F_{ext} are the magnetic and external forces, m, c and k are respectively the mass of the moving object, the damping coefficient and the stiffness of the spring. It may be noted that (10) is a particular case of (8).

We consider for example in the system in Figure 1 a step source voltage in the exciting coil. The unknown variables are the current I across the coil and the displacement X of the mobile armature. The magnetic linkage flux Ψ and the magnetic force F_{mag} generally could be nonlinear function of the magnetic saturation and the mechanical motion. To solve the problem we have to consider Equations (4)–(7) with the mechanical and circuit equations (9)–(10). Generally, the coupling of EM domain with the mechanical domain needs simultaneous strong solution of the equations due to non-linearity of behaviors and closeness of the time constants.

EM and thermal coupled problem. We consider the case of EMS where in addition to EM the thermal domain is present in the form of heating production [28] or resulting undesirable heating [29]. Heat production by means of EMS can be magnetic induction heating by eddy currents in conducing metals owning high conductivity or electric induction microwave heating in dielectric materials possessing high permittivity [30]. The coupling of EM and thermal domains involves phenomena with very different time constants. Moreover, the problem may include nonlinear behaviors and/or variables that are interdependent. Here we need a weak separately iterative coupling.

Material intrinsic couplings. This class of couplings is relative to functional nature regarding material intrinsic interactions. These concern mainly smart materials that each linking two phenomena: magnetostrictive (magnetic–mechanic), electrostrictive (electric–mechanic), shape-memory (thermic–mechanic), and thermoelectric (thermic–electric).

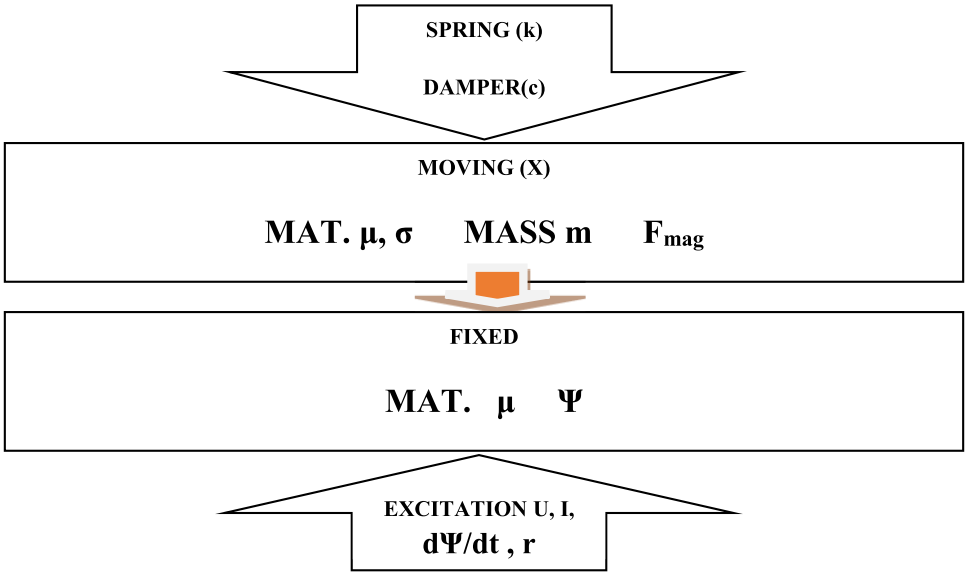

Figure 1. Schematic of an electromagnet involving electro–magneto–mechanical aspects [3].

The couplings in these cases relate to two groups. The first reflects linear behavior (electrostrictive) and/or very different time constants (shape-memory, thermoelectric). In this case, we can practice separate solutions or coupled iterative solutions for respectively independent or interdependent behavior [31, 32]. The second concerns non-linear behavior and/or close time constants (magnetostrictive). In function of the complexity of the nonlinear relationships, we use strong coupling or multiscale methodologies [33, 34].

3.3.3. *Supervised energy conversion systems*

Energy conversion drives are frequently used in a wide range of applications ranging from small household appliances of a few watts to heavy industrial needs in megawatts, including mobility, medical, robotics applications.... These drives are supervised in several ways depending on the nature of the application in terms of required accuracy and required response time, ranging from slow to instantaneous; see e.g. [35–37]. In any case, we need the most accurate model of the drive involved in the control, which allows efficient and robust supervision. These energy conversion devices can be involved in simple automated systems or in complex supervised adaptive and dynamic procedures. This topic will be discussed in the next section.

4. Online matching of the observation–modeling pair

In Section 2, we surveyed the virtues of offline observation–modeling pairing. This duo is actively involved in many natural and artificial processes operating in online (real-time) pairing mode. This concerns both simple automated systems and complex procedures.

4.1. *Automated procedures*

Automated systems are used in various fields related to energy, industrial manufacturing, mobility, health.... In various automated procedures, sensors are commonly used to determine specific operating variables and system parameters. However, in some situations, estimation can

be used for variables or parameters that are difficult to measure. Accurate parameter estimation plays a crucial role in the operation of automated systems. The implementation of an estimation algorithm on an embedded controller platform requires the simplification of the mathematical model of the system. That is why we often have to do this estimation offline to get reasonable accuracy. For this, one can use Computer Aided Design (CAD) tools based on complete models representing the systems in their environments (see Section 3.3). In such a case, the matching of the estimated parameters with the actual parameters would be successful. However, the problem is that pairing cannot be instantaneous with the system running. Various studies have proposed a compromise between the precision of the estimation and the speed of the matching by implementing, more sophisticated algorithms, on specialized platforms of embedded controllers [35–37]. For this, in automated systems, different types of observers, state filters and controllers are offered as estimators. The robustness of the controller is supported by the use of adaptive methods. Large-capacity microcontrollers can improve controller board design and software required for estimation, which iteratively targets the match simultaneously.

4.2. *Observation–modeling pairing in complex procedures*

Real-time pairings in complex processes are present in different natural circumstances practiced or involved in functions. In addition, online matching of complex procedures is used in many innovative applications.

4.2.1. *Modeling matching observation in natural processes*

As mentioned in Section 1, creatures often engage in the practice of sensory observation and simultaneously use deductive skills to manage their natural lives. Also that the activities of deduction and prediction associated with observation are one of the first natural duties born in the world. In this section, we will discuss and analyze two natural processes, the dynamic adaptive camouflage in ecology and the Bayesian Brain theory in neuroscience.

Dynamic camouflage. In nature, based on observation, cases of mimetic simulation (imitation strategy) are very frequent allowing camouflage [1]. This permits creatures to blend into their surroundings. It may be a predation strategy or an anti-predation adaptation. It relates to camouflage and imitation that may involve visual, olfactory or auditory cover-up through sensory systems. There are two main categories of camouflage. A form of camouflage consists in the selection of a support, of the environment on which to “land” or/and “disappear”. The second form of camouflage is that of dynamic metamorphosis. The first corresponds to choose a matched environment in a single step, and the second corresponds to a self-adapting (transfiguration) dynamic matching. Thus, we have an offline matching resulting from a single observational imitation in the first case and an online dynamic adapting matching in the second. There is a significant literature regarding the multiplicity, processes, roles, and evolution of camouflage, which is measured by the sensory systems of predators targeted by camouflage; see e.g. [38, 39]. This depends on the ability of predators to identify the impacts of predation-enforced selection, where changes in environmental characteristics can be quantified. The victim needs, even if it is complex, to identify changes in the visual systems, cognition and behavior of predators. Just as any victim often uses multiple forms of encryption; it is likely that their predators have multiple ways to defeat them, in response to multiple types of prey. Indeed, the mimetic victim individual adopts the appearance and colors of its environment and remains motionless so as not to be detected by its predators. In addition to color, some organisms are also able to take on the shape of their viewpoint object. Many insects can thus take on the appearance of branches or leaves. This defensive imitation gives the individual protection against predation. There are also cases of offensive imitation, which allows the mimetic individual to chase his victim without being noticed.

The junction between observation capacities and mimetic capacities is practiced in a successive way, which allows the improvement of these capacities.

Bayesian brain theory. The Bayesian theory of the brain in neuroscience is widely recognized when it comes to brain function. This theory briefly indicates that after a cerebral sensory observation (vision, smell, hearing, etc.), the predictive model of the brain generates, from the learned data, cerebral perspectives of the observed phenomenon or object. Note that in this case, the predictive model is managed by a sophisticated supercomputer (Human brain: 10^{11} neurons each linked to 10^4 others). Bayesian brain theory explains the cognitive abilities of the brain to work under circumstances of uncertainty to reach the optimum advocated by Bayesian methodologies [40]. It is assumed that neural structure retains inner probabilistic patterns revised by sensory information via neural processing [41]. Bayesian inference works at the level of cortical macrocircuits, which are structured according to a hierarchy that mirrors the observable object scenes around us. The brain encodes a model of these objects and makes predictions about their sensory input: predictive coding. The corresponding areas of brain activity will be near the top hierarchy. The links from the upper zones to the lower zones then convert a model describing the scenes. The lowest-level predictions are compared to the sensory inputs and the prediction error is distributed up the hierarchy. This happens simultaneously at all hierarchical levels. Predictions are sent and prediction errors are returned in a dynamic process. The prediction error indicates that the actual model did not fully account for the input. The next level readjustment can increase the accuracy and reduce the prediction error [42, 43]. It is clear that the observation–prediction duo works in a real-time two-way matching process.

4.2.2. *Matching twins in complex procedures*

In this section, matched twins in complex procedures will be examined, which helps to expose the concept of digital twin. In Section 4.1, we examined the role of the matching of estimated and actual parameters in automated procedures. This illustrated the need to improve the matching of virtual models to their real procedures. We have seen that the nature of a real system and the uncertainty of the emulation process often makes it difficult to build a realistic virtual system and that we need a compromise between estimation accuracy and speed adaptation in automated systems. These two remarks are related to the improvement of the matching of virtual models to their real procedures. Such an action depends on the qualities of the virtual model and its interaction with the real procedure. The quality of the virtual model is associated with its ability to account for the environmental phenomena involved in the actual procedure. The characteristic of the "real–virtual" link is connected to detection, processing and control capabilities. The weight of the matching improvement becomes particularly crucial in compound procedures where the complexity concerns the various incorporated components accounting for the physical phenomena involved (the notion of complexity will be discussed in the next paragraph). To handle such complex procedures, one can practice the Internet of Things (IoT) which intensely deliberates in the physical domain via direct real-time data collection, or Computer Aided Design (CAD), which focuses exclusively on digital territory. However, it is essential to temper and control the irregular and unnecessary behaviors that occur in these complex procedures. Achieving such a goal requires a matched observation–model twin practiced in the relevant procedure [44]. A consistent representation of such a matched twin is shown in Figure 2. Such a twin differs from both IoT and CAD by focusing on both the physical and digital spheres. This twin requires the practice of different skills mainly involving detection (observation side), calculation (model side) and the information and control link (between observation side and model side). Detection on the observation side concerns the various recognitions of the sensors. Model-side computation could involve simulation, optimization, design, diagnosis, prediction,

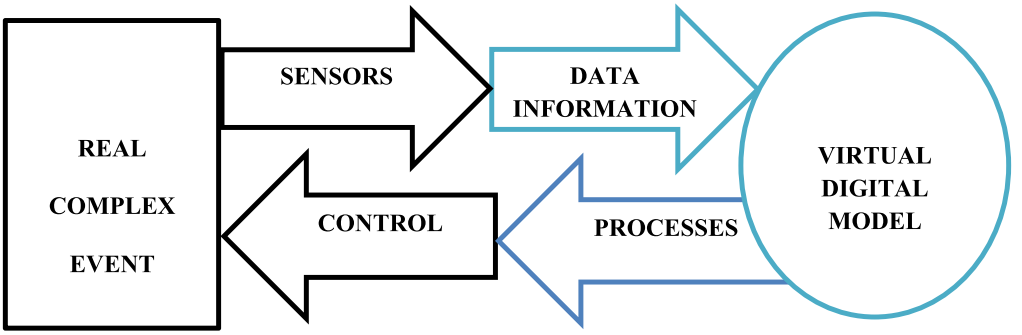

Figure 2. Schematics of a real-time bidirectional matched observation–model twin in a complex procedure.

and testing. These operations can use learned collected data in addition to sensor data. The link between the observation side and the model side is bidirectional. The observation part provides sensor measurements in processed form to the model part while the latter sends process and control information to the observation part.

4.2.3. *Complex systems*

Generally, in the so-called complex procedure, the complexity concerns the components and the physical phenomena involved. Complexity can be defined in terms of interactions [45]. These can be classified into three forms: simple, complicated and complex interactions. The former simply behaves in a direct or linear manner, complicated interactions are linear and loosely coupled while complex interactions with tightly coupled links would be characteristic of a complex system or procedure. Such a classification is reminiscent of the one mentioned previously in Section 3.3, relating to the coupling of different phenomena.

Coupling in a complex system involves its various components. This could represent an oversized model and we can use model reduction techniques, see e.g. [46], while preserving accuracy depending on the application concerned (modeling, design, optimization or online supervision).

4.2.4. *Digital twin concept*

The twin described in Section 4.2.2 (Figure 2) corresponds to the Digital Twin DT. Grieves [44] first introduced this concept in 2002. It is distinguished by a beneficial two-way communication between the digital and physical spheres. The three components of a DT are a paired physical observable, a real-time replicated digital element, and their sensory, processing, control, and pairing links. The physical element dynamically adjusts its behavior in real time according to the recommendations made by the digital element. While the digital item correctly reproduces the real state of the territory of the physical product. Thus, DT offers an intelligent alliance of the physical and digital domains. Thus, in DT technology, physical observation and virtual modeling are interconnected in a reciprocal exchange in real time. The observed element corrects the virtual error and the virtual element corrects the observed sensory data. This iterative process leads to a more objective and intelligent association. The DT concept is mainly used for fault diagnosis, predictive maintenance, performance analysis and product design [47]. This concerns various fields and innovative industrial devices such as energy and utilities, aerospace and defense, automotive transport, machinery manufacturing, healthcare and consumer goods.

Note that similar uses of the concept of DT existed [48] before its introduction in 2002 by Grieves [44]. As early as 1993, in “Mirror Worlds”, David Gelernter evoked a similar concept,

the possibilities of software models, which represent a portion of reality [49]. However, even before that, NASA used complex simulations to monitor spacecraft safety [50]; then came the unexpected explosion of the oxygen tank of the Apollo 13 mission in 1970 [51]. Following this accident, the mission modified several high-fidelity simulators to adapt them to the real conditions of the damaged spacecraft and used them to land safely [52]. This was probably one of the first real applications of a DT. This involved several basic features of a DT, although it was not a familiar concept in 1970.

4.2.5. *Examples of applications of DT*

Given the huge number of publications on DT, and to illustrate the range of applications, from manufacturing to smart cities, we will provide several examples from different areas of this work. One of DT's most widely used businesses is industrial manufacturing and product design. For example, the pairing of physical and virtual products can be used for the iterative redesign of an existing product or for the creation of a new product. Such DT-based product design can guide manufacturers to support the product design process, see e.g. [53, 54]. Additionally, the integration of manufacturing data and sensory data in the development of DT virtual products that can enhance cyber-physical manufacturing capabilities can be valuable [55]. Another activity of DT concerns predictive maintenance, which is used in many fields. In the context of industrial procedures, predictive maintenance has become an important concern; the main objective is to optimize the maintenance schedule by predicting system and process failures. Such an approach will result in a reduction in unplanned system downtime and severe outages. In addition, the advantages are the minimization of costs and the reduction of the substitution of fundamental elements of the system, see e.g. [56–59]. Additionally, we can mention healthcare services using DT technology as an exciting and encouraging approach that can promote progress efforts in medical innovations and improve clinical and societal health outcomes [60, 61]. In addition, DT's security business as Cyber DT designed for cybersecurity protection [62] and security of DT-based industrial automation and control systems [63]. Also in control, DT technology is used for applications in control centers of electrical systems and in mechatronic systems [64]. Another activity concerns the application of DT technology in EV smart electric vehicles. This concerns various aspects such as autonomous navigation control, driver assistance systems, vehicle health monitoring, battery management systems, electronics and electric drive systems [65, 66]. In addition to the mentioned examples of using DT, we can mention some innovative applications. The application of DT in the livestock sector to improve large-scale precision farming practices, machinery and equipment use, and the health and well-being of a wide variety of animals [48]. Moreover, the application of DT in smart cities to ensure smart aspects in real estate, transportation, construction, health system, building, home, transportation and parking [67].

5. Conclusions

The analysis, discussion and evaluation carried out in this contribution have brought to light the following points. Offline matching in the observation–theory link has proven effective in managing and governing elegant theories. We can synthesize the characters of this duo as follows, a mathematical theory simply needs observation to be credible and observation needs a theory to be universal allowing further research. Real-time pairing in the observation–modeling link governs natural phenomena and requires comprehensive models in the supervision of automated and complex physical procedures to behave in the most advantageous manner. The DT concept has shown a wide range of innovative applications with promising capabilities in various modern everyday uses.

Declaration of interests

The authors do not work for, advise, own shares in, or receive funds from any organization that could benefit from this article, and have declared no affiliations other than their research organizations.

Funding

This research received no external funding.

References

[1] H. W. Bates, "Contributions to an Insect Fauna of the Amazon Valley. Lepidoptera: Heliconidae", *Trans. Linnean Soc. Lond.* **23** (1862), no. 3, p. 495-566.
[2] J. C. Maxwell, "A dynamical theory of the electromagnetic field", *Phil. Trans. R. Soc. Lond.* **155** (1865), p. 459-512.
[3] A. Razek, "Coupled models in electromagnetic and energy conversion systems from smart theories paradigm to that of complex events: a review", *Appl. Sci.* **12** (2022), article no. 4675.
[4] A. Razek, "Review of pairing exercises involving a real event and its virtual model up to the supervision of complex procedures", *J. Human Earth Future* **2** (2021), no. 4, p. 424-437.
[5] P. Leitão *et al.*, "Smart agents in industrial cyber-physical systems", *Proc. IEEE* **104** (2016), no. 5, p. 1086-1101.
[6] M. Abramovici *et al.*, "Reconfiguration of smart products during their use phase based on virtual product twins", *CIRP Annals - Manuf. Technol.* **66** (2017), no. 1, p. 165-168.
[7] W. Kritzinger *et al.*, "Digital twin in manufacturing: a categorical literature review and classification", *IFAC-Pap. Online* **51** (2018), no. 11, p. 1016-1022.
[8] D. Jones *et al.*, "Characterising the digital twin: a systematic literature review", *CIRP J. Manuf. Sci. Technol.* **29** (2020), p. 36-52.
[9] C. Lévi-Strauss, *Structural Anthropology*, Basic Books, Paris, 1958.
[10] H. Spiegelberg, "The phenomenological philosophy of Maurice Merleau-Ponty (1908–1961)", in *The Phenomenological Movement*, Springer, Dordrecht, 1971, Second Edition. Mouton de Gruyter, Berlin, New York, 1991, p. 516-562.
[11] E. Schrödinger, "An undulatory theory of the mechanics of atoms and molecules", *Phys. Rev.* **28** (1926), no. 6, p. 1049-1070.
[12] D. J. Wineland *et al.*, "Experimental issues in coherent quantum-state manipulation of trapped atomic ions", *J. Res. Nat. Inst. Standards Technol.* **103** (1998), no. 3, p. 259-338.
[13] M. Brune, S. Haroche *et al.*, "Manipulation of photons in a cavity by dispersive atom–field coupling: quantum-nondemolition measurements and generation of Schrödinger cat states", *Phys. Rev. A* **45** (1992), no. 7, p. 5193-5214.
[14] J. C. Maxwell, *A Treatise on Electricity & Magnetism*, Dover Publications, New York, 1873, ISBN 0-486-60636-8 (Vol. 1) & 0-486-60637-6 (Vol. 2): https://www.aproged.pt/biblioteca/MaxwellI.pdf.
[15] E. H. Hall, "On a new action of the magnet on electric currents", *Amer. J. Math.* **2** (1879), no. 3, p. 287-292.
[16] A. Laesecke, "Through measurement to knowledge: the inaugural lecture of Heike Kamerlingh Onnes (1882)", *J. Res. Nat. Inst. Standards Technol.* **107** (2002), no. 3, p. 261-277.
[17] S. Haykin, "Neural networks: a guided tour", in *Soft Computing and Intelligent Systems*, Academic Press, San Diego, 2000, Chapter 3, p. 71-80.
[18] G. W. Burr *et al.*, "Neuromorphic computing using non-volatile memory", *Adv. Phys.: X* **2** (2016), no. 1, p. 89-124.
[19] R. P. Feynman, "Simulating physics with computers", *Int. J. Theoret. Phys.* **21** (1982), no. 6–7, p. 467-488.
[20] D. Castelvecchi, "Quantum computers ready to leap out of the lab in 2017", *Nature* **541** (2017), no. 7635, p. 9-10.
[21] A. K. Fedorov, E. O. Kiktenko, A. I. Lvovsky, "Quantum computers put blockchain security at risk", *Nature* **563** (2018), no. 7732, p. 465-467.
[22] Z. Ren, A. Razek, "New technique for solving three-dimensional multiply connected eddy-current problems", *IEE Proc. A: Phys. Soc. Meas. Instr.* **137** (1990), no. 3, p. 135-140.
[23] C. Li, Z. Ren, A. Razek, "An approach to adaptive mesh refinement for three-dimensional eddy-current computations", *IEEE Trans. Magn.* **30** (1994), no. 1, p. 113-117.
[24] F. Piriou, A. Razek, "A non-linear coupled 3D model for magnetic field and electric circuit equations", *IEEE Trans. Magn.* **28** (1992), no. 2, p. 1295-1298.
[25] F. Piriou, A. Razek, "Numerical simulation of a nonconventional alternator connected to a rectifier", *IEEE Trans. Energy Conv.* **5** (1990), no. 3, p. 512-518.
[26] E. Mendes *et al.*, "Losses minimization of a field oriented controlled induction machine", in *Seventh International Conference on Electrical Machines and Drives (IET)*, IET, Durham, 1995, p. 310-314.

[27] Z. Ren, A. Razek, "A strong-coupled model for analyzing dynamic behaviors of non-linear electromechanical systems", *IEEE Trans. Magn.* **30** (1994), no. 5, p. 3252-3255.
[28] F. Bay *et al.*, "A numerical model for induction heating processes coupling electromagnetism and thermo-mechanics", *Int. J. Numer. Meth. Eng.* **58** (2003), p. 839-867.
[29] C. Jörgens, M. Clemens, "Electric field and temperature simulations of high-voltage direct current cables considering the soil environment", *Energies* **14** (2021), article no. 4910.
[30] A. Sekkak, L. Pichon, A. Razek, "3-D FEM magneto-thermal analysis in microwave ovens", *IEEE Trans. Magn.* **30** (1994), no. 5, p. 3347-3350.
[31] H. Hariri *et al.*, "Dual piezoelectric beam robot: the effect of piezoelectric patches' positions", *J. Intel. Mat. Syst. Struct.* **26** (2015), no. 18, p. 2577-2590.
[32] S. A. Rios, A. J. Fleming, Y. K. Yong, "Miniature resonant ambulatory robot", *IEEE Robot. Autom. Lett.* **2** (2017), no. 1, p. 337-343.
[33] M. Besbes, Z. Ren, A. Razek, "A generalized finite element model of magnetostriction phenomena", *IEEE Trans. Magn.* **37** (2001), no. 5, p. 3324-3328.
[34] O. Bottauscio, P. E. Roccato, M. Zucca, "Modeling the dynamic behavior of magnetostrictive actuators", *IEEE Trans. Magn.* **46** (2010), no. 8, p. 3022-3028.
[35] G. Soto *et al.*, "Reduced-order observers for rotor flux, rotor resistance and speed estimation for vector control induction motor drives using the extended Kalman filter technique", *IEE Proc.-Elec. P. App.* **146** (1999), no. 3, p. 282-288.
[36] F. Alonge *et al.*, "Sensorless control of induction-motor drive based on robust Kalman filter and adaptive speed estimation", *IEEE Trans. Indust. Electron.* **61** (2014), no. 3, p. 1444-1453.
[37] C. El Moucary, E. Mendes, A. Razek, "Decoupled direct control for PWM inverter-fed induction motor drives", *IEEE Trans. Indust. Appl.* **38** (2002), p. 1307-1315.
[38] J. Galloway *et al.*, "Finding a signal hidden among noise: how can predators overcome camouflage strategies?", *Phil. Trans. R. Soc.* **375** (2020), no. 1802, article no. 20190478.
[39] N. Price *et al.*, "Background matching and disruptive coloration as habitat-specific strategies for camouflage", *Sci. Rep.* **9** (2019), article no. 7840.
[40] D. C. Knill, A. Pouget, "The Bayesian brain: the role of uncertainty in neural coding and computation", *Trends Neurosci.* **27** (2004), no. 12, p. 712-719.
[41] W. Penny, "Bayesian models of brain and behaviour", *ISRN Biomath.* **2012** (2012), p. 1-19.
[42] A. Pouget *et al.*, "Probabilistic brains: knowns and unknowns", *Nat. Neurosci.* **16** (2013), no. 9, p. 1170-1178.
[43] J. Hohwy, "Priors in perception: top-down modulation, Bayesian perceptual learning rate, and prediction error minimization", *Conscious. Cogn.* **47** (2017), p. 75-85.
[44] M. Grieves, J. Vickers, "Digital twin: mitigating unpredictable, undesirable emergent behavior in complex systems", in *Transd Perspe on Complex Systems*, Springer, Cham, 2017, p. 85-113.
[45] C. Perrow, *Normal Accidents: Living with High Risk Technologies - Updated Edition*, Princeton University Press, Princeton, NJ, 2011.
[46] B. Besselink *et al.*, "A comparison of model reduction techniques from structural dynamics, numerical mathematics and systems and control", *J. Sound Vibr.* **332** (2013), no. 19, p. 4403-4422.
[47] B. He, K. J. Bai, "Digital twin-based sustainable intelligent manufacturing: a review", *Adv. Manuf.* **9** (2021), no. 1, p. 1-21.
[48] S. Neethirajan, B. Kemp, "Digital twins in livestock farming", *Animals* **11** (2021), no. 4, article no. 1008.
[49] D. Gelernter, *Mirror Worlds: Or the Day Software Puts the Universe in a Shoebox … How It Will Happen and What It Will Mean*, Oxford University Press, Oxford, 1993.
[50] F. Tao *et al.*, "Make more digital twins", *Nature* **573** (2019), no. 7775, p. 490-491.
[51] G. A. Boy, *Human–Systems Integration: From Virtual to Tangible*, CRC Press, Florida, 2020.
[52] C. Zhuang *et al.*, "The connotation of digital twin, and the construction and application method of shop-floor digital twin", *Robot. Comput.-Integr. Manuf.* **68** (2021), p. 1-16.
[53] F. Tao *et al.*, "Digital twin-driven product design framework", *Int. J. Product. Res.* **57** (2019), no. 12, p. 3935-3953.
[54] B. He, K. J. Bai, "Digital twin-based sustainable intelligent manufacturing: a review", *Adv. Manuf.* **9** (2021), no. 1, p. 1-21.
[55] Y. Cai *et al.*, "Sensor data and information fusion to construct digital-twins virtual machine tools for cyber-physical manufacturing", *Proc. Manuf.* **10** (2017), p. 1031-1042.
[56] Ş. Y. Selçuk *et al.*, "A workflow for synthetic data generation and predictive maintenance for vibration data", *Information (Switzerland)* **12** (2021), no. 10, article no. 386.
[57] J. J. Montero Jimenez *et al.*, "Towards multi-model approaches to predictive maintenance: a systematic literature survey on diagnostics and prognostics", *J. Manuf. Syst.* **56** (2020), p. 539-557.
[58] M. Nacchia *et al.*, "A systematic mapping of the advancing use of machine learning techniques for predictive maintenance in the manufacturing sector", *Appl. Sci. (Switzerland)* **11** (2021), no. 6, article no. 2546.

[59] Z. Liu, N. Meyendorf, N. Mrad, "The role of data fusion in predictive maintenance using digital twin", *AIP Conf. Proc.* **1949** (2018), article no. 020023.
[60] Y. Liu *et al.*, "A novel cloud-based framework for the elderly healthcare services using digital twin", *IEEE Access* **7** (2019), p. 49088-49101.
[61] M. N. Kamel Boulos, P. Zhang, "Digital twins: from personalised medicine to precision public health", *J. Person. Med.* **11** (2021), no. 8, article no. 745.
[62] D. Holmes *et al.*, "Digital twins and cyber security – solution or challenge?", in *Computer Engineering, Computer Networks and Social Media Conference (SEEDA-CECNSM, 1–8)*, 2021.
[63] C. Gehrmann, M. Gunnarsson, "A digital twin based industrial automation and control system security architecture", *IEEE Trans. Indust. Inform.* **16** (2020), no. 1, p. 669-680.
[64] S. Boschert, R. Rosen, *Digital Twin-The Simulation Aspect. Mechatronic Futures: Challenges and Solutions for Mechatronic Systems and Their Designers*, Springer, Switzerland, 2016.
[65] G. Bhatti, H. Mohan, R. Raja Singh, "Towards the future of smart electric vehicles: digital twin technology", *Renew. Sustain. Energy Rev.* **141** (2021), article no. 110801.
[66] X. Chen *et al.*, "Dynamic safety measurement-control technology for intelligent connected vehicles based on digital twin system", *Vibroeng. Proc.* **37** (2021), p. 78-85.
[67] S. Shirowzhan *et al.*, "Digital twin and CyberGIS for improving connectivity and measuring the impact of infrastructure construction planning in smart cities", *ISPRS Int. J. Geo-Inf.* **9** (2020), no. 4, article no. 240.

Comptes Rendus

Physique

Objectif de la revue

Les *Comptes Rendus Physique* sont une revue électronique évaluée par les pairs de niveau international, qui couvre l'ensemble des domaines de la physique et de l'astrophysique.

Ils publient des numéros thématiques, des articles originaux de recherche, des articles de synthèse, des mises en perspective historiques, des textes à visée pédagogique, ou encore des actes de colloque, en anglais ou en français, sans limite de longueur et dans un format aussi souple que possible (figures, données associées, etc.).

Depuis 2020, les *Comptes Rendus Physique* sont publiés avec le centre Mersenne pour l'édition scientifique ouverte, selon une politique vertueuse de libre accès diamant, gratuit pour les auteurs (pas de frais de publication) comme pour les lecteurs (accès libre, immédiat et pérenne).

À propos de la revue

Les *Comptes Rendus Physique* sont exclusivement publiés au format électronique.

Toutes les informations sur la revue, ainsi que le texte intégral de l'ensemble des articles, sont disponibles sur son site internet, à l'adresse https://comptes-rendus.academie-sciences.fr/physique/.

Informations pour les auteurs

Pour toute question relative à la soumission d'un manuscrit, merci de consulter le site internet de la revue : https://comptes-rendus.academie-sciences.fr/physique/.

Contact

Académie des sciences
23 quai de Conti
75006 Paris (France)
cr-physique@academie-sciences.fr

Comptes Rendus
de l'Académie des sciences

Physique

Volume 25, nº S1, 2024

Special issue / *Numéro spécial*

Energy in the heart of EM waves: modelling, measurements and management / *L'énergie au cœur des ondes électromagnétiques : modélisation, mesures et gestion*

Guest editors / *Rédacteurs en chef invités*

Emmanuelle Conil (ANFR, France), François Costa (ENS Paris-Saclay, Université Paris-Saclay, Université Paris-Est Créteil, France) and Lionel Pichon (CNRS, CentraleSupélec, Université Paris-Saclay, Sorbonne Université, France)

Cover illustration / *Illustration de couverture*

"Electromagnetic waves: artist's view". Credit: Daniel de Fornel.
« Ondes électromagnétiques : vue d'artiste ». Crédit : Daniel de Fornel.

Contents / *Sommaire*

1878-1535 (electronic)

Académie des sciences — Paris

COMPTES RENDUS
DE L'ACADÉMIE DES SCIENCES

Physique

Volume 25, nº S1, 2024